X-ray CCDs for Space Applications: Calibration, Radiation Hardness, and Use for Measuring the Spectrum of the Cosmic X-ray Background

by

Keith Charles Gendreau

B.A., Cornell University (1989)

Submitted to the Department of Physics
in partial fulfillment of the requirements for the degree of

Doctor of Philosophy

at the

MASSACHUSETTS INSTITUTE OF TECHNOLOGY

May 1995

Author .....
Department of Physics
May 14, 1995

Certified by .....
George R. Ricker
Senior Research Scientist
Thesis Supervisor

Accepted by .....
George F. Koster
Chairman, Graduate Committee

X-ray CCDs for Space Applications: Calibration, Radiation Hardness, and Use for Measuring the Spectrum of the Cosmic X-ray Background

by

Keith Charles Gendreau

Submitted to the Department of Physics
on May 14, 1995, in partial fulfillment of the
requirements for the degree of
Doctor of Philosophy

Abstract

This thesis has two distinct components. One concerns the physics of the high energy resolution X-ray Charge Coupled Devices (CCD) detectors used to measure the cosmic X-ray background (XRB) spectrum. The other involves the measurements and analysis of the XRB spectrum and instrumental background with these detectors on board the Advanced Satellite for Cosmology and Astrophysics (ASCA).

The XRB has a soft component and a hard component divided at $\sim$2 keV. The hard component is extremely isotropic, suggesting a cosmological origin. The soft component is extremely anisotropic. A galactic component most likely dominates the soft band with X-ray line emission due to a hot plasma surrounding the solar system. ASCA is one of the first of a class of missions designed to overlap the hard and soft X-ray bands.

The X-ray CCD's energy resolution allows us to spectrally separate the galactic and cosmological components. Also, the resolution offers the ability to test several specific cosmological models which would make up the XRB. I have concentrated on models for the XRB origin which include active galactic nuclei (AGN) as principal components. I use ASCA data to put spectral constraints on the AGN synthesis model for the XRB.

The instrumental portion of this thesis concerns the development and calibration of the X-ray CCDs. I designed, built and operated an X-ray calibration facility for these detectors. It makes use of a reflection grating spectrometer to measure absolute detection efficiency, characteristic absorption edge strengths, and spectral redistribution in the CCD response function.

Part of my thesis research includes a study of radiation damage mechanisms in CCDs. This work revealed radiation damage-induced degradation in the spectral response to X-rays. It also uncovered systematic effects which affect both data analysis and CCD design. I have developed a model involving trap energy levels in the CCD band gap structure. These traps reduce the efficiency in which charge transfers through the CCD. I have used the model to extract information about characteristic trapping and detrapping times for electrons in these energy levels out of the X-ray data.

Thesis Supervisor: George R. Ricker
Title: Senior Research Scientist

To my family

Acknowledgments

This thesis would have been impossible were it not for the friendship and help of many people across the globe. Of particular importance to me have been my friends in the CCD laboratory at MIT's Center for Space Research. Mark Bautz has been my instrumentation "sensai". He has also been a very good friend. I thank Mark for his patience, understanding, and support during all the phases of my graduate career at MIT. Mark successfully managed the efforts at the CCD lab to produce the SIS detectors flying on ASCA. Other people at MIT who contributed significantly to the development of the SIS detector include Tye Brady, Steve Kissel, Roland Vanderspek, Pete Tappan, Jimmy O'Conner, Fred Miller, Bitching David Breslau, John Doty, Ed Boughan, Gregory Prighozin, Takashi Isobe, and Andy Rasmussen. John Doty designed many parts of the SIS. Ed Boughan took the electrical designs and made them work. Steve Kissel took the mechanical designs and made them work. A hidden but important part of this effort has been the uninterrupted flow of necessary funding. Thanks to George Ricker for making the proposals with excellent insight which made this possible. At Lincoln Laboratory, Barry Burke and his collegues developed and produced the CCDs used for the ASCA mission. I thank Kenton Phillips, Robin Hood of the Internet Superhighway, for keeping our computers afloat. I thank Rosemary Hanlon for taking care of all us "geeks".

In Japan, SIS team members include Kazu Mitsuda, Hiroshi Tsunemi, T. Dotani, and T. Kotani. Hiroshi Tsunemi taught me almost everything I know about proportional counters and was the driving effort in making the FPC reference detector in the low energy calibration work. Kazu Mitsuda figured out what the DE should do. He also was instrumental in understanding the results of the calibration. Both Kazu and Hiroshi have been excellent friends and teachers of non-standard Japanese language.

ASCA has been a success due to people involved with all components of the satellite. K. Makeshima and his team made the GIS detectors on ASCA. The GIS compliments the SIS very nicely. Peter Serlimitsos and the XRT team at Nagoya and Goddard made the telescopes which provided the broad bandpass. I respect Peter's desire to get the most out of ASCA. I thank "Commander" Kii for his unselfish and constant efforts to keep ASCA running smoothly. He sacrificed much of his time where he could have been doing science so that others could reap the benefits of ASCA. F. Nagase, M. Itoh, C. Otani, R. Fujimoto, and Alex Antunes are among the many who kept ASCA going strong. The powerful army of Japanese students has been invaluable for the day to day operations of ASCA.

Nick White's group at Goddard Space Flight Center wrote much of the standard software for ASCA analysis. They refined some initially rough implements into an excellent collection of tools. This group includes Eric Gotthelf, Ken Ebisawa, Koji Mukai, and Charles Day. I thank Nick White for accepting my "animal" software ways and providing support for me to work in Japan and at GSFC.

The driving force behind ASCA has been Dr. Yasuo Tanaka. It was Tanaka-sensei's leadership and insight which brought people from very different cultures and backgrounds together. It is because of him, that I have many new friends in Japan and elsewhere. He also brought together the people of the instrument teams with scientists who knew exactly what to do with the marvelous capabilities of ASCA.

Working on ASCA, I had the great pleasure to know several key astronomers including Andy Fabian, Richard Mushotzky, and Shri Kulkarni. Andy and Richard told me what was important about the XRB and how to use ASCA to learn more. I thank them both.

Richard, a walking library/cruise director of astronomy, has been my "practical" scientific advisor. Without Richard's constant efforts and interest, this thesis would only be a fraction of what it is. I thank Tahir Yaqoob for writing the XSPEC AGN synthesis model which I used in this thesis. Several others have contributed in a variety of ways to this work. They include Dan McCammon, Gunther Hasinger, Georgio Matt, John Nousek, H. Inoue, Ed Bertschinger, Claude Canizares, Tom Markert, and Gordan Garmire. I thank them all.

A number of people have made life at MIT fun and interesting. In addition to the MIT SIS team members, these people include Chris Becker, Bob Rutledge, Gerry Luppino, Pat Mock, Tom Markert, Francois Martel, Mike Pivavorof, Saul Rappaport, Tim Jones, Steve Jones, Hans Krimm, Amanda Hubbard, and Al Cangahuala.

Shep Doleman has used the essence of "Ying and Yang" to make life unusual and pleasant here at MIT. He has helped me to keep my sanity here through acts and words bordering on insanity during spontaneous coffee breaks and Ninja fights. There is no experience quite like sharing a class with Shep where boring and tasteless concepts such as the ' 'Aharonov-Bohm Effect", the "Saha Equation", and the "Lane Emden Equation" become the "Abomidable Effect", "Ha Ha Equation" and "the Lame Equation"

I thank Hale Bradt and Kathy Flannegan for going beyond the call of duty by supporting me through my introduction to the "special oral exam" club.

I am indebted to Roland, Steve, Mark, Shep, and Rosemary for being the best of friends during several stressful crises during the past few years.

I also appreciate the support of my old Cornell friends Shoko Sakai and Bill Kaplan. It really is nice to have some life outside of MIT.

My friends in Japan made me feel at home on the otherside of the world. I thank Y. Ogasaka, Y. Ikebe, R. Fujimoto, T. Aoki, T. Sonobe, T. Kotani, M. Ishida, Choi-san, and Y. Komhura for including me in their parties both at ISAS and at the local establishments. I cannot thank these people enough for enriching my Japanese vocabulary. I thank Kazumi Asai for always alerting me to dinner and lunch- even when I was on the otherside of the world.

I thank F. Iwata for dealing with all of us strange geigin at ISAS. I am particularly indebted for her switching around of my room number in the guest lodge during certain critical periods of my stay at ISAS.

I thank my friends at Osaka University for their help and support. In particular, I thank Hiroshi Tsunemi, Emi Miyata, Tamura-kun, and Terada-kun.

Finally, I thank my family: Mom, Dad, Kyle, Craig, Mim and Pip Demers, and Mim and Pip Gendreau for always being there.

Contents

List of Figures

List of Tables

Chapter 1

The X-ray Observatory ASCA

This thesis revolves about several aspects of the satellite "ASCA". ASCA stands for "Advanced Satellite for Cosmology and Astrophysics" and was formerly known as "ASTRO-D" before its launch on 20 February 1993 (Tanaka, Inoue, and Holt, 1995). ASCA, a collaborative effort between Japan and the United States, is the fourth Japanese X-ray astronomy satellite. As an observatory, ASCA provides high quality simultaneous spectroscopic and imaging data of the X-ray universe within the 0.5 to 12 keV bandpass. The focal plane detectors are two CCD X-ray cameras and two gas scintillation imaging proportional counters. In this chapter, I will briefly describe the satellite, with particular emphasis on the description of the Charge Coupled Device (CCD) detectors on ASCA. I will start with a very brief history of the X-ray background to motivate why ASCA is important. I will also outline the thesis.

1.1 Introduction

The focus of this thesis is the spectrum of the cosmic X-ray background (XRB). Exellent reviews of the XRB can be found in Fabian and Barcons (1992), McCammon and Sanders (1990), and Schwartz and Gursky (1974). This thesis has two distinct components. One concerns the physics of the latest detectors used to measure the XRB spectrum. The second has to do with the measurements and analysis of the XRB spectrum and instrumental background with these detectors onboard the Advanced Satellite for Cosmology and Astrophysics (ASCA).

Discovered in 1962 during a sounding rocket designed to look for X-rays from the moon

(Giacconi *et al* 1962), the XRB is the oldest known cosmological background radiation field and predates the discovery of the microwave background. In the years after the discovery, it was found that there were two distinct components to the XRB: an extremely anisotropic soft component and an extremely isotropic hard component. The spectral boundary between these components is at roughly 2 keV.

It is commonly thought that the soft XRB is primarily due to 1-2 million degree component of the interstellar medium (ISM) of our own galaxy (McCammon and Sanders 1990). Part of the soft XRB may also have an extragalactic origin. The soft XRB anisotropy is due to various bright and dim local regions as well as to varying optical path lengths through the hot ISM. There is evidence for line emission, although most detectors before ASCA had an energy resolution which could barely resolve the lines (McCammon and Sanders 1990).

The hard XRB was discovered first with detectors sensitive to the 2-6 keV range (Giacconi *et al* 1962). It was immediately noted that the hard XRB was extremely isotropic. This isotropy suggests an extragalactic origin since commonly assumed ISM densities of 1 hydrogen atom per cm^3 would make the galaxy transparent to hard X-rays. Schwartz and Gursky (1974) show that the establishment of an extragalactic origin requires a significant fraction of the XRB to come from red shifts greater than 1. Thomson scattering of X-rays with commonly assumed intergalactic medium (IGM) densities of 10^{-7} to 10^{-5} electrons per cm^3 put upper limits on the distances to surfaces of last scattering at red shifts of about 7. Thus the XRB tells us about the universe at intermediate scales between the current epoch where optical data shows a broad spectrum of galaxy clustering and distant epochs where the microwave background reveals an extremely smooth cosmos. There have been a number of models for the origin of the hard XRB. I discuss these in chapter 4.

There are two basic experimental approaches to understanding the XRB. One is to study the isotropy of the XRB on varying angular scale sizes. The other is measure its spectrum. This thesis will ultimately be concerned with ASCA measurements of the XRB spectrum. But I will show in the following sections that ASCA has capabilites to make contributions to the understanding of the XRB isotropy.

Before the launch of ASCA in 1993, observations were only capable of studying the soft and hard XRB components separately. In both of these bands, the measurement of the spectral intensity was quite uncertain due to the strong dependence of instrumental background on the exact detector configuration and operation. For over a decade after

the XRB discovery, a number of satellites and sounding rockets made measurements of the XRB spectrum which had a rather large scatter due to unkowns about the instrumental background. The detectors in these experiments were typically gas proportional counters which had energy resolutions of about 30-40% around 1 keV and scaled as the X-ray energy to the -1/2 power.

In the late 1970's, the HEAO-1 A2 experiment made a very precise measurement of the XRB spectrum in the 3 to 45 keV band (Marshall *et al* 1980) which carefully removed the uncertainties of the instrumental background. This left the soft XRB spectrum relatively poorly determined.

A number of soft X-ray experiments have suggested that the mean XRB spectral flux exceeds the extrapolation of the HEAO-1 A2 result by as much as a factor of 2 at 1 keV (Hasinger 1992, Wu *et al* 1991). This observation has lead to the speculation that there is a steepening in the XRB in the 1-3 keV band. However, these detectors may have difficulties spectrally resolving the line emission due to the hot ISM galactic component.

ASCA is one of the first of a class of missions designed to overlap the hard and soft X-ray bands. The nominal bandpass of ASCA is 0.4-10 keV. Thus ASCA can look for the expected steepening in the XRB in the 1-3 keV band. Furthermore, the detectors of ASCA have superior spectral resolving power compared to intruments of previous missions. The instrument's high resolution allows us to spectrally separate the galactic line emission from cosmological components. I present the ASCA measurement of the XRB spectrum from 0.4-6 keV in chapter 4.

Also, the high resolution and bandpass of ASCA offers the ability to reject or accept a variety of specific cosmological models which would make up the XRB. Specifically, I have used the ASCA data to examine models for the XRB origin which include active galactic nuclei (AGN) as principal components. AGN come in many types but generally they are galaxies that harbor a very energetic central source- perhaps a massive blackhole. AGN are numerous and bright in X-rays. The X-ray emission includes several model-dependent spectral features, which ASCA can resolve. I use ASCA data to look for signatures in the XRB due to AGN in order to put spectral constraints on the AGN synthesis model for the XRB. I discuss this model and the ASCA results in chapter 4.

This work requires a very good understanding of the intrument. This knowledge came in the process of helping with the development and calibration of the instrument, which utilizes

a charge-coupled device (CCD). For ASCA, we use these CCDs as both X-ray imagers and spectrometers.

As spectrometers, the CCD works like a proportional counter. Individual X-ray photons photoelectrically liberate a number of electrons roughly proportional to the X-ray photon energy. For X-rays, the number of electrons liberated is of order 100 to 3000. Each packet of charge travels a distance of order 1 cm through silicon to an output for processing. The energy resolution is of order 50 to 200 eV in the ASCA band pass of 400 to 12000 eV.

As part of this thesis work, I designed, built and debugged an X-ray calibration facility for these detectors. In chapter 2, I describe the facility, its use, and its data products. In brief, it makes use of a reflection grating spectrometer to measure absolute detection efficiency, characteristic absorption edge strengths, and spectral redistribution in the CCD response function.

Part of my thesis research includes a detailed study of radiation damage mechanisms in CCDs. I discuss this study in chapter 3. This study is important since the CCD must work in the hazardous radiation environment of low earth orbit. At the beginning of this work, there was very little data available on the impact of radiation damage in CCDs. This work revealed the radiation damage-induced degradation in the spectral response to X-rays. It also discovered many systematic effects which affect both data analysis and CCD design. As part of this study, I have developed a detailed model involving trap energy levels in the CCD band gap structure. These traps reduce the efficiency in which charge transfers through the CCD. I have used the model to extract information about characteristic trapping and detrapping times for electrons in these energy levels out of the X-ray data.

This thesis covers a rather wide range of physics, both literally and figuratively. To understand the data which tells us about the synthesis of the XRB by AGN at distances of megaparsecs, one must first understand details in the detector physics on scales ranging from angstroms to centimeters. This thesis provides unique information about both the physics of CCD detectors as well as the origin of the XRB.

In this chapter, I will discuss the X-ray satellite ASCA, which carries the CCD detectors which I use.

1.2 The Satellite

ASCA was launched from a Japanese M-3S-II rocket into a nearly circular orbit of apogee 620 km, perigee 520 km, and inclination 31.1°. The resulting orbital period is 96 minutes. Five days after launch, the solar panels deployed to provide the 240 watts of power required by the instruments and platform systems. Nine days after launch the extendable optical bench (EOB) unfurled to provide the spacing between detectors and telescope to accommodate the 3.5 meter focal length of the optics.

Figure 1-1 shows the satellite in its operational configuration. Starting from the front of the satellite, I describe some of the basic features. A sun shade keeps optical light from the sun from impinging on the X-ray telescopes (XRTs). Next, at the top of the EOB are four co-aligned XRTs. The XRTs will be described further below. The EOB extends ASCA length from a launch configuration size of 3.5 m to the final length of 4.7 m. Near the middle of the satellite are S and X Band antennae for communication of commands and data to and from the satellite. On the sun side of the satellite are two solar panels which provide direct power for satellite systems as well as battery charging. On the anti-sun side of the satellite (hidden in figure 1-1) is a radiator for taking heat away from the CCD detectors. Next to the radiators, are two star trackers which point 90° from the X-ray optical axis and each other to provide attitude information even during earth occultations of the X-ray target. Finally, at the base of the satellite are four detectors, one for each XRT. These will be described some more below.

ASCA has a pointing accuracy of 0.5 arcminutes and a pointing stability of better than 10 arcsecs. The satellite power needs constrain its pointing ability so that the surface normal of the solar panels (the satellite "y" axis) is within 30° of the sun. This constraint makes the entire sky accessible every six months.

Five times daily, ASCA passes over its launch location at Kagoshima Space Center (KSC) in Kyushu, Japan. During these passes, real time data is transmitted down via one of the two antennae, and stored data is passed via the other available antenna. Also, commands for the next day are telemetered up to the satellite. These commands include the instrument operation modes, the attitude control system commands (ACS), and timing commands on when to dump the stored data.

As ASCA observes, it stores the scientific data on a solid state "bubble data recorder"

(BDR) which will operate at three different data densities (bit rates): HIGH, MEDIUM, and LOW. The higher the density, the faster the BDR reaches its capacity. Post-launch, it was discovered that LOW bit rate cannot accomodate the data rate of the scientific instruments. This leaves the shorter time storage bit rates HIGH and MEDIUM which requires more frequent data dumps than five a day over KSC. The NASA Deep Space Network has provided additional downlink stations around the world to increase the data recovery.

The first six months of operation were set aside for performance verification (PV) to find "bugs" in operations such as the bit rate problem above, and fix those bugs. It also served as a reward to the instrument teams who made the observatory. The data used in the astronomical portion of this thesis is from this PV phase.

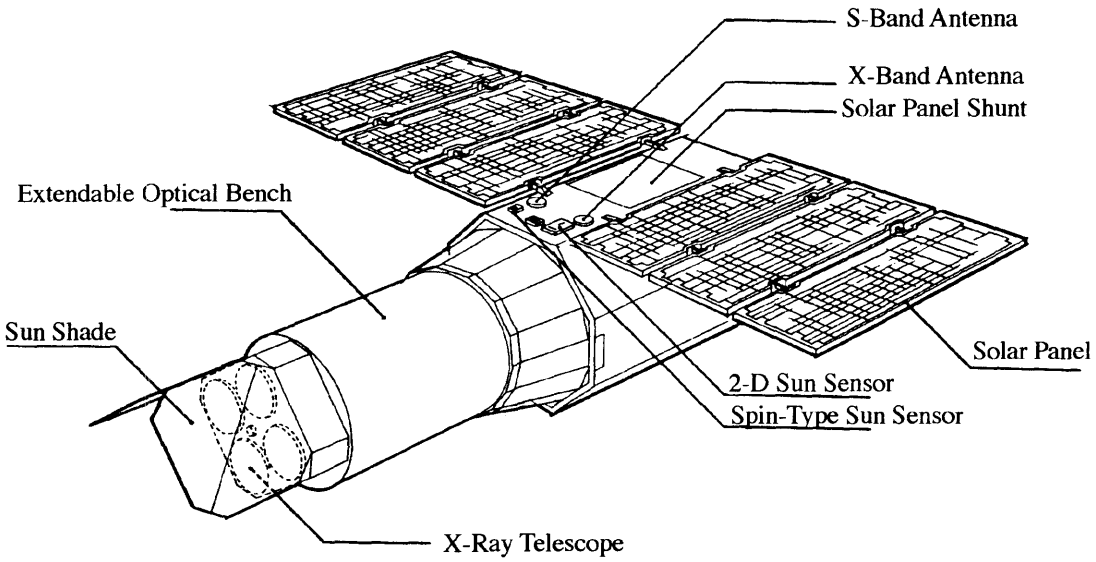

Figure 1-1: Observational Configuration of ASCA.

1.3 The Scientific Instruments

In the sections below, I describe the X-ray telescopes and focal plane detectors on ASCA.

1.3.1 The X-ray Telescopes

ASCA has four identical grazing incidence type coaligned X-ray telescopes (XRTs) (Serlemitsos *et al.*, 1995), each with its own imaging spectrometer detector. A collaborative effort between NASA's Goddard Space Flight Center (GSFC), Nagoya University, and Japan's Institute of Space and Astronautical Science (ISAS) made the XRTs. The XRTs of ASCA are extremely light weight and provide a large bandpass of high throughput X-ray collection efficiency. A review of these light weight X-ray mirrors can be found in Experimental Astronomy (Serlimitsos and Yang 1995).

Each telescope consists of 2 sets of 120 nested conical foils held together in quadrants. The foils are made of aluminum which is coated with 10 to 20 microns of acrylic followed by 60 nm of gold. X-rays reflect at grazing incidence off the first set of cones and then off the second set of cones. Thus the ASCA telescopes are "two-bounce" optics.

The telescopes can focus 50% of the flux from a distant point source within a diameter of 3 mm (which equates to 3 arcminutes with the telescope plate scale). For X-ray energies less than 3 keV, this angular resolution is moderate when compared to the best soft X-ray imagers flown. For example, the same 50% power diameter figure for the German-US mission ROSAT is about 15 arcseconds. For X-ray energies greater than 4 keV, ASCA's spatial resolution of 3 arcminutes is far superior to anything else flown. Typical angular resolution for a collimated proportional counter is usually measured in degrees. Figure 1-2 shows a typical image of a point source with ASCA. This "point spread function" (PSF) is strongly dependent on the source position relative to the optical axis. As targets move further off axis, the PSF flattens in the orthogonal direction and spreads out. The wings of the PSF are broad enough to make the analysis of non point source objects difficult. In the X-ray background chapter of this thesis, I will describe special attention that must be paid to diffuse observations.

While the ASCA XRT is only a "moderate" resolution imager, it is a superior collector. At a fraction of the weight of the ROSAT XRT, the four ASCA XRTs provides 3 times the photon collecting area at 1 keV that ROSAT's XRT provides. Furthermore, the ASCA

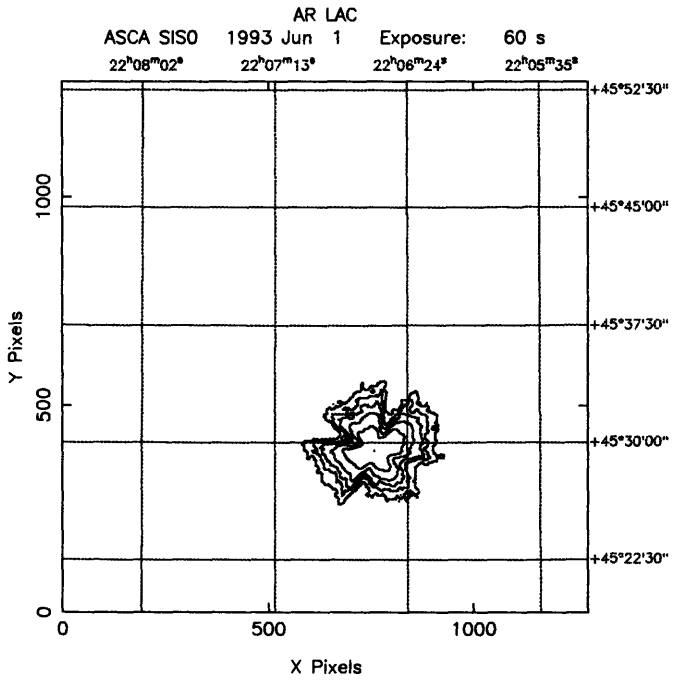

Figure 1-2: A contour image of the star AR-Lac taken by ASCA. The side of the box containing the image is approximately 30 arcminutes across. The cross shape of the point spread function is due to structures holding the individual XRT quadrants together.

XRTs provide throughput above 4 keV where the high quality imagers to date have been ineffective. Figure 1-3 shows the on-axis effective area for one ASCA XRT.

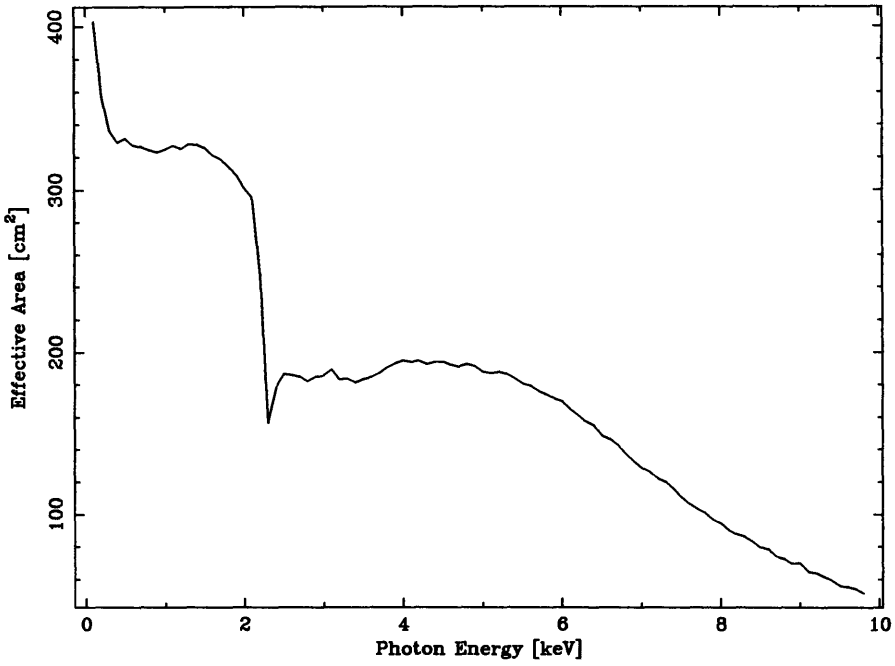

Figure 1-3: The effective detecting area for a point source on axis as a function of energy for one ASCA XRT. Note that this does not include the detector quantum efficiency.

1.3.2 The Gas Imaging Proportional Counters

At the focus of two of the XRTs are gas scintillation proportional counters. These detectors are the Gas Imaging Spectrometers (GIS). These type of detectors have flown in previous X-ray astronomy missions, but, for ASCA, they have been improved to provide somewhat better energy resolution. The GIS detectors were built by a team at Tokyo University. Here, I give only a brief description of these detectors. A more complete description of the GIS can be found elsewhere (Ohashi *et al.*1991). Table 1.1 lists some of the basic properties of the GIS.

Table 1.1: Properties of the GIS.

Energy Range ($\geq$10% efficient)	0.7-20 keV
Effective area	50 mm diameter
Energy Resolution (5.9 keV) FWHM/E	8% $\propto E^{-0.5}$
Position Resolution (5.9 keV) FWHM	0.5 mm $\propto E^{-0.5}$
Time Resolution	61 μseconds (max)
Non X-ray Background	6×10^{-4} c s^{-1} cm^{-2} keV^{-1}

Figure 1-4 shows a basic schematic of the GIS detector. X-rays pass through a beryllium window into a gas cell containing roughly 776 torr of a 96% xenon 4% helium gas mixture. The gas absorbs x-ray photons photoelectrically resulting in a cloud of electrons. These electrons are accelerated through a 8 keV potential resulting in several scintillations of UV photons per electron. The number of UV photons produced in the scintillation region of the GIS is proportional to the incident X-ray photon energy. The photons pass through a quartz window into a position sensitive photo tube which counts the photons and registers their positions.

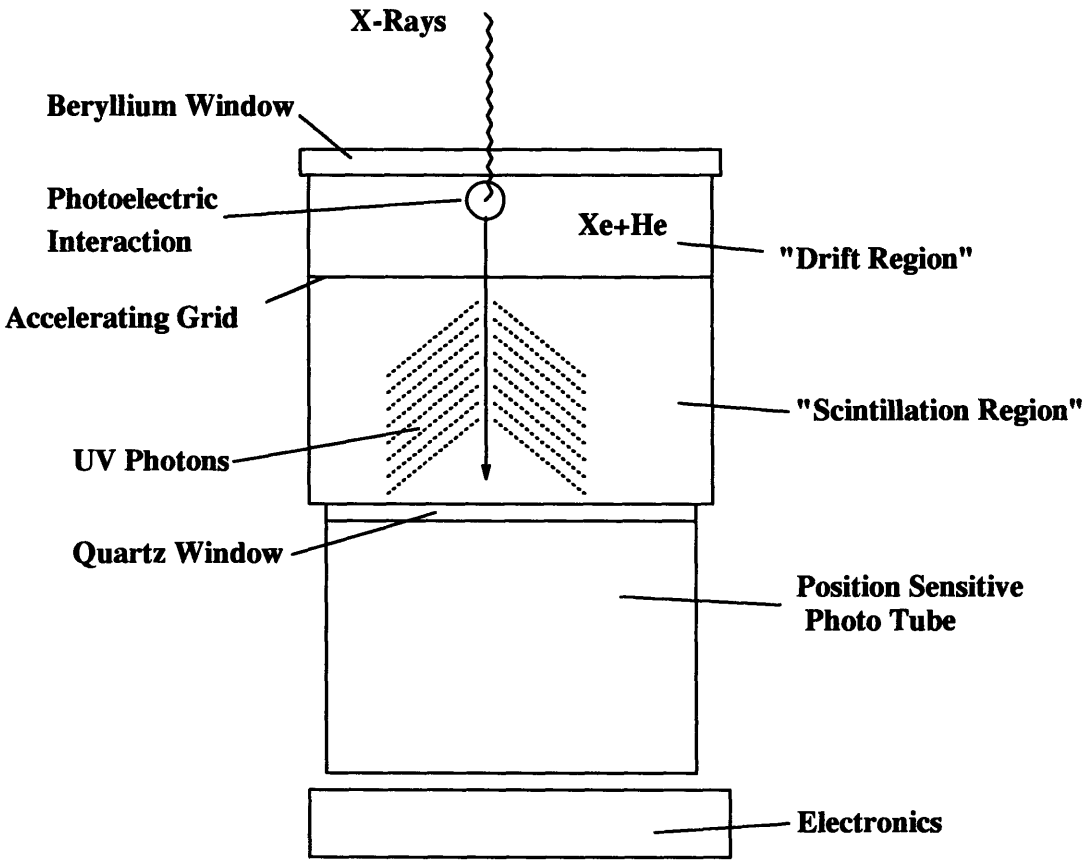

Figure 1-4: A functional schematic of the GIS. X-rays enter from above and interact photoelectrically with a xenon(96%) helium (4%) gas mixture. The electrons are accelerated into a scintillation region where they produce UV photons which are detected in a position sensitive photo tube at the bottom. The number of photons counted is proportional to the X-ray energy.

1.3.3 The X-ray CCD Detectors

Basic Characteristics of the CCDs

Two of the XRTs have X-ray CCD detectors at their focal planes. The CCD detectors are called the Solid State Imaging Spectrometers (SIS). The SIS is the collaborative effort of MIT's CCD Laboratory, MIT's Lincoln Laboratories, ISAS, Osaka University, and The Pennsylvania State University. Some of the basic properties of the SIS are listed in table 1.2.

Table 1.2: Properties of the SIS.

Energy Range ($\geq$10% efficient)	0.45-15 keV
Effective area	22×22 mm^2
Energy Resolution (5.9 keV) FWHM/E	2% $\propto E^{-0.5}$
Position Resolution	27μm
Time Resolution	16 ms (max, non imaging mode) 4 s (max, imaging mode)
Non X-ray Background	6×10^{-4} c s^{-1} cm^{-2} keV^{-1}

The SIS detects X-rays through photo electric absorption. The absorbing material is silicon. When a photon interacts in the silicon, a complex sequence of events takes place to liberate a number of electrons proportional to the photon energy. The "packet" of liberated electrons is collected in a one of many spatially defined potential wells in the CCD. The SIS electronics then manipulates these wells to transfer the packets in an orderly fashion out of the CCD and into a signal processing chain. In this way, the SIS records photon energy and position information. Appendix A describes the fundamental operations of a CCD. While this may seem very similar to a conventional proportional counter, the X-ray CCD provides superior energy resolution, compared to that of a more traditional detector such as the GIS. Compare tables 1.2 and 1.1. The nominal energy resolution (in eV) of the SIS CCDs is given by

$$\Delta E_{FWHM} = 2.354 \times 3.65\sqrt{N^2 + \frac{FE}{3.65}} \tag{1.1}$$

where, "F" is the Fano Factor (~0.1 for silicon), E is the photon energy (in eV), and N is the system noise (~5 electrons RMS for the SIS). Figure 1-5 shows the expected energy resolution as a function of energy for a several system noise levels. These resolution

curves are actually upper limits. There are several issues which make equation 1.1 more complicated. Chapter 2 discusses the finer points of this equation.

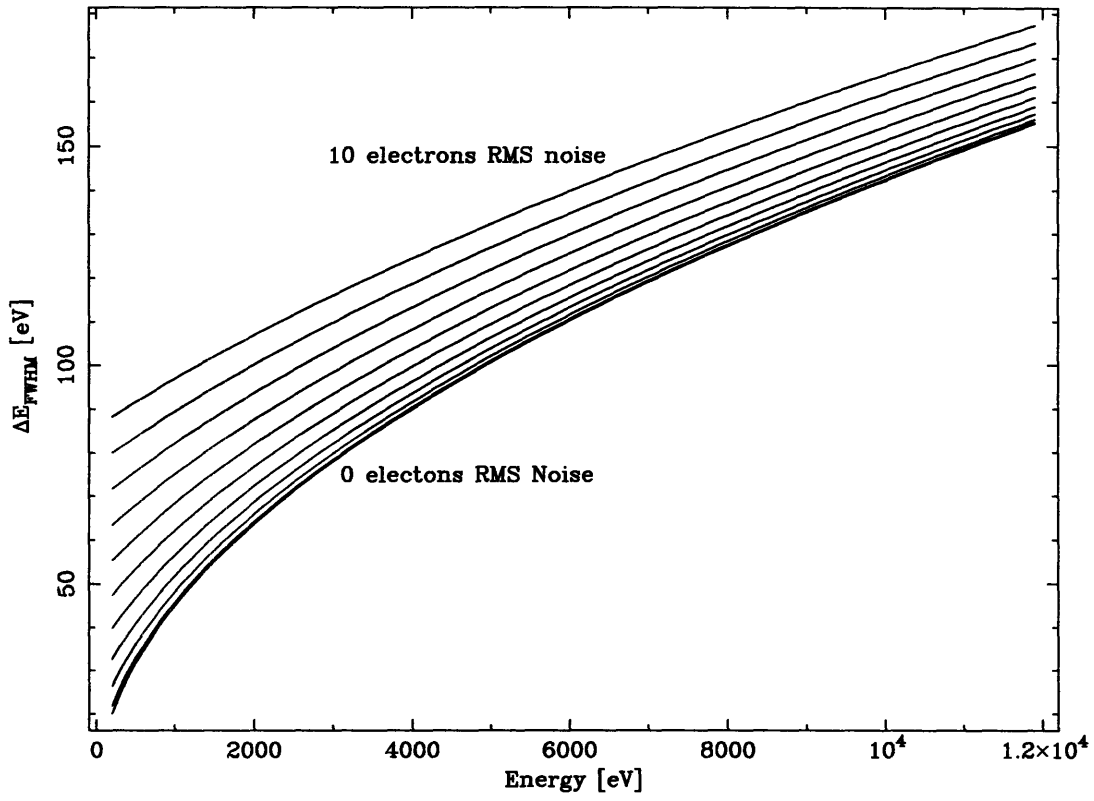

Figure 1-5: The expected energy resolution as a function of energy for system noises ranging from 0 electrons RMS to 10 electrons RMS in 1 electron RMS steps.

SIS Detector, Analog Electronics, and Digital Electronics

Figure 1-6 shows a schematic of the overall SIS system. On ASCA, there are two SIS sensors. Each sensor has a an independent set of analog electronics (AE) and digital electronics (DE). The satellite has a single digital processor (DP) which communicates directly with each AE and DE as well as with other satellite subsystems such as the telemetry and data storage systems. Each sensor is connected thermally through a heat pipe to a radiator. This connection cools the baseplate of each sensor to approximately -40° C under normal SIS operation.

Figure 1-7 shows more detail of an SIS sensor. Lexan supports hold the CCD focal plane inside of a gold plated aluminum housing. The focal plane holds a hybrid CCD developed and fabricated by MIT's Lincoln Laboratory (LL). Figure 1-8 shows a face on view of a SIS focal plane. LL combined four of its own CCID7 CCDs on a ceramic motherboard in a kovar package with a temperature sensor and heating element.

LL originally made the CCID7 CCD for optical work in a US Air force program. The CCID7 is a three phase frame transfer imaging CCD (see appendix A, Burke *et al*, 1991). It is composed of four basic parts, an imaging array, a frame store array, an output register, and an output node. The imaging array is a matrix of 422×420 27×27 micron^2 pixels. The imaging array collects charge clouds from impinging X-rays and optical photons during a set exposure time. The contents of the imaging array then transfer into the 422×420 frame store array. In normal use, a shield covers the frame store array, as it is also sensitive to X-rays and optical photons. Typically, the transfer time from the imaging array to the frame store array is a much smaller fraction of the imaging array integration time. Once this transfer occurs, the imaging array begins it next integration. While the next exposure is taking place, the contents of the frame store array transfer row by row into an orthogonal output register of length 424 pixels. This output register (also called the "serial array") then transfers the charge packets one by one into an output node. The output node is a JFET which essentially acts as a capacitor converting the charge to a voltage. An amplifier then enhances the signal for later processing.

Since the signals for a CCID7 interface at a single edge of the device, a CCID7 is a three side abuttable device. This allows multiple CCID7 devices to be combined for hybrid arrays such as the ASCA SIS focal plane.

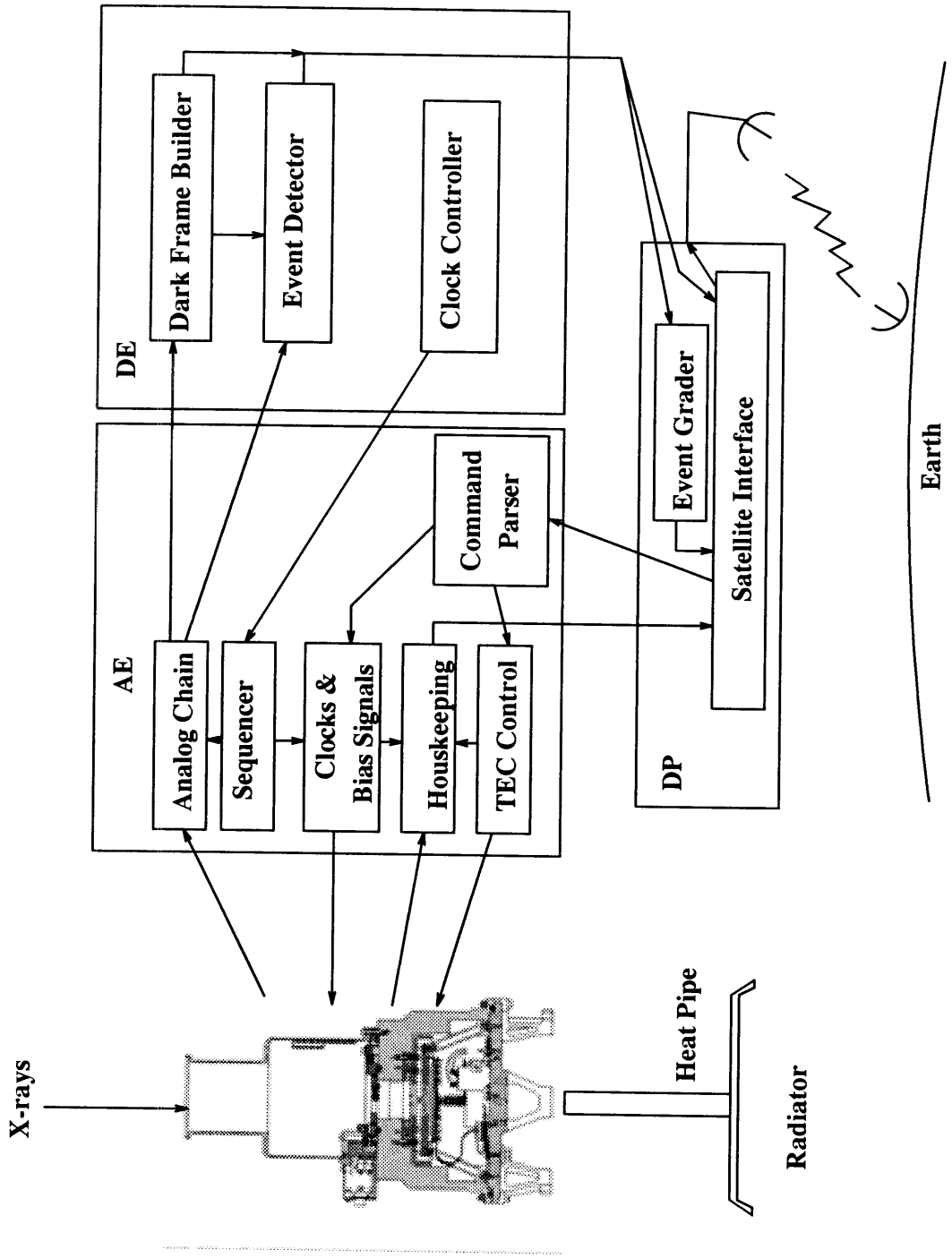

Figure 1-6: Overview of SIS system including the sensor, analog electronics, digital electronics, and satellite interface.

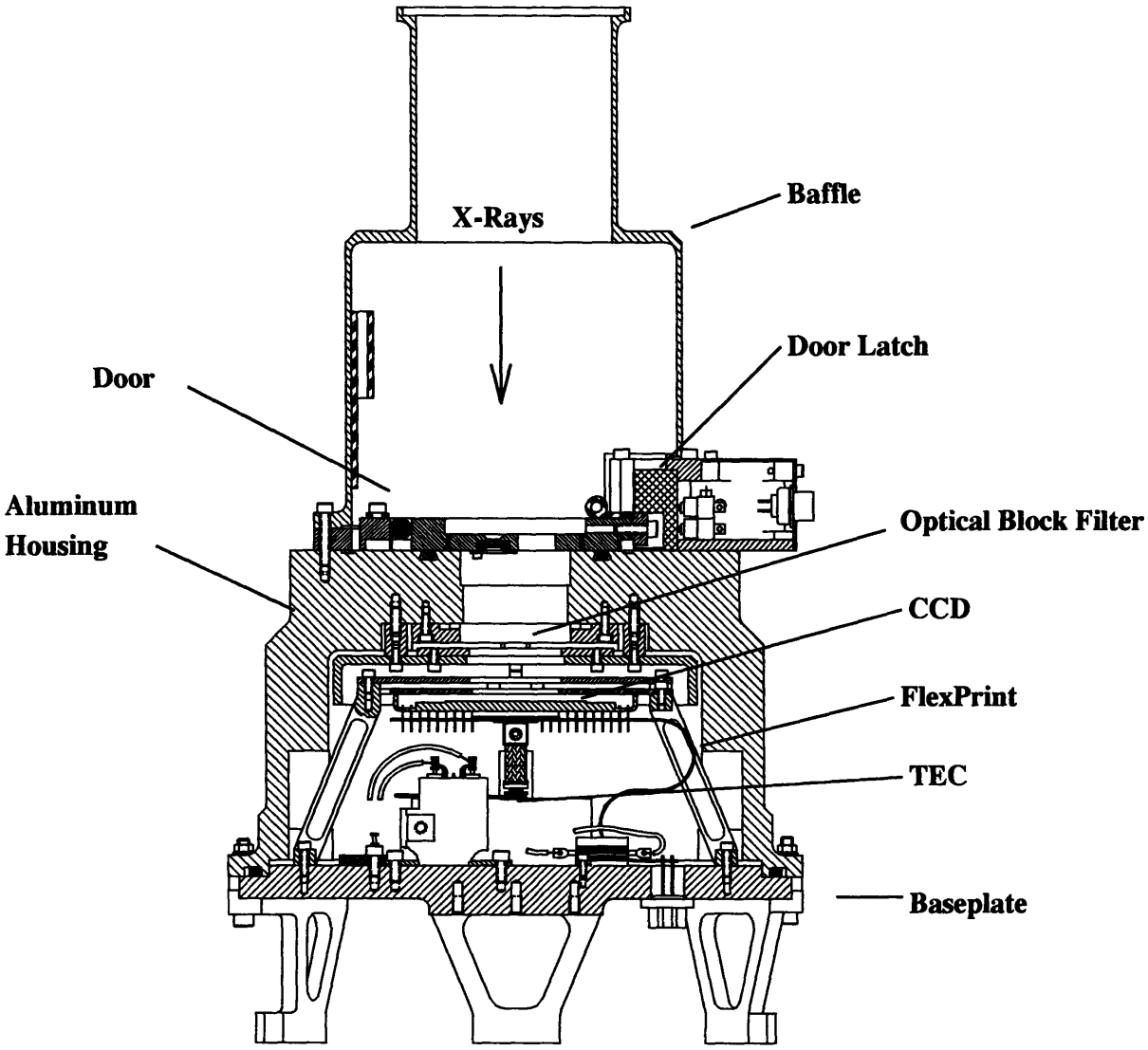

Figure 1-7: Cross section of SIS.

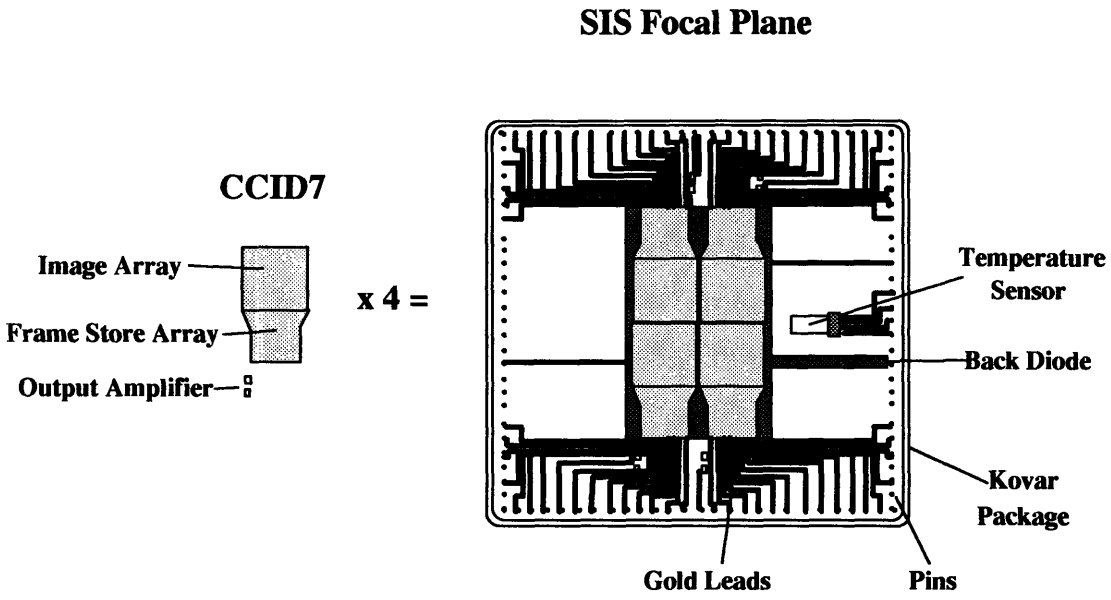

Figure 1-8: Four individual CCID7 CCDs (left) are combined in a single package to make a single SIS focal plane (right).

For X-ray detection, LL made several modifications to the base design of the optical CCID7. To enhance the CCID7's low energy X-ray response, LL thinned a scratch glass covering from about 1 micron thick to 100 nm thick. To see the effect this would have on the detection efficiency, see figure 2-3 in chapter 2. Also to this end, LL worked hard to thin the silicon gates of the CCD. To enhance the high energy response of the CCID7, LL made the devices out of a very high resistivity (6500 Ωcm as opposed to the typical $\sim$10 Ωcm) silicon material. Electric fields penetrate deeper into high resistivity material. The penetration depth goes as the square root of the silicon's resistivity (see appendix A). Thus the CCD can detect high energy, deeply interacting X-ray photons. The depth at which the electric field goes to zero is called the depletion depth. For the high resistivity CCID7, depletion depths of 20-40 microns are achievable. Burke *et al.*(1991, 1993, 1994) describe the CCID7 in considerably more detail.

The X-ray CCID7 is still sensitive to optical light. To address this issue, an optical blocking filter sits above the CCD. The filter is a 1000 $\AA$ thick unsupported film of lexan sandwiched between two layers each of 400 $\AA$ aluminum. Luxel corporation built the filters used for ASCA. The filter is designed to block optical light from a star as bright as Vega. It does not block all the light from the earth or moon.

On ASCA, we planned to operate the CCDs at a temperature of -70° C. After we set this goal, we discovered that an even colder operating temperature would be better (see chapter 3). However, the thermal design was complicated and the power budget for cooling was small. Infact, the SIS CCDs operate at a temperature of about -62° C. As shown in figure 1-7, a thermal electric cooler (TEC) is located directly beneath the focal plane. In a TEC, the Peltier effect transfers heat from a "cold" side to a "warm" side. The focal plane is in thermal contact to the TEC's cold side while the baseplate of the sensor is attached to the warm side. A thermal pipe transfers heat away from the baseplate to a radiator attached to the anti-sun side of the satellite. The satellite thermal interface specified an unregulated baseplate temperature of colder than -20° C. A thermal control circuit in the SIS AE operates the TEC so as to regulate the focal plane temperature to its operating temperature with an accuracy of 0.05° C. To reduce the thermal load on the TEC system, thin crossection lexan supports hold the focal plane nearly thermally isolated inside a gold plated aluminum bonnet. Also, signals to and from the CCD travel through a specially made "flex print" of high thermal impedance conductors. The optical light blocking filter

also serves the thermal system by acting as a thermal radiation shield.

An aluminum housing surrounds the the CCD. This serves several purposes. First, it provides a mechanical interface to the satellite. Second, it protects the focal plane from damage due to handling and contamination during ground testing. Third, it protects the thin optical blocking filter against the tremendous acoustic load during launch. A door seals the X-ray aperture during launch to hold a vacuum which further reduces the acoustic load. This door opens once the satellite is in orbit and ground controllers give the command. The door opening is a delicate procedure, since the sudden opening of the door would generate turbulence in any residual gas in the housing. This turbulence would break the filter and negate all our efforts. Since every man made vacuum container leaks at some level, we expected some residual atmosphere in the housing after launch. To remove this gas in a gentle fashion, a deliberate slow leak vent pipe is attached to the sensor housing. A sublimation actuated valve opens the slow leak after the satellite is in the vacuum of space for 3-6 days.

Finally, the housing provides shielding against some of the background radiation typical of the low earth orbit ASCA resides in. Not shown in figure 1-7 is a polyethelyn shield surrounding the SIS aluminum housing. This provides even more shielding. This shielding is necessary as the performance of the CCDs degrades due to radiation damage (see chapter 3).

Each SIS sensor has its own analog electronics (AE) unit. The AE serves as the electrical interface between the SIS sensor and the rest of the satellite. The AE provides a number of services for the SIS. Each AE has seven subsystems to provide these services.

One of these subsystems is the command controller. The DP sends commands to this subsystem to perform such tasks as switching on the sensor, opening the door, setting CCD voltage levels, setting focal plane temperature, and so on. The AE command controller signals the other subsystems appropriately to execute the DP command.

One of the other subsystems provides the bias and clocked voltage levels for the CCDs. One can specify particular voltage levels digitally to this subsystem through the command controller. Digital to analog converters (DACs) transform the digital command to analog voltages. For some CCD signals, the voltages are constant (DC), while for others, a time variable wave form is required. For our CCDs, the time variability is of a simple "square wave" form. In this case, two DACS provide the upper (high) and lower (low) levels for the waveform. The sequencer, another AE subsystem, provides digital level clocks which toggle

analog gates between the high and low analog levels. Figure 1-9 shows a schematic of a DC bias level and clocked waveform driver.

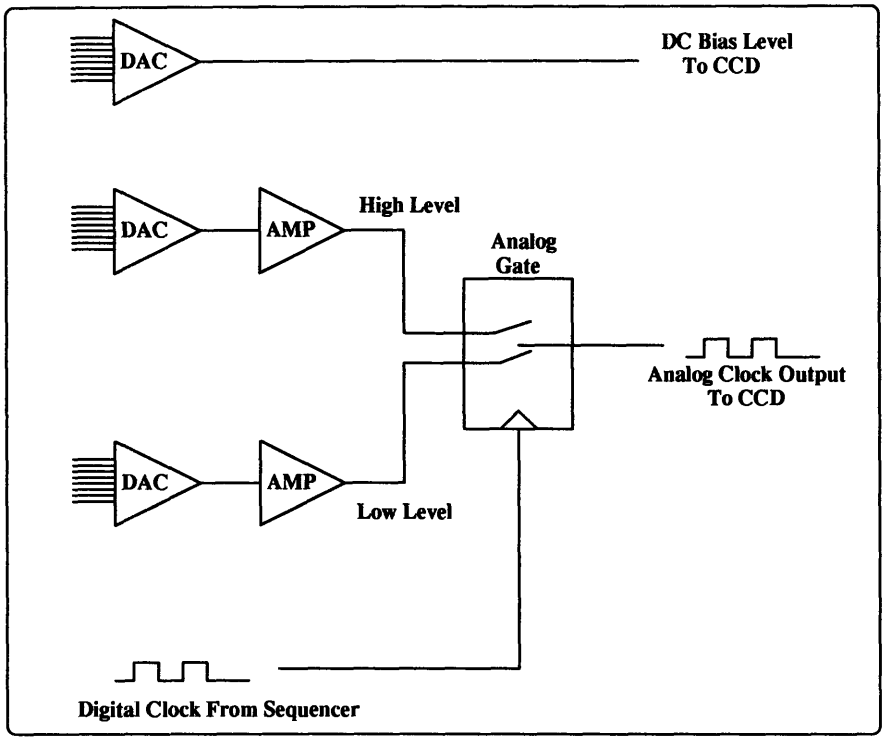

Figure 1-9: Schematic showing a DC bias level driver and a clocked waveform driver.

The sequencer accepts four "seed" digital clock signals from the DE. These signals are called "STCLK", "LNCLK", "PXCLK", and "CCDID". CCDID specifies which one of the four focal plane CCDS is to be clocked. The three other DE clocks enable pixel to pixel transfer sequences as shown in figure A-3 of appendix A. STCLK synchronizes pixel to pixel transfers during the imaging array to frame store array shift. LNCLK synchronizes pixel to pixel transfers during the frame store array to output register shift. PXCLK synchronizes pixel to pixel transfers during the output register to output node shift. For each of these three DE clocks, the sequencer board provides the necessary wave forms for each of the three phases of the appropriate CCD registers. This is done in hardware as a series of frequency dividers and multipliers driven by the base DE clock.

A fourth AE subsystem is the analog processing board. This subsystem accepts CCD output, amplifies it, and digitizes it. The digitization is accurate to 12 bits. The AE then

passes the digitized CCD output, pixel by pixel, to the DE for further processing.

A fifth subsystem is the TEC controller. As described earlier, this controls the TEC which cools the focal plane of the SIS. The sixth subsystem of the AE is the housekeeping (HK) monitor. The HK system monitors bias levels, focal plane temperatures, and other hardware signals. The HK system digitizes these signals and passes them on to the DP. The final subsystem of the AE is the power control system which will turn the SIS on and off.

Each SIS also has a set of digital electronics (DE) which two important tasks. First, it provides the "seed" clocks, discussed above, for the AE sequencer. Second, it processes the digitized pulse height data coming from the AE's analog processing system. Both the "seed" clock generation and the data processing depend on the observation mode. The DP tells the DE what the observation mode is. The DE then sends the appropriate seed clocks and processes the data accordingly. The DE passes the results of the processing to the DP which does the final data processing and packaging for the telemetry stream.

Operation Modes

There are three classes of observation modes for the SIS: imaging, timing, and diagnostic. I describe these classes below in increasing order of frequency of use.

Diagnostic modes provide detailed detector information at the expense of science data. Diagnostic modes include "frame mode", "integration mode", "dark frame mode", and "histogram mode". Frame and integration modes are modes where the pulse height value of every pixel is sent down to the earth. Frame mode data is data where the CCDs have been integrating for 16 seconds. Integration mode data is data where the CCDs have been integrating for 160 seconds. These modes are telemetry intensive operations but provide useful information on the quality of event detection algorithms. Dark frame mode passes the dark image to the earth. I discuss the role of the dark image in appendix B. Histogram mode creates a histogram of pixel pulse heights for every pixel in a CCD frame.

The highest time resolution observation mode is called fast mode. In fast mode, the electronics reads out the CCD one dimensionally to improve timing. Specifically, this mode sums several rows of the CCD onto the output register, destroying one dimension of position information. I do not use this mode in this thesis, so I will not discuss it further.

The final and most commonly used observation mode of the SIS is imaging mode. This

mode preserves two dimension information as well as pulse height and crude timing resolution. There are several different clocking modes available in imaging mode. They differ in the number of CCDs read out. While other possibilities exist, the used clocking modes are one, two, and four CCD mode. The AE's analog subsystem only has capacity to process one CCD at a time. It takes four seconds for the analog chain to process one CCDs output. This constrains the possible clocking modes. Figure 1-10 schematically shows the available imaging modes. In four CCD mode, each of the four CCDs are read out in sequence. A given CCD will integrate signal in its imaging array for 16 seconds. The CCD then clocks the charge rapidly ($\sim$17 milliseconds) from the imaging array to the frame store array, where it proceeds orderly out of the CCD and into the analog chain. During this readout time, the imaging array is already integrating its next image. When the readout is done, the electronics reads out the next CCD. Note that the imaging array of the previous CCD is still integrating. This will continue until the electronics reads out all of the CCDs and the process begins again. In two CCD mode, the process cycles between two specified CCDs. The imaging array integration time for a particular CCD in two CCD mode is 8 seconds. In one CCD mode, the electronics cycles through a single specified CCD continuously. In one CCD mode, the exposure time for the imaging array for one cycle is 4 seconds.

In imaging mode, the DE extracts events from the CCD data. Information concerning these events are sent down through the telemetry stream. This mode does not pass down information from pixels not associated with events. For imaging mode, there are two possible data modes: Faint and Bright mode. Depending on the data mode, the DP will either pass the entirety of the DE's information on a given event or limited information on a given event. Appendix B discusses the event selection process as well as the differences between faint and bright mode.

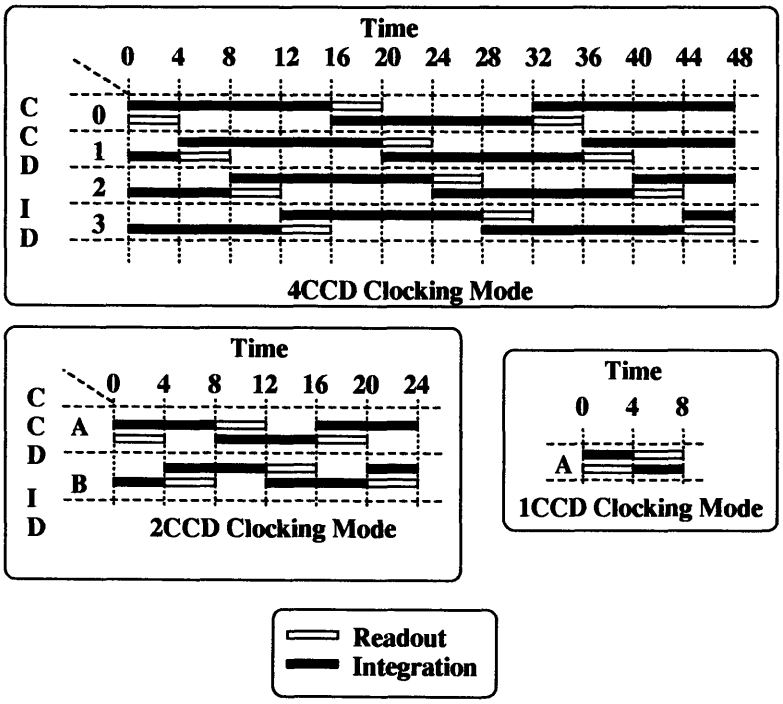

Figure 1-10: Three possible clocking modes used for imaging. In each figure, a diagram showing CCD state (image integration and image readout) as a function of time is depicted for each CCD used. In four CCD mode, each CCD is used. Since there is only one analog processing chain per SIS, the readouts are staggered. In the two CCD mode figure, the letters A and B represent the two CCDs being used. In the one CCD mode figure, the letter A represents the one CCD being used.

Chapter 2

Low Energy Calibration of the SIS CCDs on the Ground

I present here a description of the apparatus used in the low energy calibration of the SIS detectors on ASCA. I also show examples of some of the many data products of this calibration. I use a variable spaced grating spectrometer in conjunction with an X-Ray CCD and flow proportional counter to measure filter transmissions, detector quantum efficiencies, and detector spectral redistribution from about 200 eV to almost 2 keV. The system is nearly entirely computer controlled, allowing for automated calibration.

2.1 Introduction

The X-ray quantum efficiency (QE) of a detector is its efficiency to detect X-ray photons. The QE of the SIS detectors on ASCA is given by the expression:

$$QE(E) = T_{filter}(E) \times T_{deadlayer}(E) \times (1 - T_{depletion}(E)) \times B(E, thresholds, grade) \quad (2.1)$$

Where,

E = the photon energy,

$T_{filter}(E)$ = the transmission of the optical block filter on the SIS,

$T_{deadlayer}(E)$ = the transmission of the $Si/SiO_2/Si_3N_4$ dead layer on the CCD,

$(1 - T_{depletion}(E))$ = the absorption probability within the depletion depth of the CCD,

$B(E, thresholds, grade)$ = a term dependent on the event detection criteria.

Figures 2-1 and 2-2 show schematic cross sections of the SIS CCD. In these figures, an optical blocking filter composed of 800 angstroms of aluminum sandwiched around a 1000 angstrom thick lexan film is not shown. Various oxide, nitride, and silicon layers in the gate structure of the CCD make up a CCD deadlayer. The sensitive region is the depletion region. In order that an X-ray photon will be detected, it must first traverse the optical filter and the CCD dead layer. Next, the photon must interact within the depletion region of the CCD- the probability of this happening is the compliment of the probability that the photon has passed through the depletion region, hence $(1 - T_{depletion}(E))$. The interaction results in the production of an electron charge cloud whose charge is proportional to the photon energy with some scatter. Finally, the detection of the event must be of sufficient quality- given by $B(E, thresholds, grade)$.

The complicated structures shown in figures 2-1 and 2-2 result in a very complicated expression for $T_{deadlayer}(E)$ in equation 2.1. Notice that with this complicated structure, there are 12 parameters indicated in the figures. I use two simple approximations to this complicated structure in order to have a manageable number of parameters for comparison to data. The first of these is the "slab" approximation, where the complicated structure is approximated by stacks of uniform thickness, materially homogeneous slabs. In the slab model, there are six parameters: the thickness of aluminum, the thickness of lexan, the thickness of dead layer silicon, the thickness of silicon oxide, the thickness of silicon nitride, and the thickness of photosensitive depleted silicon. Equation 2.2 shows the slab approximation for the SIS quantum efficiency.

$$\begin{aligned} QE_{slab}(E) &= e^{-d_{lexan}/\lambda_{lexan}(E)} e^{-d_{Al}/\lambda_{Al}(E)} \\ &\quad \times e^{-d_{SiO_2}/\lambda_{SiO_2}(E)} e^{-d_{Si_3N_4}/\lambda_{Si_3N_4}(E)} \\ &\quad \times e^{-d_{SiGate}/\lambda_{Si}(E)} (1 - e^{-d_{depletion}/\lambda_{Si}(E)}) \end{aligned} \tag{2.2}$$

Here, d_X is the thickness of the slab of material X and $\lambda_X(E)$ is the 1/e attenuation length of photons in the material X as shown in figure 2-3.

A slightly more complicated version of the slab model is the "slab and stop" model, which is a slab model with additional structure to describe the silicon dioxide and silicon channel stop structure shown in figure 2-2. This adds four new parameters to the slab

model. Equation 2.3 shows the slab and stop approximation to the SIS quantum efficiency.

$$QE_{slab+stop}(E) = QE_{slab}(E) \times \left(\frac{W-C}{W} + \frac{C}{W} \times e^{-d_{CS-SiO_2}/\lambda_{SiO_2}(E)} \times e^{-d_{CS-Si}/\lambda_{Si}(E)}\right) \quad (2.3)$$

Here, the pixel width is W, C is the channel stop width , $CS - SiO_2$ is the thickness of the oxide part of the channel stop, and $CD - Si$ is the thickness of the silicon part of the channel stop. For the CCID7, $W = 27$ microns, $C \sim 6$ microns, $CS - SiO_2 \sim 1$ micron, and $CS - Si \sim 0.75$ microns.

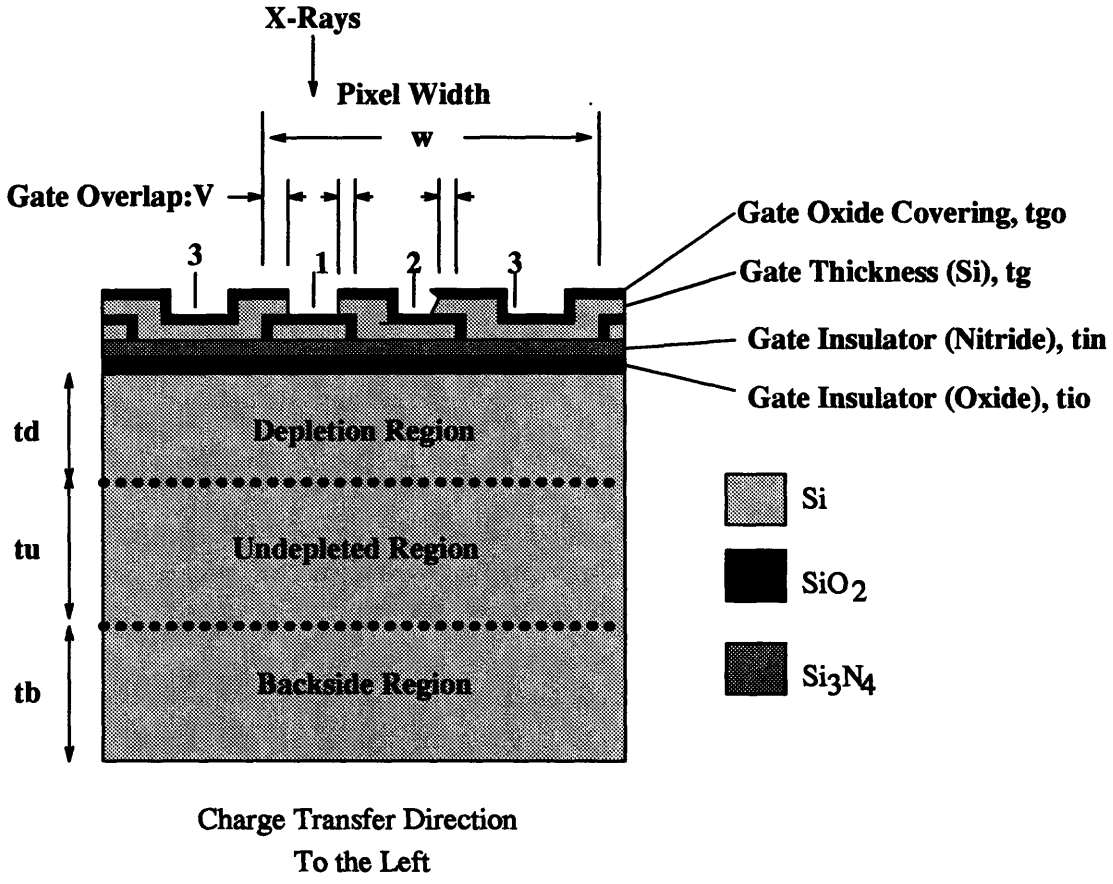

Figure 2-1: This is a schematic cross section of the SIS emphasizing the features affecting the quantum efficiency of the detector. The cross section is along the column direction of a pixel, so that, in this figure, charge transfers horizontally across the page.

Figure 2-3 shows the 1/e attenuation lengths of photons in material found in the CCD

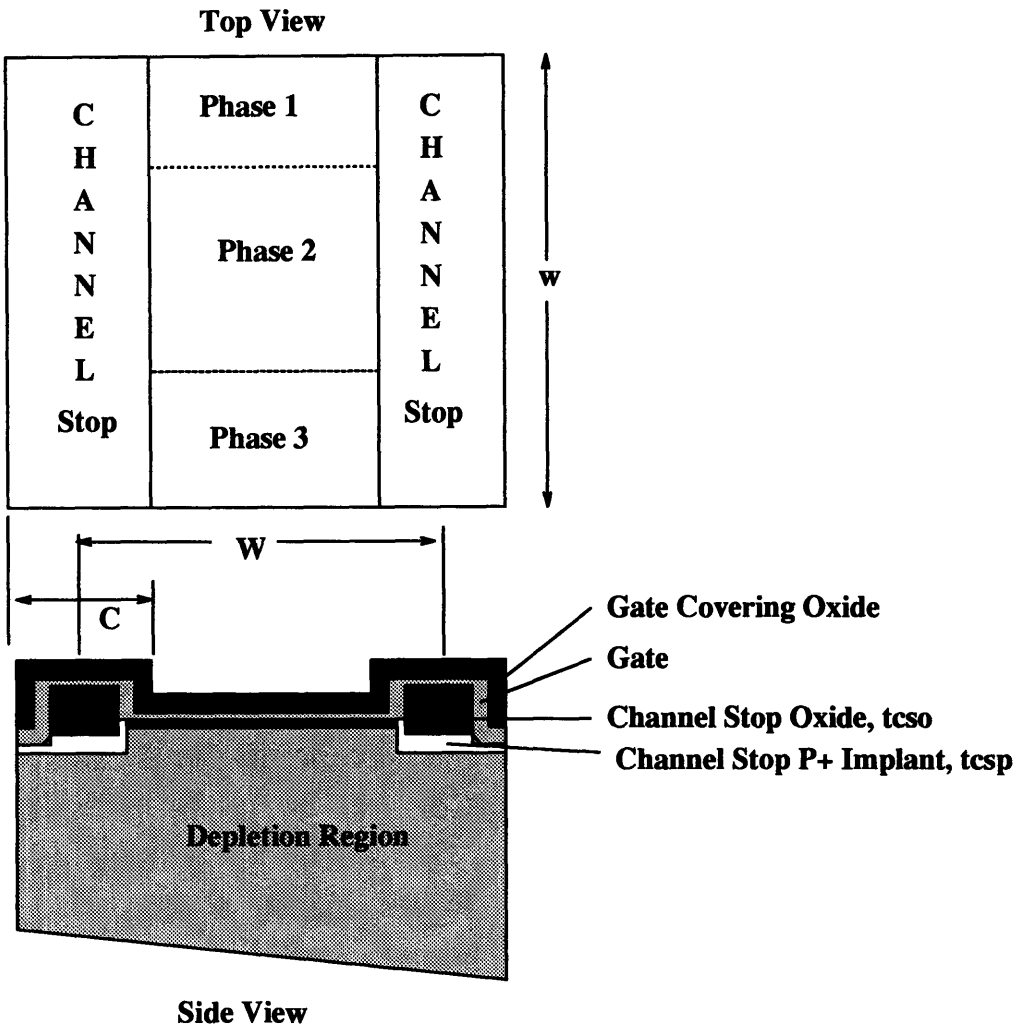

Figure 2-2: This is an other schematic cross section of the SIS CCD along with a top view of one pixel. In the top view, charge moves down the page. One can see the relative sizes of the channel stop and the pixel. In the side view, charge moves out of the page.

and optical filter. Table 2.1 shows some of the characteristic thicknesses of materials on the CCD using the slab model. Given these thicknesses, one can use the slab model to show that X-ray measurements made in the 0.4-1.5 keV range are most affected by the transmission through the optical filter and CCD dead layer. The depletion layer thickness of about 20-30 microns is at least 2 1/e attenuations lengths over the 0.4-1.5 keV band resulting in near unity detection efficiency- assuming the photons traversed the filter and dead layer. Thus a principle goal of the low energy calibration of the ASCA SIS CCDs is to measure the first two terms in equation (1): $T_{filter}(E)$ and $T_{deadlayer}(E)$. In attaining this information, we will also be getting data on the shapes of events and thus the final term in equation (1): $B(E, thresholds, grade)$. We will also learn about the gain from photon energy to detected

charge as well as the spectral resolution of the CCD. All of these factors are essential to a good device model and a proper response function. I do not consider the high energy response here. The depletion depth is a principle component in the higher energy response. I have developed some new techniques to measure the depletion depth (see appendix D).

Table 2.1: Characteristic thicknesses of materials in the SIS.

Region	Material	Thickness [μm]
Optical Filter	Al	0.08
	Lexan [$C_{16}H_{14}O_3$]	0.1
CCD Dead Layer	Si	0.3
	SiO_2	0.5
	Si_3N_4	0.04
Depletion Region	Si	25

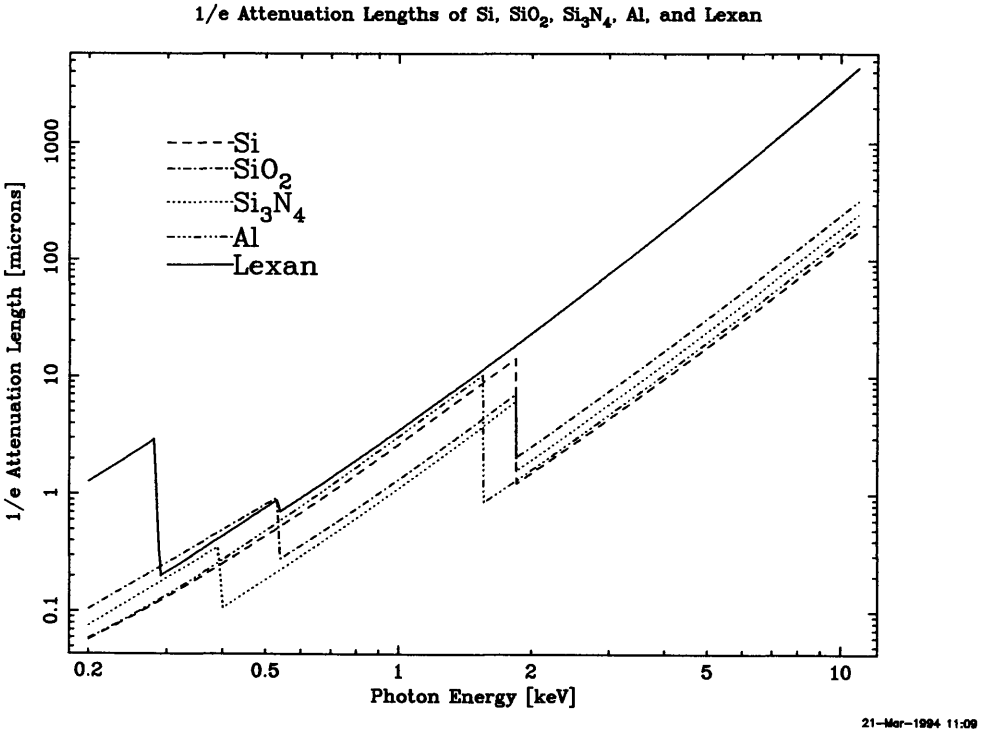

Figure 2-3: The attenuation lengths of X-rays as a function of energy in various materials found in the SIS. The sharp discontinuities at 0.284 keV, 0.392 keV, 0.532 keV, 1.56 keV, and 1.84 keV are the K-absorption edges of carbon, nitrogen, oxygen, aluminum, and silicon, respectively.

To measure the low energy response of the SIS, I made a soft X-ray calibration facility out of a combination of comercially available and in house made components. In the facility, an electron bombardment X-ray source illuminates a variable spaced grating spectrometer

which disperses a spectrum on a flat plane where a controllable aperture plate either picks off monoenergetic X-rays or allows the full spectrum to pass to a movable array containing the SIS and a flow proportional counter reference detector.

In addition to the hardware mentioned above, I developed a sophisticated procedure making use of several computers and the Internet to accomplish the SIS low energy calibration in a semi-automatic way. In the sections that follow, I describe each component of this calibration setup. Finally, I will describe the data products as well as there relation to the terms of the QE equation.

2.2 The Low Energy Calibration Facility: Hardware

An overview of the apparatus is shown in figure 2-4.

An electron bombardment X-ray source made by Manson Company provides the input to a spectrometer (HIREFS) made by Hettrick Scientific Company which disperses the X-rays by wavelength along a flat plane sampled by an X-Ray CCD camera developed at MIT and a flow proportional counter (FPC) made by Manson Company. The CCD and FPC are on a linear translation stage and may be moved along a plane just behind the focal plane of the HIREFS. A movable aperture plate in the HIREFS focal plane allows the system to switch between "spectrometer mode" and "monochromator mode". When in "monochromator mode", successive measurements with the FPC and the CCD can be made to yield quantum efficiency curves for the CCD. There are three positions between the Manson source and the HIREFS where filters or windows whose transmissions are to be measured can be moved in and out of the X-Ray beam. By comparing the CCD data with and without the filter in the beam, we can measure the filters' transmission.

Each part of the setup will be described in more detail below.

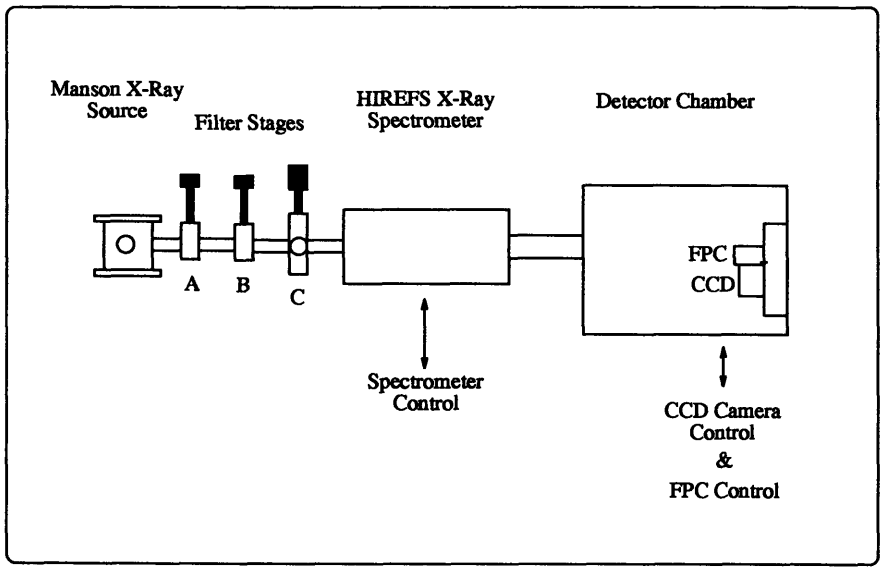

Figure 2-4: Basic schematic of the Low Energy Calibration Facility apparatus.

2.2.1 The Manson Source

The Manson X-Ray source is an electron bombardment style source. Figure 2-5 shows a basic schematic of a Manson source. Electrons boil off a resistively heated tungsten filament and then accelerate through a 5 kV potential drop onto an anode cap. The anode cap and filament are inside of a cylindrical cavity which forms a simple electrostatic lens. The lens focusses the electrons onto a spot about 1mm in diameter on the anode cap. It is from this spot where the X-rays originate. The electron beam current from the filament to the anode cape are 0.05 to 0.4 mA.

The X-rays produced are some function of the anode cap material, but basically include bremsstrahlung and characteristic line emission due the materials present in the anode. The anode caps are interchangeable and easy to fabricate. We have made basic caps out of aluminum, stainless steel, copper, and graphite. In addition, we have made several "hybrid" anode caps by attaching target material to a base aluminum anode cap with electrically conductive epoxy. In this fashion, we have made anodes with gold, palladium, silver, molybdenum, niobium, and salt targets (to name a few). For most calibration work, I have used gold anodes. The high atomic number of gold results in a large bremsstrahlung continuum component. This allows for calibration at almost any energy.

The stability of the source depends on the anode material, operating pressure, and filament condition. For typical operating procedures and simple target materials the stability can be as good as 5%. The stability is best under conditions of high vacuum operation. For this calibration, the Manson source chamber achieves a vacuum of $\sim 10^{-5}$ Torr.

The Manson source is also an intense source of UV and optical light. Since the CCD is sensitive to UV and optical light, our system must try to eliminate this contamination.

2.2.2 The Filter Stages

I address the uv light blockage in the next stage of our system: the filter positions. Of the three filter holder positions in our system (see figure 2-4), we typically use position A to hold a thin UV/optical blocking filter. The material we use for the UV block is aluminized mylar or lexan with thicknesses of 1000-2000 angstroms. Positions A and B are modified 2.75 inch gate valves which allow us to move filters in and out of the beam. We have replaced the doors of these gate valves with filter holders. Figure 2-6 shows a filter holder

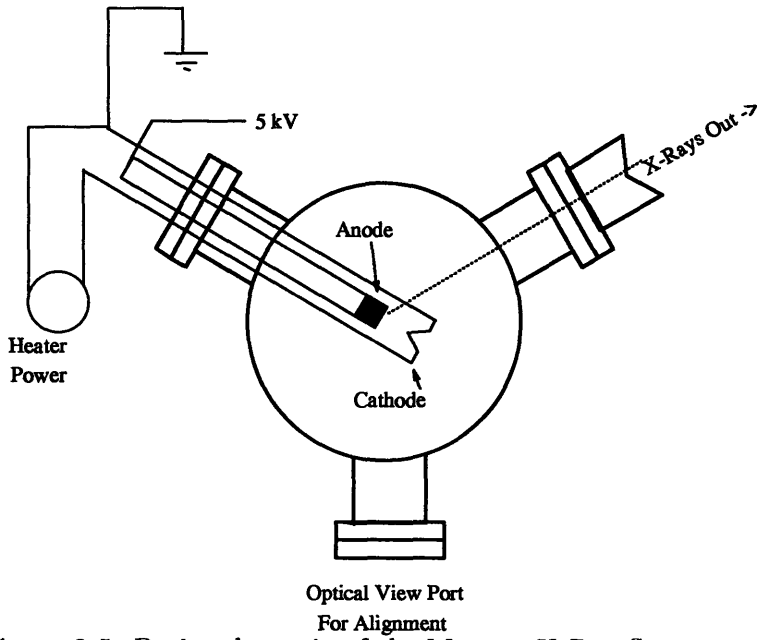

Figure 2-5: Basic schematic of the Manson X-Ray Source.

modification for one of these gate valves. These modifications are simple to implement for measurements of special filters or windows. We put the UV blocking filter for the X-Ray source on such a valve so that the the filter can be retracted to a position which has less turbulence during the venting and pumping of the vacuum system. The sudden pressure changes during the venting and pumping of the system can rupture the thin filter material if such precautions are not taken.

As mentioned above, both position A and position B are modified gate valves. While position A holds the UV blocking filter necessitated by the UV emission of the Manson source, position B is available for test filters. The modified gate valve filter stages have only 2 repeatable states: in beam and out of beam. For most transmission measurements this is adequate. Sometimes, however, more control is required.

Position C in figure 2-4 contains a filter holder which can be moved more precisely than the modified gate valves. For this position we use a one dimension linear translation stage. With this stage several parts of one filter may be measured to check uniformity. Also, small filters or windows can be measured with this stage with more confidence than with the gate valves in regards to X-ray beam alignment. In fact, I measured the transmission of the flow proportional counter (FPC) window used in the low energy calibration chamber with this

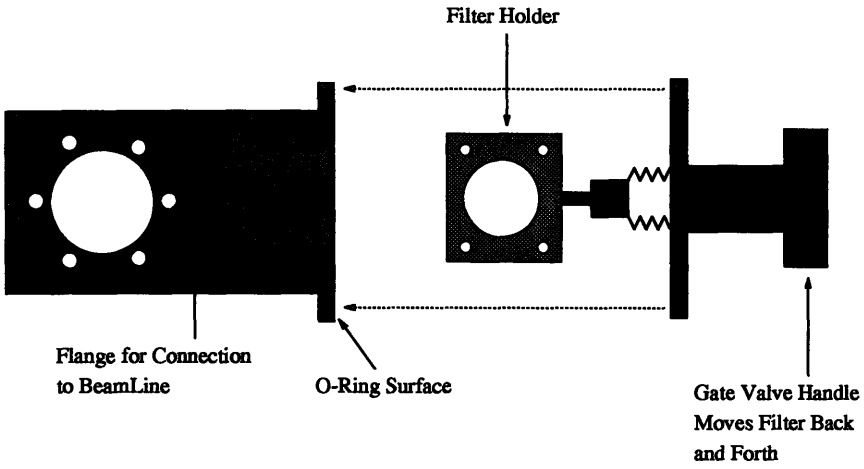

Figure 2-6: Modified gate valve filter stage.

stage. Figure 2-7 shows the arrangement of the C position hardware.

2.2.3 The HIREFS Spectrometer

From the filter stage, X-rays enter the HIREFS spectrometer, made by Hettrick Scientific Co. Figure 2-8 shows a simple schematic of how the HIREFS spectrometer works. Most of the optics within the spectrometer are controllable through vacuum feedthroughs.

A gold coated glass cylindrical mirror collects X-rays after they first pass through an entrance slit. It is the entrance slit which effectively defines the extent of the beam as far as our filter measurements go. The slit also determines the energy resolution of the HIREFS. The slit is adjustable up to 400 microns in width, which is what is usually used for the measurements. Thus the beam size is about 400 microns. The resolution of the HIREFS is typically a few electron volts.

The cylindrical mirror can be tilted to move the final image of the spectrum in the cross-dispersion direction for detector alignment (aiming). Also, the curvature of the cylindrical mirror can be adjusted to astigmatize the spectrum in the cross-dispersion direction. The astigmatization spreads out the spectrum in the cross-dispersion direction on the detector focal plane. This allows us to calibrate several sections of the detector simultaneously and it also reduces "pile-up" and "dead-time" in the imaging detectors for a given flux.

The cylindrical mirror reflects the X-rays onto a gold coated glass spherical mirror. The

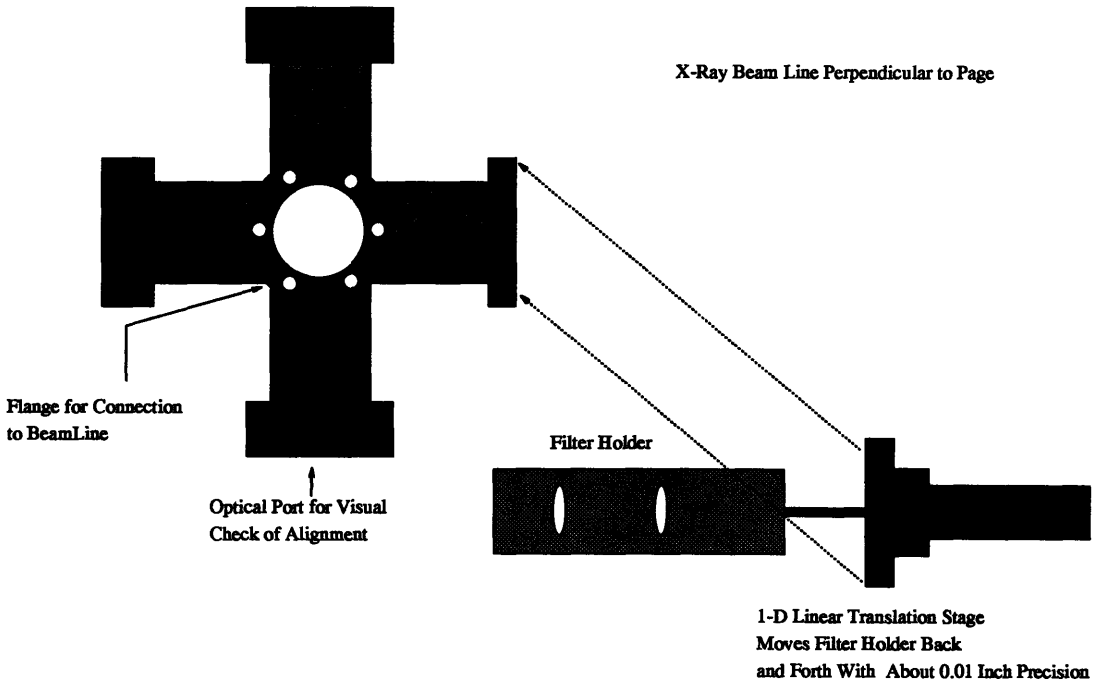

Figure 2-7: Precision Filter Transmission Stage. This stage uses a 1-D linear motion vacuum feed through to position filters accurately in the X-ray beam. There are two identical cutouts in the filter holder: one for the test filter, the other for an open position.

spherical mirror is used for focusing in both the dispersion and cross-dispersion directions (in practice, this is hardly ever done).

From the focusing spherical mirror, X-rays continue on to the reflecting gratings. The gratings are somewhat different from standard reflecting gratings in that the rulings are variably spaced. This results in a spectrum image which is flat as opposed to being dispersed onto a Rowlands circle in the case of linearly spaced grating rulings. This flat image makes the design of the detector chamber much easier than in the usual Rowland circle case.

Figure 2-9 shows a sample of the output from the HIREFS spectrometer as seen by a CCD in the focal plane. Using the imaging capability of the CCD, one sees lines and continuum dispersed in the vertical direction. The grating places multiple orders on top of each other in this image according to the grating equation (refer to figure 2-10):

$$m\lambda = (sin\beta - sin\alpha)\sigma_0 \tag{2.4}$$

where:

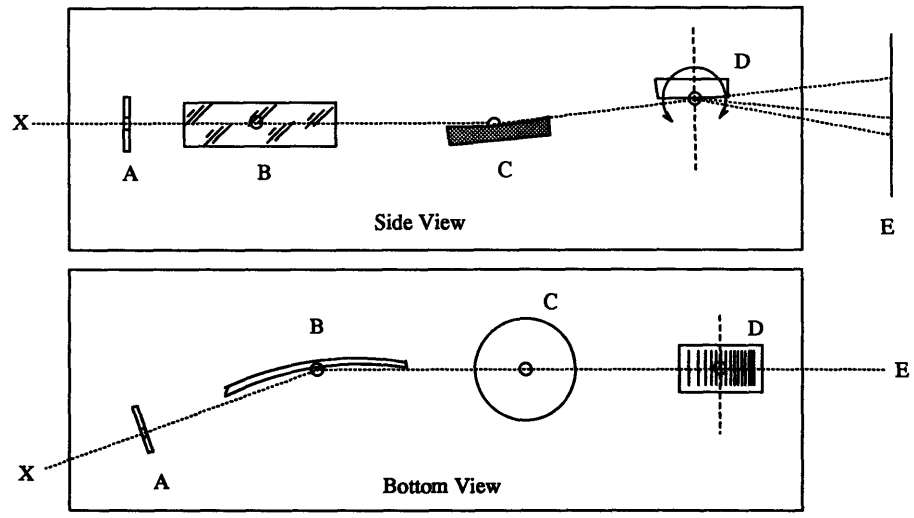

Figure 2-8: Top and bottom view schematics of the HIREFS spectrometer. The entrance slit (A) width is adjustable. The X-rays from the source (X) are collected with a cylindrical mirror (B) which can be tilted (aimed) about an axis parallel to the dispersion direction. The cylindrical mirror can also be warped slightly to astigmatize the image in the cross dispersion direction. The focus mirror (C) is a spherical mirror which passes the X-rays onto the grating (D) for dispersion on to the focal plane (E). The grating rulings are variably spaced to produce a flat focal plane image. This is an adaptation of figures 6 and 7 in US Patent no. 4,776,696.

m is the spectral order,

λ is the wavelength of X-rays dispersed through the angle β,

β is the angle (relative to the grating normal) of the exiting X-ray,

α is the incident angle (relative to the grating normal),

σ_0 is the groove spacing at the grating center (10^7/480 mm).

The diffraction angle β is given by:

$$\beta = 2\theta - \alpha + arctan\frac{x - x_c}{L} \tag{2.5}$$

β is the angle between the grating normal and a vector between the grating center and a position x in the focal plane. x_c is the position on the focal plane from which a vector normal to the focal plane interecepts the center of the grating. β_c is the angle between the

grating normal and a vector between the grating center and the position x_c on the focal plane. L is the distance between the focal plane and the grating center. The included angle, 2θ is:

$$\begin{aligned} 2\theta &= \alpha + \beta_c \\ &= 176^o \end{aligned} \tag{2.6}$$

The included angle of 176^0 comes from 180^o minus 2^o (graze angle) for both the incident and diffracted beams. For a given spectrometer setting, α and x_c are determined numerically by iterating the following set of equations for two known X-ray lines until the error becomes acceptable (refer to figure 2-10):

$$\begin{aligned} error &= x_2 - x_1 + L(tan(\beta_1 - \beta_c) - tan(\beta_2 - \beta_c)) \\ \beta_1 &= arcsin(\frac{m\lambda_1}{\sigma_0} + sin\alpha) \\ \beta_2 &= arcsin(\frac{m\lambda_2}{\sigma_0} + sin\alpha) \\ \alpha &= \theta - arcsin\frac{m\lambda_c}{2\sigma_0 cos\theta} \end{aligned}$$

The two X-ray lines have wavelengths λ_1 and λ_2 and focal plane positions x_1 and x_2. β_1 and β_2 corresponding to x_1 and x_2 are as described above.

The set of equations above is adapted from the user manual for the HIREFS spectrometer.

Using the CCDs energy dispersive properties, the overlapping orders may be separated as shown in the right hand panel of figure 2-9.

More details of the HIREFS can be found in the HIREFS operation manual and in US Patent No. 4,776,696.

The grating angle is controlled via a stepper motor with a serial communications link to a Sun workstation tied to the Internet. It is through this link that users can specify the X-ray energy scale of the output of the spectrometer. I require this Internet link inorder to run the calibration automatically.

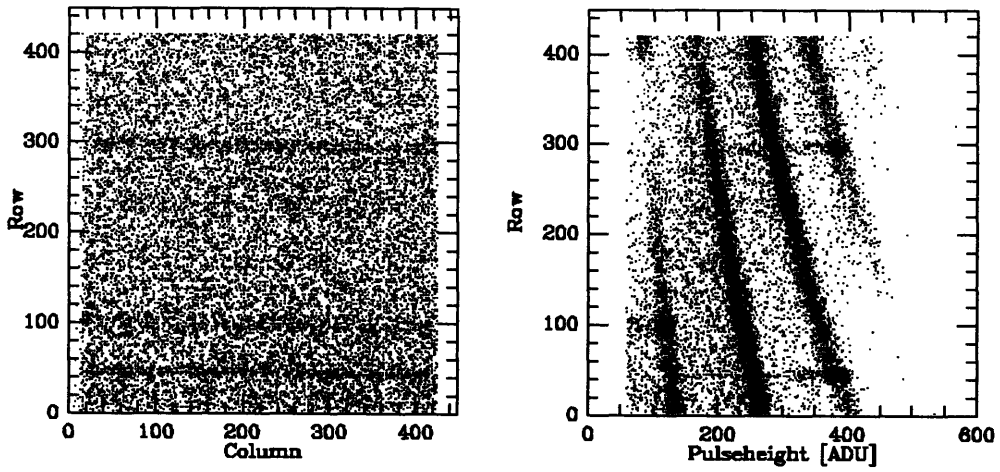

Figure 2-9: HIREFS data taken with a CCD in the focal plane of the spectrometer. The left hand panel shows a 2 dimensional image of the HIREFS output. The physical size of this image is 11×11 mm. The dispersion direction of the spectrometer is along the rows. The astigmatism was adjusted to fill the ccd. The right hand panel shows the same data plotted row vs CCD pulse height. In this panel, we see the wavelength dispersive features of the grating spectrometer vs energy dispersive features of the CCD. Multiple orders of the grating are separated by the CCD. Magnesium Kα in 3rd and 4th order are at rows 50 and 295. Carbon Kα in first order is at row 90.

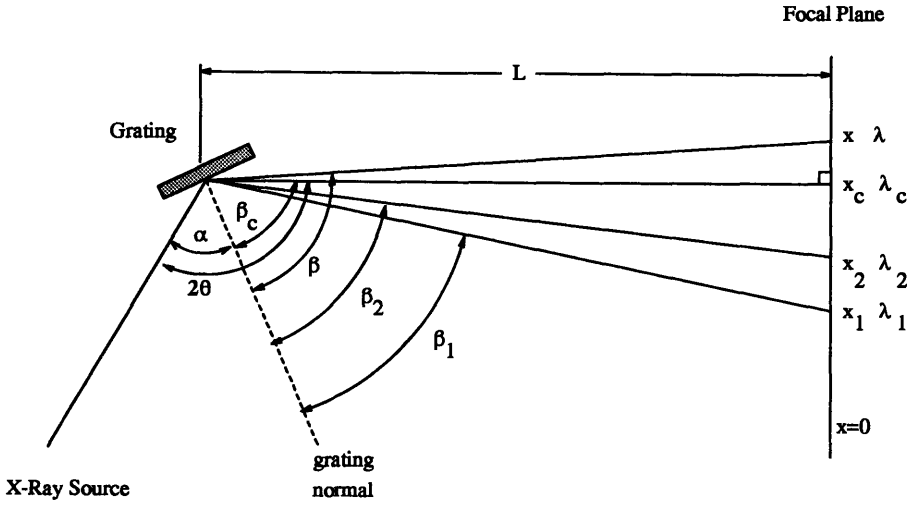

Figure 2-10: Figure showing terms of the grating equation

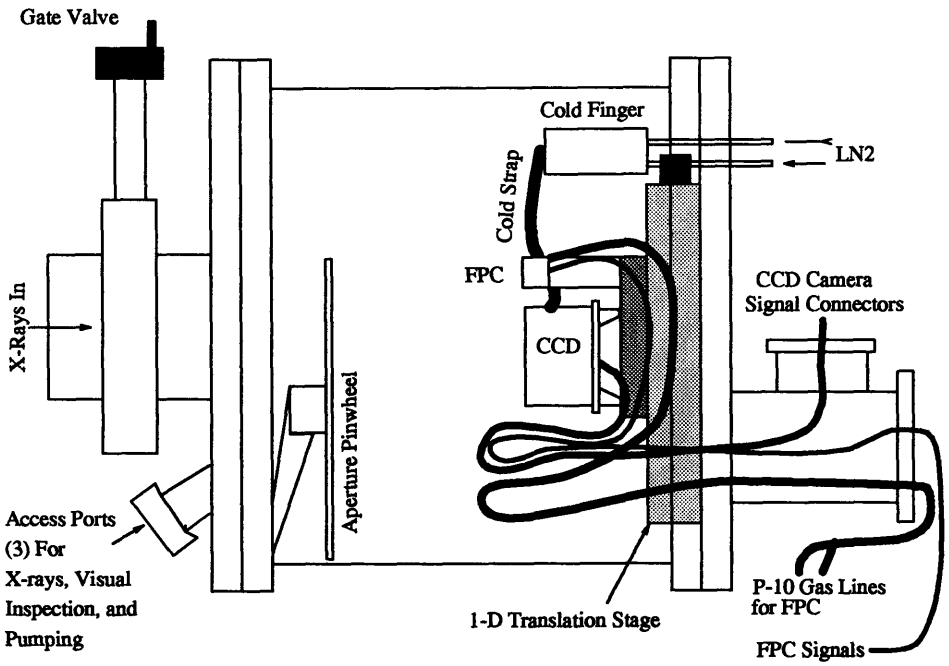

Figure 2-11: Schematic of the detector chamber. The chamber vacuum can be isolated from the rest of the system by closing the gate valve to the left. When the gate valve is open, X-rays from the spectrometer then pass through an adjustable aperture plate mounted on a pinwheel to be intercepted by either a FPC or CCD detector. The detectors are mounted on a 1D translation stage which moves up and down, in this figure. The cold strap which transfers heat from the CCD to an LN2 cooled cold finger also moves, as do the various signal cables and gas lines. Three access ports to the left allow the experimenter to visual inspect or illuminate the detectors with X-Rays from a radioactive source.

2.2.4 The Detector Chamber

The HIREFS spectrometer disperses the X-rays by wavelength onto a flat focal plane about 28 inches from its exit flange. Around this focal plane, I have built a detector chamber. Figure 2-11 shows the basic schematic of the detector chamber. I sometimes call this chamber, "the camera".

The camera interfaces with the rest of the low energy calibration facility through a 6 inch gate valve attached to the camera front plate. This gives us the opportunity to isolate the camera vacuum from the rest of the vacuum system during times when we need to modify the X-ray source, change filters, or change the CCD detector. We also used the

gate valve as a shutter to block emission from the rest of the system when dark frames are required.

Also on the camera front plate, are three access ports. These ports are standard 2.75 inch knife-edge flanges at 45 degree angles to the front plate. On one of these ports, a 5 mil thick beryllium window is mounted so that hard X-rays (usually from an ^{55}Fe source) may be injected into the chamber to illuminate the detectors for calibration and debugging purposes. Off of the same port, we have attached a 50 liter per second turbomolecular pump. It is through this port, that most of the pumping for the detector chamber is accomplished. Additional pumping occurs when the 6 inch isolation gate valve is opened (while the rest of the system is under vacuum) and when liquid nitrogen is pumped through the CCD camera cooling system (described later on). An optical view port is on one of the other access ports. We use this port both for visual inspections of the hardware and also as an optical light source for the detectors. On the third access port, an electrical feedthrough allows signals to be passed to a controllable aperture wheel.

The aperture wheel (or "pinwheel") lies in the focal plane of the spectrometer. Since the optics of the HIREFS spectrometer are very slow ($\sim$ f/100), both the aperture wheel and the detector plane (located about 1.5 inches further away from the HIREFS) are effectively in the HIREFS focal plane. With this aperture wheel, the facility can be switched between "monochromator mode" and "spectroscopic mode". It has a set of open apertures, a pinhole mask, and two slit masks. Figure 2-12 shows the configuration of the aperture wheel. The slits are arranged so that a rotation will place them approximately orthogonal to the wavelength dispersion direction. The pinwheel position is controlled with a stepper motor connected via an RS232 interface to a SUN workstation. Through this link, the pinwheel can be controlled across the Internet.

The aperture wheel is necessary since the FPC is a non imaging detector. The aperture wheel defines the spot size on the CCD to be calibrated absolutely relative to the reference FPC detector. Note that if the reference detector could image, then the aperture wheel would not be necessary, and the calibration throughput would be much higher.

The backplate of the detector chamber holds the CCD and flow proportional counter (FPC). The FPC and CCD are mounted on a vacuum qualified one dimensional translation stage made by New England Affiliated Technologies (NEAT) as shown in figure 2-11. The stage can position with a repeatability of 0.5 microns. The stage is driven by a stepper

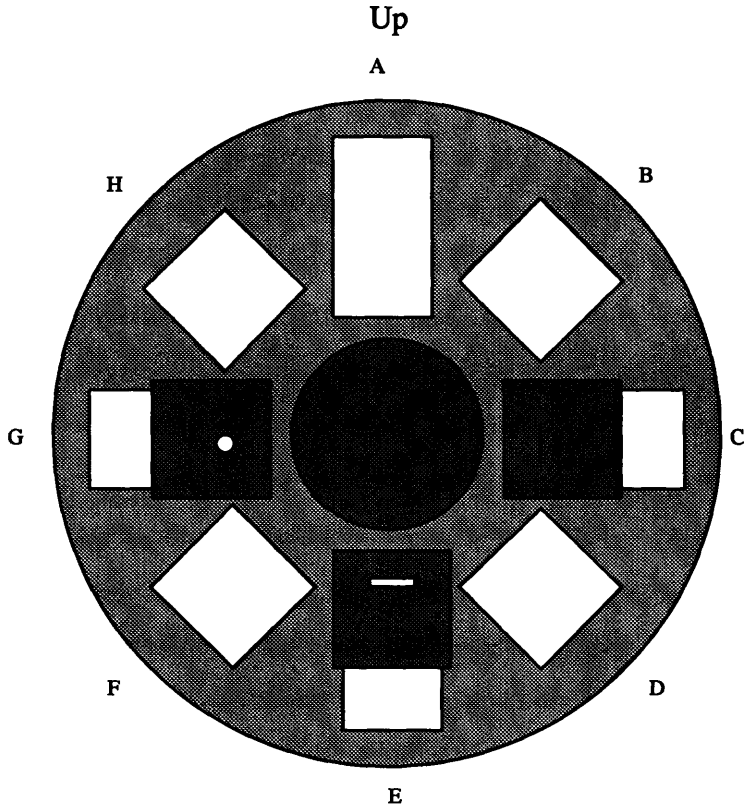

Figure 2-12: Pinwheel configuration as of 9 April 1994. A 400 micron diameter pinhole is at position G. The Wide calibration slit is at position E. A narrow calibration slit is at position C. The other positions are open.

motor which is connected via a serial communication link to a Sun workstation, and thus controllable across the Internet.

The backplate also contains feedthroughs for thermal, electrical, and gas connections to the detectors. Gas tubes and wires are arranged so that the motion of the detector stage does not result in binding. Below, I describe the two detectors on the backplate.

The Flow Proportional Counter

The reference detector used for the low energy SIS ground calibration was a flow proportional counter made by Manson Co. A diagram of the FPC is shown in figure 2-13. The FPC was chosen for this application because: 1) the quantum efficiency is large and easily determined, 2) it has no sensitivity to UV or optical flux, 3) it is operated at room temperature. One disadvantage of using the FPC is that it cannot image- thus it requires the aperture pinwheel described above.

The FPC operates on the same principle as the CCD. An X-ray photon passes through a dead layer (the counter window) and then interacts photo electrically in the gas of the detection region to produce a cloud of electrons. The number of electrons produced is proportional to the photon energy. The resulting electron cloud is collected on an anode to produce a pulse of current which is amplified by a preamplifier and binned by a multichannel analyzer (MCA). The counter gas flows continuously into the counter since the window is thin for soft X-ray efficiency and thus usually leaks at low levels. A more detailed discussion of FPC principles can be found in Knoll (1979).

The MCA is connected to a Sun workstation via a serial communication link. Through this link, commands can be sent to the MCA for data acquisition from the FPC. Also, data can be sent back to the Sun workstation where it is generally available on the Internet.

The FPC Calibration

The detection efficiency of the fpc is given by the following:

$$QE_{FPC}(E) = T_{window}(E) \times (1 - T_{gas}(E)) \times B(thresholds, flux) \qquad (2.7)$$

Where,

E = the photon energy,

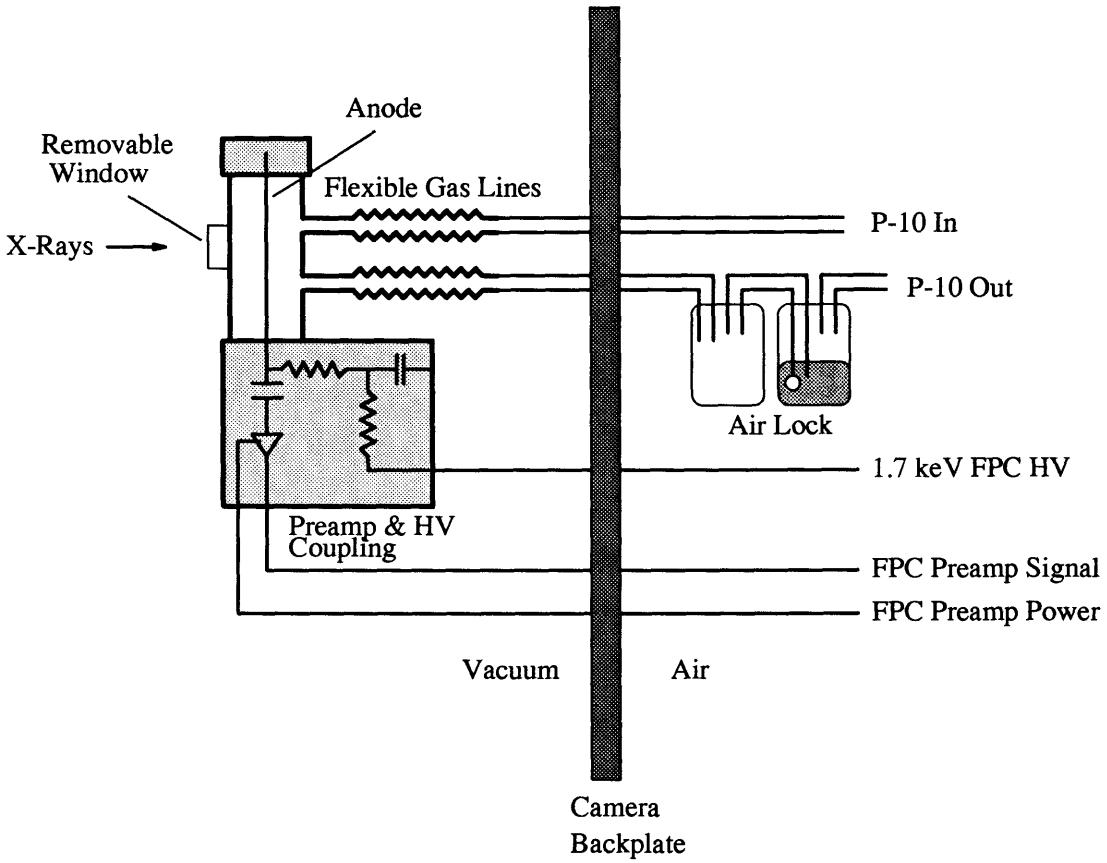

Figure 2-13: A simple schematic of the FPC. P-10 (90% Argon, 10% Methane mix) is flowed through the counter chamber via flexible stainless steel lines into an airlock at 1 atmosphere of pressure. The flow rate is adjusted so that a few bubbles per second appear in the water of the airlock. An anode biased at 1.7 keV collects electrons from photo electrically generated charge clouds. The signal is sent through a preamplifier in the vacuum chamber and then passed to the pulse shaper and multichannel analyzer. X-rays enter through a removable thin window.

$T_{window}(E)$ = the transmission of the FPC window,

$(1 - T_{gas}(E))$ = the absorption probability within the counters gas volume,

$B(thresholds, flux)$ = a term dependent on the event detection criteria.

One of the advantages of using the FPC as a reference detector is that each component of equation 2 is measurable or calculable. Below, we outline how these components were determined.

The FPC window used in our experiments was a thin film (~10 microns) of "VYNS" supported by a 67% transmission nickel mesh across a 1.5mm×10mm hole in a removable aluminum frame. VYNS is a co-polymer of vinyl chloride and vinyl acetate. The composition by weight is 5% H, 41% C, 5% O, and 49% Cl. Thus, for our work, the energy dependence of the window transmission is dominated by the K-edges of carbon and oxygen and the L edge of chlorine at 284 eV, 532 eV, and 185 eV respectively. The nickel support mesh is a square grid of 12 micron wide electro-formed nickel lines spaced at 61 micron intervals. The mesh spacing was confirmed with a microscope.

To measure the transmission of the window, we used the filter transmission stage shown in figure 2-14. In that stage are two identical apertures for holding filters or thin windows. In one aperture, we put an actual FPC window, while in the other we put an empty aluminum window frame. A CCD in the detector chamber collected pulse height and position information on photons passing from the Manson source, through the filter stage and finally through the spectrometer. The transmission measurement is made by taking data with the window in the beam and out of the beam. To compensate for drift in the X-ray source output and estimate systematic errors, 6 iterations ("chops") of window/no window data were taken. Each chop collected 200 seconds of data for both the window and no window states. The combined data set is shown in figure 2-14.

The data sets were divided into individual orders by filtering the event lists by pulse height and position. The grating equation for the the experiment was solved as described earlier using the Magnesium Kα line in third and fourth order. The order divided event list were binned by row number, which was converted to photon energy using the grating equation solution. This binning produces histograms of counts versus energy with and without the window in place. Dividing the window histograms by the no window data produces the transmission curve. Figure 2-15 shows the data and best fit model to the combined data set. Table 2.2 shows the results of fits to the individual iterations ("chops").

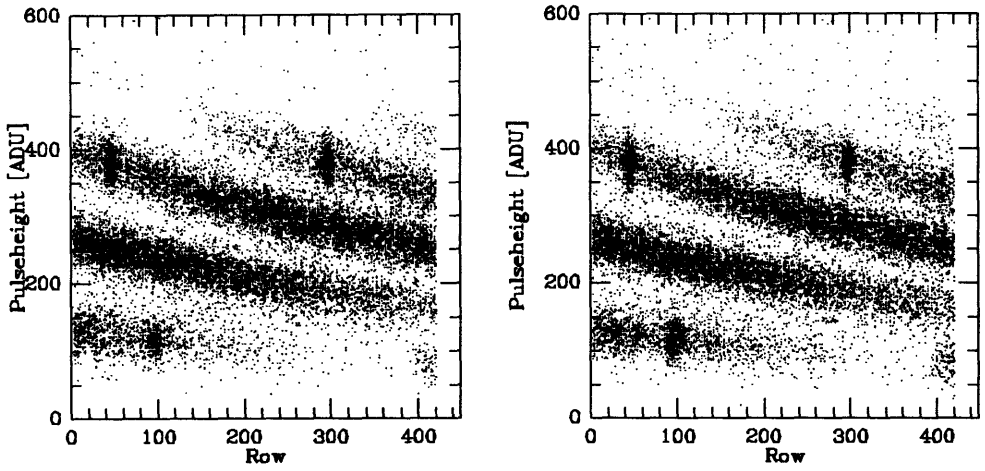

Figure 2-14: The CCD data with and without the fpc window in the beam. The CCD was arranged so that the dispersion direction of the HIREFS spectrometer was parallel to the columns. The data is shown as CCD pulse height vs row. Data with and without the FPC window in the beam are shown in the left and right hand panels, respectively. Magnesium Kα in 3rd and 4th order are at rows 50 and 295. Carbon Kα in first order is at row 90.

The statistical precision in the fitted models is about 5%. There is a one sigma scatter in the X-ray transmission measurements of about 13% in the mesh transmission. This systematic effect is probably associated with positioning errors with the window transmission stage. This is supported by the lack of any apparent systematic variations in the VYNS thickness. A careful analysis of the data may reduce this systematic effect to a lower level resulting in a net precision of 5 to 10%.

The FPC QE also depends on the interaction probability of photons in the counter gas. For this experiment, we have chosen P-10, a 90% argon 10% methane mix, as the counter gas. The mean free path length as a function of energy in the counter gas is shown in figure 2-16 for standard atmospheric pressure and 10% variations about this pressure.

There are two lengths of reference included in the figure: the depth of the counter and the window mesh spacing. The counter depth is indicated since it determines the high energy efficiency of the detector. The probability that a photon, which has already passed through the window, interacts within the FPC gas is given by:

$$1 - T_{gas}(E) = 1 - e^{-\frac{\lambda_{gas}(E)}{counterdepth}} \tag{2.8}$$

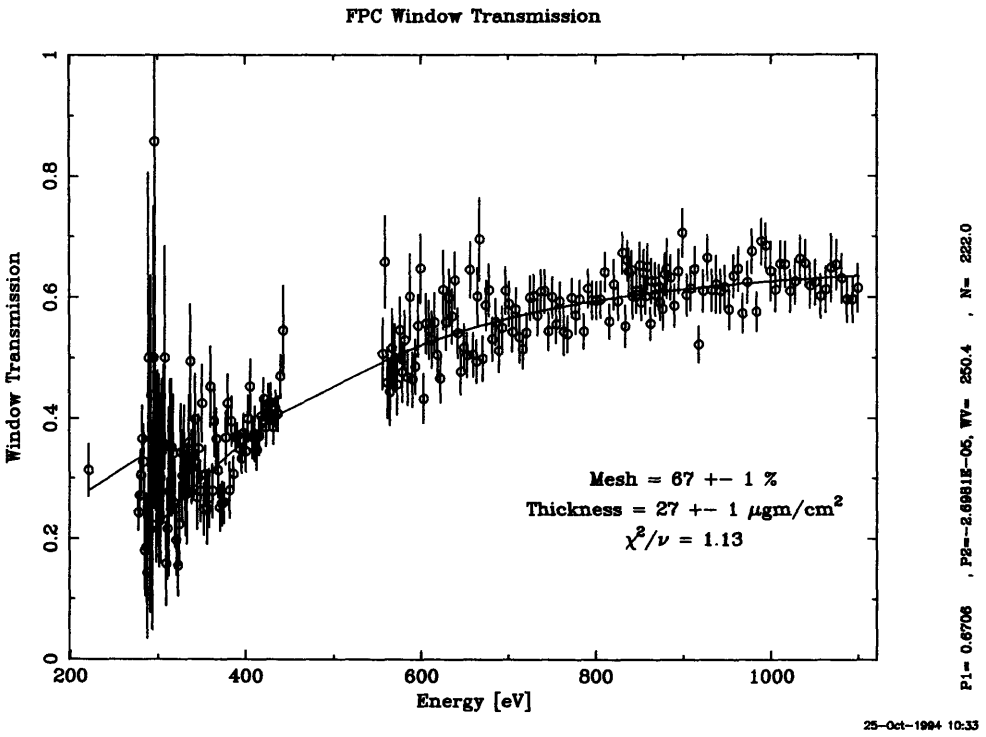

Figure 2-15: FPC window transmission data with best fit model for the combined data set. The best fit support mesh transmission is 67± 1 % and the best fit VYNS thickness is 27 ± 1 $\mu gm/cm^2$. The gap in data between 450 and 550 eV is due to the limited bandpass of the spectrometer sampled by the CCD.

Subset	Mesh Transmission [%]	Thickness [$\mu g/cm^2$]	χ^2/ν
Chop 1	59 ± 2	25 ± 3	1.02
Chop 2	61 ± 2	28 ± 3	1.18
Chop 3	77 ± 3	27 ± 3	0.81
Chop 4	59 ± 2	28 ± 3	1.10
Chop 5	76 ± 3	28 ± 3	0.89
Chop 6	75 ± 2	26 ± 3	0.79
Combined	67 ± 1	27 ± 1	1.13
Nominal	60	27	
Microscope	63 ± 2		

Table 2.2: Window Fit Results For Various Subsets of the Data. The nominal (as advertised by Manson Co.) values are shown as are the results of the microscope measurements of the mesh pitch. Statistically, the data seems good to 5%. There are systematic errors of 13% for the mesh transmission which are probably due to the positioning of the filter transmission stage. This estimate of the systematic errors comes from the scatter of the best fits for each chop. A more detailed analysis may reduce this effect. All the VYNS thickness results appear consistent.

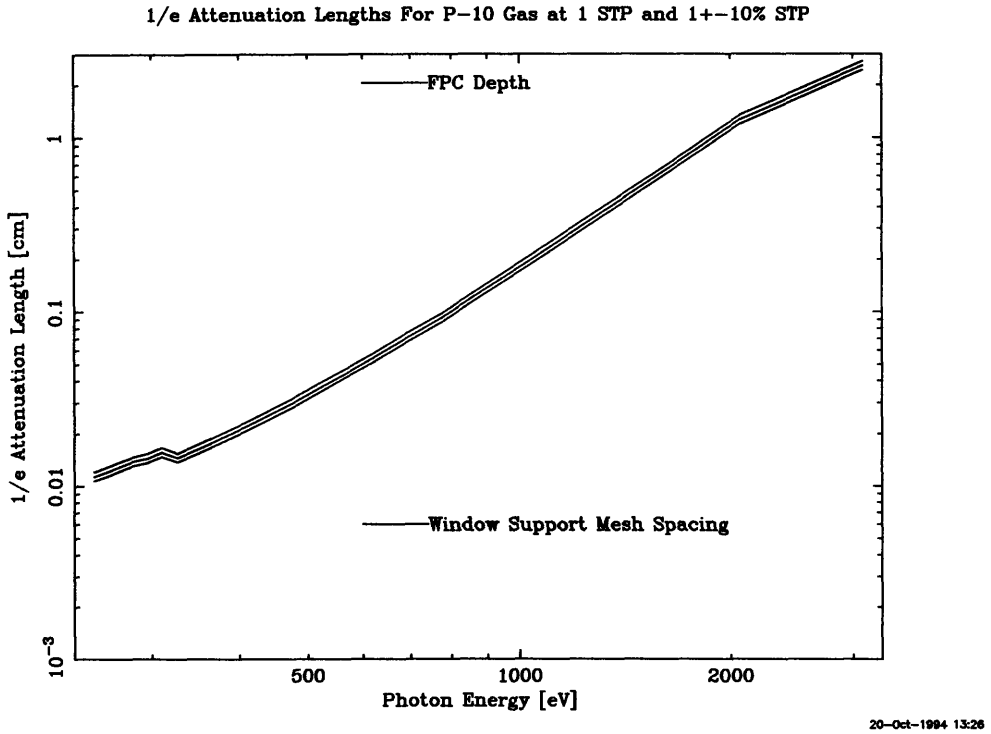

Figure 2-16: The attenuation lengths of X-rays as a function of energy for P-10 at 1 atmosphere and 23° C. Also shown are the attenuation functions for 10% variations in the pressure. The maximum size of the X-ray path in the FPC is 2.05 cm while the spacing of the window support mesh is about 61 micons.

where $\lambda_{gas}(E)$ is the mean free path of photons in the counter gas as shown in figure 2-16. The window mesh spacing is indicated since it determines the length scale where the electric field between the FPC window and the anode wire becomes irregular. The nickel mesh provides both pressure support and an electric potential reference. Photoelectrically induced charge clouds produced too close to the window will be incompletely collected at the anode due to this affect. The attenuation lengths of photons with energies within our range of interest in this low energy calibration are well within the mesh spacing and gas depth size.

The final term in the FPC QE equation is $B(thresholds, flux)$ which is dependent on the event detection criteria. This term is nearly unity except for when the fluence of X-rays on the counter is high. When the mean time between interaction is small compared to the pulse rise time (of order one microsecond), then some X-rays will not be detected. This is known as dead time. In our calibration, the dead time was negligible since the fluences were so low.

Combining the gas absorption calculation with the window transmission measure, we

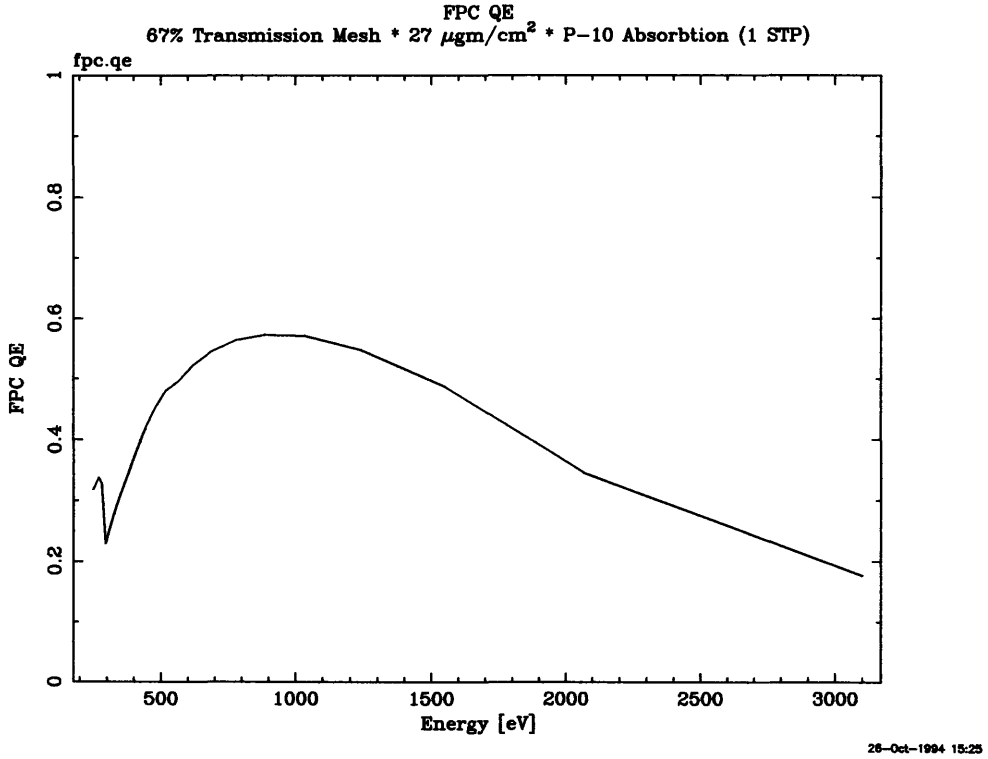

Figure 2-17: The FPC detection efficiency as a function of energy. The counter gas is P-10 at 1 atmosphere and 23° C. The window transmission function is for 27 $\mu gm/cm^2$ of VYNS on a 67% transmission mesh.

can get the FPC QE. Figure 2-17 shows the resulting FPC detection efficiency.

2.2.5 The SIS Interface

The SIS containing the CCD/filter to be calibrated is mounted just below the FPC on the one dimensional translation stage (figure 2-11). For the calibration, we used electrical and mechanical interfaces between the SIS and the detector chamber similar to those prescribed for the joining of the SIS with the ASCA satellite.

To reduce the thermal noise, we operate our CCDs at low temperatures. Originally, the CCD temperature was supposed to be -70° C, but the thermal performance of the flight models did not meet expectations. Thermal tests predicted a minimum focal plane temperature of -60° C. For this reason, the calibration was done with the focal plane at ~-50° C (10° margin of error). To achieve this, one of mechanical interfaces is that the baseplate of the SIS be kept at a temperature of roughly -20° to -40° C. The thermal electric cooler (TEC, see chapter 1) then takes the CCD temperature down to -50°.

In the detector chamber for the low energy calibration facility, this baseplate temperature is achieved with liquid nitrogen (LN2, 77° K). LN2 flows from a storage tank in the laboratory, through a liquid feedthrough mounted on the detector chamber backplate, into a copper cavity in the detector chamber, and finally out through the the same liquid feedthrough which it entered. The flow of nitrogen is controlled by a valve and feedback mechanism which tries to regulate the temperature of a sensor on the exit portion of the liquid feedthrough. A copper/tin flexible braid couples the copper cavity with the SIS baseplate through a thermally isolated strain reliever. In this way, we regulated the baseplate temperature to about -35±3° C, while retaining the ability to freely move the SIS up and down the translation stage of the detector chamber.

The SIS also has electrical interface requirements. Specifically, signals to and from both the CCD and the CCD temperature control system must pass through the detector chamber walls. Flexible cables connect the SIS to the SIS analog electronics (AE) through three vacuum electrical feedthroughs. The AE then accepts its commands through a small micro computer called the COSMAC which is connected to the general Internet via a serial interface to a Sun workstation. The COSMAC replaces the DE and DP described in chapter 1 during ground testing. The CCD output of the SIS/AE system is sent to a Next machine DSP port which makes the data available on the Internet.

2.3 The Low Energy Calibration Facility: Operation

The facility described in the previous sections was used to calibrate the low energy response of flight SIS detectors for ASCA. In this section, I outline some of the procedures used to acquire the data.

2.3.1 Alignment

A first step in using the facility is to align its various components.

The Source

The Manson source must be aligned with the HIREFS. This is done with the source alignment laser in the HIREFS. The grating is replaced with a mirror to reflect a laser through the HIREFS toward the source. The alignment reduces to moving the source so that the laser lands on the 0.5 mm diameter X-ray spot on the anode cap of the Manson source.

The Pinwheel, FPC, and CCD

The FPC is mounted on the NEAT stage directly above the SIS. Due to the small size of the FPC (10 mm×1.5 mm), the FPC cannot cover the entire width of the SIS CCD array (22 mm across). During the absolute calibration, The FPC window was positioned directly above chips 2 and 1 as shown in figure 2-18.

In order to calibrate the CCDs, we need to determine the relative positions of the FPC and the CCD. Specifically, we need to know which pixels of the CCD lie directly below usable positions of the FPC. To do this, the 400 micron diameter pinhole on the pinwheel aperture is moved into the beam of the spectrometer. First, the pinwheel and NEAT stage are moved until the image of the pinhole appears on the CCD. Moving the pinhole by rotating the pinwheel, we sample the HIREFS output in the cross dispersion direction. Moving the NEAT stage, we move the CCD up and down the dispersion direction. Once the relative position of the CCD and the pinhole are determined, it is easy to move the pinhole horizontally in specified increments. The calibration of the relative horizontal alignment of CCD and FPC is then carried out by scanning the NEAT translation stage up and down while monitoring the FPC count rate. This scanning is done for known pinhole-CCD horizontal positions- ie. just look at the CCD image. The relative horizontal positions of

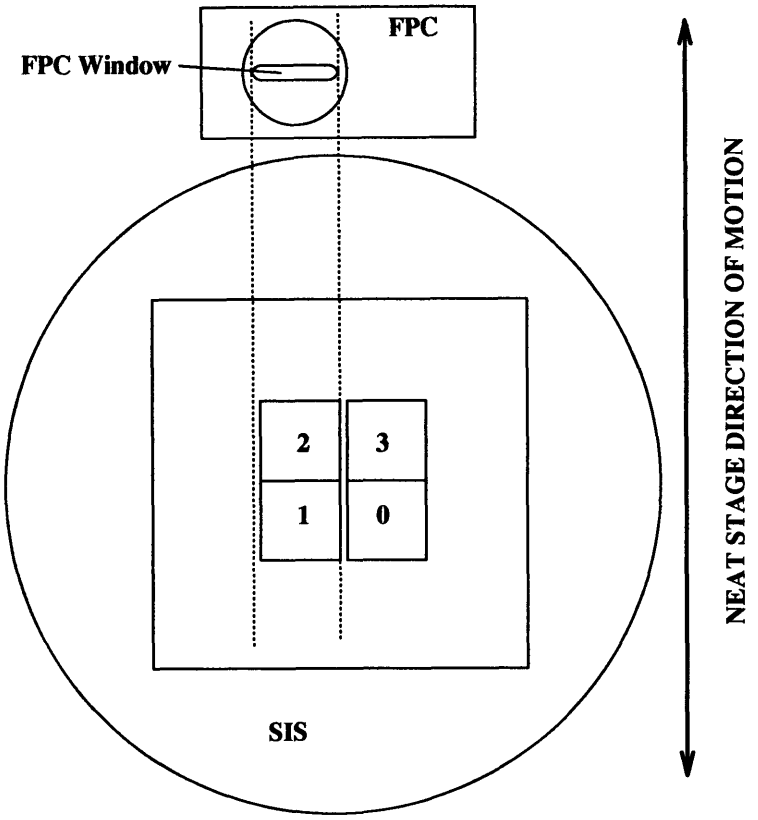

Figure 2-18: The view from the spectrometer of the FPC-CCD calibration focal plane. This shows that the FPC window is arranged above chips 1 and 2 of the SIS. The absolute calibration of the SIS was made between the FPC and positions on chip 1.

the FPC and CCD can be determined by noting which pinhole-CCD positions result in a positive versus a negative FPC signal during a NEAT stage scan. In this way, we learn which pixels on the CCD to be calibrated are below the FPC window.

2.3.2 Absolute Calibration

I made absolute calibration measurements using the slit aperture in the pinwheel at five positions of one CCD (CCD ID1) of each SIS as indicated in figure 2-19. These measurements allow us to look for row dependencies in the CCD quantum efficiency. For each of these positions, on the flight sensors, measurements were made for six different spectrometer grating positions. For the flight spare SIS, we had more time for calibration, so 16

spectrometer settings were used. Each of these spectrometer settings provided an average of three orders useful for calibration. Thus we calibrated absolutely the flight SIS sensors at a a total of 18 X-ray energies and the flight spare SIS sensor at about 50 energies. I made measurements at three additional positions using the 400 micron diameter circular aperture in the pinwheel for one HIREFS setting. These additional measurements provide column dependence information on the CCD quantum efficiency.

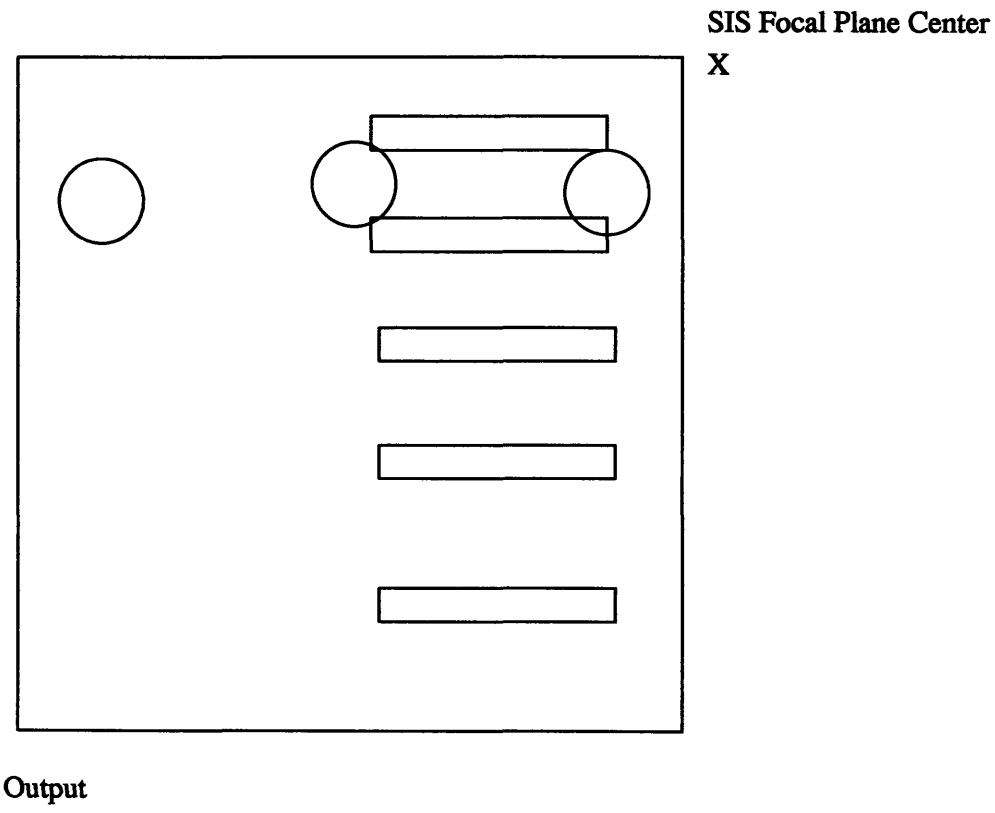

Figure 2-19: Absolutely calibrated positions on CCD 1. The rectangular slit in the pinwheel assembly was used to calibrate 5 positions along the column direction. A circular aperture was used to calibrate along the row direction. The center of the SIS is to the upper right hand corner of the figure. Other CCDs are above and to the right of the CCD depicted. The figure is not to scale.

A UNIX "csh" script automatically controlled the entire absolute calibration after the user made the necessary alignments described above and a few template files described below. Here, I describe the control script, what it required, and what it did. The script itself is in appendix G.

For each of the positions to be calibrated, I make a file describing the subarray on the CCD. For clarity, I call this file the "subarray file". This file is in a standard format called the Flexible Image Transport Standard (FITS). The data acquisition software (called "cineplex") reads this file and uses it to extract only the relevant subarray from the CCD data stream. This is done for two purposes. First, since the subarray is only about 5% the size of the entire CCD array, the size of a resulting data file is much smaller, allowing for more data to be taken before data storage drives fill up. Second, when the data acquisition system tries to read entire CCD images and write them to the data storage drive, the system starts to come out of synchronization and becomes less efficient, increasing the total real time to acquire useful data by as much as a factor of two. For multiple positions, there are multiple subarray files.

When the control script commands the CCD to take data for calibration of a particular CCD position described by the subarray file, it commands the pinwheel and NEAT translation stage to move so as to illuminate the desired portion of the CCD with X-rays. A "position calibration" file lists the information describing the pinwheel and NEAT stage positions corresponding to to the states where the CCD or FPC are in the X-ray beam.

For a particular CCD position to be calibrated and for a particular HIREFS setting, the control script commands multiple iterations ("chops") of the following procedure. First, move the CCD position to be calibrated into the X-ray beam. Then take CCD data for 200 seconds in 1-CCD mode. The data is in the format FITS images. Event lists and spectra are extracted from these FITS images at a later date. Next, move the FPC into the X-ray beam. Take FPC data is in the form of a pulse height spectrum for 250 seconds. In practice, this procedure is done for 6 "chops" in order to average out changes in the Manson source output.

Figures 2-20 and 2-21 show samples of CCD and FPC spectra taken by this procedure. In these figures, pulse height spectra from all five positions of SIS-S1's absolute calibration effort are shown. Both figures are for the same HIREFS setting. Comparing both figures, one notes why the CCD is such a promising instrument for X-ray astronomy. The CCD clearly separates the multiple orders from the spectrometer, while the FPC, a more traditional tool, blends the orders.

The detector quantum efficiency at a particular energy is computed by taking the ratio of the CCD measured flux at that energy to the FPC measured flux corrected by the FPC

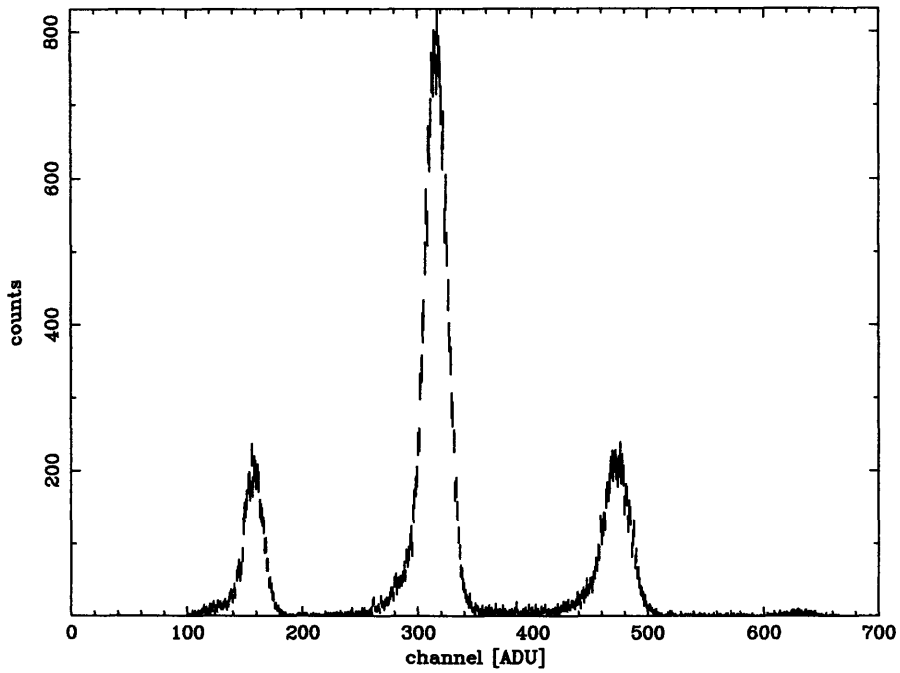

Figure 2-20: CCD from all 5 absolutely calibrated positions for one of the 7 spectrometer settings (scan=3600). Note that 4 orders are present and that they are evenly spaced. These "lines" are actually continuum passed through the HIREFS spectrometer and picked out with the slit aperture.

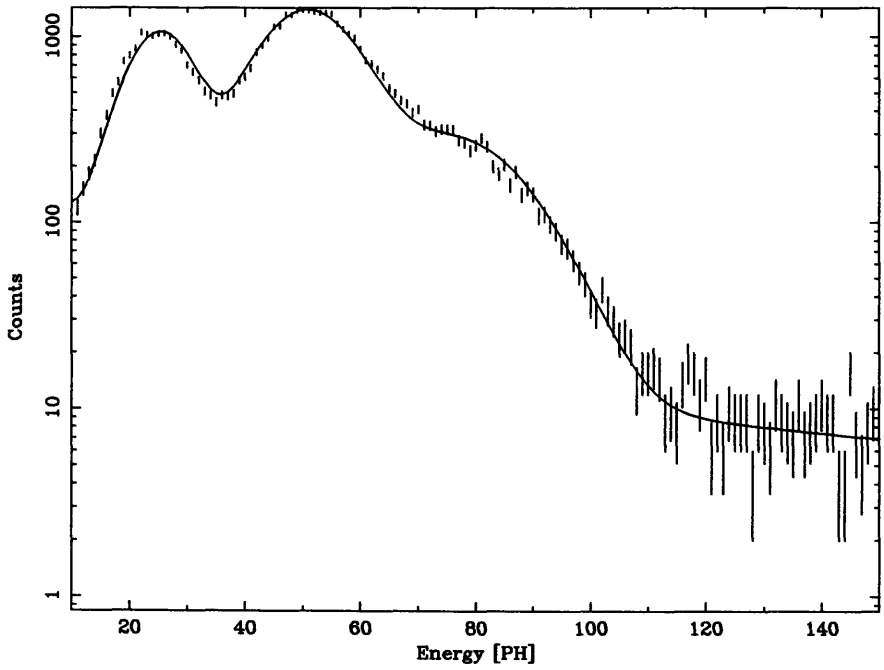

Figure 2-21: MCA data for the same spectrometer setting (scan=3600) as in the previous figure. Note that 3 orders are barely distinguishable. The model drawn on the data is for three gaussians for the X-rays plus a power law for the background.

quantum efficiency (eg. figure 2-17). The fluxes of each order in both the CCD and the MCA are calculated by fitting gaussians to the pulse height spectra and then normalizing by the corresponding exposure time. I use grade 0, 2, 3, and 4 events to produce the CCD spectra. A more careful analysis would include a more realistic function to fit the spectra based on the expected charge redistribution. Figure 2-22 shows a typical QE plot based on our data for a flight sensor. Since this absolute QE data does not sample energies around 0.4 keV and above 1.84 keV, this data is insensitive to the Si_3N_4 dead layer thickness as well as the silicon depletion layer thickness. Since we had more time for the flight spare, we more finely sampled the QE function as shown in figure 2-23.

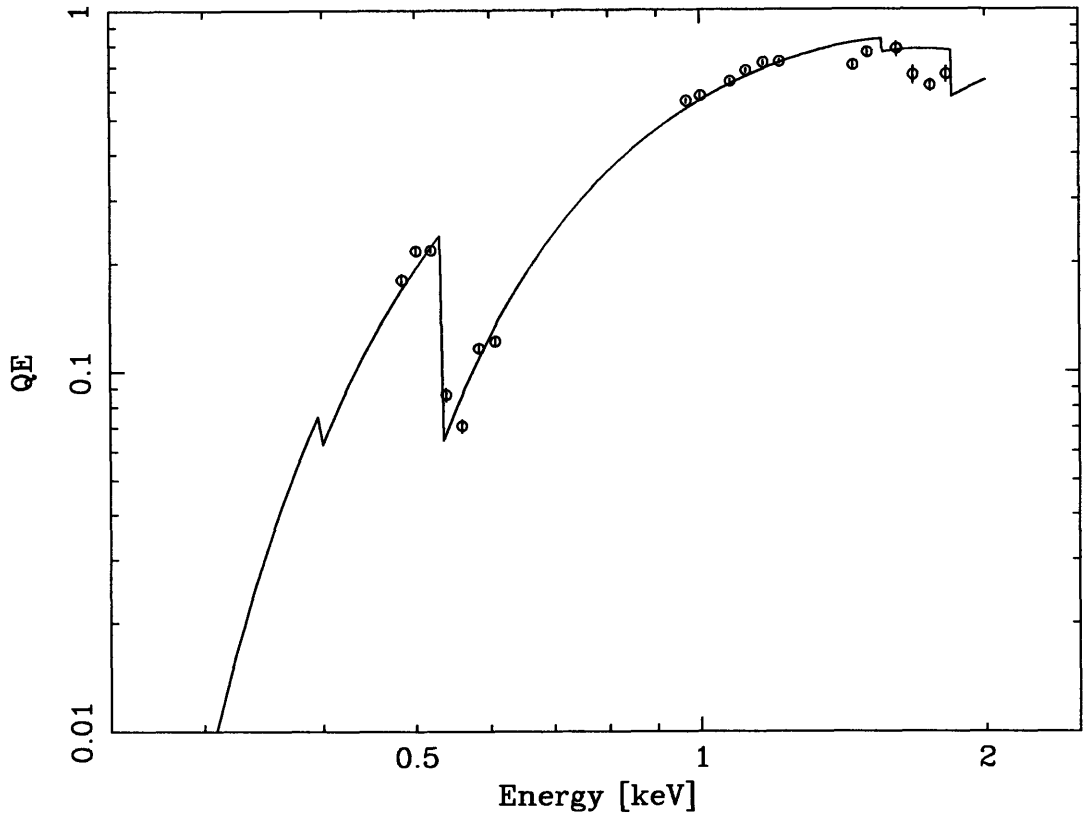

Figure 2-22: Fitted QE data for one of the SIS flight CCDs. The "slab and stop" model parameters are 0.18 $\pm$0.01 microns polysilicon dead layer, 0.46 $\pm$0.015 microns SiO_2 dead layer, 0.04 microns Si_3N_4 dead layer (fixed), 0.08 microns Al dead layer (fixed), 0.1 microns lexan dead layer (fixed), 30 microns depletion depth (fixed), and 6 microns (fixed) wide channel stops of 1 micron (fixed) thick SiO_2 and 0.74 micron (fixed) thick Si.

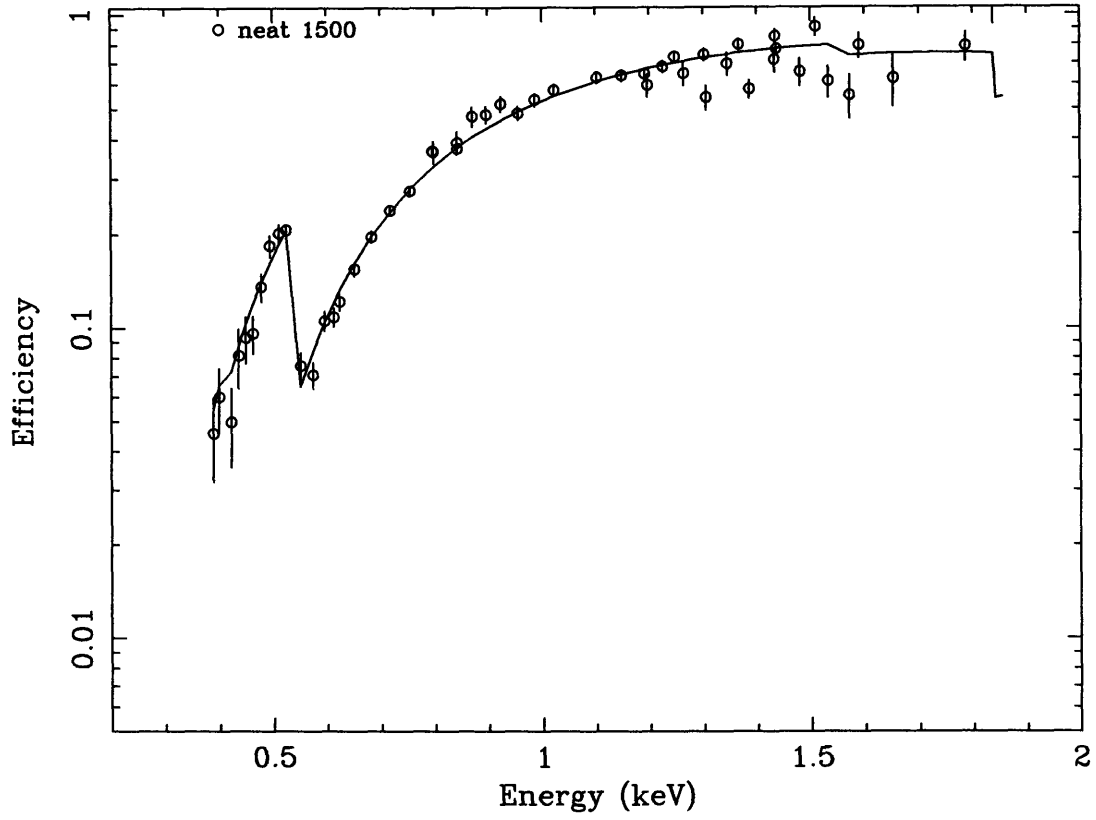

Figure 2-23: Fitted QE data for the SIS flight spare CCD. The "slab and stop" model parameters are 0.2 $\pm$0.02 microns polysilicon dead layer, 0.50 $\pm$0.02 microns SiO_2 dead layer, 0.04 microns Si_3N_4 dead layer, 0.08 microns Al dead layer, 0.1 microns lexan dead layer, 30 microns depletion depth, and 6 microns wide channel stops of 1 micron thick SiO_2 and 0.74 micron thick Si. Notice that this data is nearly insensitive to the Si_3N_4 dead layer thickness as well as the silicon depletion layer thickness. We have fixed the aluminum thickness to match the independently measured value done by the optical block filter manufacturer.

2.3.3 Relative Calibration

It is impractical to perform the absolute calibration for all positions on the SIS CCDs. Nearly forty-eight hours were required to perform the absolute calibration described above for one CCD of one flight sensor. Since the CCD detector is an imaging detector, a much more efficient procedure is possible, provided some positions on the CCD are already absolutely calibrated against the FPC. Since the CCD is an imaging detector, the aperture wheel is not required. So an open aperture is rotated into place and full frame data is taken across the entire CCD. This dramatically increases the calibration speed.

To transfer the calibration across the SIS, we now use the absolutely calibrated positions as the reference detector. The procedure is very similar in spirit to the procedure with the FPC: previously calibrated reference locations and new target locations of the CCD alternately sample an X-ray beam. The fluxes measured at the calibrated positions and the target positions are compared to determine relative quantum efficiency.

For each HIREFS setting, the NEAT stage is moved back and forth a distance equal to approximately half the spacing between the absolutely calibrated positions shown in figure 2-19. This is done multiple times ("chops") to average out Manson source fluctuations. Notice that this effectively transfers the calibration to 6 additional positions on the CCD. Also notice that four of the new positions, in between previously calibrated positions, are calibrated relative to two of the reference areas. Due to the multiple orders that come out of the HIREFS, this means that those four positions are calibrated at about 6 energies for a given HIREFS setting. Each of the other two new positions at the extreme edges of the CCD are calibrated relative to only one reference area, resulting in only about three energies. This procedure was done for six HIREFS settings. In the end, we calibrated eleven positions on the CCD with about twenty energies.

Once we have calibrated one CCD in this way, we can transfer the calibration to the others in the focal plane array. Here the procedure is identical to that outlined above, except that the "chopping" distance is equal to the spacing between centers of the individual CCDs in the array.

As is apparent in figure 2-18, this procedure will measure the QE of chip 2 relative to chip 1 and the QE of chip 3 relative to chip 0. Since chip 1 is the only absolutely calibrated CCD, this procedure as described will transfer absolute calibration only to chip

2. To transfer to the other CCDs, the SIS must be rotated 90°. In the setup, this can only be done by warming up the detectors, venting the chamber, and rotating the SIS by hand. This takes a long time. In the final calibration, we did not have enough time to do this. Thus only chips 1 and 2 of each flight sensor are absolutely calibrated.

To address this issue, a possible approach is to look at the scatter in relative QE between CCDs. This approach is statistical in nature and subject to systematic errors. One systematic error is that wafers, from which CCDs come from, may differ. This systematic can be explored done between pairs of CCDs made from the same original wafer versus pairs made on different wafers. See appendix E for a list of CCD wafer IDs. It is interesting to note that the absolutely calibrated positions on the two flight SIS sensors and the flight spare sensor show no gradient with position and that relative QEs between chips 1 and 2 of sensor SIS-S1 are identical to a few percent. This analysis was not done for this thesis-but it should be done. It is particularly important for SIS-S0, where three wafers provided CCDs for the focal plane array.

Another approach is to make use of the full frame data taken for the relative calibration and directly measure the edge strengths of dead layer materials. This data is available for several positions of all four CCDs for each of the two flight SIS detectors. It is also an independent check to the absolution calibration results. It assumes, however, that the Manson source, the spectrometer, and all UV blocking filters (except for the flight filters) do not have significant dead layer thickness of the same materials.

2.3.4 Edge Strengths

An edge strength is a measure of the magnitude of the discontinuous jump in detection efficiency at a characteristic absorption edge. In the energy range of this low energy calibration, there are 4 edges in the SIS response to consider. Table 2.3 lists these edges, their energies, their sources, and other useful information. The edge strength is directly related to the effective thickness of deadlayers in the detector. Consider continuum falling across an edge. The fluxes just below and above the absorption edge given by f_{low} and f_{high}, respectively, are related to the absorber thickness, d, and the 1/e attenuation lengths, as listed in table 2.3 by:

$$\frac{f_{low}}{f_{high}} = \frac{e^{-d/\lambda_{low}}}{e^{-d/\lambda_{high}}} \tag{2.9}$$

Through a simple model such as the "slab" approximation, one can use this information to predict quantum efficiencies at other energies. As mentioned above, this assumes that the source and other associated components in the calibration facility do not contribute significantly to the detector edges listed in table 2.3.

Table 2.3: Characteristic Edges in the SIS Response. The materials in the SIS contributing to the edge are listed as are the 1/e attenuation lengths of X-rays just below and just above the edge.

Edge	Energy [keV]	Sources	λ_{low} [μm]	λ_{high} [μm]
Nitrogen K	0.399	Si_3N_4	0.37	0.11
Oxygen K	0.5317	SiO_2	0.94	0.27
		Lexan	0.90	0.68
Aluminum K	1.5599	Aluminum	10.5	0.86
Silicon K	1.84	Si_3N_4	14.31	1.23
		SiO_2	7.07	2.06
		Si	6.14	1.58

Using the relative calibration data, one can extract some information about these edges. The procedure is to first separate the various spectrometer orders by sorting event lists according to event pulse height and row. Next, use the grating equation described earlier to convert event row to wavelength dispersed energy. Plot counts per row versus row with this conversion. Here, the HIREFS determines the energy resolution (better than 5 eV). If it is strong enough, an edge stands out clearly as in figure 2-24 for the oxygen K edge. For each edge, consider the range of energies surrounding the edge energy. The Manson source produces a strong continuum across all these edge energies. It also produces a few emission lines in inconvenient locations. In figure 2-24, a strong oxygen Kα emission line (525 eV) is just to low energy side of the oxygen K edge.

If the range of energies is small enough, then one can approximate the continuum in the vicinity of the edge as a power law of index γ and normalization N, $I(E) = N \times E^{\gamma}$. A material, X, of thickness d_X contributing to the edge will absorb the power law by an energy dependent factor, $e^{-d_X/\lambda_X(E)}$. Here, $\lambda_X(E)$ is the 1/e attenuation length for material X as shown in figure 2-3. Gaussians describe the line emission components well. In total, a sum of gaussians and edge absorbed power law continuum will describe the data in the vicinity of an edge well. Using such a sum, one can fit for the thickness of a material contributing to an edge.

In figure 2-24, I have done this for the oxygen K-edge of SIS-S1 Chip 1. In the figure, I have fit for the power law components and the thickness of SiO_2 in the CCD gate structure. Lexan in the optical blocking filter also contributes to the oxygen edge. Here, I have fixed the contribution due to lexan according to the filter's nominal thickness of 0.1 microns lexan. The edge strength estimate of the SiO_2 thickness is 0.45 ± 0.018 microns which is in excellent agreement with the absolute quantum efficiency fit result of 0.46 ± 0.015 microns shown in figure 2-22. This excellent agreement suggests that the deadlayer of oxygen in the Manson source producing the strong oxygen Kα emissio line is small, since the absolute QE measurement has taken out any effect of the source oxygen edge. Thus the edge strength measurements on chips 0 and 3 should yield valuable information about the absolute quantum efficiency on these CCDs. Notice that the fit is not perfect, especially around the edge. The edge model assumes the HIREFS has perfect energy resolution. Infact the energy resolution is approximately the width of the oxygen Kα line. A better way to do this fit would be to convolve a response function for the HIREFS with the photon spectrum model. I have not done this here.

In figures 2-25 and 2-26 show the corresponding data across the nitrogen and aluminum K edges, respectively. The models in these figures have the nominal thickness for each material contributing to the edge. The poor statistics of the data in these figures are not adequate to obtain nitride dead layer thickness and aluminum dead layer thickness. However, one may be able to use relative data taken with different HIREFS settings to attack this problem. I have not done this here.

One important goal of the low energy calibration was to measure the silicon edge strength. Three hurdles prevented me from getting adequate data for this measurement. One was that the HIREFS throughput at energies near the silicon edge (1.84 keV) is very low, resulting in poor statistics. Second, the grating admits more scattered X-rays at the shallow graze angles which diffract around 1.84 keV. This results in a non negligable background. Third, the Manson source produces tungsten characteristic lines which contaminate the data near the silicon edge. The tungsten Mβ line at 1.835 keV is particularly bad. Figure 2-27 shows the situation for this edge.

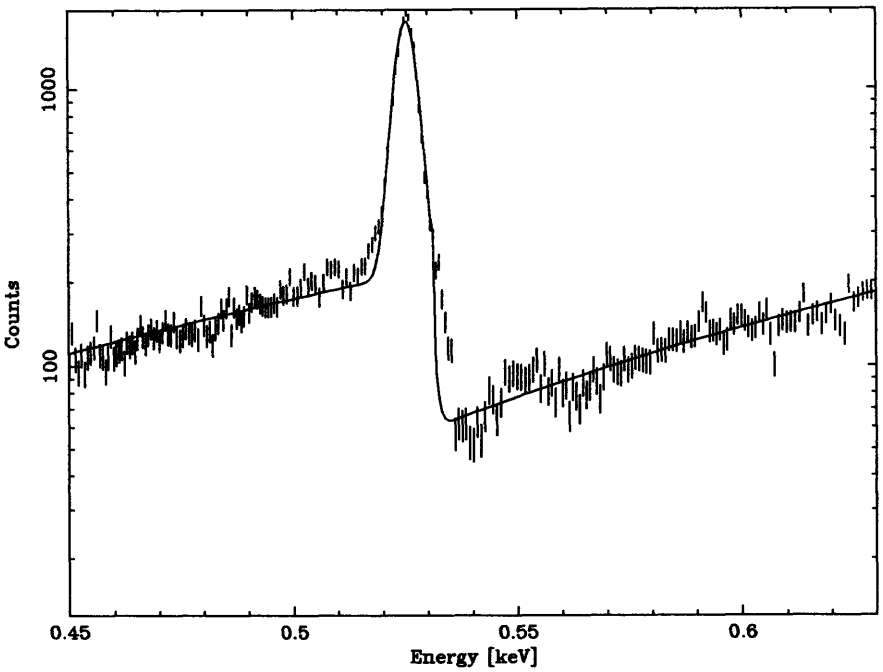

Figure 2-24: A portion of first order from one of the open aperture, full frame relative calibration data sets for the same CCD as used in figure 2-22. This portion covers the oxygen K-edge. The model is a gaussian (for oxygen Kα, 0.525 keV) plus power law absorbed by 0.1 microns (fixed) of lexan and 0.45$\pm$0.018 (fitted) microns of SiO_2.

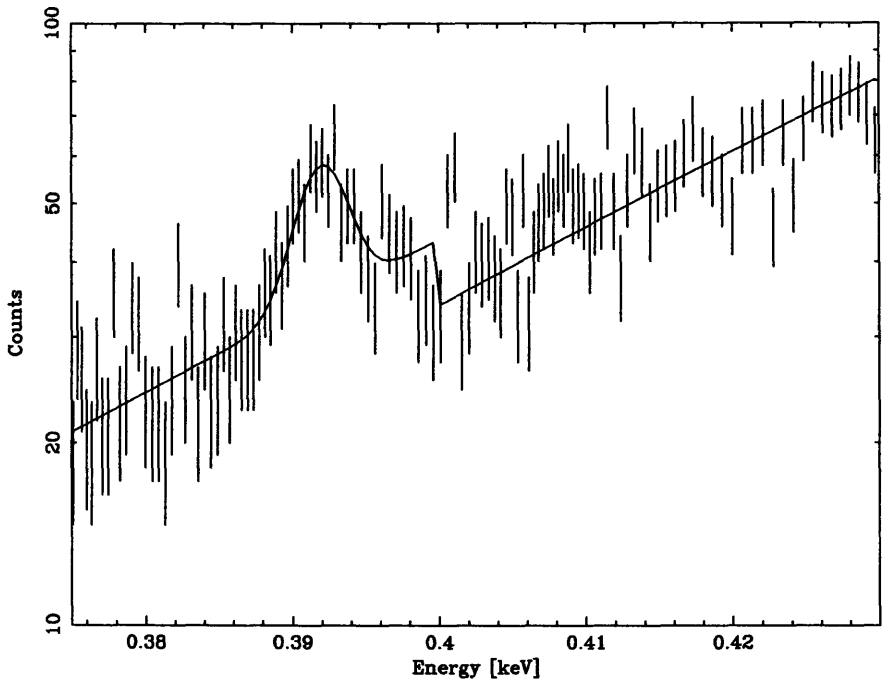

Figure 2-25: A portion of first order from one of the open aperture, full frame relative calibration data sets for the same CCD as used in figure 2-22. This portion covers the nitrogen K-edge. The model is a gaussian (for nitrogen Kα, 0.392 keV) plus power law absorbed by 0.04 microns (fixed) of Si_3N_4. There is not enough data in this figure to fit the nitrogen edge.

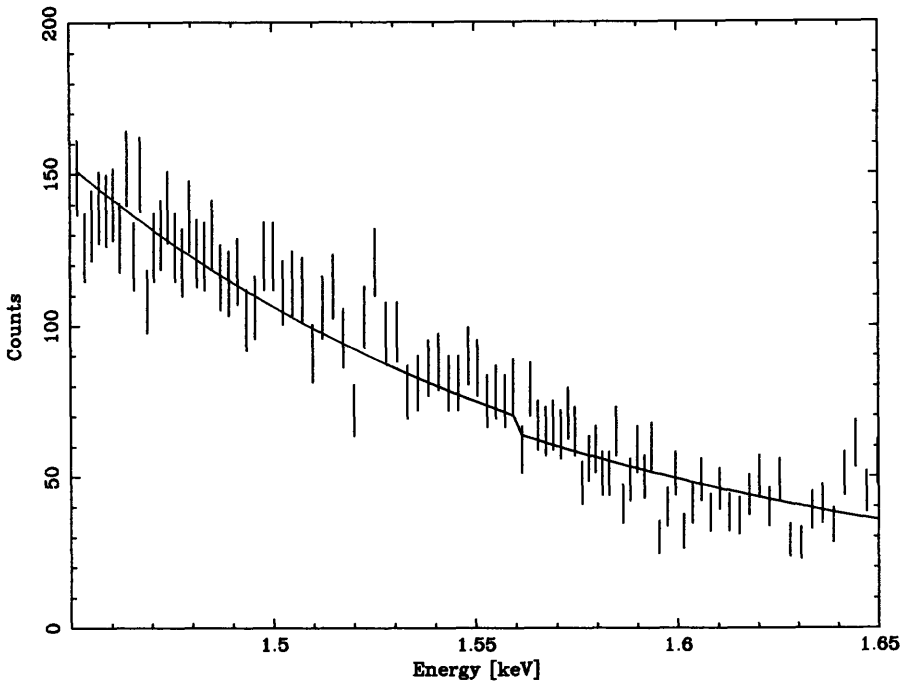

Figure 2-26: A portion of third order from one of the open aperture, full frame relative calibration data sets for the same CCD as used in figure 2-22. This portion covers the aluminum K-edge. The model is a power law absorbed by 0.08 microns (fixed) of aluminum. There is not enough data in this figure to fit the aluminum edge.

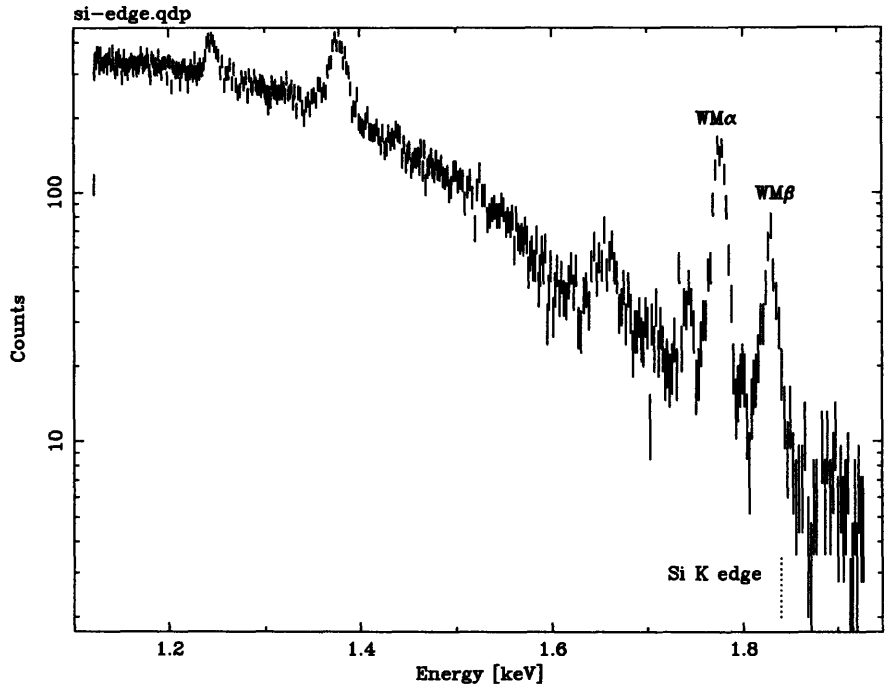

Figure 2-27: Third order from one of the open aperture, full frame relative calibration data sets for the same CCD as used in figure 2-22. The silicon edge is difficult to measure as a (time variable) tungston Mβ emission line contaminates the Si K edge at 1.84 keV

2.3.5 Spectral Redistribution

Both the relative and absolute calibration data can be used to assess the spectral redistribution of the CCD used as an X-ray detector. By "spectral redistribution", I refer to how a monoenergetic photon will transfer its energy to detector channels. When a photon interacts in the CCD, several processes are available to distribute the photon energy, depending on the photon energy. For CCD operation, the net effect is that a number of electron hole pairs will be separated. The number separated is roughly proportional to the incident photon energy except for a few cases. A fundamental energy which divides the spectral redistribution issue into two camps is the K-edge energy of silicon (1.84 keV).

If the photon has an energy above the K-edge energy, then the K-shell electron of the silicon atom which stopped the photon, has a finite probability to escape. The excited ionized atom left behind by the electron has several processes available to relax. Approximately 4.6% of the time, the atom will de-excite by emitting a silicon Kα photon. This is called "fluorescence", and the 4.6% figure is the "fluorescence yield". Depending on where the atom is located in the CCD structure (eg. the dead layer or the depletion region) and where the fluorescence photon ends up (eg. in or outside of the detection region of the CCD), there are four broad possibilities for what the resultant pulse height will be for the incident photon. One is that the final pulse height will reflect the total energy of the incident photon as in the case where the incident photon and the fluorescence photon both get detected in the same CCD cell. Another is that the resultant pulse height will reflect only the fluorescent photon energy of 1.84 keV as in the case where some non detection region of the CCD such as the dead layer intercepts the incident photon and the fluorescent photon stops in the CCD detection cell. This case results in the silicon fluorescence feature seen in the CCD. Another case is that the incident photon stops in the detection region and the fluorescence photon escapes. This is called the escape feature in the CCD response. The final possibility is the uninteresting case where both the incident photon and the fluorescence photon are not detected. Appendix C discusses these processes (particularly the escape feature) in more detail.

The low energy calibration considers photons of an energy below the silicon K-edge, so we do not consider all the special cases due to fluorescence. Since the number of possible detailed processes available to distribute the incident photons energy is so large and since

the physics itself can be extremely intricate, I will present only phenomenological results with some limited taste of the underlying physics.

When the incident photon interacts within the detection region of the CCD, it essentially produces a cloud of electrons. There are three basic periods in this charge clouds history which govern the energy resolution and spectral redistribution properties of the CCD. The first has to do with the messy physical processes associated with liberating the charge. The second has to do with how the charge cloud distributes itself among individual CCD pixels. The third has to do with the electrical and thermal noise associated with processing the charge cloud for measurement.

The number of electrons in this cloud is proportional to the incident X-ray energy with some scatter. The proportionality constant, ϵ, or "ionization energy" for X-rays in silicon is 3.65 eV per electron at typical CCD operating temperatures. The fluctuation in the number of electrons produced for a given photon energy is directly related to energy resolution of the CCD. Fano (1947) was one of the first to point out that the fluctuation in the number of charge-hole pairs produced by either a photon or particle interaction in detector material is somewhat smaller than one would expect based on counting statistics. For example, the distribution of number of electrons produced per photon interaction due to a beam of photons of a fixed energy E has a mean value of E/ϵ electrons, while the one sigma width of the distribution is a factor "$F^{\frac{1}{2}}$" times the spread expected by counting statistics of $(E/\epsilon)^{\frac{1}{2}}$. "F" is the "Fano factor" and has a value near 0.1 for silicon. The ionization energy and Fano factor for silicon are much smaller than they are for typical proportional counter gases which is part of the reason why silicon detectors have superior energy resolution.

A factor which affects this, however, is the spatial redistribution of the initial charge cloud among individual CCD pixels. This is also plagued with a nearly infinite variety of participating physical processes. The initial size of a charge cloud is roughly 1 micron in diameter for a 10 keV X-ray and varies as the X-ray energy to the 1.7 power (Janesick 1987). The photoelectrons produced will have some distribution of kinetic energy. The future of a given electron will depend on its kinetic energy compared to the local potential energy and thermal energy. In addition, the process of hole-electron recombination competes at various levels with the ionization process which produced the cloud. Finally, the location of the X-ray interaction compared to pixel boundaries also affects this redistribution.

In practice, these relative effect of these types of distortions depends on the event se-

lection criteria. For the SIS, detected events are classified according to their shape (see appendix B). The event selection parameters which affect resolution the most are the split threshold and event grade. Figure 2-28 shows CCD energy resolution as a function of energy for a few typical grades and split thresholds.

The data in figure 2-28 comes from one set of full frame "relative calibration" data. Here, I show data from SIS-S1, Chip 1. For each CCD, there is approximately 75 times more data. Different split threshold and grade selection criteria were used on the same data to produce the comparison. For this figure, events were taken from strips 5 pixels (135 microns) wide of the CCD in the dispersion direction of the spectrometer. Each strip corresponds to a different set of energies due to the multiple order output of the spectrometer. The bandpass of each strip is position and order dependent and ranges from about 4 eV for first order to 8 eV for second order to 12 eV for third order. This plot makes use of only the first two orders. Comparing these bandpass widths to the energy resolution of the CCD, we see that the energies passed in a given order by a particular strip are effectively monoenergetic for the CCD. I have binned in energy space the pulse heights of the events. I then fit a simple gaussian to the resulting line spectra. These fits result in the full width half maximum (FWHM) scale on the figure.

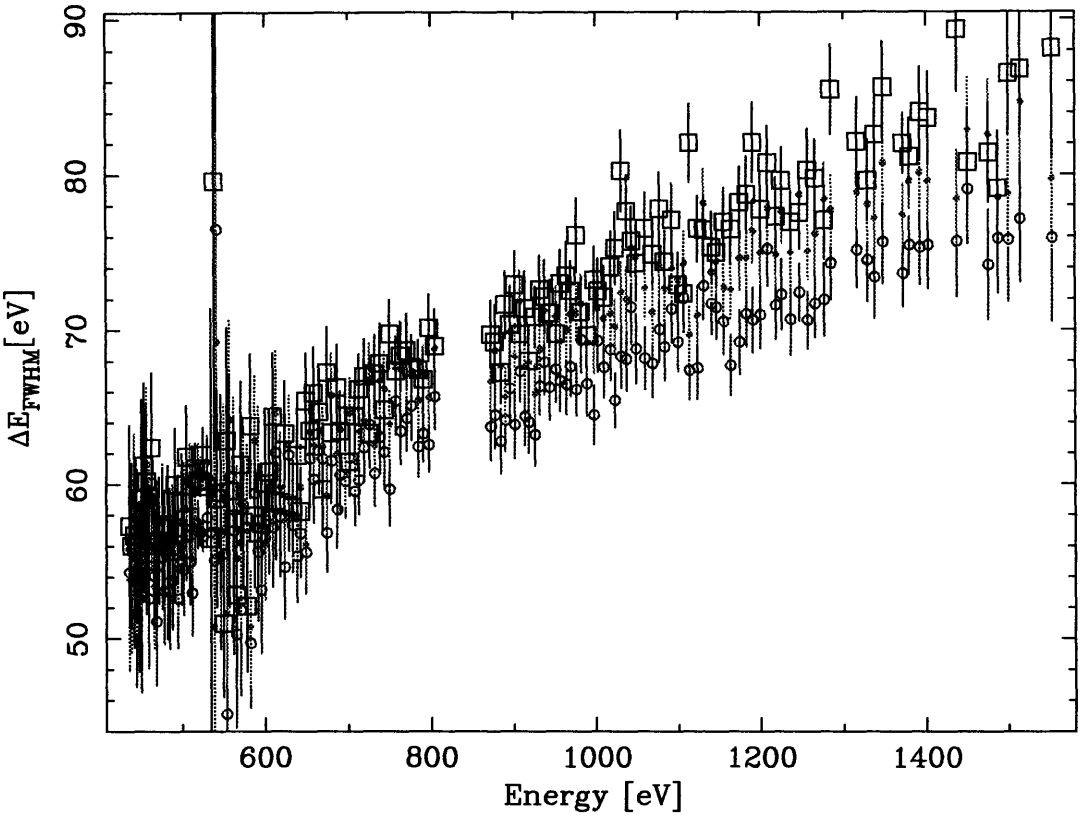

Figure 2-28: The energy resolution as a function of energy from some of the relative quantum efficiency measurements. The squares correspond to split level 40 grades 0, 2, 3, and 4. The open circles correspond to split level 10 event grade 0. The closed circles correspond to split level 10 grades 0, 2, 3, and 4.

Dark current in the CCD conspire with optical light and electrical noise to further degrade the resolution. Some of these effects (especially dark current) are strongly temperature dependent. I took calibration data with a CCD temperature of -50° C. The SIS achieved a temperature of -61° C on orbit. Thus the resolution results found in the ground calibration will be some what different from those achieved in flight data. In this calibration, I shut off the output of the Manson source/ spectrometer by closing a gate valve. This allows us to get a measure of the total system noise. For the CCD which provided the data shown in figure 2-28, the measured total system noise (dark current plus electrical) was found to be 5.5 electrons RMS.

I have fit equation 1.1 to each of the set of points in figure 2-28 in order to get a measure of the system noise and the Fano factor. Table 2.4 lists the results. Knoll (1979) reports that measurements of the Fano factor for silicon range from 0.084 to 0.143. Event selection effects force this calibration measurement of the Fano factor across the range of previously reported values. In addition, the use of the split grades 2, 3, and 4 (see appendix B) adds more read noise due to the additional pixel involved. Clearly, a more systematic analysis of these effects must predate a discussion of the ability of this calibration to contribute to the knowledge on the Fano factor.

Table 2.4: Noise and Fano Factor Fit Results For SIS-S1, Chip 1.

Split Threshold	Event Grades	Noise (electrons RMS)	Fano Factor	χ^2/d.o.f.
10	0	4.77 ± 0.2	0.141±0.007	80/154
10	0	5.5 (fixed)	0.110±0.002	133.6/154
10	0234	4.95 ± 0.2	0.159± 0.008	106/154
10	0234	5.5 (fixed)	0.135±0.003	137/154
40	0234	4.56 ± 0.2	0.189±0.009	110/154
40	0234	5.5 (fixed)	0.150±0.004	176/154

Finally, I present some data showing the energy dependence of event grading- the "branching ratios". Branching ratios are the fractional composition by grade of events due to photons of a particular energy. In a practical sense, for ASCA, I define the branching ratio for a particular grade to be the ratio of the number events detected in that grade to the number of events detected in grades 0, 2, 3, and 4. Figure 2-29 shows the branching ratios, as a function of energy, for events classified with a split threshold level of 20 to be grades 0, 2, 3, and 4.

Notice the discontinuity in grades 3 and 4 (left and right split events) at the oxygen K edge (532 eV). No such discontinuity is seen in the grade 2 (vertically split) events. Qualitatively, this is due to the fact that the horizontal boundaries of the CCD pixels are defined by channel stops (see above) while the vertical boundaries are defined by potential wells. The channel stops are essentially slabs of SiO_2 about 1 micron thick and 6 microns wide. Since the pixels are squares 27 microns wide on a side, one can compute the ratio of transmissions through the CCD dead layer along horizontal and vertical pixel boundaries:

$$ratio_{H/V} = \frac{27 \times T_{cs}}{(27 - W) + W \times T_{cs}}, \tag{2.10}$$

where, W is the width of the channel stop, and T_{cs} is the transmission through the channel stop given by:

$$T_{cs} = e^{\frac{D}{\lambda_{SiO_2}(E)}} \tag{2.11}$$

where D is the channel stop thickness and $\lambda_{SiO_2}(E)$ is the attenuation length of photons of energy E in SiO_2 (as in figure 2-3). Figure 2-30 shows the ratio of horizontal to vertical events for the data shown in figure 2-29. Plotted in the same figure is the equation 2.10 fitted for D and W.

Notice that these branching ratios are also a function of the split level threshold used to determine the event classification. Figure 2-31 shows how the grade 0 (single events) varies with energy for 2 different split thresholds. Increasing the split threshold decreases the "quality control" in selecting events. Thus there are more events for a larger split threshold, but somewhat worse energy resolution as shown in figure 2-28. A particular consequence of this is that quantum efficiency curves such as shown in figure 2-23 depend on grade and split threshold.

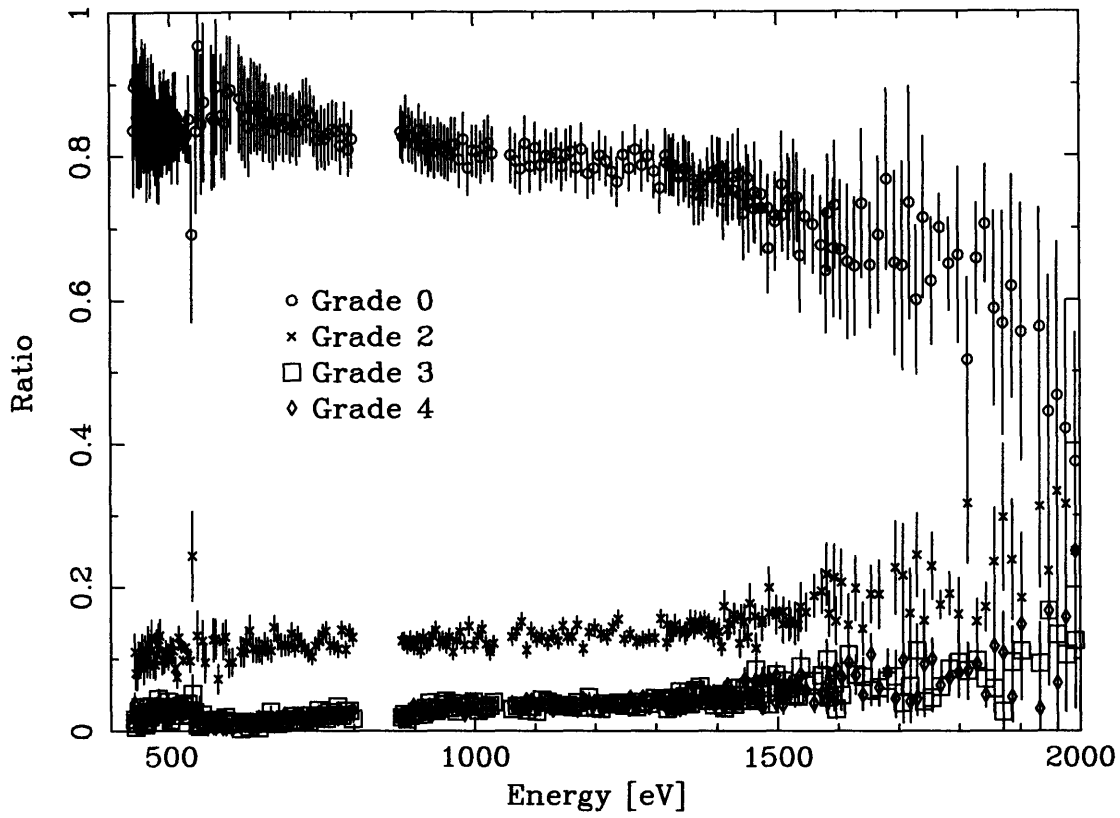

Figure 2-29: The branching ratios as a function of energy for events graded with a split threshold of 20. The data comes from chip 1 of Sensor SIS-S1. The ratios shown are the ratio of counts of events with the designated grade to the total number of grade 0, 2 ,3, and 4 events.

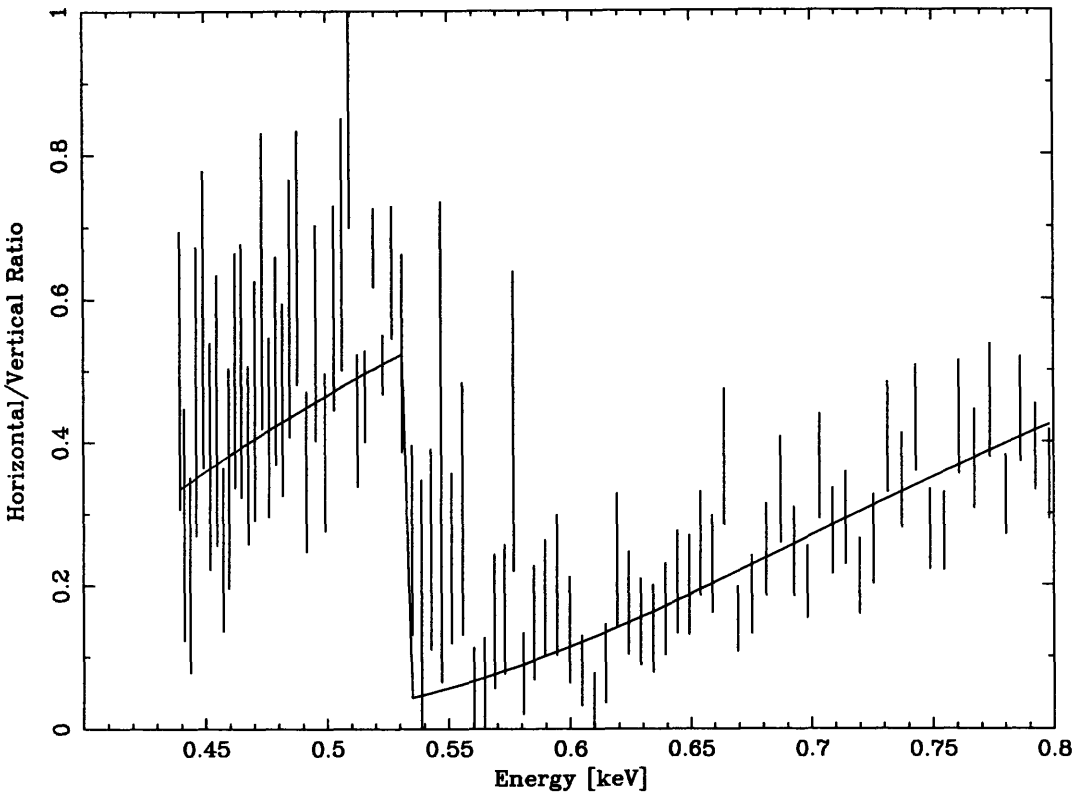

Figure 2-30: The ratio of the horizontally split events to the vertically split events (split threshold=20) for the SIS-S1 Chip 1 data. The curve is the predicted ratio if the difference between vertical and horizontal splits is merely due to the transmission through the SiO_2 channel stops which form the horizontal boundaries of the pixels. The oxygen K edge is clearly visible.

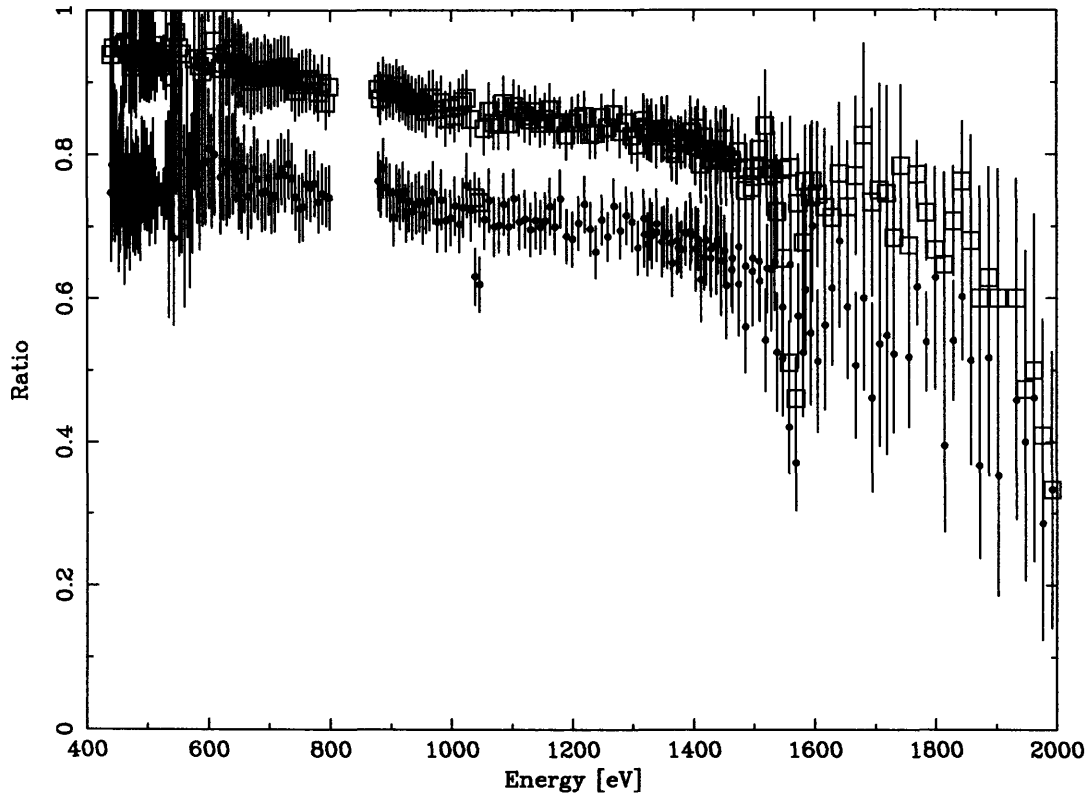

Figure 2-31: The singles fractions (ie. the branching ratios for grade 0 events) for split threshold 50 (upper data set) and split threshold 10 (lower data set).

Chapter 3

Proton Damage in X-Ray CCDs Ground Evaluation Techniques and Effects on Flight Performance

I report measurements of effects of 2.1 MeV and 40 MeV protons on Charge Coupled Device X-ray detectors of a type used on *ASCA*. I discuss ground performance characterization techniques and compare measurements to simple models of the detector damage mechanism. Traps associated with radiation induced defects are the basic cause of the damage. I describe how trap characteristics can be extracted from the CCD data. I compare the predictions of detector performance degradation rates in low-earth orbit to early flight data obtained from the Solid State Imaging Spectrometer (SIS) focal plane instrument mounted on the Japan/US X-ray astronomy satellite *ASCA*.

3.1 Introduction

It has been known for some time that the space radiation environment (especially the proton flux) can affect CCD performance on time scales of years or less (Janesick *et al.* 1991 and references therein). The performance of photon-counting X-ray CCDs is particularly sensitive to radiation damage because very small charge packets (100 - 2000 electrons) must

be transferred with high efficiency (charge transfer inefficiency $< 10^{-5}$ per pixel).

In this chapter I report on a series of experiments to determine the sensitivity of our X-ray CCD detectors to the trapped proton field we expect to encounter in low earth orbit. First, I will discuss the test irradiations. Then I will discuss the post-irradiation experimental evaluation of the radiation damage. Next, I will describe a model which explains the observations and suggests more refined measurements. Then, I will describe the model refined measurements. Finally, I discuss some of the real problems encountered on orbit.

I have discovered that the performance of an irradiated detector depends strongly upon both detector temperature and the flux of X-rays used to characterize the detector. The latter dependence must be carefully controlled if meaningful measurements of radiation effects are to be made. I compare our measurements to predictions of simple models of the radiation damage mechanism.

These laboratory measurements have been used to estimate on-orbit performance degradation rates for various detector shielding configurations (Gendreau *et al.* 1993).

3.2 Laboratory Irradiations

ASCA operates in a low earth orbit with several daily passes through the South Atlantic Anomaly (SAA). The initial orbit is 525 km $\times$ 620 km with an inclination of 31°, very close to the pre-launch expectation. Results from a NASA charged particle environment study of the predicted *ASCA* orbit (Stassinopoulos and Barth, 1991) indicated that geomagnetically trapped protons are the greatest concern for radiation damage. Figure 3-1 shows the predicted proton spectrum incident on the CCDs based on this study assuming the shielding currently employed on *ASCA*. Figure 3-2 shows the specific energy loss for protons in silicon. Integrating the product of figures 3-1 and 3-2 yield the daily dose in "rads" of silicon expected to be about 0.5 rads per day. A rad is the a unit of energy loss equal to 100 ergs per gram. Our experiments have measured damage cross sections at two representative energies: 2.1 MeV at the MIT Plasma Fusion Center (PFC) and 40 MeV at the Harvard Cyclotron Laboratory (HCL).

At the PFC, a Cockroft-Walton accelerator was used to induce a D-D nuclear reaction which produced protons with an energy distribution peaked at 2.1 MeV with a full width at

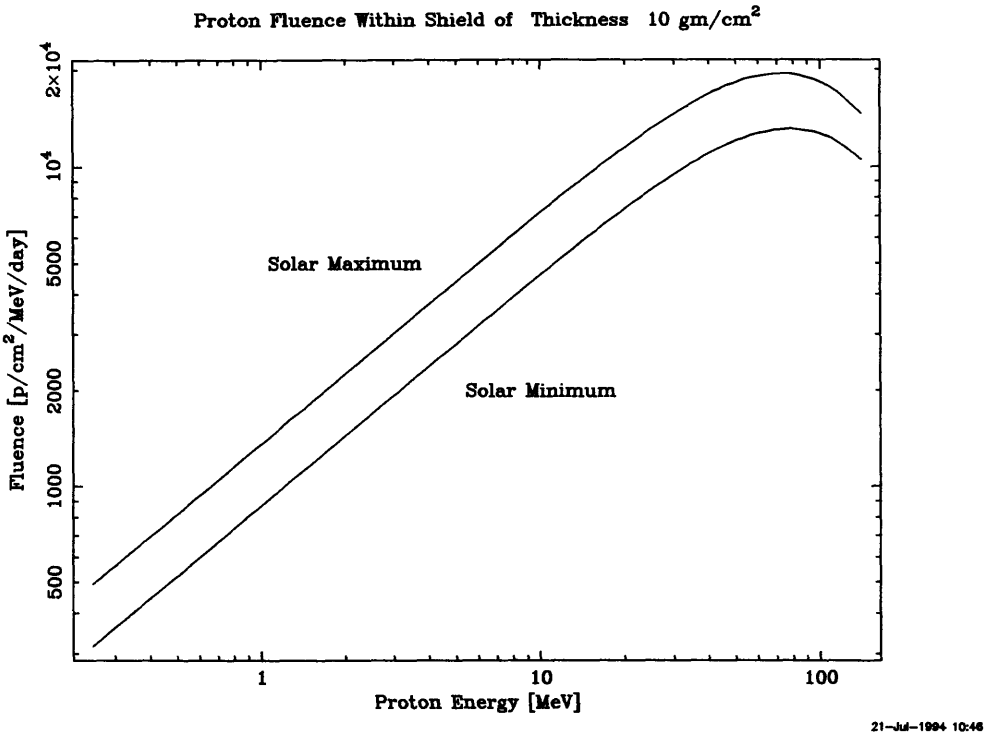

Figure 3-1: The predicted proton spectrum inside a simple model of the SIS shielding. The shielding is assumed to be spherically symmetric with a thickness of 10 gm cm^{-2}. Figure courtesy M. Bautz.

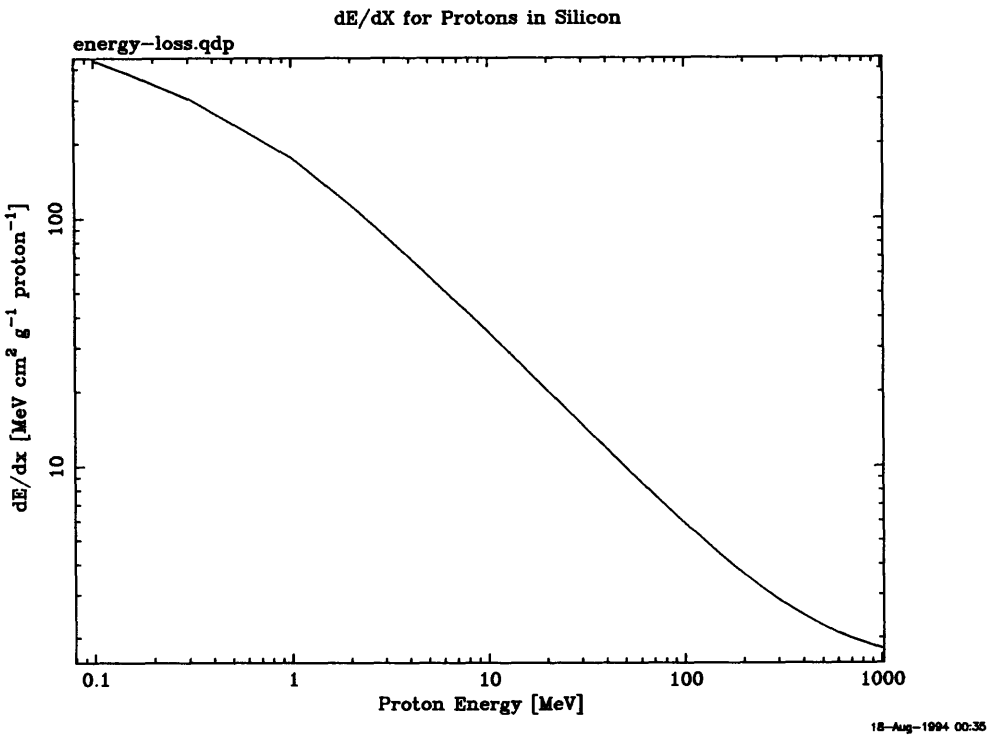

Figure 3-2: The specific energy loss for protons in silicon.

half maximum of 120 keV. For more details about the setup, see Wenzel et al (1992). The typical dose at the PFC was 1.2×10^8 protons/cm^2 (200 rads in silicon) accumulated over several hours. This dose is equivalent to what will be encountered by the CCDs after about one year in orbit. The mean flux was 1.5×10^4 protons/cm^2/sec. The flux was monitored continuously during the irradiation by surface barrier detectors. The uncertainty in total fluence was approximately 5 %. Figure 3-3 shows the arrangement for the irradiations at the PFC. Irradiations at the PFC were carried out with the CCDs at room temperature with the CCD signal and power leads grounded.

At the HCL, the 160 MeV primary beam of protons was degraded with lexan blocks to a spectrum peaked at 40 MeV with a full width at half maximum of about 4 MeV. The typical dose used at HCL was 6.4×10^9 protons/cm^2 (1200 rads in silicon) accumulated over a period of about two minutes. This dose is equivalent to what would be expected after about 6.5 years in orbit. The mean flux was 2×10^7 protons/cm^2/sec. Irradiations at HCL were carried out with the CCDs at room temperature as well as at a operating temperature (-70 C). No differences were seen between devices irradiated warm and devices irradiated cold. Irradiations were carried out with the CCD both powered on and powered off. No

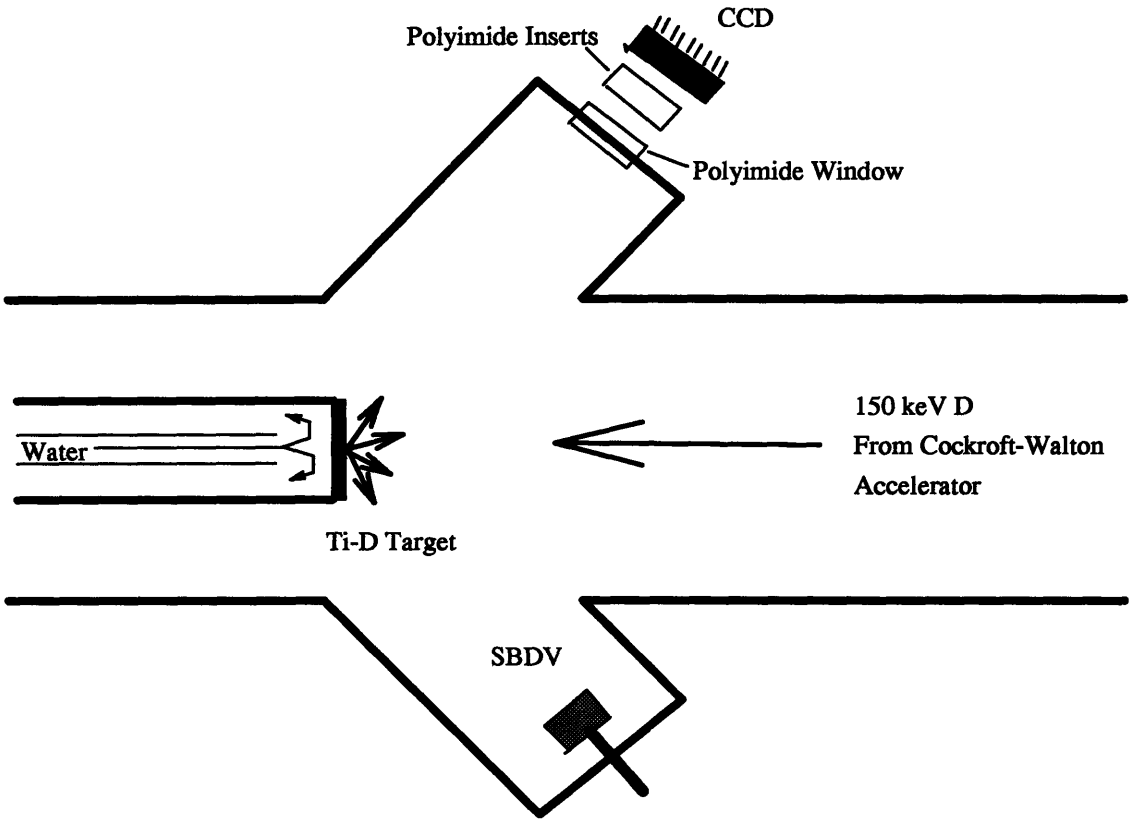

Figure 3-3: PFC Irradiation Setup: Deuterons are accelerated to about 150 keV in a Cockroft Walton Accelerator. They then strike a water cooled deuterium saturated titanium target where a DD reaction occurs. The CCD to be irradiated is at an angle of 120 degrees to the incident D beam. Kinematics then leads to a proton beam of energy about 2.83 MeV. The polyimide window and inserts degrade the beam so that it has a peak at about 2.1 MeV. The window also blocks the tritons and Helium-3 biproducts of the DD reaction. The flux is calibrated by replacing the CCD with a Surface barrier diode (SBD) and correlating its counting rate with the monitor surface barrier diode in vacuum (SBDV).

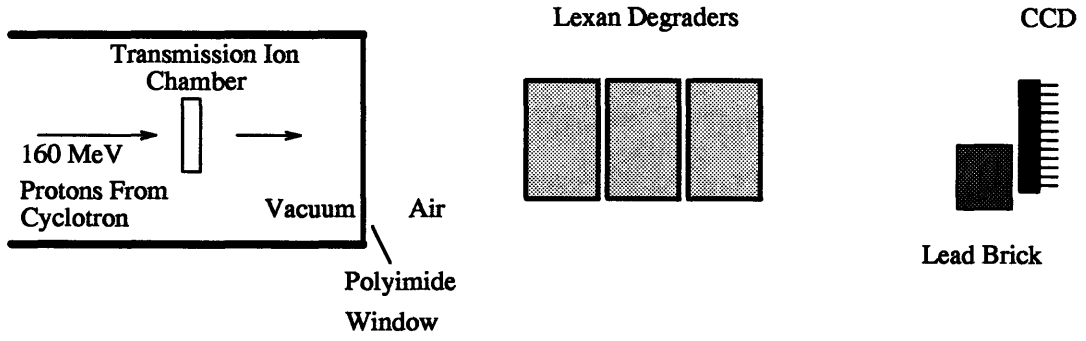

Figure 3-4: HCL Irradiation Setup: A beam of 160 MeV protons emerges from the cyclotron and passes through a transmission ion chamber. The protons then pass through a polyimide window and about a meter of air. Lexan blocks are put into the beam to further degrade the beam. The flux was calibrated by placing a Faraday Cup at the CCD position and correlating its counting rate to a transmission ion chamber counting rate.

differences were noted. The dosemetry was established using a transmission ion chamber calibrated by a Faraday cup. The fluence measurements were repeatable at the 10 % level. Figure 3-4 shows the arrangement for the irradiations at the HCL.

All irradiations were at normal incidence to the front of the devices. For most irradiations, a shield was used to protect half of each device, used as a control. At the HCL, a 50 mm lead shield was used, while at the PFC, a 3 mm aluminum shield was used. For some experiments at the HCL, some CCDs with position dependent architecture were irradiated without shielding to evaluate relative hardnesses for variations of the basic CCD design.

In total, more than 10 CCDs were used in the study. Each CCD was evaluated before and after irradiation. Some CCDs were evaluated minutes after fractional doses at the HCL- but these results proved unreliable due to short term (3 minute half life) irradiation induced radioactivity.

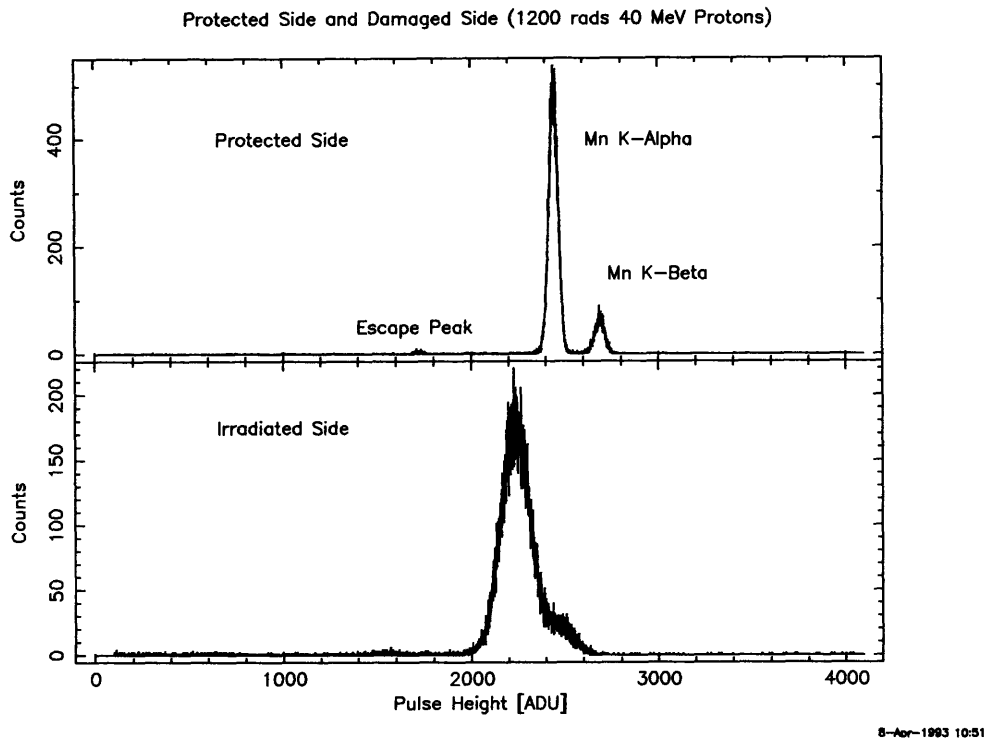

Figure 3-5: Fe 55 Spectra:Irradiated Side and Protected (Control) Side

3.3 Evaluation Of Radiation Damage In Ground Experiments

For our purposes, the effects of radiation damage are determined by the degradation in X-ray spectral resolution. Our evaluations make use of the characteristic Mn K X-rays from radioactive Fe-55 sources (5.9 and 6.4 keV). I measure peak pulse heights and full width at half maxima (FWHM) around the peak pulse height of the detected spectra. Figure 3-5 compares pulse height spectra from an Fe-55 source using the irradiated and non-irradiated regions of one of our test devices. I also measure the charge transfer inefficiency (CTI) which is a measure of the CCD's ability to transfer charge from pixel to pixel. In addition, I monitor the CCD dark current before and after irradiation. A particularly important result from this study is an understanding of systematic errors commonly made in measurements of these quantities.

In irradiated CCDs operated at sufficiently low temperatures, CTI effects on the spectral resolution are larger than the effects of dark current. CTI broadens the width of measured X-ray lines by taking charge away from the original charge packet induced by the X-ray

event. Thus, it is a measure of the fraction of a charge packet that will be lost in a single pixel to pixel transfer. The pulse height spectrum due to a monoenergetic X-ray line will have a broad low energy tail due to poor CTI. CTI will also result in a downward shift in the peak pulse height. For our detectors, the CTI is less than 1.5×10^{-6} before irradiation and can degrade to 3×10^{-4} for a device irradiated with 1200 rads of 40 MeV protons.

CTI is determined by measuring the shift in peak pulse height as a function of position for a CCD uniformly illuminated with monoenergetic X-rays. The fluences of X-rays are low- typically 10-1000 photons/cm^2/frame. With these Fe-55 X-ray fluences, the one sigma errors on our measurements of CTI are on the order of 1.5×10^{-6}.

For most of my work, I make use of the 5.9 keV X-ray line from the Fe-55 source. However, results depend on on the amount of charge liberated by the X-ray photon used for the hardness evaluation. Fe-55 results in 5 different pulse height features: the Mn K-α line, the Mn K-β line, the two escape features due to the Mn-Kα and β lines, and a Si-Kα fluorescence feature at 1.8 keV. I will discuss separately the pulse height dependence. Unless stated, all results below refer to those using the 5.9 keV Mn Kα line.

3.3.1 Factors Affecting Measured Radiation Damage Using Monoenergetic X-Rays

I find that the measured value of CTI for a damaged device depends on several factors. These factors include: proton dose, X-ray flux, operating temperature, operating voltages, and clocking rates. Some of these factors affect the measured performance through similar mechanisms. Thus the effects of two or more of these factors may or may not be independent. Below, I discuss these factors. A model connecting the various observations will be presented later on.

Temperature Dependence of Measured Radiation Damage

The X-ray response of an irradiated CCD is strongly temperature dependent. Figure 3-6 shows how CTI, pulse height, and FWHM vary as a function of temperature for one of the CCDs irradiated at the HCL with 1200 rads of 40 MeV protons. Similar results are obtained for CCDs irradiated at the PFC. I observe that the performance is best at low temperatures (less than $\sim$-70 C or 203). Figure 3-7 shows the pulse height spectra obtained with the same device at two temperatures. At temperatures below -70 C, the

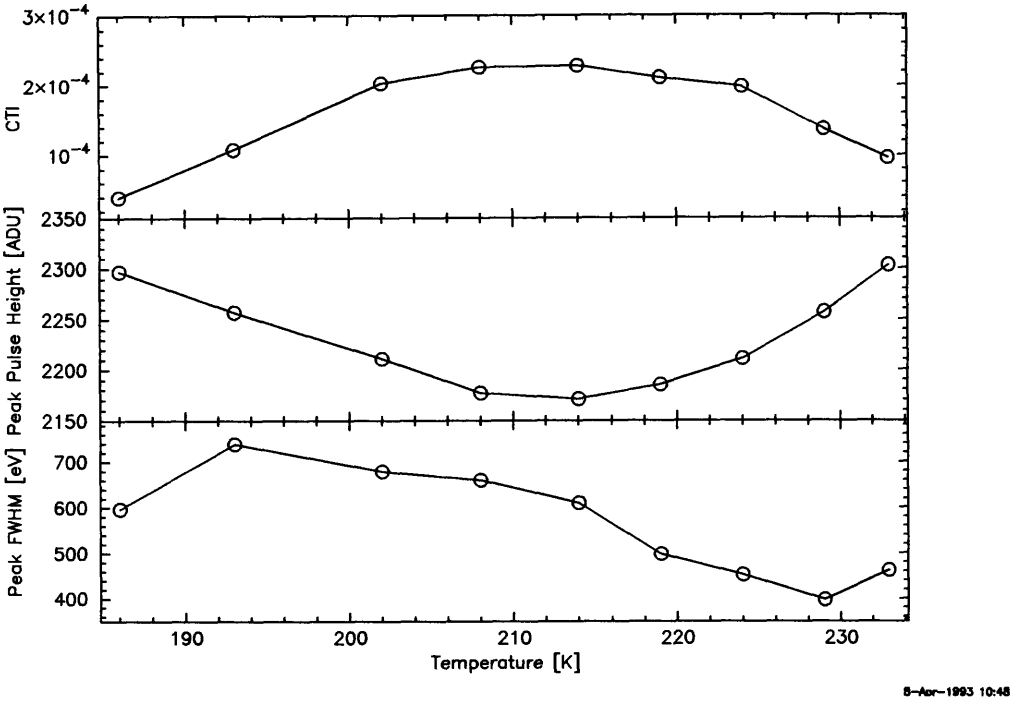

Figure 3-6: The temperature dependence of charge transfer efficiency, peak Pulse Height, and energy resolution in an irradiated CCD is shown above. The errors in CTI, peak pulse height, and full width at half maximum are estimated to be 1.5×10^{-6}, 1 ADU, and 10 eV respectively. In our electronics, 1 ADU in pulse height corresponds to approximately 0.9 electrons.

CTI decreases, the energy resolution improves, and the peak pulse height increases. CTI also decreases with increasing temperature above approximately -70 C. However, the energy resolution degrades at temperatures above approximately -45 C.

Figure 3-8 shows how the average dark current varies with temperature for the same CCD as shown in figures 3-6 and 3-7. Also shown in figure 3-8 is the dark current for the protected half of the device.

These results suggest that low temperatures are the best for X-Ray CCD operation. Unfortunately for ASCA, the CCDs cannot obtain temperatures below -61 C due to our power budget and thermal constraints. However, for AXAF, much lower temperatures are possible.

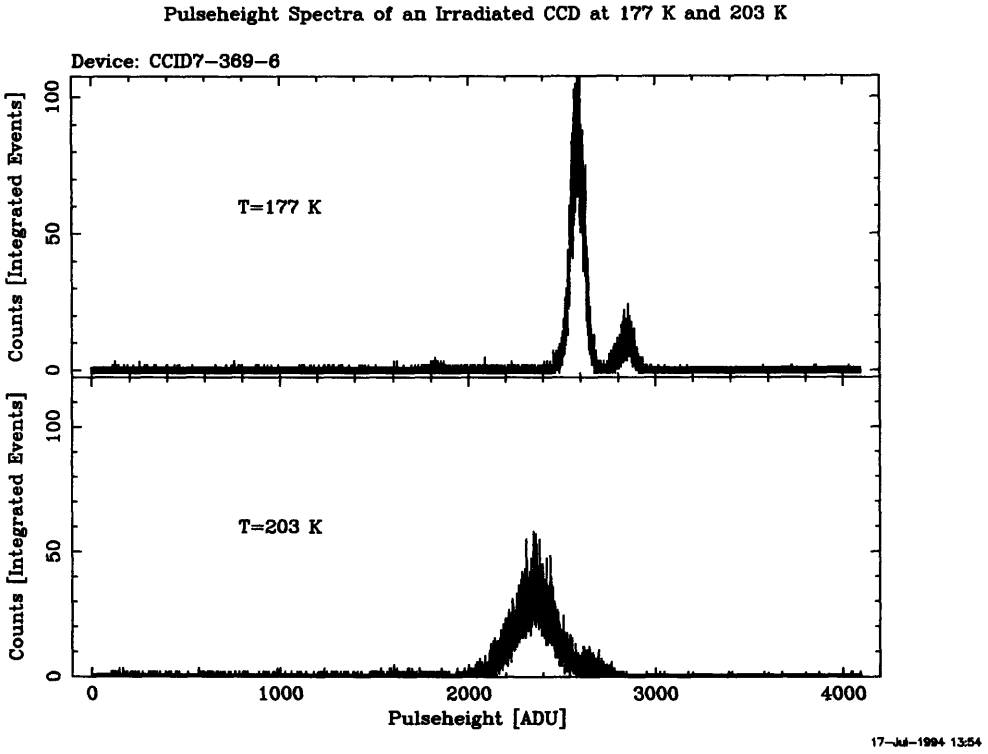

Figure 3-7: Pulse height spectra of an Fe-55 source taken with an HCL irradiated CCD at two temperatures: 177 K and 203 K. Operating at low temperatures yields obvious benefits. Note that the Mn K-α and K-β peaks clearly separate at 177 K. Also, the escape peak is more apparent at the lower temperature.

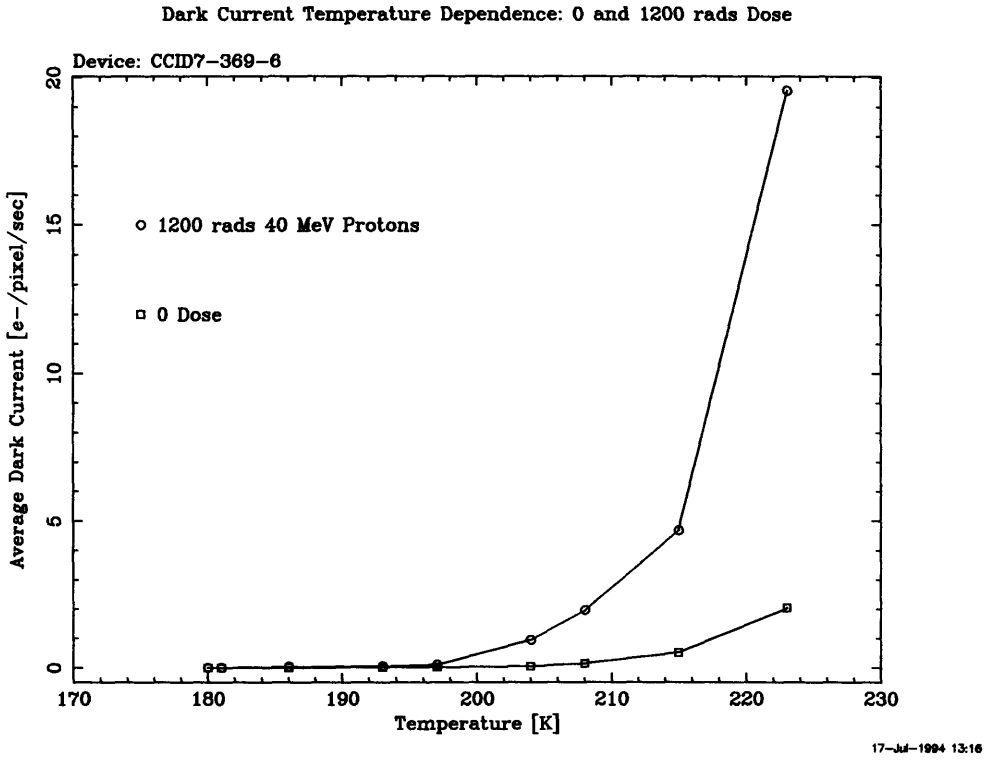

Figure 3-8: The temperature dependence of the average dark current for the protected and irradiated halves of a device used at the HCL.

Effects due to X-Ray Fluence

A very significant result of my experiments is the dependence of CCD spectral response on the number of X-rays per frame of data. By "frame" of data, I mean the data accumulated in the imaging array of the CCD for an integration time (here this is 4 seconds). I control the X-ray fluence by moving the X-ray source to various distances from the CCD. For a fixed integration time, this changes the number of detected X-ray events per frame. The effect is that the performance of an irradiated device is best if the X-ray fluence is high. This effect was not noticed before and puts into question the value of CTI measurement as a measure of radiation damage. Figure 3-9 shows how X-ray fluence affects pulse height, FWHM, and CTI for an irradiated device. The effects are most dramatic at low fluences- typical of most ASCA observations. As the X-ray flux increases, the CTI decreases, the FWHM decreases, and the pulse height increases. This effect is seen only on irradiated devices- not on flight quality devices. It clearly reflects on the radiation damage mechanism. An important conclusion from my work is that meaningful measurements of radiation damage effects must be made with reference to this dependence. Later on in this chapter, I will

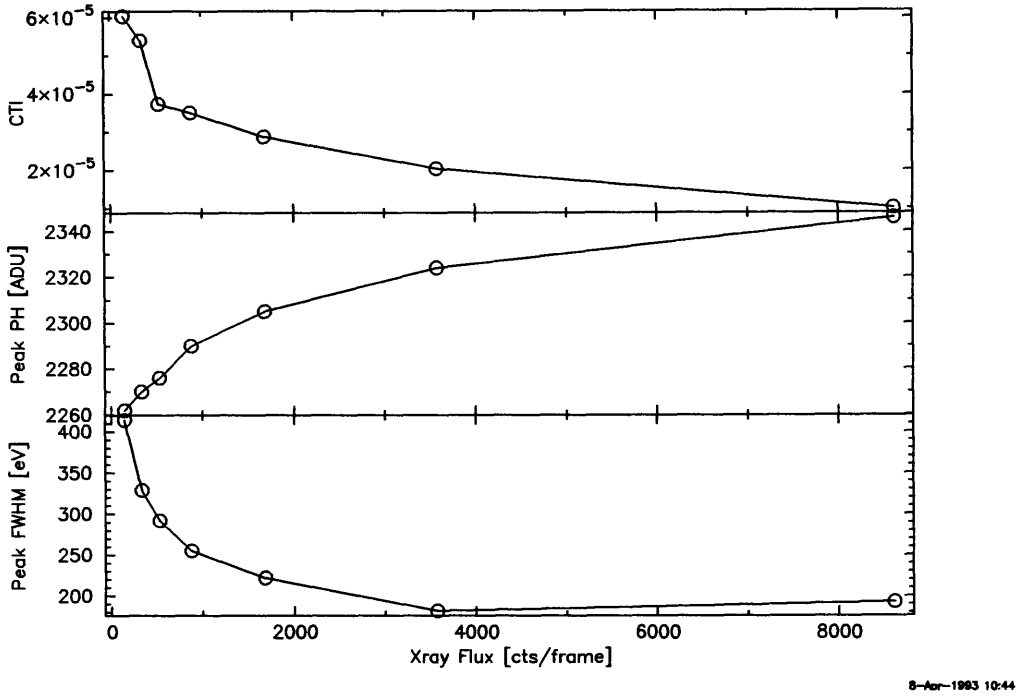

Figure 3-9: Effect of X-ray fluence on radiation damage evaluation.

explain this observation.

Clocking Rate Effects

The performance of an irradiated CCD depends on the rate at which charge is transferred from pixel to pixel. Normally, our CCDs operate as frame transfer devices. X-rays are collected in the imaging area for a few seconds. The charge in the imaging area is then transferred to the frame store area. The transfer time for the imaging to frame shift is 15.83 milliseconds for *ASCA*. Once in the frame store region, charge is transferred row by row into the serial register. Between each of the parallel frame store shifts, the serial register is clocked out at roughly 20 microseconds per pixel. As there are 422 columns and 19 overclocks, the pixel to pixel transfer time in the parallel frame store to serial operation is roughly 8.8 msec.

Note that when using frame transfer mode, the CCDs on *ASCA* have four characteristic transfer times:

1) The integration time for the exposure.

2) The time it takes to transfer charge from one pixel to the next in the parallel direction

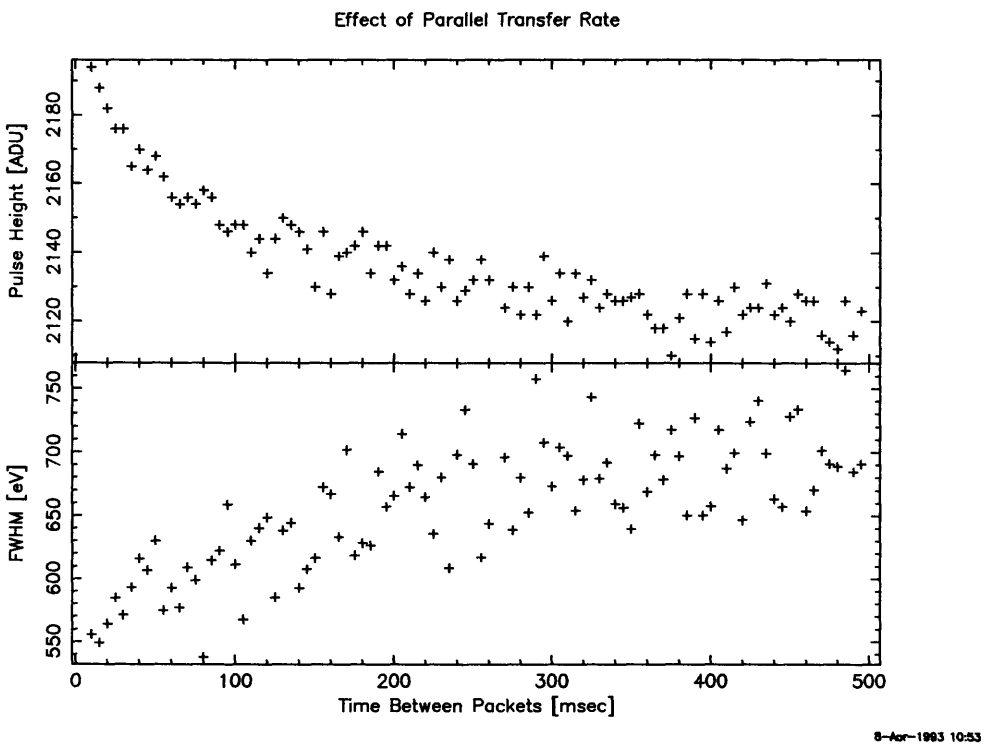

Figure 3-10: Pulse Height and Spectral Resolution of Fe 55 Spectra Taken with an Irradiated CCD at several Parallel Transfer Speeds

during the image to frame store area transfer.

3) The time between parallel transfers in the frame store area to serial register shift.

4) The time between transfers in the serial register shifts.

There is also the times it takes to transfer charge from subpixel to subpixel- but we will discuss these times later when describing the pulse height dependencies. In our experiments thus far, I have adjusted the parallel transfer rate from the image area to frame store area to look for effects in the measured radiation damage. Figure 3-10 shows how peak pulse height and width depend on the pixel rate in transferring charge packets in the parallel direction from the imaging area to the frame store area. The time axis in this figure is actually the mean time between charge packets crossing a given pixel on the CCD during the image to frame store shift. This is calculated by multiplying the mean number of pixels per X-ray interaction (a function of the incident X-ray fluence) by the transfer time per pixel in the parallel shift. As I will discuss later, the mean time between X-ray induced charge packets is a critical factor in radiation hardness measurements.

Clock Amplitude Effects

I have also found that adjusting the amplitudes of clocks used in the parallel charge transfer registers can affect the measured performance of an irradiated CCD. We operate the CCDs on *ASCA* using two level square-wave clocks. Typically, the level of the high phases of these clocks is roughly plus six volts, while the level of the low phases of these clocks is roughly minus six volts. In a situation where the X-ray fluence is low, the performance is improved by making more positive the high phase for the parallel registers, while worsened by making the low phase more negative. Specifically, the depletion depth and hence the quantum efficiency at 5.9 and 6.4 keV increases as the parallel clock levels are made more positive. This variation in quantum efficiency leads to a variation of detected X-ray fluence when using a fixed Fe 55 source. See appendix D for more details on how quantum efficiency depends on register voltage. Thus varying parallel clock levels introduces X-ray fluence effects as described above as well as effects due intrinsically to the varying potentials. Figure 3-11 shows two Fe 55 spectra from an irradiated device operated at two different values for the parallel clock high phase voltage. In this figure, the Fe 55 source is held at a fixed distance to the CCD and the exposure times per readout are fixed. The low level of the parallel clocks was fixed at -6 volts. The measured count rates for the 0.67 and 16 volt spectrum was about 680 and 900 counts per frame respectively. This corresponds well with the low fluence range of the results shown in figure 3-9. Notice how the resolution improves sufficiently to separate the Mn Kβ (6.5 keV) and the Mn Kα (5.9 keV) X-ray peaks. Figures 3-12 and 3-13 show how the FWHM and pulse height of the 5.9 keV feature vary with high and low level voltages, respectively, for the damaged half of a device irradiated at the HCL. Notice that the effect is smaller with the low level than it is for high level as you would expect if the effect is a result of depletion depth dependent quantum efficiency. Variations of the low level should affect the depletion depth very slightly (See appendix A).

Other Factors: Irradiation Conditions

I have irradiated CCDs both at operating temperatures (-70 C) and at room temperature. I have also irradiated CCDs with biases on and off. I observe that the CCD temperature and power status at the time of the irradiation are not factors on the performance.

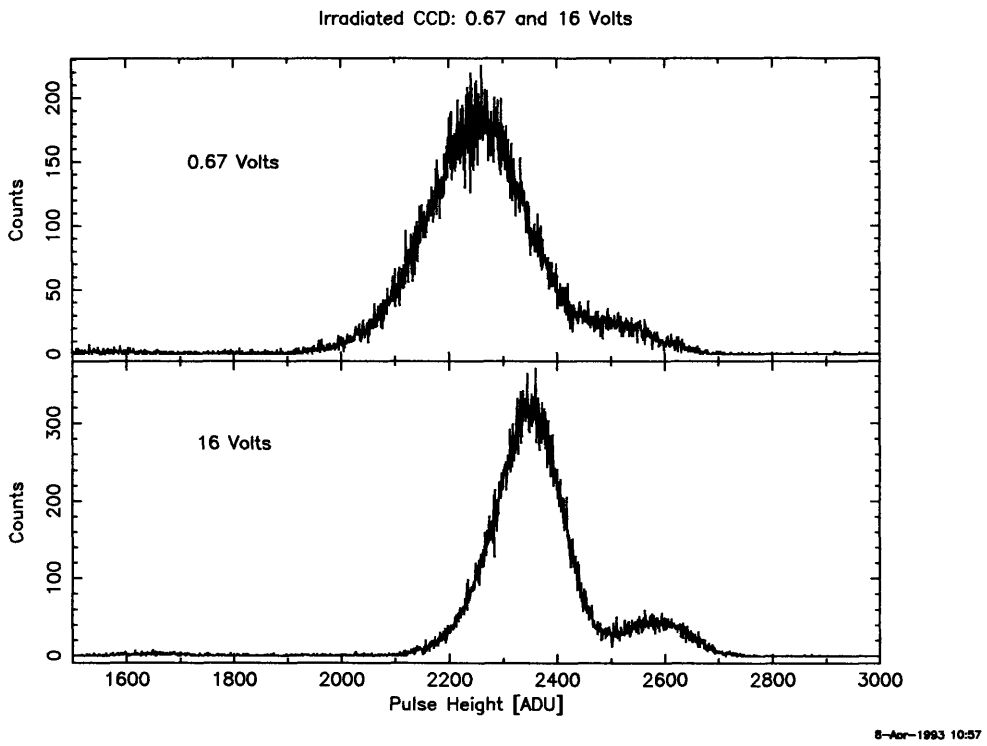

Figure 3-11: Fe 55 Spectra Taken with an Irradiated CCD at Two Parallel Clock High Phase Voltages

3.3.2 Pulse height Dependence of Spectral Response

In general, the measured performance should depend on the size of the charge packet used in the characterization. As I mentioned earlier, the use of an Fe-55 source results in 5 characteristic charge packet sizes if I make use of the two primary line features (Mn K-α, β), their corresponding escape peak features, and the silicon fluorescence feature (Si K-α). If enough data is collected, an additional feature can be used- the weak fluorescent argon K-α line, produced by fluorescence of the air by the Fe-55 source.

Figure 3-14 shows a comparison of the Fe-55 pulse height spectra from a particularly large data set for the damaged and protected sides of a CCD irradiated at the HCL with 1200 rads of 40 MeV protons. Using this data set, I can measure the amount of charge loss due to radiation damage induced CTI on the damaged side by comparing to corresponding features on the protected side. Figure 3-15 shows a plot of charge loss vs initial charge packet size. Notice that the amount of charge loss is smaller for smaller initial charge packet sizes and that the relation is slightly non linear.

Unfortunately, most of our data sets are not so large. Furthermore, no data was collected

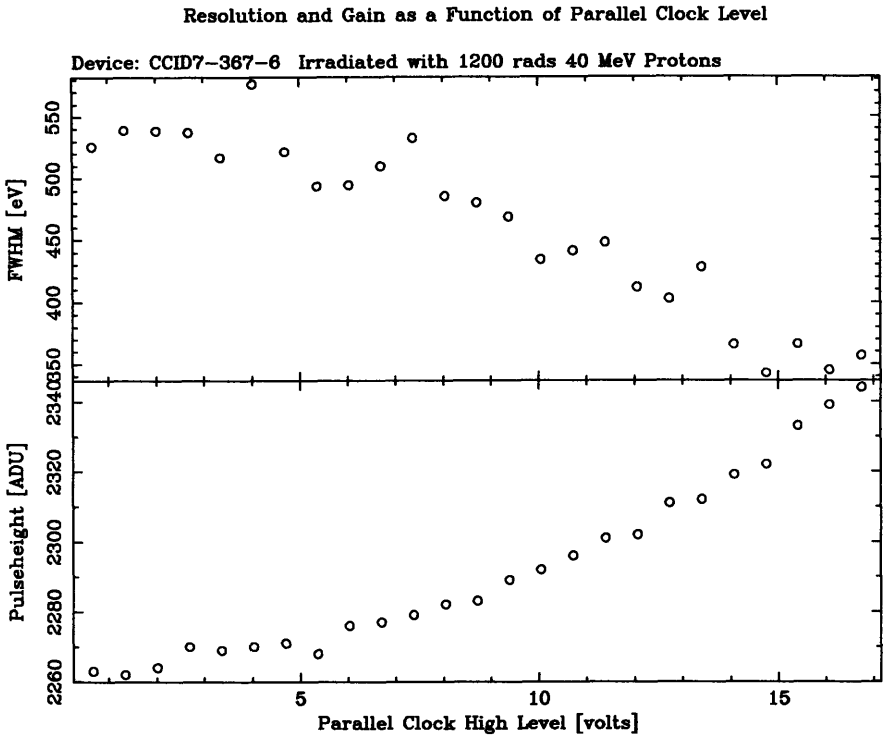

Figure 3-12: Fe 55 Spectral characteristics as the parallel high level is varied for the damaged side of a device irradiated at the HCL.

with a low energy source in our radiation damage studies. However, in many data sets, the escape peak due to the Mn-Kα line can be used to get some handle on systematics related to the pulse height dependence. This study will yield many interesting results on the physics of CCDs, but it is beyond the scope of this thesis.

3.4 Radiation Damage Model in X-Ray CCDs

Proton radiation reduces CCD spectral resolution capability due to two major mechanisms: CTI and dark current. It is widely believed that both of these phenomena result from traps due to proton induced displacements in the silicon lattice (Janesick, 1991; Holland, 1990; Lumb and Nousek, 1992, and references therein). When a proton dislodges a silicon atom in the lattice of the CCD, the vacancy produced is fairly mobile. It will move through the lattice and possible reach the edge of the lattice where it is no longer a vacancy. Sometimes, the vacancy will come into the vincinity of another vacancy or an impurity atom also in the lattice. Often, the pair will form a complex which have a minimum energy and become physically stuck at a localized position in the lattice. The complex modifies the silicon band

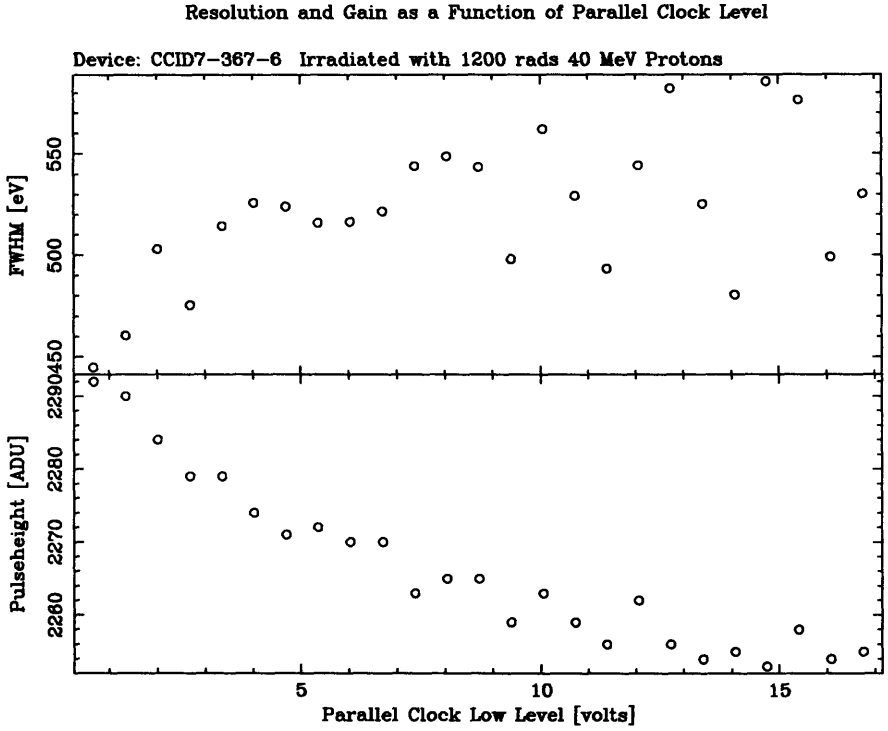

Figure 3-13: Fe 55 Spectral characteristics as the parallel low level is varied for the damaged side of a device irradiated at the HCL. Notice that the effect here is smaller than for the case of varying the high level of the parallel clock. Here, the voltages are negative.

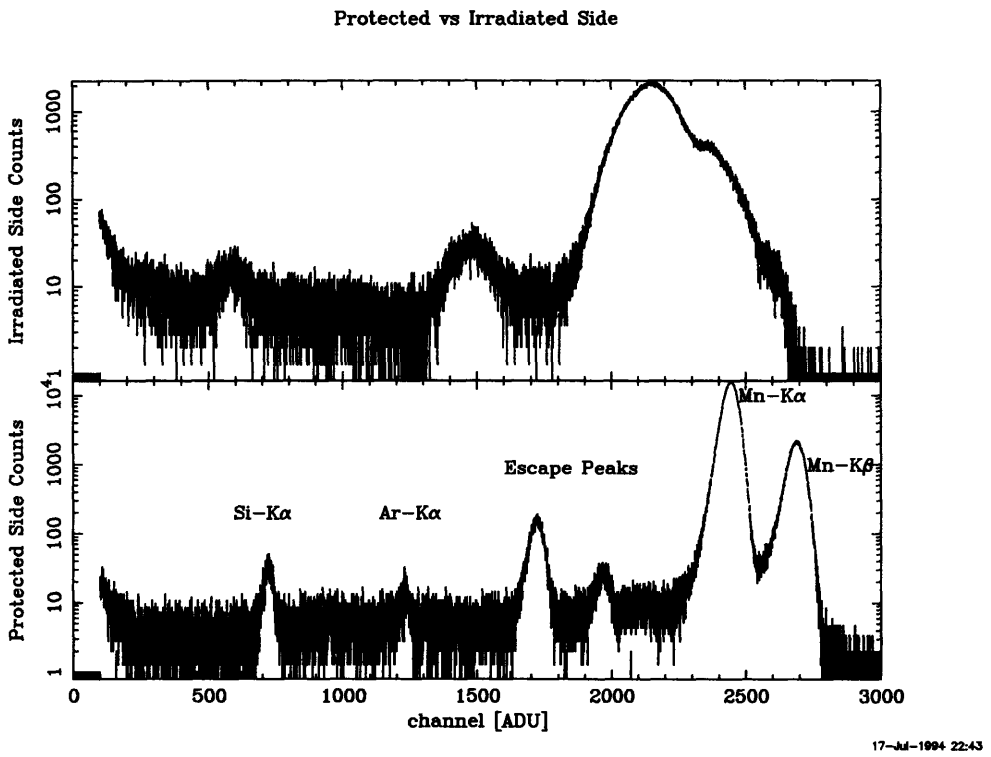

Figure 3-14: Fe 55 Spectra for the protected and damaged side of a device irradiated at the HCL. The data set used is particularly large, yielding 6 spectral features (labeled) on the protected side, of which only 4 are distinguishable on the damaged side.

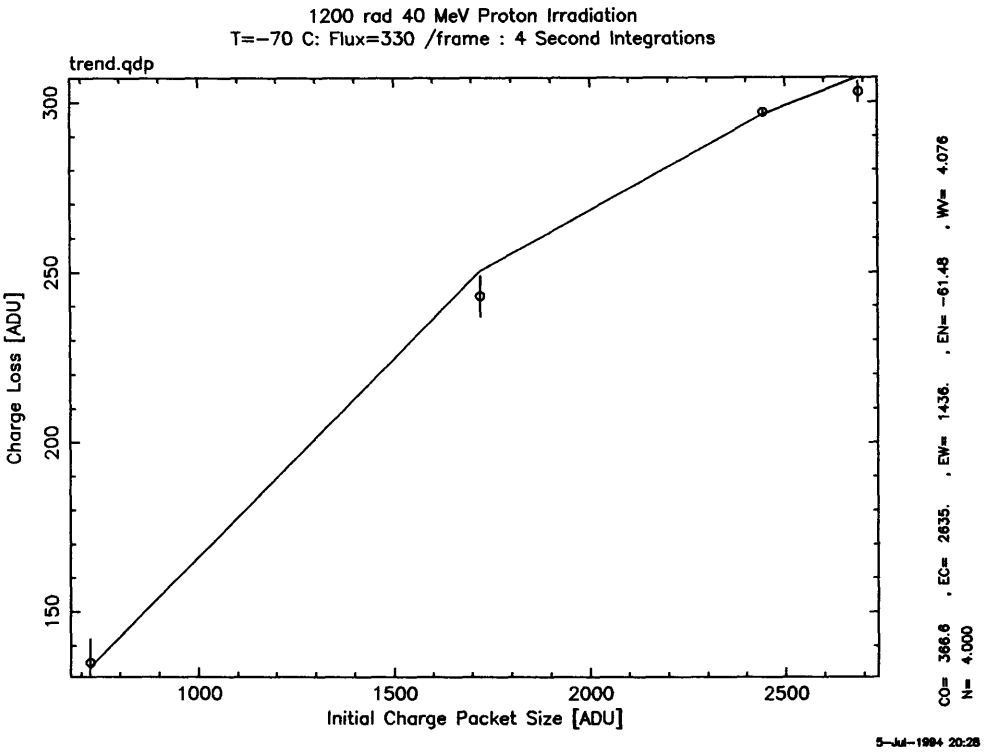

Figure 3-15: Charge loss on the damaged side vs initial charge packet size (determined by inspecting the protected side spectra). The loss is nonlinear in initial charge packet size and gets smaller for smaller initial charge packet sizes.

gap structure of the local lattice by introducing a mid band gap energy level. The exact energy of this level depends on the components of the trap complex. I describe here how these traps affects CTI.

Shockley-Read-Hall theory (Shockley and Read, 1952) describes the dependence of minority carrier capture and release time scales on temperature and carrier density. Traps capture electrons from passing charge packets in a capture time scale t_c:

$$t_c = \frac{1}{v_t n \sigma} \tag{3.1}$$

The traps then release the captured electrons on an escape time scale t_e:

$$t_e = \frac{1}{v_t N_c \sigma e^{\frac{-(E_c - E_t)}{kT}}} \tag{3.2}$$

The resulting trap occupancy rate is given by:

$$\frac{dn_t}{dt} = -\frac{n_t}{t_e} + \frac{N_t - n_t}{t_c} \tag{3.3}$$

Where:

σ	is the electron capture cross section
v_t	is the thermal velocity of an electron
n	is the number density of free electrons
N_c	is the density of states in the conduction band
E_c	is the band gap
E_t	is the trap energy
k	is Boltzmann's constant
T	is the temperature
n_t	is the number density of trapped electrons
N_t	is the number density of traps.

The phosphorus-vacancy (P-V) complex is a displacement induced trap which is regarded by many workers to be the most significant in the phosphorus doped buried channels of CCDs such as the devices we are using for *ASCA* (Janesick, 1991; Holland, 1990; Lumb and Nousek, 1992). In our devices, phosphorus doping yields the n-type buried channel (see

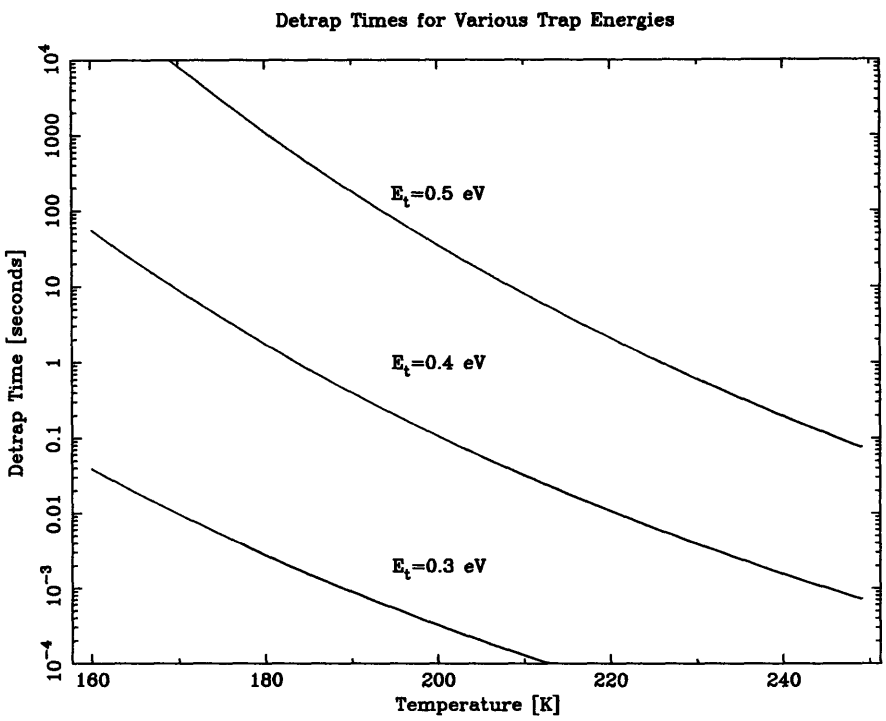

Figure 3-16: Detrapping times for traps of various energies as a function of temperature.The P-V center trap has an energy level of 0.4 eV. The trap cross section is fixed at $3.5 \times 10^{-15} cm^2$ for each curve.

appendix A. The proton induced lattice vacancies combine with the phosphorus atoms to make P-V complexes. The P-V trap is characterized with a cross section of $3.5 \times 10^{-15} cm^2$ and a trap energy of $\sim$0.4 eV. With such a trap and a typical charge packet of 1000 electrons, the capture time is virtually instantaneous (less than 10^{-7} s) compared to transfer rates used in our devices (tens of microseconds per shift). However, as shown in equation 3.1, the trapping time is a function of the density. For small charge packets (0-10 electrons for dark current and 50-3000 for X-ray signals), the density of electrons is difficult to calculate. However, the density should be within an order of magnitude of the phosphorus dopant density ($2 \times 10^{16} cm^{-3}$). The detrapping times, however, are on the order of tens of milliseconds.

Figure 3-16 shows the detrapping times for traps of varies energies as a function of temperature, using equation 3.2.

The P-V center trapping model explains the X-ray pulse height, fluence, clocking, and temperature dependence of our X-ray CCD performance. When a charge packet from

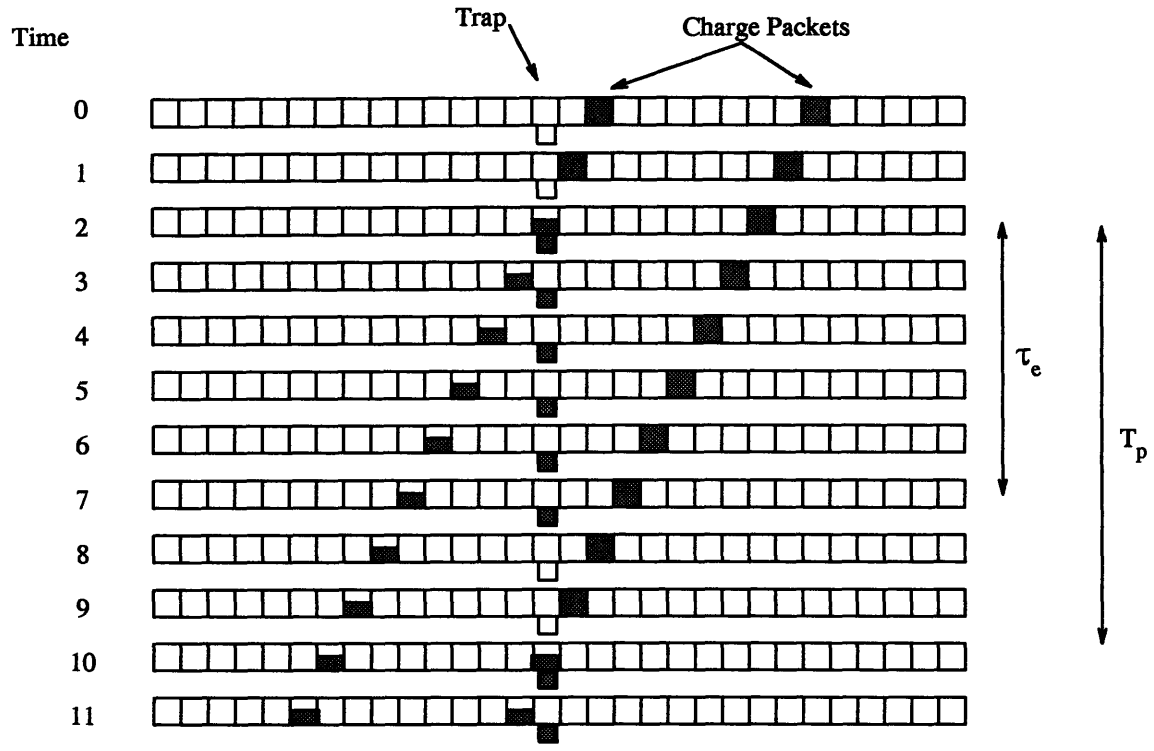

Figure 3-17: The case where both charge packets loose electrons to a given trap. The detrapping time is less than the time between passing charge packets.

an incident X-ray encounters an empty trap during a CCD readout, the trapping time is sufficiently short that by the time the charge packet is shifted away, it is very possible that the trap is left full and the charge packet has lost charge and will contribute poorly to the spectral resolution. Each trap has the capacity to hold a single electron. Given an empty trap, the probability that a passing charge packet will lose an electron is nearly unity.

Once a given charge packet has suffered a loss to a trap, if the detrapping time is long compared to the time till the next X-ray induced charge packet arrives, the trap will remain filled and will not affect the second charge packet- thus minimizing the spectral degradation. If the detrapping time is short compared to the time till the next X-ray induced charge packet arrives, the trap will probably have emptied and would have a chance to degrade the second charge packet- thus maximizing the damage to the spectral response. These two situations are shown in figures 3-17 and 3-18.

At lower temperatures, the detrapping time increases, improving the situation for charge packets following the original charge packet. I call this charge packet the "sacrificial charge packet" (SCP). I call the charge packets which benefit from the SCPs "beneficiary charge

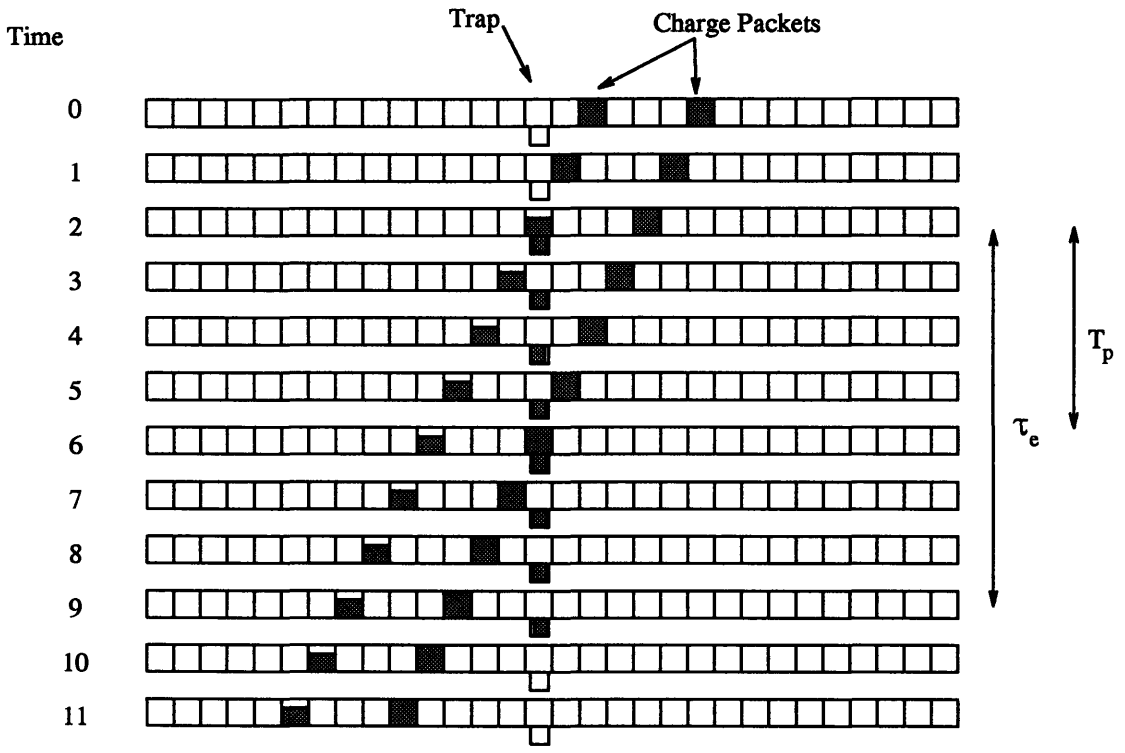

Figure 3-18: The case where only one of the charge packets looses electrons to a given trap. The detrapping time is greater than the time between passing charge packets.

packets" (BCP). The X-ray fluence and clock rate results are also explained by this model since they control the mean time between charge packets for a trap in a register.

The improvement in performance as the device temperature goes from -70 to -50 C as shown in figure 3-6, may be a result of the increase of dark current (figure 3-8) which would fill traps. This type of trap filling, where a uniform coverage of charge is used, is called the "fat zero" method. The degradation in performance above -50 C would indicate that the benefit of having the traps filled is outweighed by the extra poisson noise added as the dark current becomes too large.

To further test this model, we can analyze the X-ray data in such a way as to extract the trap densities and detrapping times. In the next section, I describe how this analysis can be done.

3.5 A Double Pulse Experiment Using X-Rays

In normal operation of our frame transfer CCDs, we illuminate the imaging array with X-rays for a given exposure time. After the exposure is over, the charge in the imaging array is transferred at a high speed into the X-ray shielded frame store region. Once the transfer is complete, the imaging array begins accumulating its next exposure while the frame store array is slowly readout. The readout is accomplished by transferring the frame store array row by row into the serial register, where each row is clocked out serially into an output node. Typically tens to hundreds of frames of X-rays are collected. Typically, in the laboratory, Mn-Kα and Mn-Kβ from an Fe^{55} source are used to provide the X-rays. Event lists containing pulse height, position, and frame time data are built out of these frames.

By taking suitably chosen subsets of these event lists for a given CCD operating temperature, we can derive trap densities and energies for displacement damage in the CCD. If there is more than one type of trap population in the CCD channel, then multiple temperature data may be required to derive these quantities. I have made event list subsets containing events which have a neighboring event (the SCP) lower in the same column of the same readout frame with in a certain range of distances, and no other events closer. The SCP is not included in the event list subset. Different subsets are made for different ranges of row distance between the SCP and subset member events. Similarly, selections can be made for events which are in the same row, but differ by a given range of columns.

Pulse height spectra made for each event list will indicate how much charge is lost due to traps as a function of the event spacing. If the incident spectrum of photons is simple (*eg* Fe^{55}) and the illumination is uniform, the quantity of data required is not much. In the case of uniform illumination by a monoenergetic source like Fe^{55}, the charge loss for a particular range is simply the original charge packet size minus the center position of a gaussian fitted to the pulse height spectrum measured in the subset. Figure 3-19 shows the measured pulse height as a function of the range to the sacrificial charge packet in a set of Fe^{55} data collected with a radiation damaged ASCA like CCD operated at 206 K.

Charge is lost from the BCP with increasing distance to the SCP because the increasing distance corresponds to an increasing time and an increasing probability that the traps filled by the SCP have detrapped. In frame transfer mode, the distance between packets corresponds to two time scales because of the different transfer rates during the image array

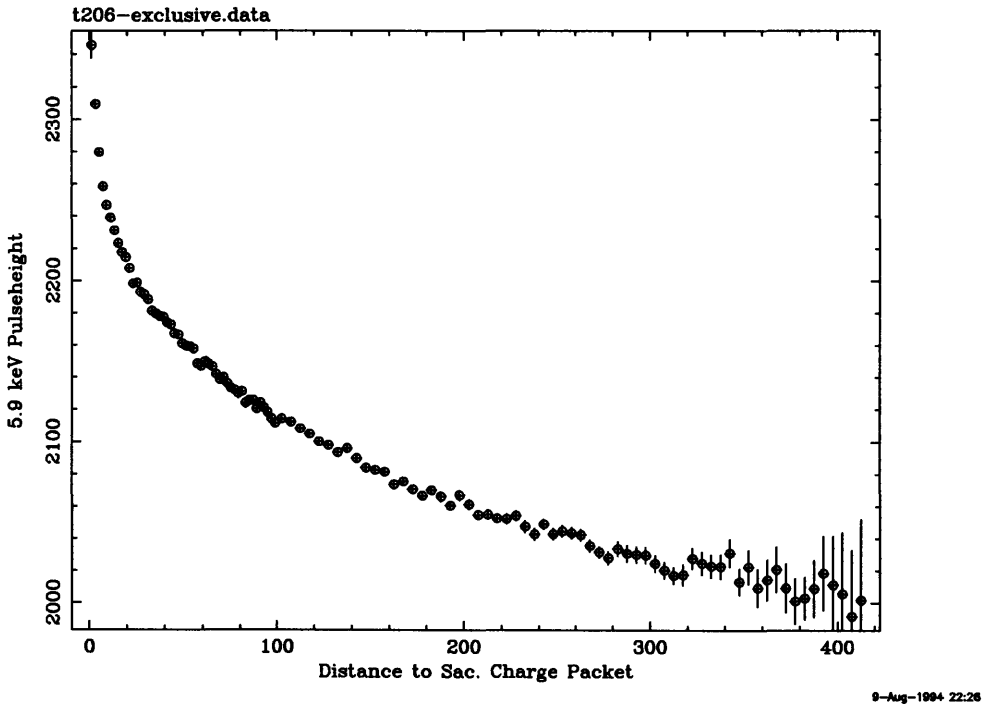

Figure 3-19: Measured pulse height centroid as a function of distance to sacrificial charge packet. The CCD used is an ASCA like CCD operated at 206 kelvin. The device was previously irradiated with 1200 rads of 40 MeV protons at the Harvard Cyclotron Laboratory. Note that the measured gain varies by 20%. The transfer rates used to collect the data for this figure are different than those used on ASCA.

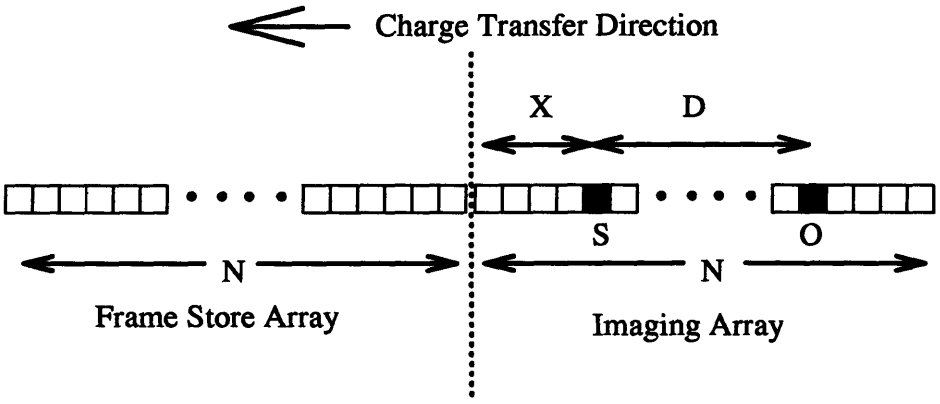

Figure 3-20: Two charge packets in the same column of the imaging array. Both the imaging array and frame store array have N pixels. The sacrificial charge packet, S, is located at pixel "x" and the beneficiary charge packet "O" is located a distance "d" behind S.

to frame store transfer and the frame store to serial register transfer. In our devices, we have a further complication in that the lengths of the frame store pixels are slightly different than the widths. Below, I formulate a relation between charge loss and distance which will allow us to fit for trap density and detrapping time in a "general" frame store transfer device for monoenergetic X-rays. I make a fundamental assumption that a trap can contain at most one electron. This formulation will be compared to laboratory results. Next, we will generalize the formulation for arbitrary pulse height charge packets.

Consider two charge packets in one column of the image array as shown in figure 3-20. Both the imaging array and frame store array have N pixels. The sacrificial charge packet, S, is located at pixel "x" and the beneficiary charge packet "O" is located a distance "d" behind S. The following constraint holds on x, d, and N:

$$(x + d), x \leq N \tag{3.4}$$

Thus for a given distance to the sacrificial charge packet, the maximum row number

that the sacrificial charge packet could come from is:

$$x_{max} = N - d \tag{3.5}$$

Other important parameters in the formulation are:

- t_e is the trap emission time constant,
- N_L is the number of traps per micron along the transfer direction,
- p_f is the pixel length along the transfer direction in the frame store array,
- p_i is the pixel length along the transfer direction in the image array,
- c_{if} is the time it takes to transfer from one pixel to the next during the image array to frame store array transfer,
- c_{fs} is the time it takes to transfer from one pixel to the next during the frame store array to serial array transfer,

The number of traps per pixel in the imaging and frame store arrays are respectively given by:

$$\begin{aligned} N_i &= N_L p_i, \\ N_f &= N_L p_f \end{aligned} \tag{3.6}$$

Given this, I calculate the total number of traps seen by each packet shown in figure 3-20. The number seen by the SCP ("S") is:

$$N_s = N N_f + x N_i \tag{3.7}$$

and the number of traps seen by the BCP ("O") is:

$$N_o = N N_f + x N_i + d N_i \tag{3.8}$$

For simplicity, we assume that the charge packets are large enough so that the capture times are miniscule compared to the pixel to pixel transfer times so that empty traps have unity probability of capturing electrons from the passing packets. Assuming this, I calculate

the number of empty traps (N_e) seen by the BCP:

$$\begin{aligned} N_e(x,d) &= N_i d + N_i x(1-e^{\frac{-dc_{if}}{\tau_e}}) + N_f(N-x-d)(1-e^{\frac{-dc_{if}}{\tau_e}}) \\ &\quad + N_f x(1-e^{\frac{-dc_{fs}}{\tau_e}}) \\ &\quad + N_f \sum_{j=1}^{d}(1-e^{\frac{-dc_{if}+j(c_{if}-c_{fs})}{\tau_e}}) \end{aligned} \tag{3.9}$$

The first three terms in equation 3.9 describe traps encountered by both packets exclusively during the image to frame store transfer. The first term corresponds to the traps which could not be touched by the SCP. The expression $(1-e^{\frac{-dc_{if}}{\tau_e}})$ is the availability of traps which increases with a time constant τ_e or equivalently with a position constant $\frac{\tau_e}{c_{if}}$. The fourth term corresponds to traps encountered by both packets exclusively during the frame store to serial transfer. The availability of these traps have a position constant $\frac{\tau_e}{c_{fs}}$. For the ASCA CCDs, $c_{fs}/c_{if} = 280$. Figure 3-21 shows how a 40 msec time constant would then get mapped to position for the image to frame store operation and for the frame store to serial register operation. The fifth term is due to traps filled by the SCP during the image to frame store transfer, but seen by the BCP during the frame store to serial transfer. For these traps, the passing time between the SCP and BCP is a function of position- each term in the summation corresponds to a different pixel. The summation term is given by:

$$N_f \sum_{j=1}^{d}(1-e^{\frac{-dc_{if}+j(c_{if}-c_{fs})}{\tau_e}}) = N_f\{d - \frac{e^{(c_{if}-dc_{if}-dc_{fs})/\tau_e}\{e^{dc_{fs}/\tau_e} - e^{dc_{if}/\tau_e}\}}{e^{c_{fs}/\tau_e} - e^{c_{if}/\tau_e}}\} \tag{3.10}$$

So for N_e, we get:

$$\begin{aligned} N_e(x,d) &= N_i d + N_f N(1-e^{\frac{-dc_{if}}{\tau_e}}) \\ &\quad - N_f\{d(1-e^{\frac{-dc_{if}}{\tau_e}}) \\ &\quad - d + \frac{e^{(c_{if}-dc_{if}-dc_{fs})/\tau_e}\{e^{dc_{fs}/\tau_e} - e^{dc_{if}/\tau_e}\}}{e^{c_{fs}/\tau_e} - e^{c_{if}/\tau_e}}\} \\ &\quad + x\{(N_i - N_f)(1-e^{\frac{-dc_{if}}{\tau_e}}) + N_f(1-e^{\frac{-dc_{fs}}{\tau_e}})\} \end{aligned} \tag{3.11}$$

Suppose that the flux of X-rays per row is given by the function $g(x)$, then we can

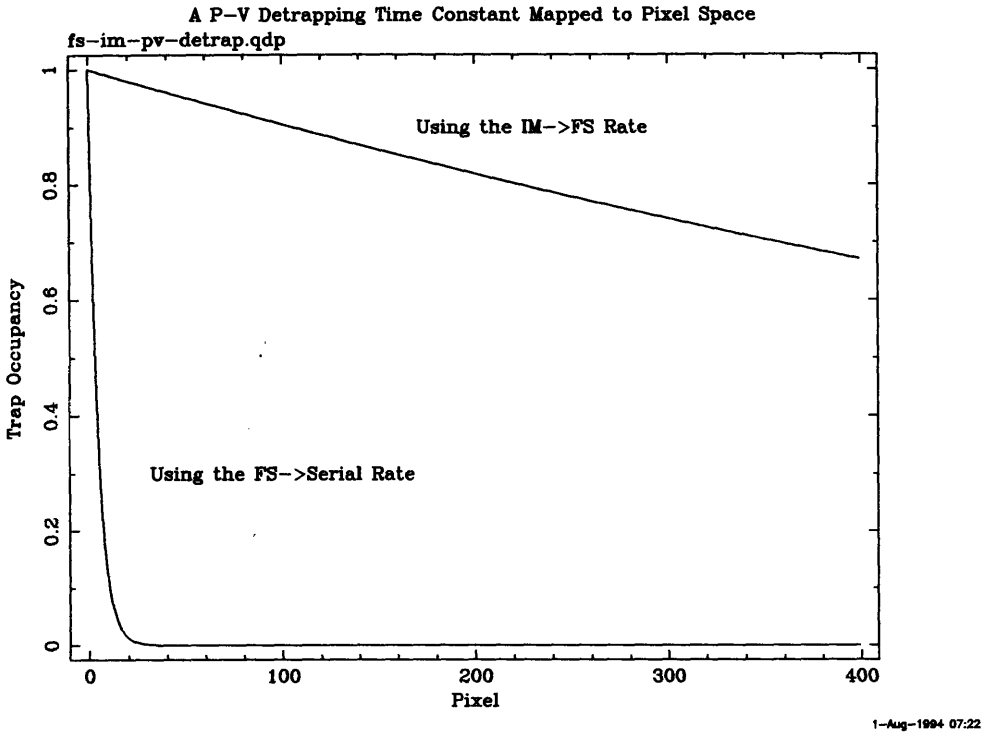

Figure 3-21: A 40 msec decay constant mapped to pixel space using the transfer rates for the two types of parallel transfer in the ASCA SIS.

calculate the average number of empty traps, $N_{avg}(d)$ seen by charge packets a distance d away from SCPs. This would then be the average loss of charge due to trapping and is given by:

$$N_{avg}(d) = \sum_{x=0}^{x_{max}} f(x,d) N_e(x,d), \tag{3.12}$$

where,

$$f(x,d) = \frac{g(x)}{\sum_{x=0}^{x_{max}} g(x)}. \tag{3.13}$$

In order to determine the trap density for the ASCA CCDs using flight data, the flux per row, $g(x)$, must be determined for a given observation by looking at the image. In general, the resulting $f(x,d)$ may be very complicated.

In the case of uniform illumination,

$$f(x,d) = \frac{1}{x_{max}}$$

$$= \frac{1}{N-d}. \tag{3.14}$$

and equation 3.12 becomes:

$$\begin{aligned}
N_{avg}(d) &= \frac{1}{x_{max}} \sum_{x=0}^{x_{max}} N_e(x,d) \\
&= (N_i + N_f)d + N_f N(1 - e^{\frac{-dc_{if}}{\tau_e}}) \\
&\quad -N_f\{d(1 - e^{\frac{-dc_{if}}{\tau_e}}) \\
&\quad + \frac{e^{(c_{if}-dc_{if}-dc_{fs})/\tau_e}\{e^{dc_{fs}/\tau_e} - e^{dc_{if}/\tau_e}\}}{e^{c_{fs}/\tau_e} - e^{c_{if}/\tau_e}}\} \\
&\quad + \frac{(x_{max}+1)}{2}\{(N_i - N_f)(1 - e^{\frac{-dc_{if}}{\tau_e}}) + N_f(1 - e^{\frac{-dc_{fs}}{\tau_e}})\} \qquad (3.15) \\
&= N_L\{(p_f + p_i)d + p_f N(1 - e^{\frac{-dc_{if}}{\tau_e}}) \\
&\quad -p_f\{d(1 - e^{\frac{-dc_{if}}{\tau_e}}) \\
&\quad + \frac{e^{(c_{if}-dc_{if}-dc_{fs})/\tau_e}\{e^{dc_{fs}/\tau_e} - e^{dc_{if}/\tau_e}\}}{e^{c_{fs}/\tau_e} - e^{c_{if}/\tau_e}}\} \\
&\quad + \frac{(x_{max}+1)}{2}\{(p_i - p_f)(1 - e^{\frac{-dc_{if}}{\tau_e}}) + p_f(1 - e^{\frac{-dc_{fs}}{\tau_e}})\}\} \qquad (3.16)
\end{aligned}$$

In equation 3.16, N_L, p_i, and p_f have been put in to get rid of N_f and N_i. The only unknowns in the expression are the linear density of traps, N_L, and the detrapping time constant, τ_e. For ASCA CCDs, the following values hold:

p_f	18 microns
p_i	27 microns
c_{if}	40 microseconds
c_{fs}	8.8 msec.

Figure 3-22 shows the best fit for N_L and τ_e for the data shown in figure 3-19. The detrapping time for this data is consistent with that for the P-V trap at 206 K. Figure 3-23 shows the best fit for a different data set taken with a device irradiated with a much smaller dose of lower energy protons. The detrapping times for both devices are consistent while the trap densities differ. Figure 3-24 shows how the fitted detrapping times change as a function of temperature for a device irradiated with the small dose of low energy protons. The temperature dependence of the detrapping time is consistent with a trap of energy near 0.4 eV– the P-V trap energy. If data is taken at colder temperatures, then information on

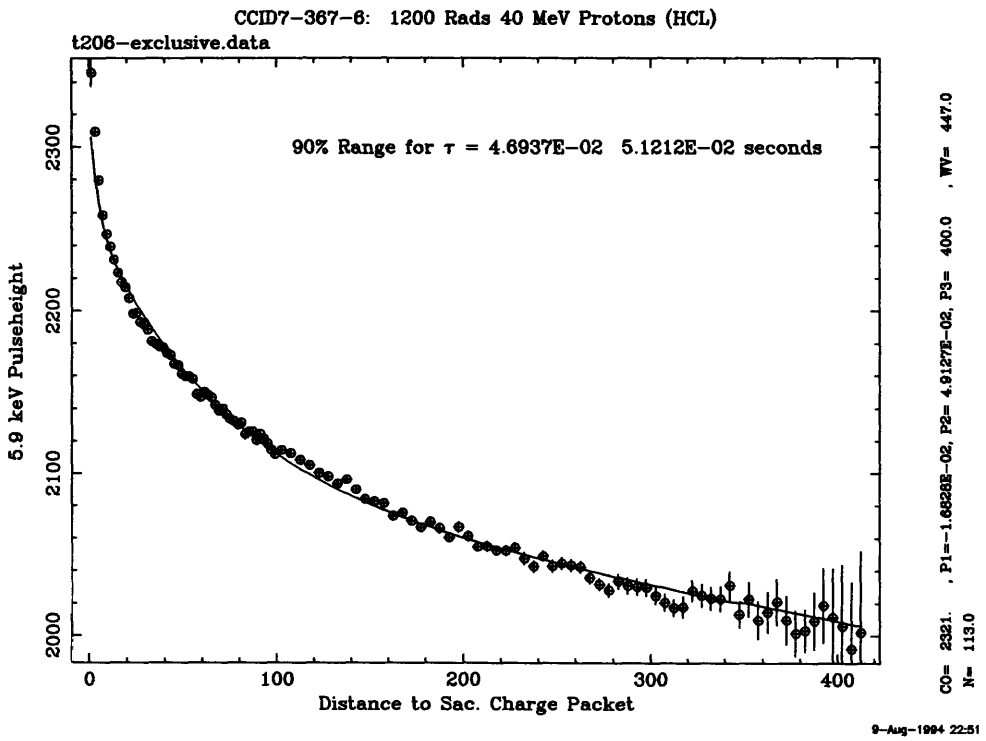

Figure 3-22: The best fit of equation 3.16 to a device irradiated at the HCL with 1200 rads of 40 MeV protons. The device was run at 206 K with $c_{if} = 600\mu seconds$ and $c_{fs} = 11msec.$ The detrapping time is comparable to that of the PV center at 206 K. The deviations from the best fit may be a result of unstable temperature, temperature gradients, or horizontally split events in adjacent columns to SCP-BCP pairs' column. The best fit has a linear trap density of 0.017 traps per micron and a detrapping time of about 50 msec.

smaller energy traps can be extracted. This would be very applicable to future missions like AXAF and XMM where the CCDs are to be run at temperatures of -100C and lower.

3.5.1 Generalization to Variable Charge Packet Size

Equation 3-16 is good for initial charge packets of a given size. There is evidence that as the number of electrons in the charge packet gets smaller, then the number of traps per unit length seen by the packets is also smaller. Figure 3-15 shows how much charge is lost in a device irradiated with 1200 rads of 40 MeV protons as a function of the initial charge packet size. The effect suggests that the different charge packets see different numbers of traps during the CCD readout. This is consistent with an increase in the spatial extent of the charge packet as the number of electrons is increased (Mohsen and Tompsett, 1974). With more volume, the larger charge packets encounter more traps. It is also consistent with a

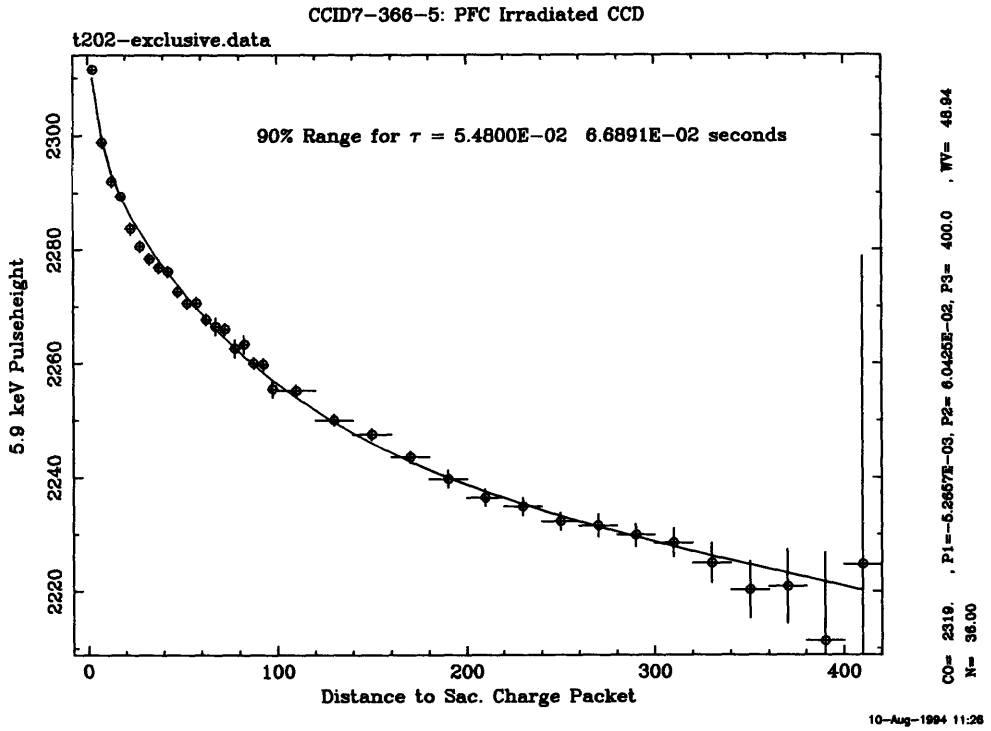

Figure 3-23: The best fit of equation 3.16 plus a constant to a device irradiated at the PFC with 1.2×10^8 2.1 MeV $protons/cm^2$. The device was run at 202 K with $c_{if} = 600 \mu seconds$ and $c_{fs} = 11 msec$. The best fit has a linear trap density of 0.0053 traps per micron and a detrapping time of about 60 msec.

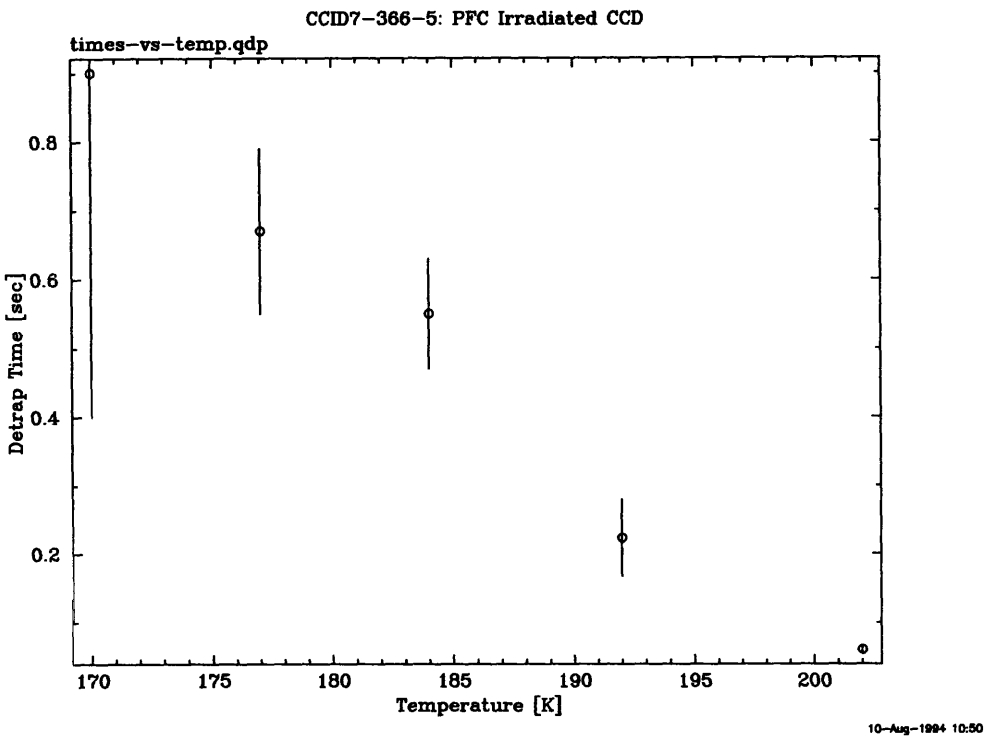

Figure 3-24: Fitted detrapping times as a function of CCD temperature for a PFC Irradiated CCD. Compare to Figure 3-16.

situation where the intrinsic density of traps is different for different size charge packets. To try to understand this, I made calculations of Poisson's equation for the region in the buried channel of the CCD to determine the spatial extent of charge packets with various numbers of electrons.

The Electron Concentration in the Buried Channel

Figure 3-25 is a basic schematic of a few pixels of a CCD. The z direction is perpendicular to the face of the CCD. The x direction is parallel with the charge transfer direction. At a given instance, there is usually a low voltage (eg. -6 volts) on one or two of the phases and a high voltage (eg. +6 volts) on the other phases. A potential well will form under the high voltage phase in the channel. Any free charges will collect into this well.

To calculate the electron distribution and potential function in the buried channel, one must solve Poisson's equation:

$$\nabla^2 \phi(x, y, z) = 4\,\pi\,\rho(x, y, z) \tag{3.17}$$

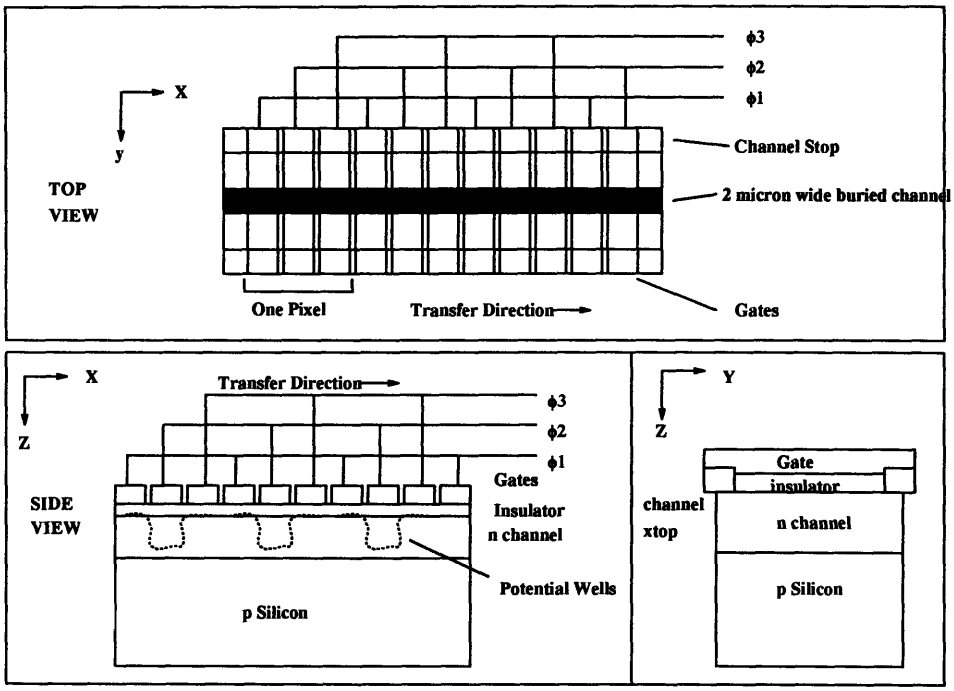

Figure 3-25: Crossections of the some pixels in the CCD

Where $\phi(x, y, z)$ and $\rho(x, y, z)$ are the potential and charge density, respectively, at position (x,y,z) in the channel. For an n-type channel as used in the CCDS for ASCA, the charge density is given by:

$$\rho(x, y, z) = e(C_P(x, y, z) + n(x, y, z)) \tag{3.18}$$

Where e is the charge of an electron, $n(x, y, z)$ is the number density of free electrons, and $C_P(x, y, z)$ is the number density of acceptors doped into the silicon to make the n channel. Our CCDs use phosphorus as the acceptor and the profile is roughly given by:

$$C_P(x, y, z) = C_o\, e^{-z^2/2\sigma^2} \tag{3.19}$$

The actual calculation of the potential and electron density was done numerically, using the 2 dimensional poisson solver "Pisces". While this is not as good as using a three dimensional calculation, it does provide some qualitative agreement with the data. Figure 3-26 is an example of a calculation made for a 3100 electron packet with the gates at +2 and -5 volts. Figure 3-27 shows the electron concentrations for packets of several electron numbers in comparison to the phosphorus concentration. The width of the packet increases slightly as the number of electrons in the packet increases. Also, the larger packets tend to shift

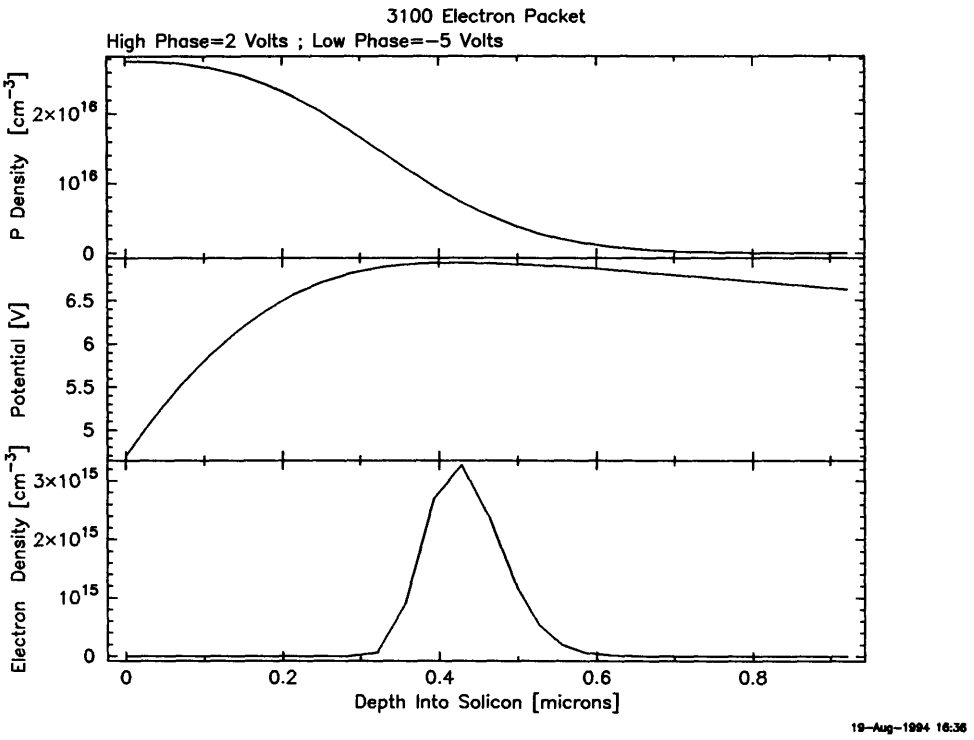

Figure 3-26: The result of a numerical solution to Poisson's equation (eqn 3-17).

closer to the gates of the CCD.

To see how this type of work can be used to understand the observed "delta-q vs q" plot (figure 3-15), consider the following. Let the trap volume density, $N_T(z)$ be a function of z, the depth into the CCD channel. This seems reasonable as one of the most likely trap candidates is the PV center, which requires phosphorus, which has a gaussian density profile in z. If the mobility of the PV center is small, then the PV trap density should be proportional to the phosphorus density profile shown in figure 3-27. In addition, the free electron density, $n_e(z)$ of a charge packet depends on z. If the densities are large enough- as they seem to be in figure 3-27, then we can calculate the loss in electron density at depth z as a packet moves from position x_2 to x_1 in the CCD:

$$n_e(z, x_2) = n_e(z, x_1)\, e^{-\sigma N_T(z)\,(x_2 - x_1)} \tag{3.20}$$

Thus the loss in electron density becomes:

$$\delta n_e(z) = n_e(z, x_1)\,(1 - e^{-\sigma N_T(z)\,(x_2 - x_1)}) \tag{3.21}$$

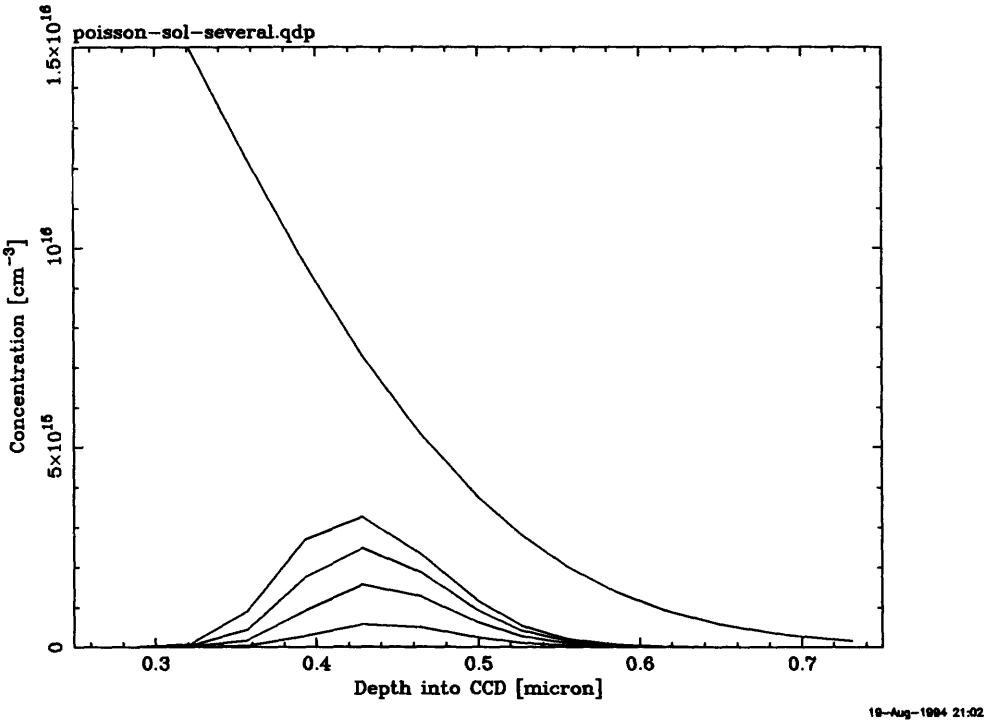

Figure 3-27: The concentrations of charge packets ranging in size from 43 (lowest curve) to 3100 (second highest curve) electrons. The highest curve in the figure is the concentration of phosphorus.

In the case where the trap density is small (as it seems to be from my double pulse experiment), then this equation simplifies to:

$$\delta n_e(z) = n_e(z, x_1)\, N_T(z)\, \sigma\, (x_2 - x_1) \tag{3.22}$$

The total loss in charge is the integral of this equation across z:

$$\delta Q = \int dz\, n_e(z, x_1)\, N_T(z)\, \sigma\, (x_2 - x_1) \tag{3.23}$$

Since I expect the PV trap density to be proportional to the phosphorus density, then I expect that integrating the product of the phosphorus concentration with the electron concentration across z should yield a number proportional to the charge loss. Figure 3-28 is a plot of such an integral as a function of the charge packet size.

Qualitatively, the result is similar to the "delta-q vs q" plot shown in figure 3-15. Quantitatively, the ratio of the measured loss at 500 electrons to the ratio of the loss at 1600 electrons in the data is very close to the corresponding ratio from the poisson equation calculation. Deviations between the model and the data may be a result of several factors. Variations in the doping profile (equation 3.19) would change the shapes of the $\sum n_e N_T$ curves. Three dimensional poisson calculations may yield closer agreement than these two dimensional calculations provide. Also, if the PV center has a non negligible mobility, then its density profile may deviate from being simply proportional to the phosphorus density profile. An interesting experiment for the future would be to see if annealing of radiation damaged devices results in a change in the "delta-q vs q" relation, thus indicating a changing of the trap density profile due to the PV trap mobility.

Note that it is the fact that the trap density depends on Z that results in a non linear relation between the charge loss vs initial charge packet size. It is possible that some types of traps may be more evenly distributed in the channel. This would result in a different "delta-q vs q" relation. Future work may yield interesting results with this.

Extension to the Double Pulse Formalism

Below, I include this effect, phenomenologically, into our formalism. Future work must be done to connect the numerical solutions of Poissons equation to the data. In fact, this "X-ray double pulse" analysis may be useful for understanding the distribution of small

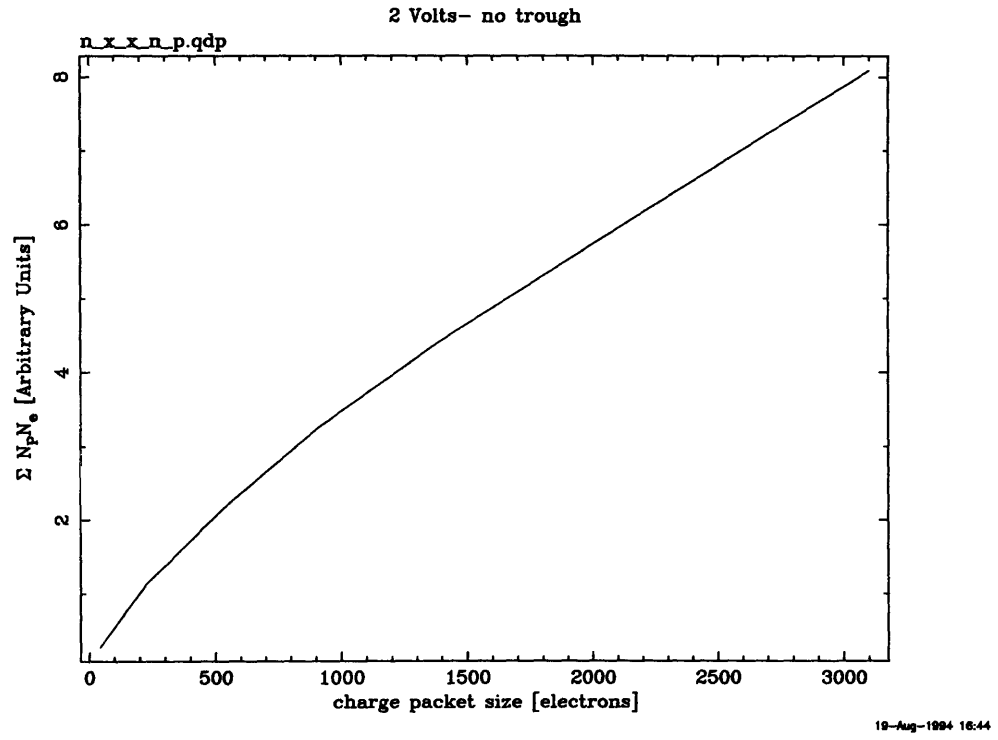

Figure 3-28: A prediction of the dependence of "delta-q vs q" (eqn 3-23). Compare with figure 3-15.

charge packets in CCDs.

Let me further specify my definition of N_L to be the linear density of traps as seen by a charge packet with 1620 electrons (as produced by the Mn-Kα X-ray of Fe^{55}). In addition, I propose the function $W(p)$ be the proportionality constant relating the linear density of traps seen by a charge packet of pulse height "p" with the linear density seen by a 1620 electron charge packet. Thus, the linear density of traps seen by a charge packet with p electrons would be $W(p)N_L$. $W(p)$ can be measured by taking the "delta-q vs q" as in figure 3-14, and normalizing the charge loss to the charge loss for a 5.9 keV X-ray.

Next consider the situation depicted in figure 3-20 as we did to generate our expressions above. However, now let us assume that the SCP has an original pulseheight P_{scp}, while the second charge packet has a pulse height P_{bcp}. Given this, there are two cases:

CASE 1: $W(P_{scp}) > W(P_{bcp})$

Here, the number of traps seen by the SCP is larger than the number of traps seen by the BCP. The number of empty traps which could be seen and filled by the BCP would be

given by multiplying equation 3.9 by $W(P_{bcp})$:

$$N_e^{P_{bcp}}(x,d) = W(P_{bcp})N_e(x,d) \tag{3.24}$$

This would also represent the number of electrons loss by the BCP in this case. Notice that when N_e does not have a superscript, it is assumed to refer to the situation where the BCP is a 1620 electron packet.

CASE 2: $W(P_{bcp}) > W(P_{scp})$

Here, the number of traps seen by the BCP is larger than the number of traps seen by the SCP. The number of empty traps which could be seen and filled by the BCP would be:

$$N_e^{P_{bcp}}(x,d) = W(P_{scp})N_e(x,d) + (W(P_{bcp}) - W(P_{scp}))N_L \tag{3.25}$$

The first term corresponds to traps seen by the SCP which detrap, while the second term corresponds to the traps unseen by the SCP which are empty until they see the BCP.

In terms of fitting for trap parameters, case 1 is easier since we only worry about the pulse height of the BCP as long as the SCP is larger. For the determination of trap densities with flight data, BCPs can be chosen per case 1 and trap densities can be fit using equation 3.16. Ground measurements of the detrapping times should be adequate for the flight data- thus we are left fitting for trap density alone.

A simple application of case 1 would be to measure the how the pulse height of a hot pixel varies as a function of distance to a large pulse height event. Hot pixels are pixels defective pixels which continuously produce charge. I discuss hot pixels below. The cosmic ray flux of 1 c/s/CCD alone, should provide enough statistics to measure trap densities in one week of data. In fact, we can measure trap densities in this way without special calibration observations as a function of time since the launch of ASCA.

Case 2 is the raw form for how to correct the pulse height of events in a damaged device where the trap parameters are known. It can be interpreted as the amount of charge to be added to the measured pulseheight.

3.6 Initial Flight Results

On February 20, 1993, *ASCA* was launched. Our first CCD data was taken on March 20, 1993. The CCD operating temperatures achieved are about -60 C, which is close to our prelaunch prediction. Here, I list some of the observed performance characteristics from the first year of space operation. Some observations were expected such as the spectral resolution degradation. Others were not expected (or at least the ramifications were not expected) such as the hot and flickering pixels on the CCDs. Finally I list some systematic effects to be concerned with when comparing ground and flight radiation hardness results. One thing that was made clear in the ground radiation damage experiments is that the problem is very complicated- making it difficult to understand what to do with the flight data.

3.6.1 Hot and Flickering Pixels

Almost immediately after the first data arrived, we noticed unexpected features in our pulse height spectra. Figure 3-29 shows an example. Specifically, spectral line like features appeared at energies where X-ray lines are not known to appear. Furthermore, the different CCDs had different spectra. In addition, there is a low energy power law like continuum in all of the CCDs.

More analysis of the problem showed that the troublesome spectral features corresponded to CCD pixels which registered events more than would be expected. For each of the "lines" in figure 3-29, there is a single pixel which produced all of the events. Some pixels register an event each time the CCD is read out. Others register an event during some large fraction of the number of readouts during an observation. To quantify and alleviate this effect, a diagnostic tool was made to help identify the bad pixels. Figure 3-30 shows a plot of how many pixels were on for at least a given number of read outs in an observation. An inspection of the plot shows that there are two distributions with a reasonable clear break. There is a population of pixels which fired only a few times as one would expect for a typical observation. This is since a typical observation will have somewhere between one and a thousand X-ray (or cosmic ray) events per 160,000 pixel CCD per readout. There is also a population of pixels which fires over a broad range of frequencies greater than expected for a typical source. I call this population the "flickering pixels". Some of these

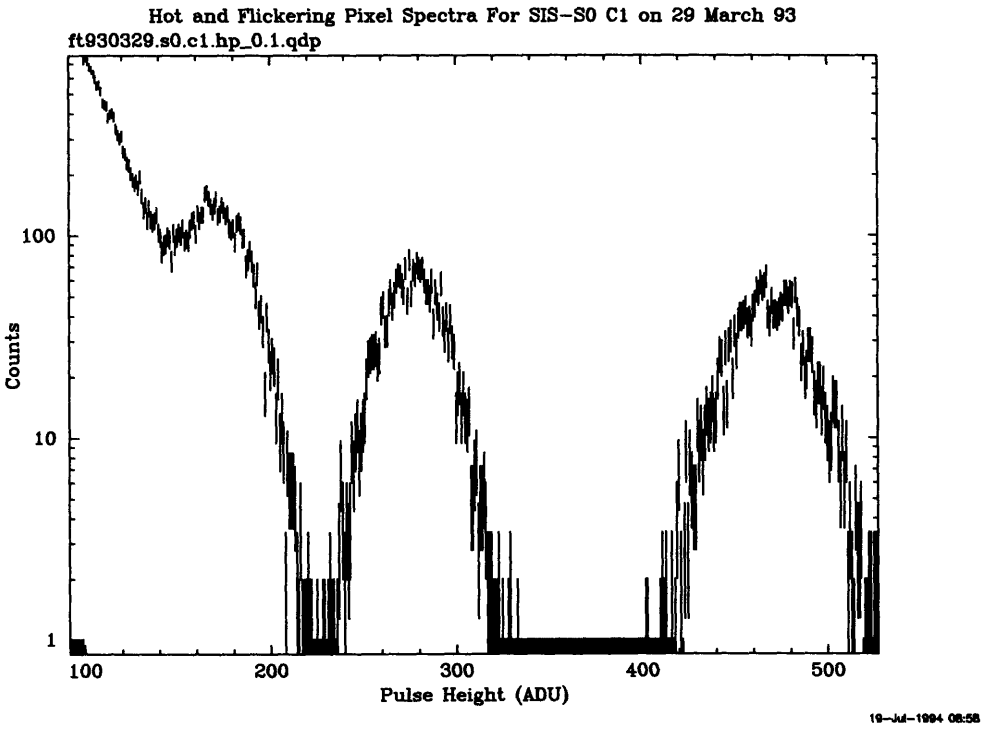

Figure 3-29: Raw pulse height Spectra from one of the CCDs in flight during late March, 1993. Each of the three obvious line features comes from an individual pixel. Most of the low energy continuum feature comes from pixels which registered events more than would be expected.

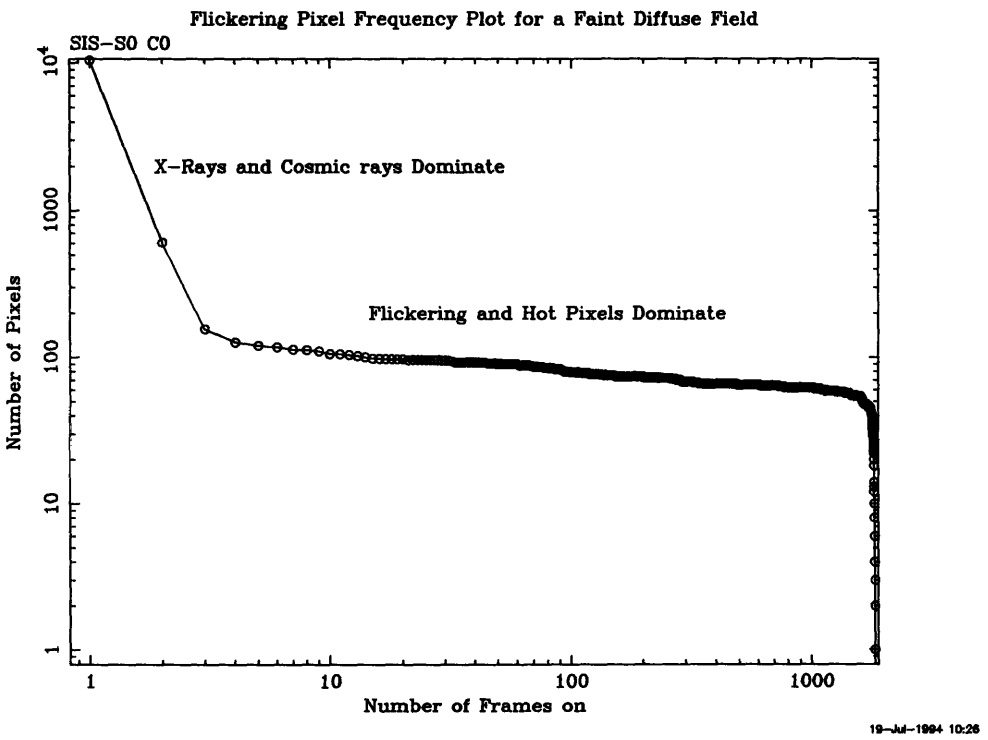

Figure 3-30: Flickering pixel frequency plot for a diffuse faint field. The X-axis is the number of readouts a pixel can register an event. The Y-axis is the number of pixels which registered an event at least that many times.

flickering pixels are on nearly continuously. I call these pixels "hot pixels". The real events make up the steep component to the frequency plot while the flickering pixel population yields the flatter component. The break point on the frequency plot is determined by the source brightness and distribution. If the X-ray source is evenly distributed in the sky, as it was for figure 3-30, then the probability for two real events to land on the same pixel is extremely small resulting in a small break point. If the source is brighter or more point-like, such as Cyg-X1, then the probability for pile up is increased and the real event population extends the break point to the right in the frequency plot as shown in figure 3-31. By using such plots, selection criteria can be made to count flickering pixels and remove them.

Below is a summary of some flickering pixel phenomenology:

(a) There is a rough anticorrelation between the pulse height generated by a flickering pixel and its frequency. Pixels which generate a line-like feature as in figure 3-29 tend to have very large duty cycles. Pixels with low duty cycles tend to produce lower pulse height events.

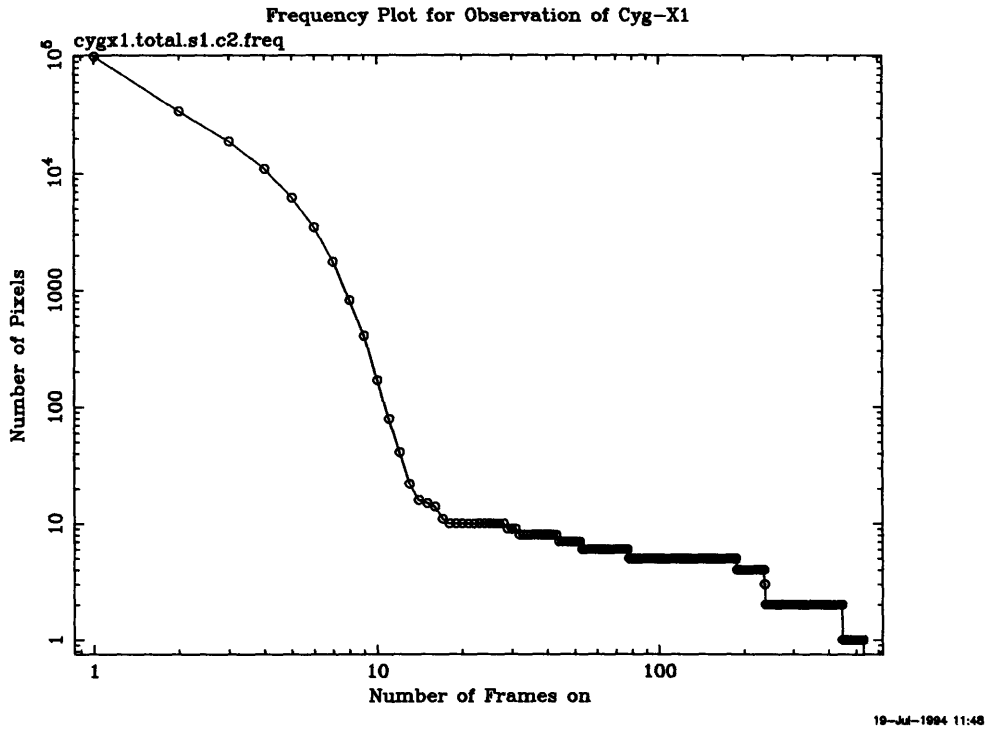

Figure 3-31: Flickering pixel frequency plot for a field with a bright point source. The X-axis is the number of readouts a pixel can register an event. The Y-axis is the number of pixels which registered an event at least that many times.

(b) There is some evidence that many of the flickering pixels which cause problems are in the imaging array as opposed to the frame store array. I expect to see more in the imaging array simply due to the fact that the frame store area is only about 60% the size of the imaging area. I also expect to see more from the imaging array since charge has more time to accumulate in the imaging array than in the rest of the CCD. If one assumes that the defect responsible for a hot pixel is a nearly constant current source, then the pulse height of the hot pixel is proportional to the exposure time. The exposure time (in the imaging array) is a function of the CCD clocking mode (4, 2, or 1 CCD mode). The exposure times for 4, 2, and 1 CCD mode are 16, 8, and 4 seconds respectively. The pulse height of a given flickering pixel scales linearly with the exposure time in the imaging array. This is consistent with a current source located around the pixel in the imaging array. A result of this is that the number of flickering pixels drops as the clocking mode goes from 4 to 2 to 1 CCD mode.

(c) The most disturbing quality of the flickering pixels is that they are increasing with time- suggesting they are a result of some radiation damage. Figure 3-32 shows the measured counting rate per CCD due to flickering pixels vs time since the mission beginning. This problem is particularly alarming as there is no way to screen these pixels from passing through the limited telemetry bandwidth to the ground. As time and the hot pixel counting rate increases, there is less space in the telemetry for data on X-ray photons.

(d) The number of hot pixels is strongly temperature dependent. Figure 3-33 shows how the number of hot pixels changes for approximately 1 degree change in focal plane temperature. Normally, the focal plane temperature is fixed at about -61.8° C, but occasionally, the baseplate temperature for the SIS gets too warm for the TEC to keep the CCD at this temperature.

The CCD temperature becomes warmer than -61.8°C when the baseplate temperature becomes warmer than about -35°C. The CCD temperature of -61.8°C is the set temperature that the TEC control system in the AE regulates. It is possible to set a lower temperature for the CCD through a command to the AE. It requires that the baseplate be cold enough so that the TEC can maintain the desired CCD temperature. Roughly, the TEC can keep the CCD at a temperature 26° colder than the baseplate temperature. The δT of 26° gets somewhat smaller at lower baseplate temperatures. To estimate how cold the SIS CCDs could be, refer to figure 3-34. In this figure are two histograms of time versus baseplate

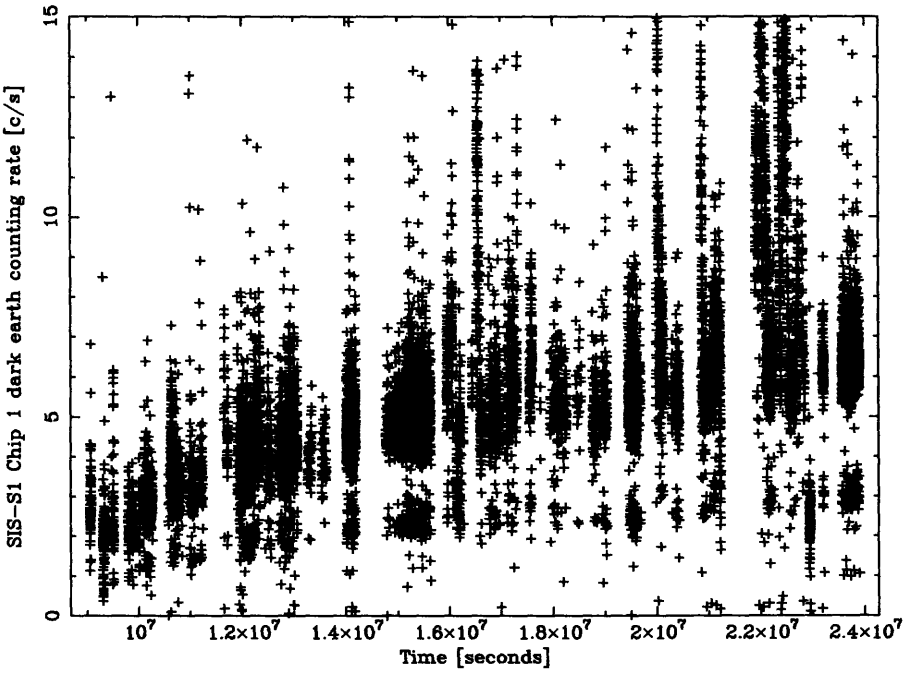

Figure 3-32: The growth in the number of flickering pixels as measured in units of counts per second. This is actually a plot of the counting rate for SIS-S1 Chip1 looking at the dark side of the earth. Since the particle background rate is about 1 count per second, this plot mostly reflects the growth in flickering pixels.

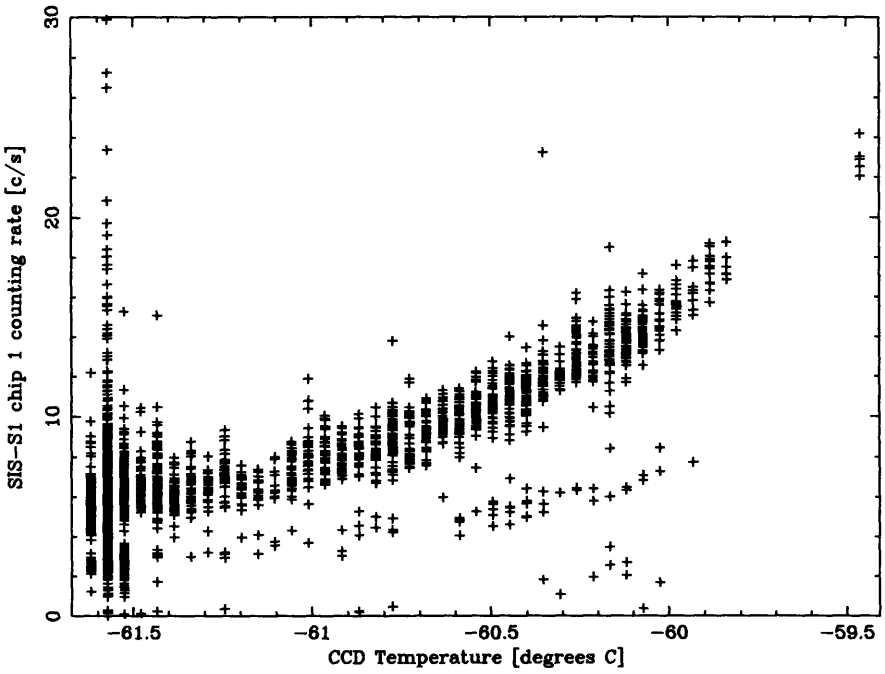

Figure 3-33: The number of flickering pixels as measured in units of counts per second as a function of CCD temperature. This is actually a plot of the counting rate for SIS-S1 Chip1 looking at the dark side of the earth.

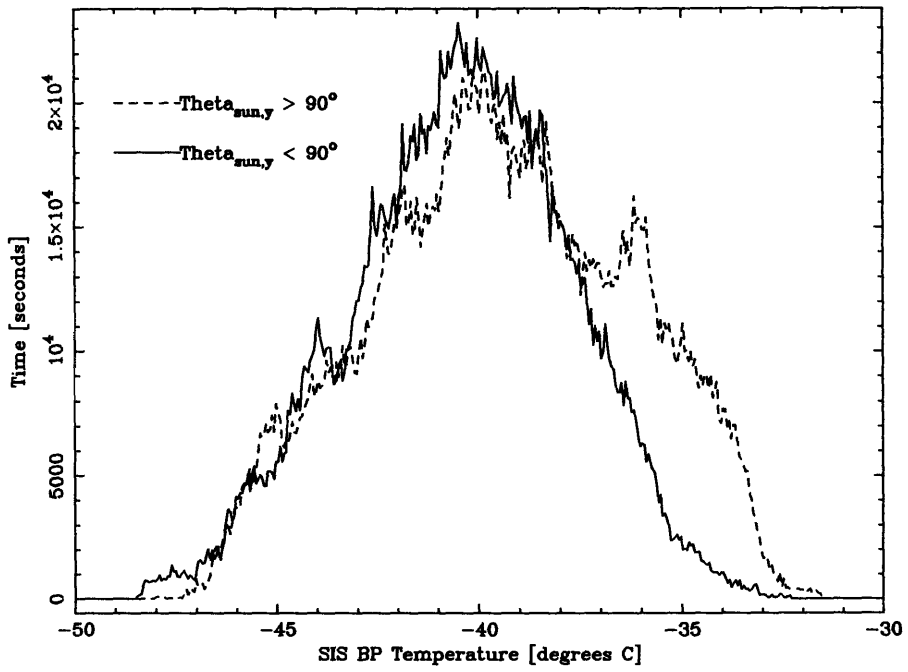

Figure 3-34: Histograms of time versus baseplate temperature for two different ranges of satellite y-axis to sun angles.

temperature for two ranges of satellite to sun orientations. It is clear that the SIS CCDs can be roughly 1 degree colder than they are now, 96% of the time for suitable satellite to sun orientations.

In figure 3-32, notice that the rate was non zero at launch. Furthermore, visual inspection of radiation damaged CCD images during our radiation damage studies clearly showed many hot pixels. Why were we so surprised about the flickering pixels? In most ground analysis, bias and dark frame subtraction was done differently than it is done on orbit. For ground analysis, bias frames integrated with X-ray sources turned away were subtracted pixel by pixel from event data- thus minimizing hot pixels directly. In orbit, we cannot do this, of course. Instead bias values computed for every 64×64 pixel square was subtracted from each pixel in the corresponding squares. This was a clear oversight by the SIS team.

There are two possible origins of these flickering pixels. One is that there are defects in the bulk silicon which produce mid band gap energy levels which act as stepping stones for charge to travel from the valence band to the conduction band. This will produce localized dark current enhancements- hot pixels. The other possible origin is that charged particles

are locally charging the oxide layer between the gate and the bulk silicon. The trapped charge changes the potential difference between the gate and the CCD channel. Thus the application of a given clock voltage level yields a different channel potential as the charging of the oxide increases. In particular, the low level clocks, which origionally put two phases of the CCD pixel into inversion may no longer be doing that. Inversion is a state where holes from the channel stops are drawn underneath the gate where they can recombine with electrons produced by surface state defects near the oxide-bulk interface. Normally, inversion reduces the dark current of the CCD. Places where there is no longer inversion may be admitting more dark current.

3.6.2 CTI Induced Spectral Degradation

Several observations were planned to check the expected degradation of the spectral response. The clearest example of the spectral degradation due to radiation induced CTI is the comparison of the 1993 and 1994 observations of the Puppis A supernova remnant. Figure 3-35 shows the full pulse height spectra of the 30 March 1993 and the 30 May 1994 observations of Puppis A overlayed on top of each other. Figure 3-36 shows more detail of the same plot.

3.6.3 Some Known Systematics to be Concerned With

There are several systematic effects to be concerned with when transferring a CTI measurement of one observation to another. Currently with *ASCA*, the bright supernova remnants Cas-A and Puppis-A are being used to evaluate the state of radiation damage. While these objects may be ideal to detect effects due to radiation damage, it may be very difficult to use this data to correct or predict the effect of radiation damage on other fainter point-like or diffuse objects.

Most observations are of faint objects. In accordance to the dependence on X-ray fluence seen in the ground experiments, I would expect large CTI values to be more appropriate to the fainter observations. However, it is not clear what the case would be for a faint point source. The important factors to keep in mind are the mean time between events and the density of traps in the CCD registers.

An interesting thing to do would be to select events based on the location and pulse height of neighboring events (including cosmic rays and flickering pixels) and see if the

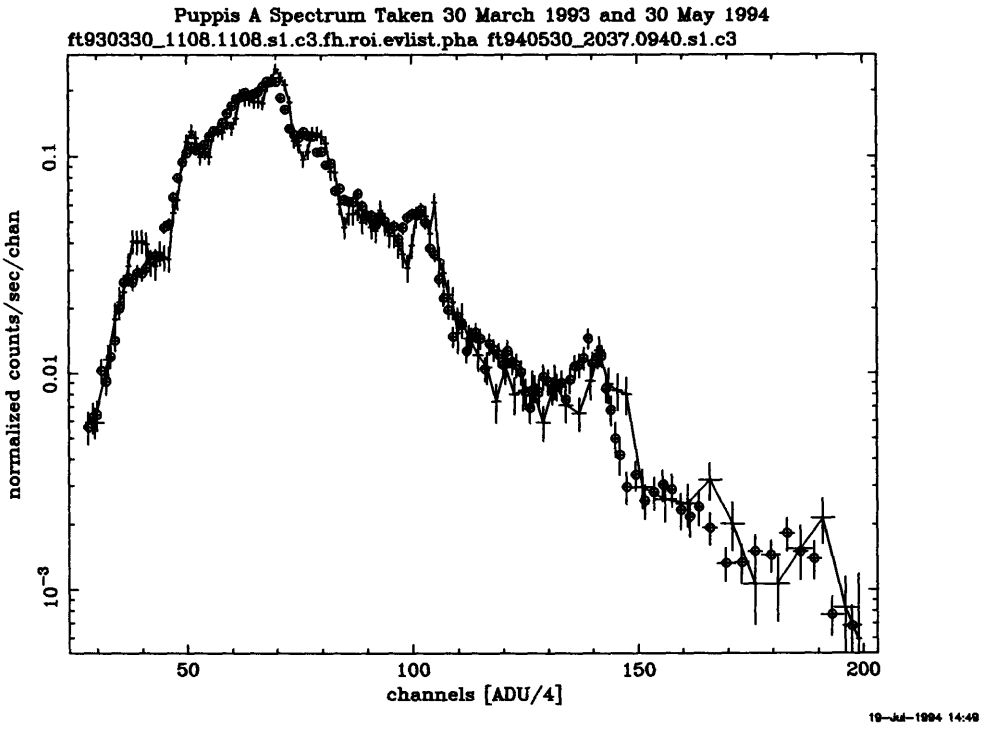

Figure 3-35: A comparison of the full pulse height spectra of the 30 March 1993 and the 30 May 1994 observations of Puppis A. The points with circles represents the later data. Clear degradation in spectral quality is seen as some line peaks disappear and shift downward in pulseheight. Figure courtesy of A. Rasmussen.

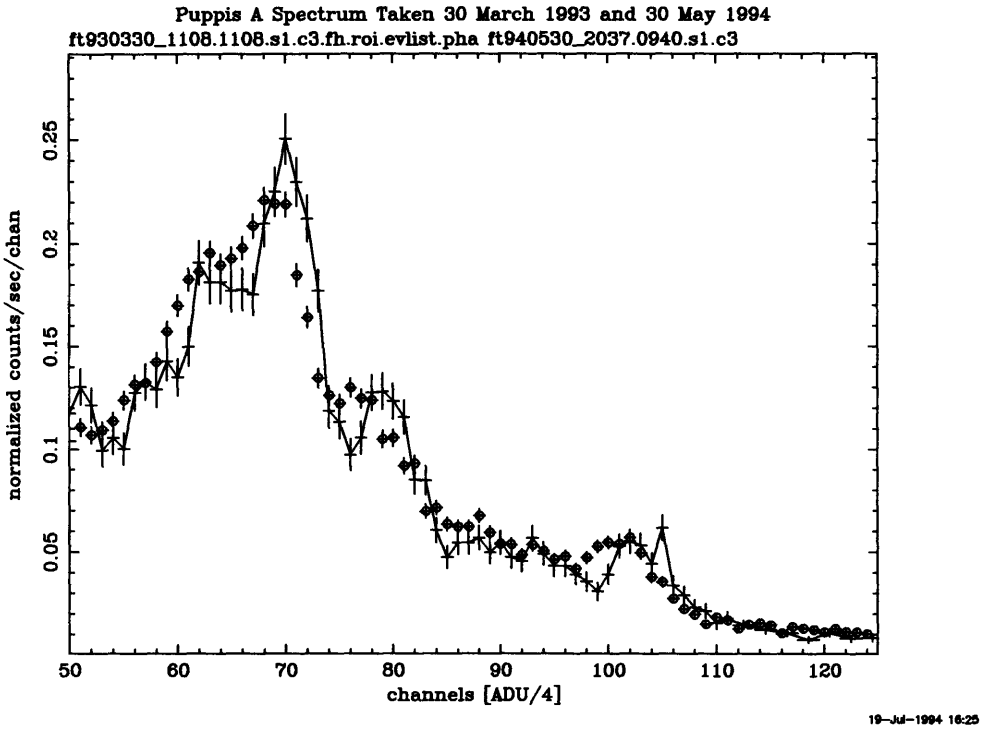

Figure 3-36: A comparison of a portion of the pulse height spectra of the 30 March 1993 and the 30 May 1994 observations of Puppis A. The points with circles represents the later data. Clear degradation in spectral quality is seen as some line peaks disappear and shift downward in pulseheight. Note this figure has a linear scale. Figure courtesy of A. Rasmussen.

resolution improves. According to our ground results (see figure 3-14), I expect that the dependence on pulse height will affect the suitability of a charge packet to be a "sacrificial charge packet". Given this, I would expect that if I select events which occur within a given number of rows (X) behind an event within a given range of pulse heights in the same column, then the pulse height spectrum would improve as the number of rows separating the events decreases. Essentially, the X-ray double pulse analysis described above should be applied to the flight data.

Also of concern is the effect of a "fat zero" on the measured CTI. A Fat Zero is a uniform distribution of charge across the CCD. This charge can also fill traps- but the trapping time is small for small levels of charge (see equation 3.1). Based on ground data results, I expect dark currents of order 1 electron/pixel/second one year after launch. Thus observations in one CCD mode will have about 4 electrons per pixel of fat zero while 4 CCD mode observations will have 16 electrons per pixel of fat zero. The Puppis-A and Cas-A observations require 1 CCD mode, since the objects are so bright. Thus when fainter objects are observed in 4 CCD mode, they will benefit from the extra dark current. In addition, the diffuse leakage of optical light through the optical blocking filters can modify the fat zero.

3.7 Future Work and Ways to Improve CCD Radiation Hardness

Clearly, this is not the last work on radiation damage in X-ray CCDs. Here, I presented some of the systematics which can affect measures of radiation damage. I have also presented a simple model which can explain many of our experimental results as well as provide interesting physical properties of traps in silicon. This work suggests many ways to help improve the hardness of future X-ray CCDs.

There are some obvious steps to take in regards to the flickering pixel problem. One is to accomodate more telemetry to the CCD detectors so that the flickering pixels do not exhaust it. Another step would be to include pixel and column masks on the on board processor so that bad pixels do not get telemetered. A less obvious approach is to use a pixel by pixel bias subtraction routine as was done in the ground data analysis rather than a coarse dark frame subtraction. The problem with improving the dark frame subtraction

algorithm is that better algorithms require more computational resources which require more power.

To address CTI induced spectral degradation, this work suggests several actions which take advantage of the "sacrificial charge packet" model. The goal is to make the mean time between charge packets passing over a trap smaller than the detrapping times. As shown in figures 3-6, 3-7, and 3-16, operation at low temperatures can make detrapping times very long. A result of this work is that the CCD operating temperature for AXAF is being designed to be very low. Another approach is to run the pixel to pixel transfer rates higher- but this requires very fast event processing routines. Another is to introduce charge artificially into designated positions (say, every 30 rows) which would act as sacrificial charge packets. The XMM mission is following this approach.

It may also be possible to optimize the acceptor doping profile to minimize the $\sum n_e N_T$ curves for typical X-ray packets.

Chapter 4

ASCA Observations of the Spectrum of the Cosmic X-ray Background

I present initial results from ASCA on the spectrum of the cosmic X-ray background (XRB) from 0.4 to 6 keV. About 271 ksec of deep survey data has been collected from the performance verification phase of ASCA. About 280 ksec of dark-earth data are used to assess the internal background. Instrumental background spectral, temporal, and spatial characteristics are described. Once I account for the instrumental background, I describe the XRB spectrum. A single power-law describes the XRB spectrum very well in the 1 to 6 keV range with no evidence for a steepening in the 1 to 3 keV range inferred by other missions. Our data clearly show an excess above the extrapolation of the single power law model below 1 keV. At least part of this excess can be accounted for with a local galactic thermal component as there is evidence for O-VII and O-VIII emission lines.

This observation of the spectrum of the XRB places constraints on models where active galactic nuclei make up the spectrum. I use the ASCA data to put spectral constraints on a unified Seyfert 1 Seyfert 2 XRB synthesis model.

This chapter is a combination of a published paper (Gendreau et al, 1995) and a paper in progress (Gendreau, Yaqoob, Mushotzky, and Fabian, in preparation). The "we" refers to the the several authors of these papers.

4.1 Introduction: Historical Overview Before ASCA

4.1.1 Observations

The cosmic X-ray background (XRB) is the oldest known of the cosmological background radiation fields (see Fabian & Barcons 1992 and Matt 1994 for recent reviews). The 1962 discovery of the XRB came as a surprise during a sounding rocket flight intended to study X-ray emission from the moon (Giacconi et al. 1962). Over the past 3 decades, a large number of satellites and sounding rockets have been launched to study the X-ray universe and, in particular, the XRB. Prior to ASCA, the results of these studies may be divided into two domains: the low energy domain (the XRB less than about 2 keV) and the high energy domain (the XRB greater than about 2 keV). The division between these domains is due to both instrumental reasons and intrinsic differences in the XRB.

In the high energy domain, we have the best spectral information from the A2 MED and HED detectors on board the US satellite HEAO1 (Marshall et al. 1980). In this experiment, great care was taken to understand the instrumental background so that it may be accurately accounted for in the data. Marshall and collaborators found that the spectrum could be extremely well characterized by a 40 keV bremsstrahlung model to an accuracy of better than 3% in the 3 to 60 keV bandpass (Marshall et al. 1980). Gruber (1992) gives an analytical fit to the XRB spectrum greater than 3 keV using the A2 result along with several other results:

$$I(E) = 7.877E^{-0.29}e^{-\frac{E}{41.13}} keV cm^{-2}s^{-1}sr^{-1}keV^{-1} \tag{4.1}$$

in the 3 to 60 keV band and a double power law in the 60 keV to 6 MeV band:

$$I(E) = 1652E^{-2.0} + 1.754E^{-0.7} keV cm^{-2}s^{-1}sr^{-1}keV^{-1}. \tag{4.2}$$

Here, E is in units of keV. The 3-20 keV band can be well approximated by a power law of energy index 0.4. Figure 4-1 shows the XRB spectrum in units of power (energy×photon intensity). In these units we can see that most of the power in the XRB is concentrated around 30 keV (the famous XRB hump).

This high energy domain appears to be isotropic to 3% to on scales down to the smallest resolvable (3 by 3 square degrees for the A2 experiment). This isotropy forces us to conclude

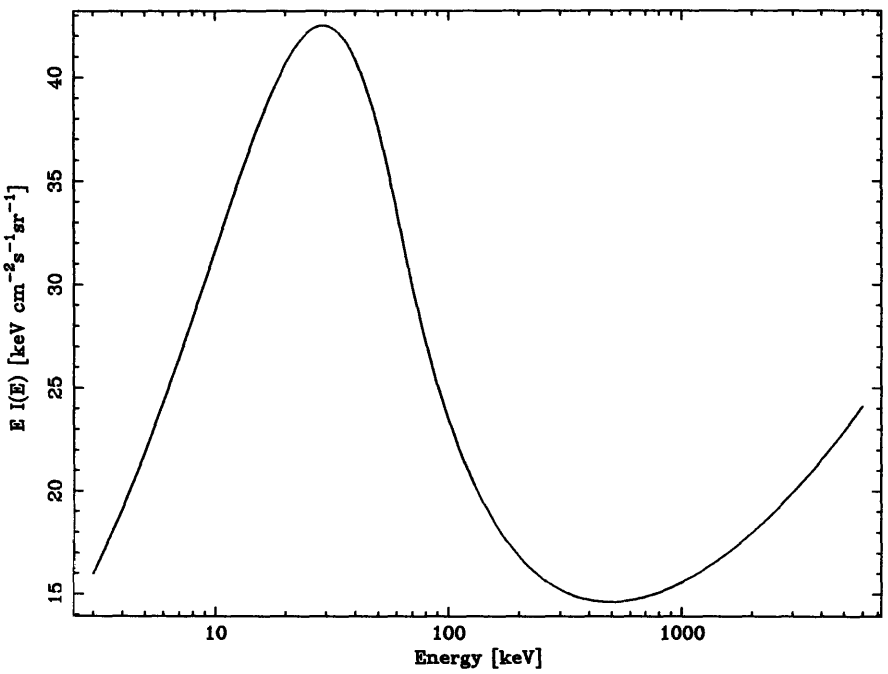

Figure 4-1: The power spectrum of the XRB from the Gruber equations. Most of the XRB power is peaked at 30 keV. This is directly related to the fact that a 40 keV bremsstrahlung spectrum describes the 3 to 60 keV data so well. The rise at high energies is the low energy side of the "MeV bump" in the gamma ray background.

that this background is primarily cosmological and not galactic.

In contrast to the high energy XRB, the XRB below 2 keV is extremely anisotropic which suggests a more local source. In addition, the 1/e attenuation lengths of these lower energy X-rays in the galaxy are smaller than the galactic dimensions. Thus most of this background is considered to be galactic, although this depends on energy and galactic coordinates. McCammon and Sanders (1990) have produced an excellent review of this softer XRB.

In this lower energy domain, the average spectrum of the XRB exceeds the extrapolation of the Gruber formula. Several studies have found that a hot thin plasma of temperature kT = 0.16 keV can explain the excess well. A thermal spectrum at this temperature is dominated by line emission which makes some of the fitting results for the spectrum dependent on the detector energy resolution.

4.1.2 Theoretical Progress

Unlike its famous partner, the cosmic microwave background (CMB), the XRB still has an undetermined origin.

Many of the initial models for the origin of the XRB suggested that a truly diffuse and hot intergalactic medium generates thermal bremsstrahlung which would account for most of the observed XRB (Coswik and Kobetich, 1972). The observation by Marshall et al (1980) that the spectrum of the XRB resembles a kT = 40 keV thin thermal bremsstrahlung model supported this view. Numerous cosmological problems arose from this model (Gulbert and Fabian, 1986). The model has been completely rejected since COBE measurements showed that the CMB spectrum is a perfect single temperature blackbody with no distortions as expected by a Sunyaev-Zeldovich effect due to the hot IGM electrons. Wright et al (1994) and Mather et al (1990) have put strict upper limits on the contribution of a truly diffuse IGM to the XRB of less than 3%.

The rejection of the hot IGM model for the XRB spectrum has required us to accept the alternate solution that the XRB is due to the sum of unresolved discrete sources. The challenge has been to find the type of source which has a spectrum capable of being summed up to make the XRB spectrum. At the lower energies, clusters of galaxies may contribute significantly, but their low temperatures (less than 10 keV) prohibit them from significantly contributing to the XRB above 3 keV. Starburst galaxies may contribute significantly, but there is little information on their properties. Active galactic nuclei (AGN, including quasars and seyfert galaxies) are strong X-ray emitters and numerous enough to account for the XRB. AGN are now considered the prime contributors to the XRB.

For a long time, the major problem with the AGN synthesis model for the XRB has been the "spectral paradox" (Holt,). The X-ray spectra of AGN in the 2-10 keV band are relatively steep. Typically, one fits power laws to AGN spectra with energy indices of about 0.7 (Mushotzky 1984, Turner and Pounds 1989). However, in the 3-10 keV band, the XRB spectrum is well approximated by a power law with energy index 0.4. How could sources which such steep spectra make the flatter XRB?

Observations by Ginga showing a flattening in AGN spectra above about 7 keV and cold iron fluorescence lines have sparked several new XRB AGN synthesis models. All these models have parameter phase spaces which satisfy the XRB spectral constraints while dif-

fering significantly in the source physics. These models may be divided into two categories: reflection models and absorption models.

In the reflection models, relatively cold matter surrounding the central engine of the AGN reprocesses primary radiation through Compton scattering and fluorescence. A general feature of the Compton reflection component is a broad hump in the 10 to 100 keV range. An appealing aspect of this model is that the in the 7 to 20 keV range the spectrum is relatively flat- once red shifted, this could make the flat XRB spectrum in the 2-20 keV range. This model requires that a large fraction of the total flux from the AGN to be the reflected component (Fabian 1990). This fraction is much higher than currently observed, except for in the case of NGC 6552, perhaps (Reynolds et al 1994; Fukazawa et al 1994).

In the absorption models, we have an application of the unified AGN model (Antonucci 1993). The essential concept here is that all AGN (or at least Seyferts) consist of a central engine surrounded by a torus of matter. This matter can reprocess X-rays by absorption and scattering. The orientation of our viewing axis to the torus axis determines the type of Seyfert we would see: looking down the axis results in a Seyfert Type 1 galaxy while looking through the torus results in a Seyfert Type 2 classification. Thus in this model, the X-ray spectra of type 2 and type 1 Seyferts differ principaly due to absorption. Several groups have shown that some mixture of type 1 and type 2 seyferts can produce the XRB (Setti & Woltjer 1989; Matt & Fabian 1994; Madau, Ghisellini, & Fabian 1994; Comastri, Setti, Zamorani, & Hasinger 1994; Morisawa et al 1990; Terisawa 1991; Grindlay & Luke 1990).

The XRB AGN synthesis models have evolved from a spectral paradox, where there seemed no room to satisfy the XRB spectrum, to a multitude of models which can explain the XRB. A subset of the acceptable model parameter space predict spectral features in the XRB spectrum due to iron in the reprocessing material. Depending on the typical geometry, intrinsic spectrum, and luminosity evolution, these spectral features can appear as broad humps or sharp wiggles in the 1 to 7 keV band of the XRB. The data prior to ASCA have been inadequate to detect these.

4.2 Where This Thesis Fits In

In this thesis, I use ASCA SIS data to examine the XRB spectrum from 0.4 to 7 keV. There are two principle advantages in using ASCA data for this work. First, ASCA is one of the first instruments to cover both the low and high energy domains (see above) which were examined separately before. Thus, I can directly examine the discrepancies between extrapolations of the previous high and low energy results. Second, the superior energy resolution of the SIS helps us both to look for weak sharp spectral signatures in the cosmological XRB as well as to separate the galactic component from the extra galactic component. The later point is model dependent and depends on our assumption that the galactic component is mostly soft thermal emission and therefore line dominated.

I will describe data selection, cleaning, and analysis. I will discuss the instrumental background as it is a critical issue in the XRB analysis. Next, I will describe the development of a special X-ray telescope response model for extended objects. I will then present a phenomenological fit to the data and compare it to other work. Next, I will discuss ASCA spectral constraints on parameters in a Seyfert 1/2 XRB synthesis model. Finally, I will discuss future work and some more analysis which needs to be done with the ASCA data.

4.3 The ASCA X-Ray Data: Cosmic

We have accumulated a spectrum of the XRB of total exposure 270 ks in each of the Solid State Imaging Spectrometers (SIS) (Burke et al 1994) on ASCA (Tanaka et al 1994). We have used carefully selected Faint and Bright SIS observation mode data from deep exposures of the Draco, North Ecliptic Pole (NEP), Lockman Hole, and Lynx fields observed during the performance verification phase (PV phase) of ASCA. Table 4.1 shows the relative exposure times in each field. The separate observations of these fields will be described elsewhere (ASCA PV team). Each field has a galactic latitude near 45 degrees and thus a low galactic absorption in the SIS energy band.

Important factors affecting data selection are optical light leakage and solar scattered X-rays. Particularly important is the angle between the earth's "bright" (sun illuminated) limb and the field of view (FOV). In the standard analysis system, this angle is called "BR_EARTH". In addition, slight energy scale shifts can occur within about 200 seconds of a satellite night/day transition due to dark frame error (DFE) (Otani et al, 1994). This

Table 4.1: Fields used in this analysis.

Field Name	α(2000) [hh mm]	δ(2000) [dd mm]	Exposure Time [seconds]
Lynx	08 49	44 50	68706
Lockman	10 52	57 22	51871
Draco	17 08	71 00	53405
NEP	17 59	66 34	97481

DFE can also lead to enhanced low pulse height hot pixel rates. To minimize contamination by these factors, we select data taken when the elevation angle between the earth bright or dark limb and the FOV was greater than 5 degrees, BR_EARTH was greater than 30 degrees, and at least 250 seconds had passed since a satellite night/day transition. Data taken near the South Atlantic Anomaly (SAA) are also avoided since the event rate is seen to increase in the SAA, just before the radiation belt monitor (RBM) turns off the SIS. The instrument background rate is also dependent on the local magnetic cut-off rigidity; we chose a minimum cut-off rigidity of 8 GeV/c. Data collected under these conditions during satellite night and satellite day appear comparable and were combined to yield the total exposure time. Care was taken to avoid times where telemetry saturation occurred. This saturation usually occurs near the SAA and when BR_EARTH is small. Telemetry saturation would modify our response as well as introduce times when the on board digital processor (DP) is failing.

The CCDs of the SIS have some bad pixels with excess dark current. Some of these pixels appear as events 100 % of the time and are called "hot pixels", while others turn on less frequently and are called "flickering pixels" (see section 3.6.1) Hot pixels and high frequency flickering pixels are relatively easy to identify and remove in the sparse fields analyzed here. Since there are many pixels on the SIS CCDs and many fewer X-ray background photons during the total exposure of the ASCA PV phase deep surveys, pixels which turned on at least twice were rejected. When pixels which were activated two or three times were left in, a strong soft component in the lowest 3 or 4 spectral channels appeared in the spectrum. This is due to the observed anticorrelation between flickering pixel frequency and pulse height.

Each SIS consists of 4 CCDs which have slightly different gains. In the first analysis of the XRB spectrum (Gendreau et al., 1995), we used eight different responses (one for each

CCD), and simultaneously fit the XRB spectrum. Here, we used the ASCA data analysis tool SISPI to combine the data of the different CCDs by adjusting gains. We are thus left with a single data file of very high signal to noise.

4.4 The X-Ray Data: Internal

To understand the XRB, I must first determine the detector internal/particle background. In the SIS, event grading rejects approximately 98 % of the cosmic ray induced events. The event grade is a measure of the event shape. This is the equivalent to the rise-time rejection used in proportional counters. We have selected data with grades 0 through 4 (see appendix B) for our X-ray analysis. Grades 5 through 7 are indicative of large charge clouds usually produced by cosmic rays (see appendices B and F). Figure 4-2 shows an image which includes both cosmic rays and X-rays.

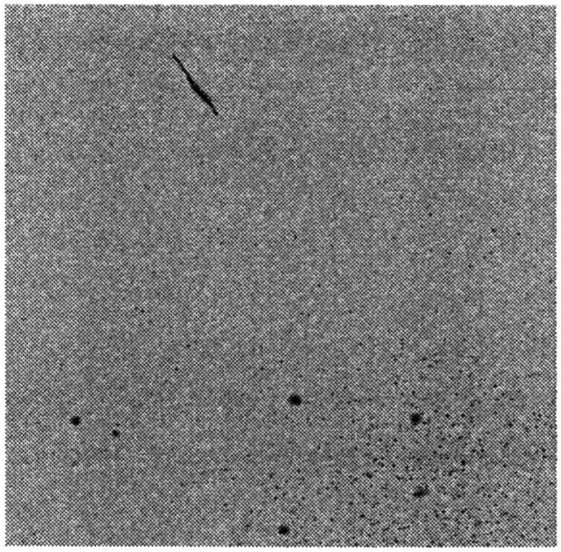

Figure 4-2: Image of Cas-A (lower right hand corner) with cosmic rays. This is a frame mode image which shows how the raw CCD data looks to the on board event processor before events are found and classified. The higher grade events are "blobby" and usually consist of cosmic rays. Good X-ray events are always smaller (one or two pixels).

However, about 2 % of the particle induced events cannot be rejected by grade. To

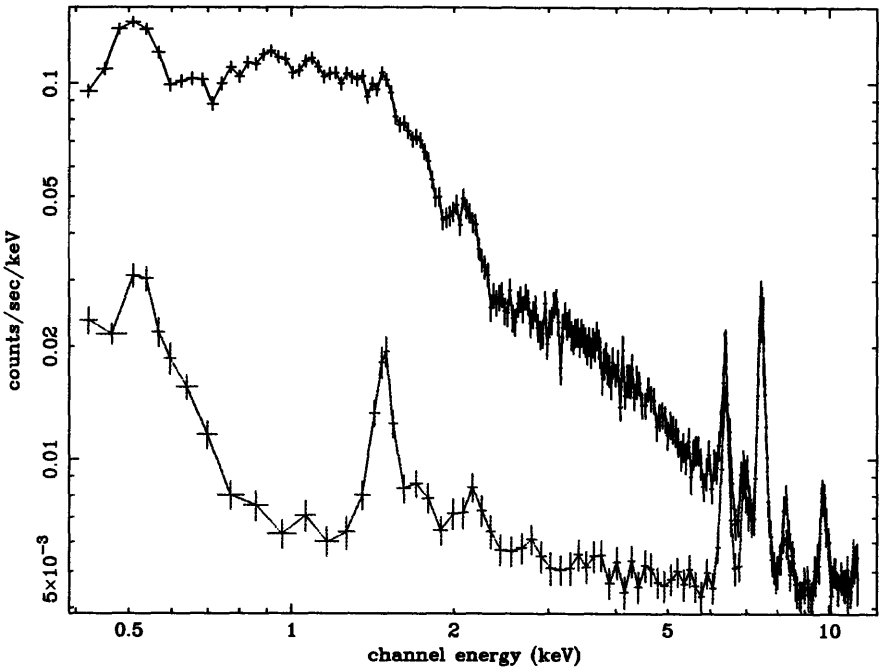

Figure 4-3: Spectrum of the XRB obtained with the eight CCDs of the SIS detectors compared to dark earth data. The total exposure time is approximately 270 ksec for the sky data and 280 ksec for the dark earth data. The dark earth data is the lower curve, while the sky data is the upper curve. Instrumental background lines due to aluminum, gold, iron, cobalt, and nickel are very clear in this figure.

account for these, I collected data while ASCA looked at the dark side of the earth. To avoid solar scattered X-rays and optical light, I collected dark-earth data taken only during satellite night, and only for times at least 250 seconds after the satellite night/day terminator. In addition, the I have avoided times when the satellite was in the SAA. Finally, I observed a slight dependence on the local magnetic rigidity in the dark earth data. To account for this, I have selected both the sky data and the dark earth data when the rigidity was greater than 8 GeV c^{-1}. I have collected about 280 ksec of dark earth data accumulated from April to September 1993. When I have combined data from all 8 chips and rebinned the spectrum to 512 channels, there are no less than 25 counts per channel, which allows us to use the χ^2 statistic.

The spectrum of the instrumental background data is characterized by a nearly flat continuum, with instrumental fluorescence lines due to iron, nickel, cobalt, aluminum, silicon, and gold. There is also an oxygen line present, which we consider to be most likely

of atmospheric origin for the following reasons: the fluorescence yield of oxygen is more than an order of magnitude smaller than that of silicon, there is much more silicon around the sensitive part of the detector, there is no Si-K line of comparable strength seen in the spectrum. The sky data probably does not have this oxygen line, since the earth elevation angle cut is so stringent. In the work presented here, the removal of the oxygen line from the internal background spectrum does not affect the results.

The average spectrum of all of the dark-earth data set from the two SIS sensors has a total intensity of 7.3×10^{-4} ct s^{-1} keV $^{-1}$ per CCD (6×10^{-4} ct s^{-1} keV $^{-1}cm^{-2}$). There is a difference of about 12% between the two independent SIS detectors on ASCA. In particular, the intensity of the various fluorescence lines differs between the two SIS sensors. The Ni Kα lines are the strongest with rates of about 5×10^{-4} ct s^{-1} per CCD. The sensor-to-sensor variations are most likely due to variations in the thickness of gold plating on portions of the kovar (an iron/nickel/cobalt alloy) CCD packaging and framestore shield. A more detailed study of the internal background is presented elsewhere (Gendreau et al, 1994, appendix F).

Figure 4-3 shows the sky data and the dark earth data. The excellent agreement at high energies between these two datasets suggests that our dark earth data is a good estimate of the instrument background since the both the telescope throughput and the expected XRB spectrum (equation 4.1) are reduced at these energies.

4.5 Fluctuations Between the Fields

I have indicated above that the XRB isotropy is energy dependent. An important question is how representative of the XRB are the fields used here. It is unfortunate that ASCA did not perform an all sky survey. Instead ASCA made many pointed observations. Most of these were of known X-ray bright objects. I have used the four of the few observations of "empty" fields. These fields do contain some resolved sources which can contribute to fluctuations of intensity among the fields. Also, variations in the galactic component will contribute to the fluctuations primarily in the lowest energy channels. Table 4.2 shows the background subtracted XRB counting rates per two SIS sensors in each of these fields. The table is divided by energy band. The errors for the average count rates are the one sigma scatter in the intensities found for the individual fields about the mean intensity.

The relative scatter are these errors divided by their corresponding mean intensities. The relative scatter suggest the magnitude of the systematic errors due to field selection.

In the 0.4-0.532 keV band, the relative scatter in intensity among the SIS fields is about 19%. This anisotropy is consistent with the fluctuations observed with the Wisconsin sounding rocket survey using proportional counters with 7 degree angular resolution (McCammon and Sanders, 1990). This low energy variance is most likely due to local anisotropic galactic X-rays.

In the harder 1-6 keV band, the relative scatter is 10% or less. It is interesting to note that this scatter is less than one would expect based on the HEAO1-A2 hard X-ray isotropy measurement of less than 3% in $\sim$9 square degree cells (Richard Mushotzky, private communication). If many individual sources make up the XRB, then to first order, the normalized fluctuations of the XRB go as the one over the square root of the number of sources included in a detection beam. The number of sources in a detection beam goes as the solid angle of the beam. Since the SIS field of view is about 1/10th of a square degree, we would expect that the SIS measurement would amplify the HEAO1-A2 3% anisotropy measure by a factor of $\sim (9/(1/10))^{0.5}$. Thus we would expect fluctuations of about 20-30% in the ASCA SIS data. The lower observed variance may be due to the fact that X-rays from outside of the nominal SIS field of view contribute to the XRB measurement. I discuss this in the next section.

Table 4.2: Fluctuations in intensity between the fields used in this analysis. The counting rates are background subtracted per two SIS detectors.

Field Name	0.4-6 keV [c s^{-1}]	0.4-0.532 keV [c s^{-1}]	0.532-1.2 keV [c s^{-1}]	1.2-6 keV [c s^{-1}]
Lynx	0.2075±0.0022	0.0212±0.0007	0.0633±0.0011	0.1190±0.0018
Lockman	0.2299±0.0027	0.0155±0.0007	0.0675±0.0013	0.1439±0.0022
Draco	0.2130±0.0026	0.0139±0.0006	0.0666±0.0013	0.1294±0.0021
NEP	0.1986±0.0018	0.0172±0.0005	0.0607±0.0009	0.1173±0.0015
Average	0.2123±0.0132	0.0170±0.0031	0.0645±0.0031	0.1274±0.0122
Relative Scatter	6%	19%	5%	10%

4.6 The XRT Response

While the response of the SIS has very little dependence on the source distribution, the X-ray telescope (XRT) response to an extended source will be different than it is for a point source. Principle differences are due to stray X-rays which reflect off of the telescope surfaces only once. Figure 4-4 shows the effects of a point source well outside of the field of view as described by the plate scale. In this figure, a one keV and five keV point source are moved from the optical bore sight towards the upper left hand corner in 15 arcmin steps. As the point sources move further off-axis, it is clear that the low energy point source contributes more significantly to counts in the center of the focal plane where the detectors are located. This is also seen in figure 4-5.

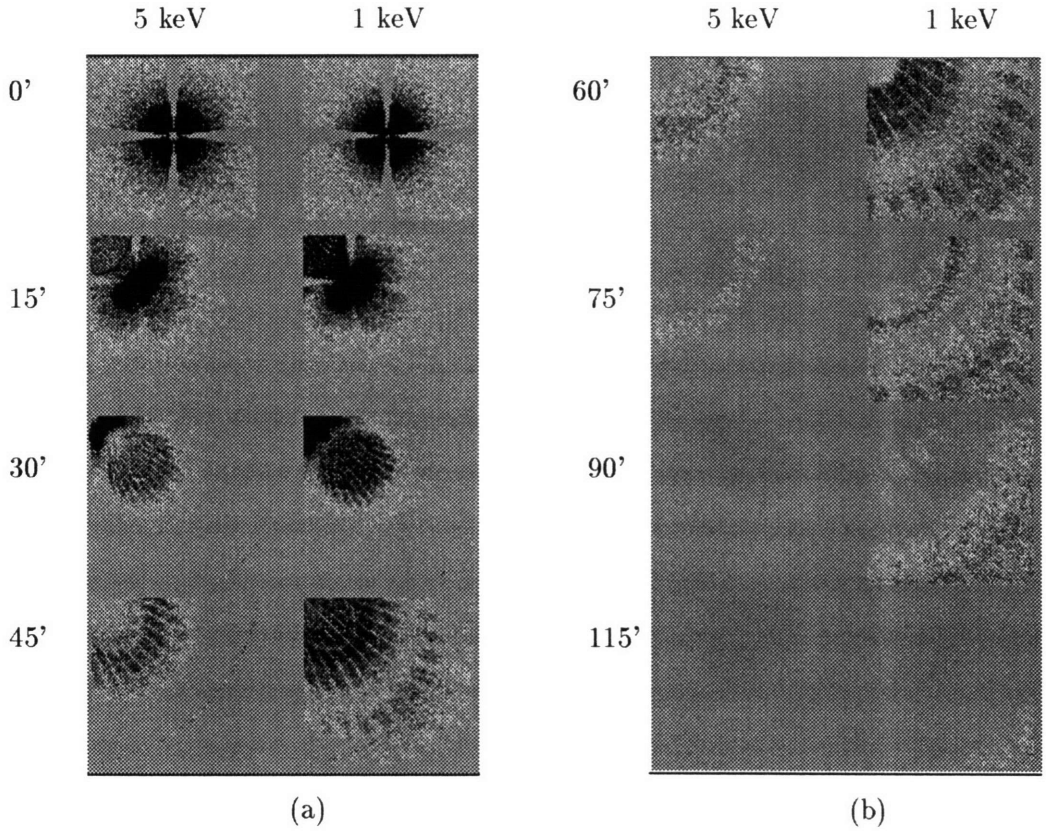

Figure 4-4: Each of the two panels above depict a series of ray traced images for 1 keV (right side of each panel) and 5 keV (left side of each panel) monochromatic X-ray point sources. Each image is 50×50 arcmin^2. The SIS FOV is about 22×22 arcmin^2 and is at the center of each image. Panel (a) shows the resulting images for the point sources at 0, 15, 30, and 45 arcmin off the optical axis, starting from the top pair of images. Similarly, panel (b) shows the resulting images for the point sources at 60, 75, 90, and 116 arcminutes off the optical axis.

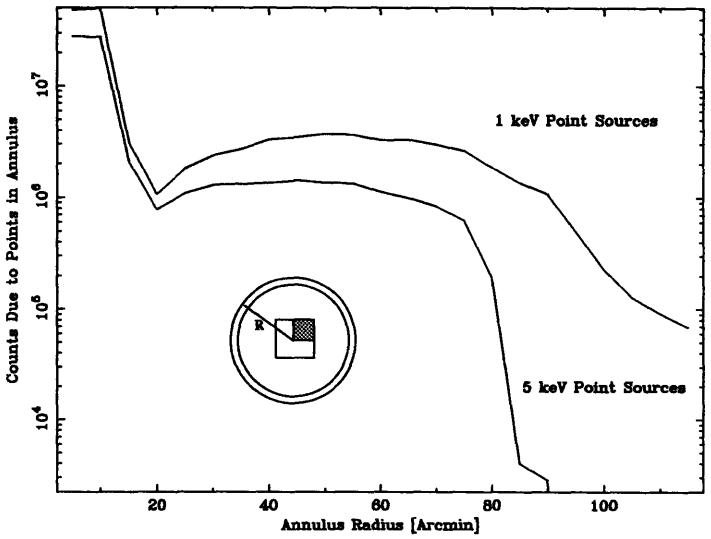

Figure 4-5: Counts detected in one CCD (the shaded box in the inset) due to point sources located in an annulus at radius R. The upper curve is for 1 keV point sources and the lower curve is for 5 keV point sources. In the simulation, 100,000 photons per point source were incident on the telescope.

For the case of the XRB, ray tracing was used to simulate the response to a flat field incident upon the XRT . For each energy from 300 eV to 12 keV, in 100 eV steps, 10^7 photons with incident angles randomly distributed between 0 and 2 degrees of the XRT optical axis were ray traced through the XRT model and collected on a focal plane. Photons landing within the regions occupied by individual CCDs of each SIS were counted and normalized to the incident surface brightness to yield an XRT throughput in units of [sr cm^2]. Since there are 8 CCDs within the 2 SIS detectors, 8 XRT responses were produced in this fashion. Figure 4-6 shows one of the 8 XRT responses generated convolved with the CCD response. Note that the units are different from the standard response (cm^2).

There is a mysterious feature around 2.2 keV in the telescope response which is not accounted for in the raytracing. This feature is seen in all observations where there is enough signal. A possible cause for this feature is multilayer enhancement of the gold reflectivity due to very small thicknesses (50 angstroms) of hydrocarbon contamination (Gordan Garmire, private communication). It can be modelled as a gaussian with a sigma of about 70 eV. Its intensity is proportional to the intrinsic intensity. We qualitatively verified this for our diffuse field analysis by using the pointings of the Coma cluster taken

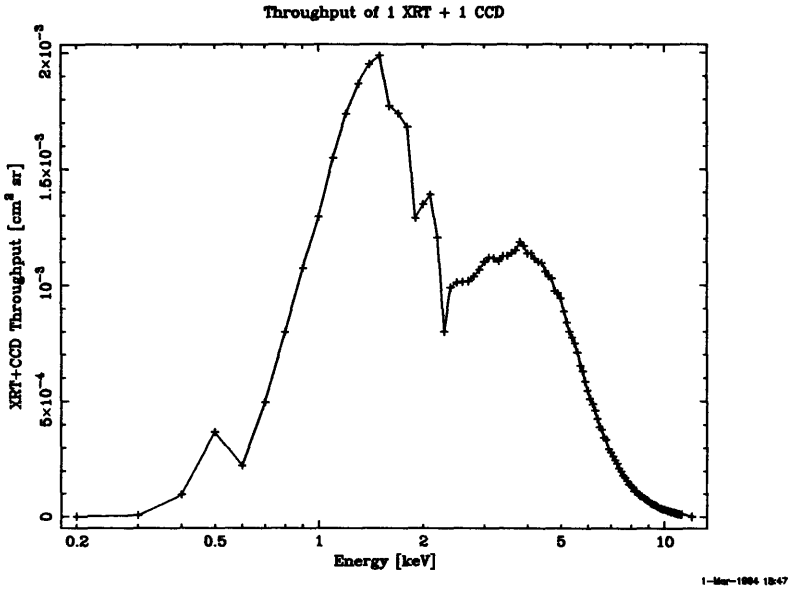

Figure 4-6: One of the 8 instrument response functions used in the fitting.

during ASCA's PV phase. Unfortunately, this feature is located very close to where we expect spectral signatures due to iron lines and edges in the AGN synthesis model. Here, we model it as a gaussian of intensity 0.12 photons s^{-1} cm^{-2} sr^{-2}.

4.7 Fitting Results: a Phenomelogical Model

In this section, I present the results of phenomelogical model fitting to the ASCA XRB data. These models are useful for comparison to the results of other XRB spectrum measurements. My strategy in fitting is first to address the hard (greater than 1 keV) spectrum and then to extend to lower energies (400 eV and greater). In all the fitting, I have subtracted the instrumental background from the sky data. I have excluded data above 6 keV where the internal background becomes comparable to the sky background.

In the 1-6 keV band, I find that a power law of photon index of 1.40 $\pm$0.02 and normalization of $Norm_{hard}$ = 9.3$\pm$0.2 keV s^{-1} cm^{-2} sr^{-1} keV^{-1} at 1 keV describes the data extremely well (χ^2/ν = 326/328). Figure 4-7 shows confidence contours for the fit. Figure 4-8 shows a plot of the ratio of the single power law model to the data. There are two data sets in this figure: one for each SIS. As a completely independent check of this result, the GIS team performed a similar analysis using the Gas Imaging Spectrometers (GIS) also flying on ASCA. From the GIS detectors, they obtain the same result that a single power law component of index about 1.4 describes the 1-10 keV data well (Ishisaki, private communication).

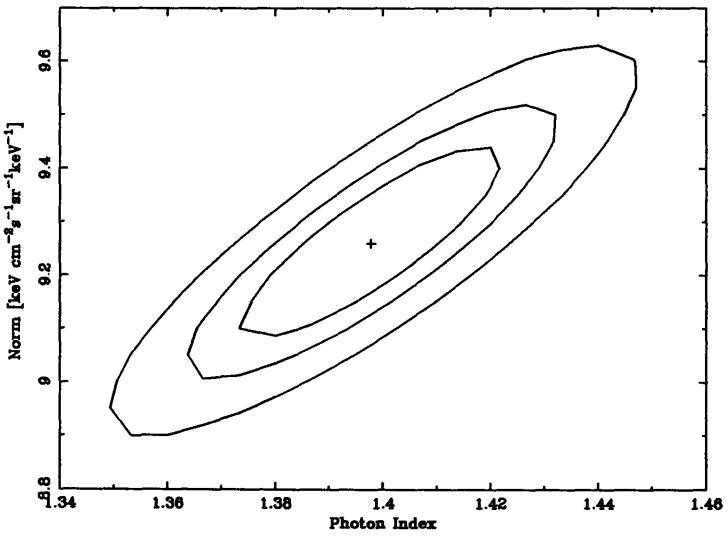

Figure 4-7: Contours of constant likelihood (associated with 67%, 90%, and 99% confidence) contours in the normalization-photon index plane for the 1-6 keV band single power law fit.

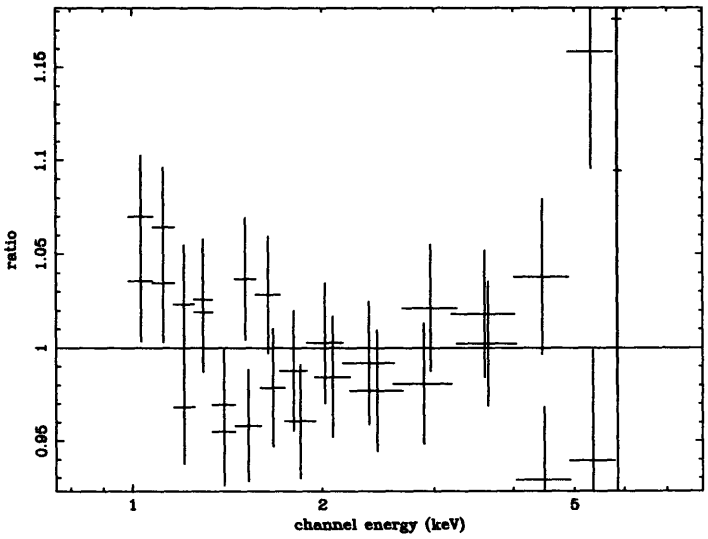

Figure 4-8: The ratio of the XRB data to a power law of index 1.4 The feature above 6 keV may be due to sensitivity to the instrument background. The line like feature at about 1.03 keV may correspond to either iron L or neon K galactic emission.

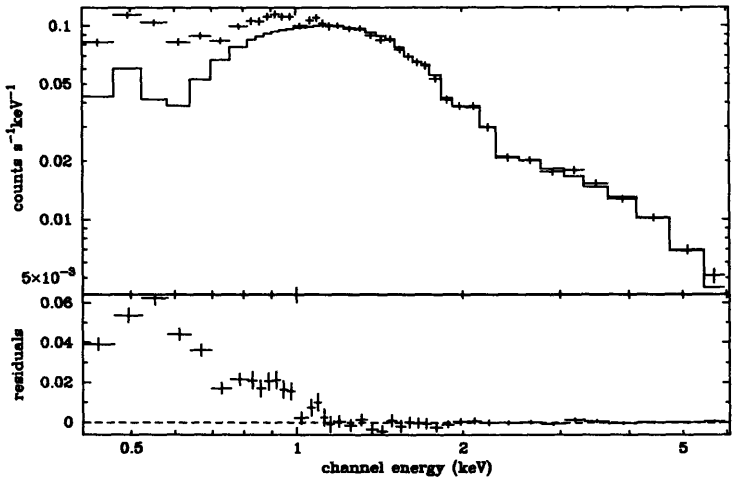

Figure 4-9: The XRB data from 0.4 to 6 keV with the best fitting power law model to the 1-6 keV band. Both the data and the model are convolved through the XRT and CCD response. The excess above the model below 1 keV is due, in part, to galactic emission.

Next, I consider the full SIS energy range down to the 0.4 keV. Figure 4-9 shows the XRB spectrum in both the soft and hard bands with the model fit established in the hard band. The discrepancy between the high energy XRB model and the low energy data is quite clearly seen in the residuals below 1 keV.

I have tried several different models to explain the excess. In each attempt, I have added a new component to the hard power law of the 1-6 keV band. I have listed the models, the parameters, and the χ^2 figures in table 4.3. First, I use simple single component thermal plasma models. These results suggest slightly more complicated multiple component models to explain the soft excess. I describe this progression of fitting below.

As a first attempt to explain the excess, I have added a Raymond-Smith (Raymond and Smith, 1977) thermal plasma component to the hard power-law. First, I force the metal abundance of the plasma to be cosmic, and I obtain a temperature of kT=0.147 ± 0.006 keV, power law photon index (Γ_{hard})=1.47 ± 0.02, and normalization $Norm_{hard} = 9.8 \pm 0.4$ keV s^{-1} cm^{-2} sr^{-1} keV^{-1}. Figures 4-10 and 4-11 show the best fit of this model to the data and the corresponding unfolded model, respectively. When I allow the abundance to become less than 0.1, the fit is improved ($\Delta\chi^2 = 49$). Fitting for the abundance also, I obtain an abundance of 0.05 ± 0.01,a temperature of 0.162 ± 0.007 keV, $\Gamma_{hard} = 1.42 \pm 0.02$, and $Norm_{hard} = 9.4 \pm 0.4$ keV s^{-1} cm^{-2} sr^{-1} keV^{-1}. This fit and unfolded model are shown in figures 4-12 and 4-13, respectively. The dominant features in this model are the oxygen VII and oxygen VIII lines at 574 and 650 eV.

The low metal abundance of a simple Raymond Smith plasma model seems implausible for the Galaxy. To address this concern, I have tried several models where a hard power law and an additional soft component complement a solar abundance Raymond Smith component. I have listed these models and their parameters in table 4.3.

In the first of these multiple soft component models, I have added a second power-law component, while fixing the thermal component to have cosmic abundance. Figure 4-14 shows the cosmic abundance plus two power-law model fit to the data of the SIS. Table 4.3 show the best fit parameters with this model. In this table, the additional soft power law component has a photon index given by Γ_{soft} and a normalization given by N_{soft}. Figure 4-15 shows the unfolded double power law model. Note that the continuum of the Raymond Smith component is parallel to the added soft power law. While this is suspicious, it allows us to "tune" the abundance in our model by adjusting the power law normalization.

I also tried replacing the soft power law with a bremsstrahlung component. The best fit ($\chi^2/d.o.f = 385.8/375$)for the bremsstrahlung component has a temperature of kT=0.3±0.1 keV while the Raymond Smith component had a temperature of kT=0.15 keV and the hard power law had a photon index of 1.40 and normalization of 9.2 keV s^{-1} cm^{-2} sr^{-1} keV^{-1}. This fit and unfolded model are shown in figures 4-12 and 4-13, respectively.

Over our bandpass, the continuum component of all the models I have tried is well approximated by a soft power law. A model which describes the data as well as the best thermal plasma plus power law model is a double power law with lines added at 574, 650, 826, and 920 eV for O VII, O VIII, Fe XVII, and Ne IX, respectively. I chose these line energies firstly since I expected the oxygen lines, and secondly since the residuals to the model suggested lines near tabulated lines. The best fit parameters for this model were $\Gamma_{hard} = 1.4$(fixed), $\text{norm}_{hard} = 9.0 \pm 0.2$ keV s^{-1} cm^{-2} sr^{-1} keV^{-1}, $\Gamma_{soft} = 4.0 \pm 0.2$, $\text{norm}_{soft} = 1.3 \pm 0.3$ keV s^{-1} cm^{-2} sr^{-1} keV^{-1}, 0.574 keV line intensity $= 2.3 \pm 0.3$ *photons* $s^{-1}sr^{-1}cm^{-2}$, 0.65 keV line intensity $= 0.6 \pm 0.15$ *photons* $s^{-1}sr^{-1}cm^{-2}$, 0.826 keV line intensity $= 0.10 \pm 0.07$ *photons* $s^{-1}sr^{-1}cm^{-2}$, and 0.92 keV line intensity $= 0.13 \pm 0.05$ *photons* $s^{-1}sr^{-1}cm^{-2}$.. Since the quoted errors indicate the 90% confidence ranges for the parameters, the oxygen line detections are highly significant. It is interesting to note that the ratio of the oxygen line intensities implies a plasma temperature of kT = 0.3± 0.05 keV (Zombeck, 1990). This temperature is inconsitant with the Raymond Smith fit temperatures.

The best fit double power law (without lines) had $\Gamma_{hard} = 1.24$, $\text{norm}_{hard} = 6.9$ keV s^{-1} cm^{-2} sr^{-1} keV^{-1}, $\Gamma_{soft} = 3.5$, $\text{norm}_{soft} = 2.9$ keV s^{-1} cm^{-2} sr^{-1} keV^{-1} and a reduced $\chi^2 = 2.7$. The poor quality of this fit further supports the model that line emission (presumably due to thermal processes) must make a contribution to the soft XRB.

Table 4.3 summarizes the model fitting.

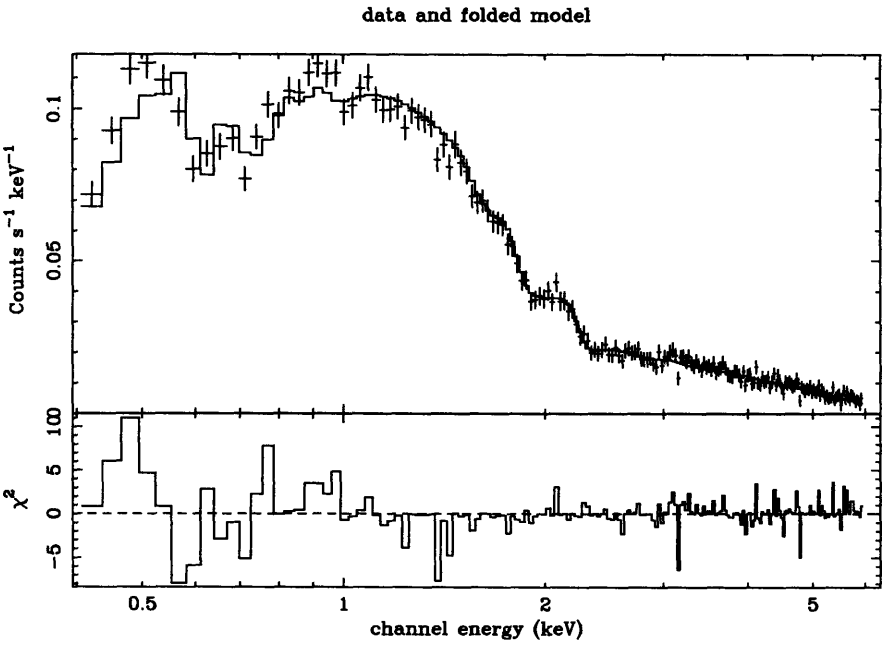

Figure 4-10: The single power law plus solar abundance thermal component fit to the data. The upper panel shows the model folded through the instrument response and compared to the data. The lower panel shows the contributions to chi square of the residuals between the model and the data.

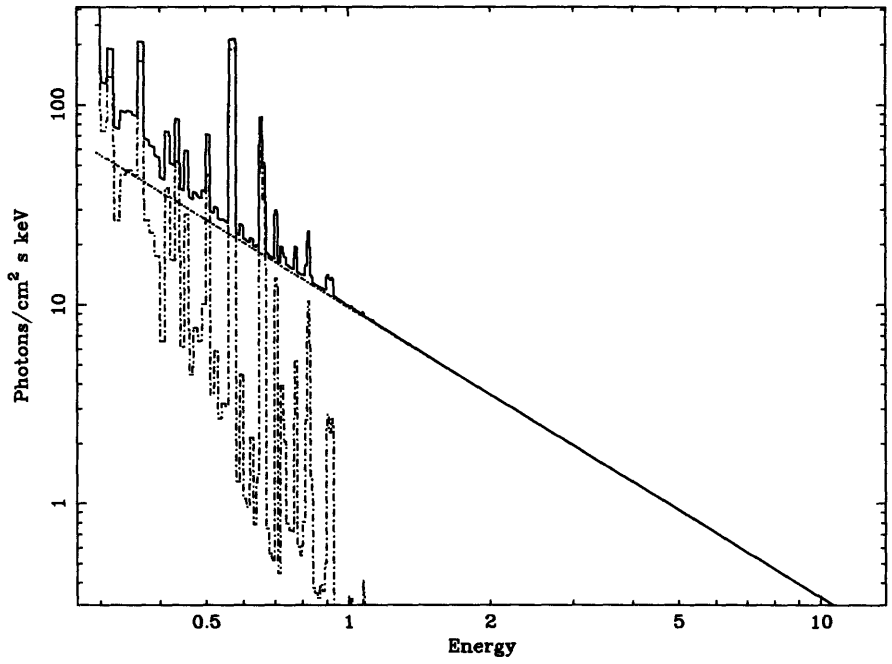

Figure 4-11: The unfolded single power law plus solar abundance thermal component model. The dotted line is the power law component, the dot-dashed line is the Raymond Smith component, and the solid line is the summed model.

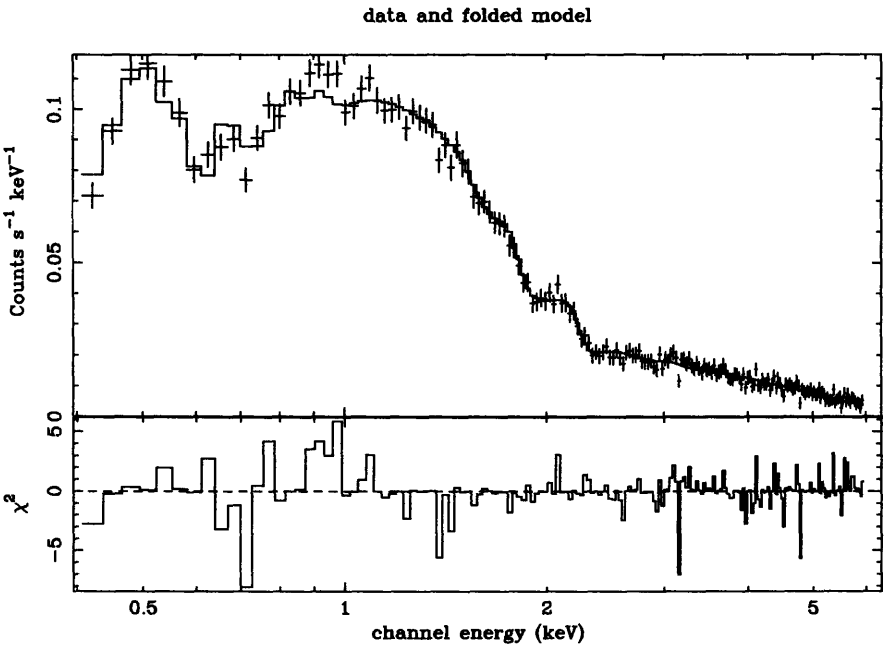

Figure 4-12: The single power law plus low abundance thermal component fit to the data.

ROSAT and Einstein data (Hasinger et al 1993, Wu et al 1992) suggest that the X-ray background steepens in the 2 to 3 keV range. Recent ROSAT results actually resolve out about 60% of the X-ray background at 1 keV into sources with an average photon index of about 2.1-2.2. With ASCA, I find that a single power law of photon index close to 1.4 fits well in the 1-6 keV range. To address this discrepancy, I have tried to see how large a contribution a soft power law component could make to the X-ray background at 1 keV. Without any constraints on the hard power law component, the 90 % confidence upper limits to the contributions of soft power law components with indices Γ_{soft} =1.7, 2.0, 2.5, and 3.0 are 94%, 71%, 43%, and 26 %, respectively, of the XRB at 1 keV. However, at these limits, the hard power law is forced to be much harder than $\Gamma_{hard} = 1.4$, inconsistent with other measurements (Marshall et al, 1980). Furthermore, all of these models exceed the C band (0.25 keV) limit of 30 keV s^{-1} cm^{-2} sr^{-1} keV^{-1} (McCammon et al, 1990) by a factor of about 3-4. Constraining the hard power law component to have an index $\Gamma_{hard} = 1.4$, the 90 % confidence upper limits to the contributions of soft power law components with indices Γ_{soft} =1.7, 2.0, 2.5, and 3.0 are 38%, 23%, 18%, and 16%, respectively, of the XRB at 1 keV. As an alternate approach, I have fixed a soft power-law component with photon

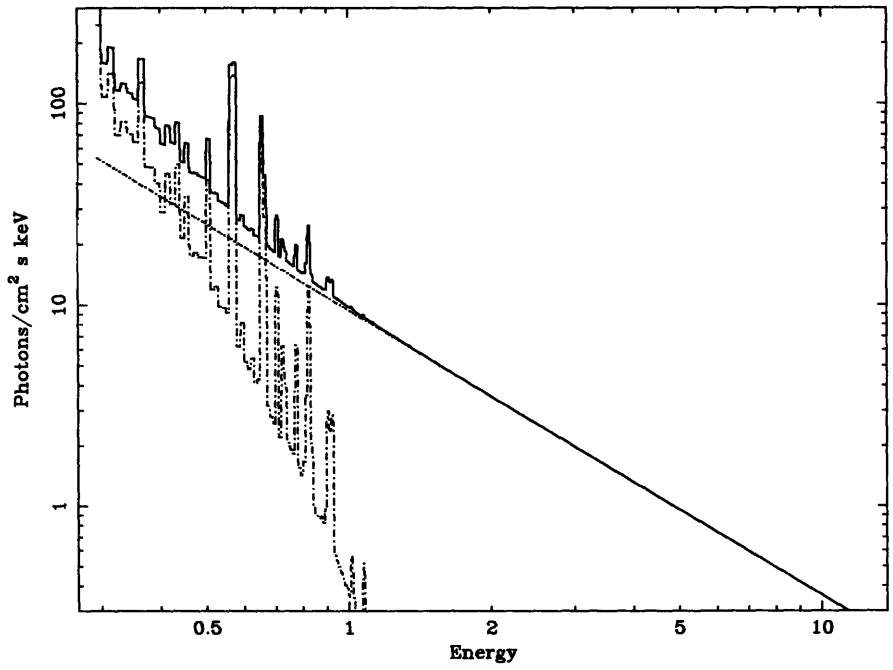

Figure 4-13: The unfolded single power law plus low abundance thermal component model.

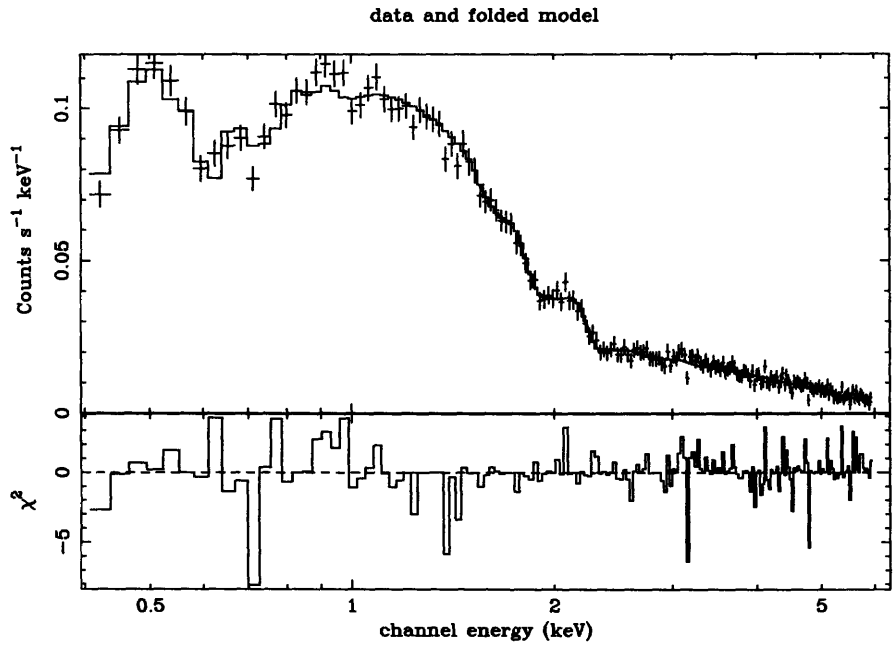

Figure 4-14: Two power laws plus a thermal component fit to the data.

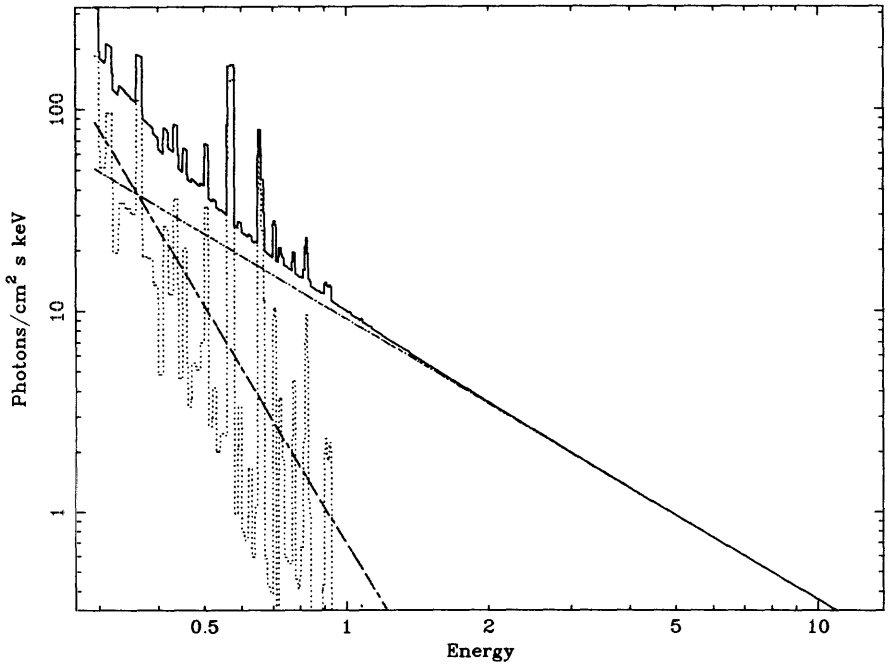

Figure 4-15: The unfolded two power laws plus a thermal component model.

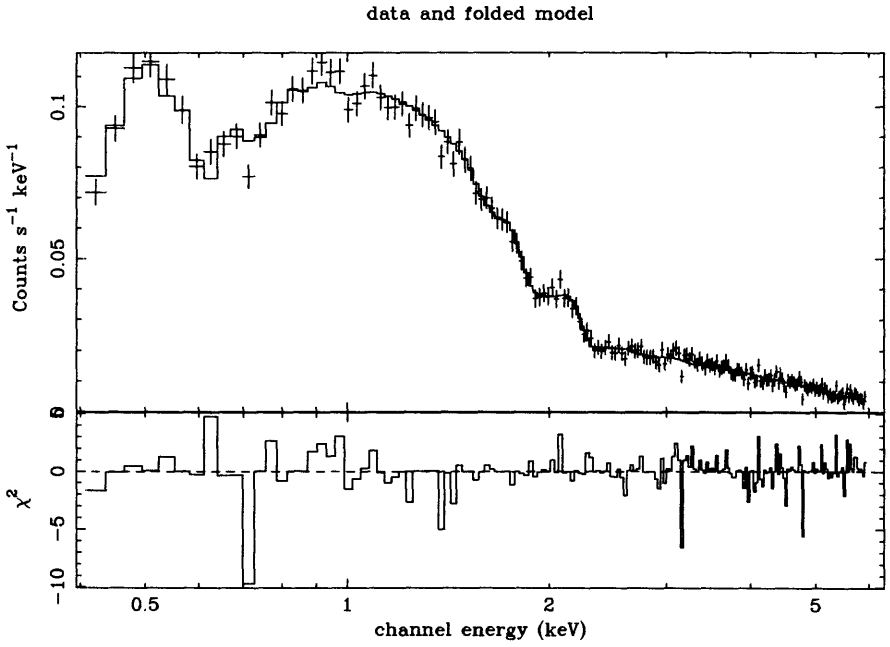

Figure 4-16: The single power laws plus bremsstrahlung plus solar abundance thermal component fit to the data.

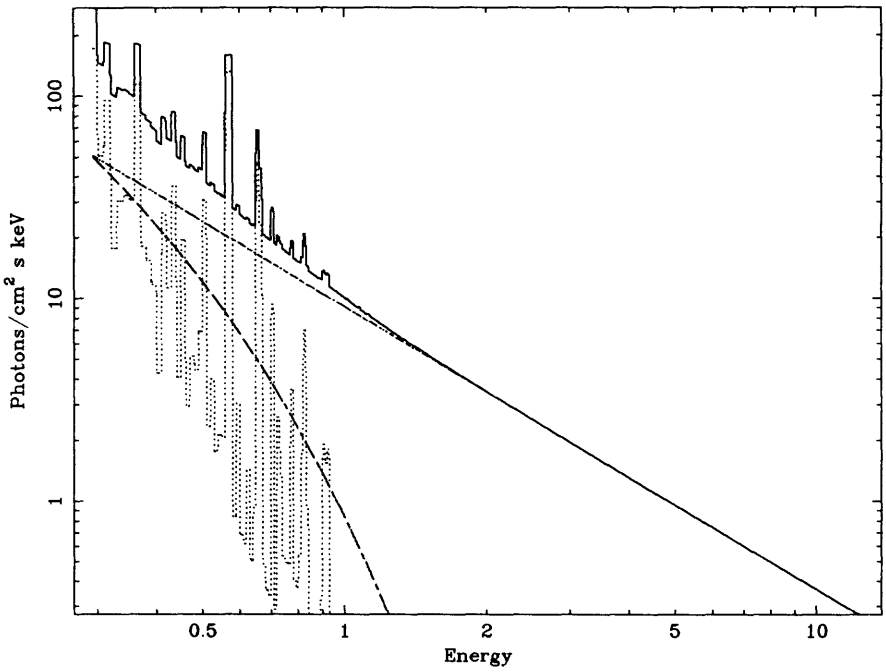

Figure 4-17: The unfolded single power laws plus bremsstrahlung plus solar abundance thermal component model.

index 2.1 and normalization equal to 30 keV s^{-1} cm^{-2} sr^{-1} keV^{-1} at 0.25 keV (or 17% of the measured background at 1 keV). To this soft power law component, I add a hard power law component and a solar abundance Raymond-Smith component. The best fit for the hard component and the thermal component in this case is: $\Gamma_{hard} = 1.39 \pm 0.03$, $\mathrm{Norm}_{hard} = 7.8 \pm 0.2$ at 1 keV, kT=0.15 $\pm$ 0.01 keV.

Table 4.3: 0.4-7 keV Fitting Results

Model	Parameters	χ^2/ν
Power Law + Raymond Smith	kT = 0.147 ± 0.006 keV, abundance=1 (fixed) $\Gamma_{hard} = 1.47 \pm 0.02$, $N_{hard} = 9.8 \pm 0.4$ keV s^{-1} cm^{-2} sr^{-1} keV^{-1}	449.3/376
Power Law + Raymond Smith	kT = 0.162 ± 0.007 keV, abundance=0.05 ± 0.01 $\Gamma_{hard} = 1.42 \pm 0.02$, $N_{hard} = 9.4 \pm 0.4$ keV s^{-1} cm^{-2} sr^{-1} keV^{-1}	400.7/375
2× Power Law + Raymond Smith	kT = 0.15 ± 0.01 keV, abundance = 1 (fixed) Γ_{hard}=1.40 (fixed) $N_{hard} = 9.0 \pm 0.2$ keV s^{-1} cm^{-2} sr^{-1} keV^{-1} $\Gamma_{soft} = 3.8 \pm 0.5$, $N_{soft} = 0.83 \pm 0.5$ keV s^{-1} cm^{-2} sr^{-1} keV^{-1}	394/374
Bremsstrahlung + Power Law + Raymond Smith	$kT_{Brems} = 0.3 \pm 0.1$ keV, $kT_{RS} = 0.15 \pm 0.01$ keV, abundance=1 (fixed) Γ_{hard}=1.40 (fixed) $N_{hard} = 9.2 \pm 0.2$ keV s^{-1} cm^{-2} sr^{-1} keV^{-1}	385.8/375
Power Law + Power Law + Line + Line + Line + Line	Γ_{hard}=1.40 (fixed) $N_{hard} = 9.0 \pm 0.2$ keV s^{-1} cm^{-2} sr^{-1} keV^{-1} $\Gamma_{soft} = 4.1 \pm 0.5$ $N_{soft} = 1.35 \pm 0.8$ keV s^{-1} cm^{-2} sr^{-1} keV^{-1} Fe XVII flux = 0.10 ± 0.07 photons s^{-1}cm^{-2}sr^{-1} Ne IX flux = 0.13 ± 0.05 photons s^{-1}cm^{-2}sr^{-1} O VIII flux = 0.74 ± 0.15 photons s^{-1}cm^{-2}sr^{-1} O VII flux = 2.36 ± 0.33 photons s^{-1}cm^{-2}sr^{-1}	387.4/373

4.7.1 Summary of the Phenomelogical Fitting

ASCA confirms the well-established power-law slope of the XRB in the 2-10 keV band. A new result from ASCA is that there is no steepening of this power law in the 1-3 keV range. Thus a single power law with index of about 1.4 fits the entire 1-6 keV range.

Below 1 keV, we see an excess which is due in part to the hot interstellar medium in which the solar system resides (Tanaka et al, 1977, Inoue et al 1979, Cox 1987, McCammon et al 1990). With ASCA we find a plasma with a temperature of about 0.16 keV which is approximately consistent with earlier sounding rocket flights and ROSAT results (Inoue et al 1979, McCammon et al 1990, Hasinger 1992, Snowden et al, 1994). In our bandpass, the thermal component is dominated by emission due to O-VII and O-VIII on top of a continuum. We find that the addition of a soft power-law with slope similar to the continuum of the thermal component allows us to vary the abundance of the thermal component while maintaining a good fit, since the equivalent width of the oxygen lines against the thermal continuum is a measure of the abundance. This softer power-law may have an extragalactic origin. Perhaps it is due to a summation of many individual sources as suggested by recent ROSAT results (Hasinger 1992). However, the soft power-law is much steeper than would be expected from AGN (Hasinger et al 1993). Alternately, it may be the case that the low abundance of the single power-law plus thermal component model reflect some state of non-equilibrium of the local interstellar plasma.

Figure 4-18 shows the unfolded ASCA data compared to data of other missions. There is a considerable spread in results for the intensity of the XRB in the 1 to 3 keV range. The discrepancy has multiple possible explanations. Some are instrumental in nature, while others are more philisophical in nature. While I am not an expert for any of the other instruments which provided the data of other missions, I put forward the possibility that the discrepancy in fluxes may be due, in part, to a blending of the bright oxygen line emission from lower energy channels into the 1-3 keV channels. This is a possibility for the other mission results since the energy resolution of the detectors used is relatively poor ($\sim$30% as compared to $\sim$10%). Another possible solution to the discrepancy is the "bright source" bias suggested by Dan Macammon (private commmunication) and Gunther Hasinger (Hasinger, 1995). Here, the discrepancy reduces to the question, "what does one consider the background?" As astronomers make X-ray observations with increasingly

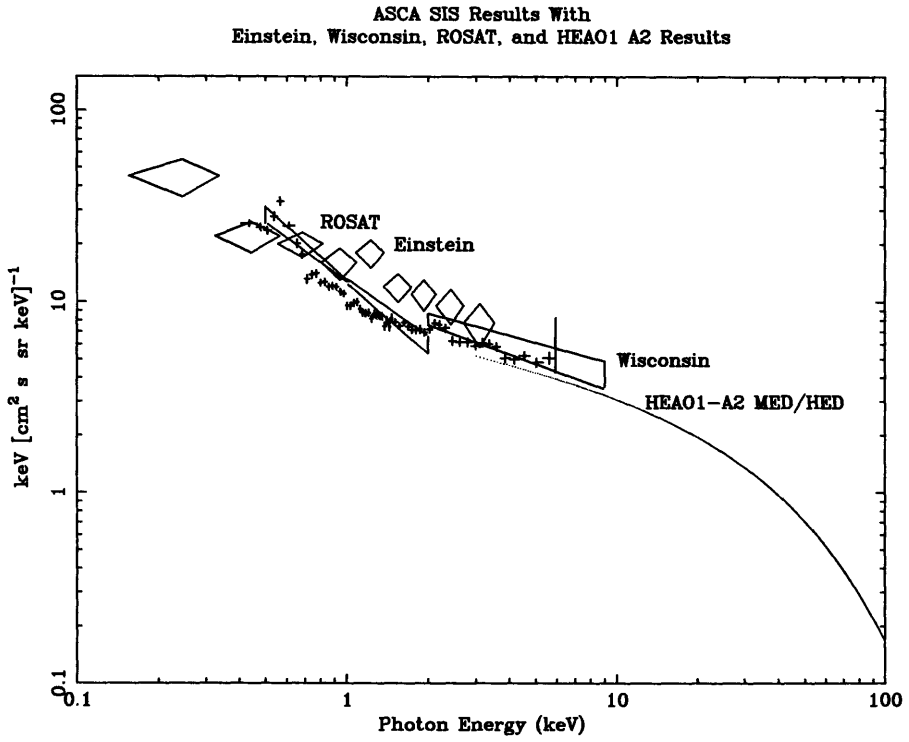

Figure 4-18: The unfolded ASCA data (crosses) with results from HEAO1-A2, Wisconsin, ROSAT, and the Einstein IPC.

finer angular resolution, they resolve out sources in what was once considered background. Typically, XRB researchers will exclude sources brighter than an arbitrary minimum flux from their background data set. Often, XRB data sets are drawn from nearly empty fields. Clearly, the choice of field will affect the minimum source exclusion flux. This type of bias could explain some of the discrepencies. A joint analysis of various fields with multiple observatories would eliminate this bias.

4.8 Constraints on an AGN synthesis model to the XRB

Above, we showed that a single power law of photon index 1.4 and normalization 9 keV s^{-1} cm^{-2} sr^{-1} keV^{-1} fit the data extremely well in the 1-6 keV band. To emphasize this, figure 4-8 shows the ratio of such a power law to the data. No spectral features (to the level of about 5%) are seen. There is marginal evidence for a feature near 6 keV- but this may be contaminated by an instrumental iron line. This result immediately rejects several of the possible models presented in Matt and Fabian (1994). In particular, the ASCA result rejects models A1, A10, A16, and A17 of Matt and Fabian (1994). See figure 4-19. However, we can put upper limits on parameters in the AGN synthesis model. In this section, we describe a model to fit the extra galactic XRB based on the unified Seyfert 1 and Seyfert 2 model. The model is a simplification of the models which Matt and Fabian explored. We then apply this model to our data and see what constraints can be made. We can infer typical parameters for AGN which would make up the XRB in this model. We also can obtain information on the AGN luminosity evolution function. As we will see below, ASCA data alone are not sufficient to completely describe the AGN synthesis model. We will show how other data can complement the ASCA results to help explain the XRB.

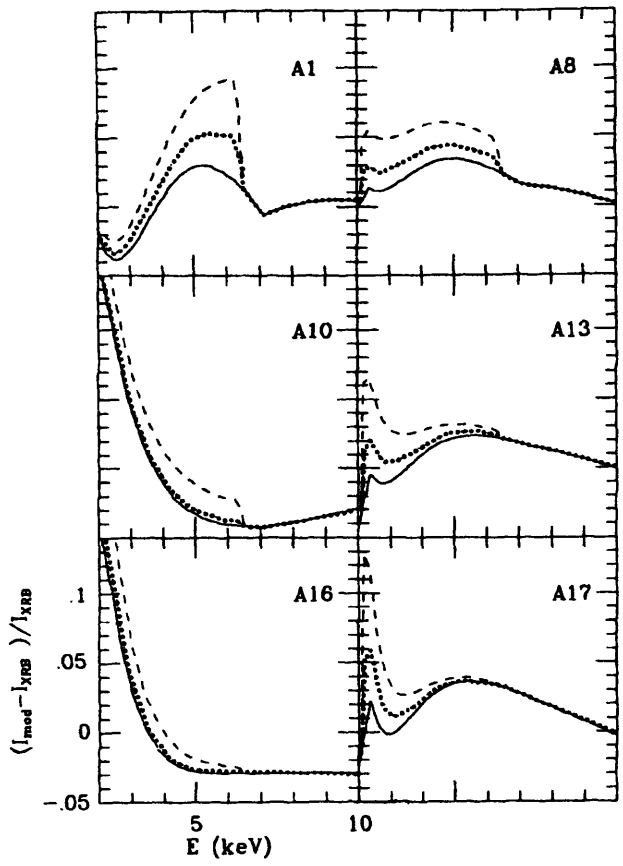

Figure 4-19: This is figure 3 from Matt and Fabian (1994). These are the fractional residuals of various Seyfert 1 and Seyfert 2 XRB synthesis models to a power law with photon index 1.4. See Matt and Fabian (1994) for details. Note that the ASCA data (particularly figure 4-8) rules out models A1, A10, A16, and A17. Figure courtesy of G. Matt.

4.8.1 The Source Contribution Model

The model of the sources we use to make the XRB is similar to the models used by Matt and Fabian (1994) and Comastri et al (1995). Namely, the intrinsic X-ray emission of all the sources is assumed to be a broken power law with low- and high- energy indices α_1 and α_2 respectively, and a break energy E_b (keV) so that the intrinsic photon spectrum is given by

$$\begin{aligned} P(E) photons\ cm^{-2}\ s^{-1}\ keV^{-1} &= A(\frac{E}{E_b})^{-\alpha_1} \qquad E \leq E_b, \\ &= A(\frac{E}{E_b})^{-\alpha_2} \qquad E > E_b. \end{aligned} \tag{4.3}$$

In order to reap the maximum amount of information from the spectral fitting, we must keep the number of free parameters in the final model to a minimum. In this light, we make the assumption that all the sources, whether they are Seyfert 1, Quasars, or Seyfert 2, have the same three parameters describing their intrinsic spectrum(equation 4.3). This is the same underlying assumption used in the unified AGN model (Antonucci 1993). In our assessment of the ASCA fits, we will make use of observational data on the parameters of the instrinsict spectral model.

We apply an absorbing column N_H to a fraction f of the intrinsic spectrum in equation 4.3. This absorption is local to the individual source. We will show how f is related to the number of observered Seyfert 1 and Seyfert 2 galaxies. We model the X-ray transmission, $T(E, N_H) = e^{-N_H \sigma(E)}$, through this column, taking into account only photoelectric absorption. Future work would be improved by taking into account the first Compton scattering using approximations such as in Yaqoob, Ptak and Serlemitsos (1995). Again to limit our number of parameters, we use single value of the column density as opposed to a distribution as in Matt & Fabian.

Thus the model source spectrum is

$$F(E) = P(E)[(1 - f) + fT(E, N_H)] \tag{4.4}$$

We add an iron K line (6.5 keV in the source rest frame) of equivalent width W_{Fe} to this spectrum to account for the observation of iron lines in AGN (Pounds *et al*, 1990).

We then integrate the source spectrum over redshift (see e.g. Boldt 1987) assuming pure luminosity evolution of the form

$$\begin{aligned} B(z) &= B_{loc}(1+z)^{\gamma_{evol}} \quad z < z_{max} \\ &= 0 \quad z > z_{max} \end{aligned} \tag{4.5}$$

where B_{loc} is the local 2-10 keV volume emissivity ($ergs\ s^{-1}\ Mpc^{-3}$). The normalization factor, A, in equation 4.3 is buried in B_{loc}.

For spectral fitting of the ASCA data there are thus a total of nine free parameters, namely, α_1, α_2, E_b, N_H, f, W_{Fe}, γ_{evol}, z_{max}, and B_{loc}. The limited bandpass of the ASCA data reduces our sensitivity to α_2 and E_b for reasonable assumptions. Note that when fitting the ASCA data alone we will only be using data up to ~ 6 keV. In this case, α_2 and E_b will not contribute to the fitting as long as sources beyond $z_{max} = (E_b/6) - 1$ do not contribute to the XRB. For $E_b = 50$ keV, $z_{max} < 7.3$. For AGN spectra, the observational situation is that E_b and α_2 are poorly determined (see e.g. Madejski et al 1994; Zdziarski et al 1995) but Matt & Fabian find that $\alpha_2 \sim 2 - 3$ and $E_b \sim 50 - 100$ keV are required to fit the broad hump in the XRB which peaks at ~ 30 keV(figure 4-1). This is consistent with the poorly determined AGN data. Thus, there are seven free parameters in the model when applied only to ASCA data.

Seven parameters is still too many to fit the seemingly featureless hard XRB data of ASCA. In the sections below, we will look at selected slices in the seven dimension parameter space. We will show confidence contours around the best fit in these slices. Next, we will use some independent constraints to limit the parameter space. These constraints include the measured values for B_{loc}, γ_{evol}, z_{max}, and the relative number of Seyfert 1 and Seyfert 2 galaxies. In addition, there is a wealth of data on the properties of individual AGN which limit the acceptable ranges for α_1, α_2, E_b, N_H, and W_{Fe}. These constraints will modify the confidence contours of the parameters around their best fit. We will show examples of how to check consistancy between independent constraints by looking at the overlap of the constraints with the ASCA data confidence contours.

4.8.2 The Fitting of the AGN Synthesis Model to the ASCA Data Without Independent Constraints

Using our AGN synthesis model, we fit the XRB in the 1.2 to 6 keV range. Going much higher in energy compromises our results to instrument background systematics. Extending to lower energies subjects our results to galactic XRB contamination. To limit the amount of parameter space explored, we step through a finite set of (z_{max}, γ_{evol}) pairs and plot confidence contours in the covering fraction- soft power law index plane. We fit for covering fraction, soft power law photon index, N_H, and local volume emissivity. In all our results shown here, we take $H_0 = 50$ and $q_0 = 0.5$.

In figure 4-20, we have arranged the confidence contours such that the evolution index increases from left to right and z_{max} increases from top to bottom. The evolution index varies from 2.5 to 3 and z_{max} ranges from 2 to 3.5. I chose these ranges since they are roughly consitant with known properties of AGN evolution. In this figure, we have fixed the iron K line to have an equivalent width of 200 eV and we have put no constraints on the local volume emissivity.

In each panel of figure 4-20, the reduced χ^2 of the best fit has an acceptable value. There are a few additional things to notice in this figure. First, the confidence contours and the best fits do not vary too much as the evolution index varies from 2.5 to 3. Second, there is a very strong difference in the confidence contours at $z_{max} = 2$ and $z_{max} > 2$. In particular, the solution space of acceptable fits at $z_{max} = 2$ are limited to the uninteresting case where the power law index of the source spectra approaches the power law index of the 1-10 keV XRB spectrum. For $z_{max} > 2$, the solution space extends into the interesting range where source spectra have power law indices similar to those of the observed AGN spectra.

To study our dependence on the iron line, we examined how much it could vary. The upper limits on the iron K equivalent width are 600 eV, 600 eV, 400 eV, and 320 eV for $z_{max} = 2$, 2.5, 3, and 3.5, respectively. There is a slight dependence in the iron equivalent width with evolution index such that it decreases for stronger evolution. Note that these are consistent with George & Fabian's (1991) "back of the envelope calculation". In their rough estimate of the iron equivalent width, George and Fabian made the following simple argument. Assume that all the iron Kα fluorescence photons made within an optical depth of the surface escape the illuminated matter. The impinging photons which could participate

in this are those which stop within one iron Kα optical depth of the material. Examination of a photoabsorption cross section graph for solar abundance material indicates that the photons which can do this are within 1 keV of the iron K edge. Since the fluorescent yield of iron is 0.3, and we expect half of the produced photons to go in the observers direction, the expected equivalent width can be at most 1 keV $\times$ 0.3 $\times$ 0.5 = 0.15 keV.

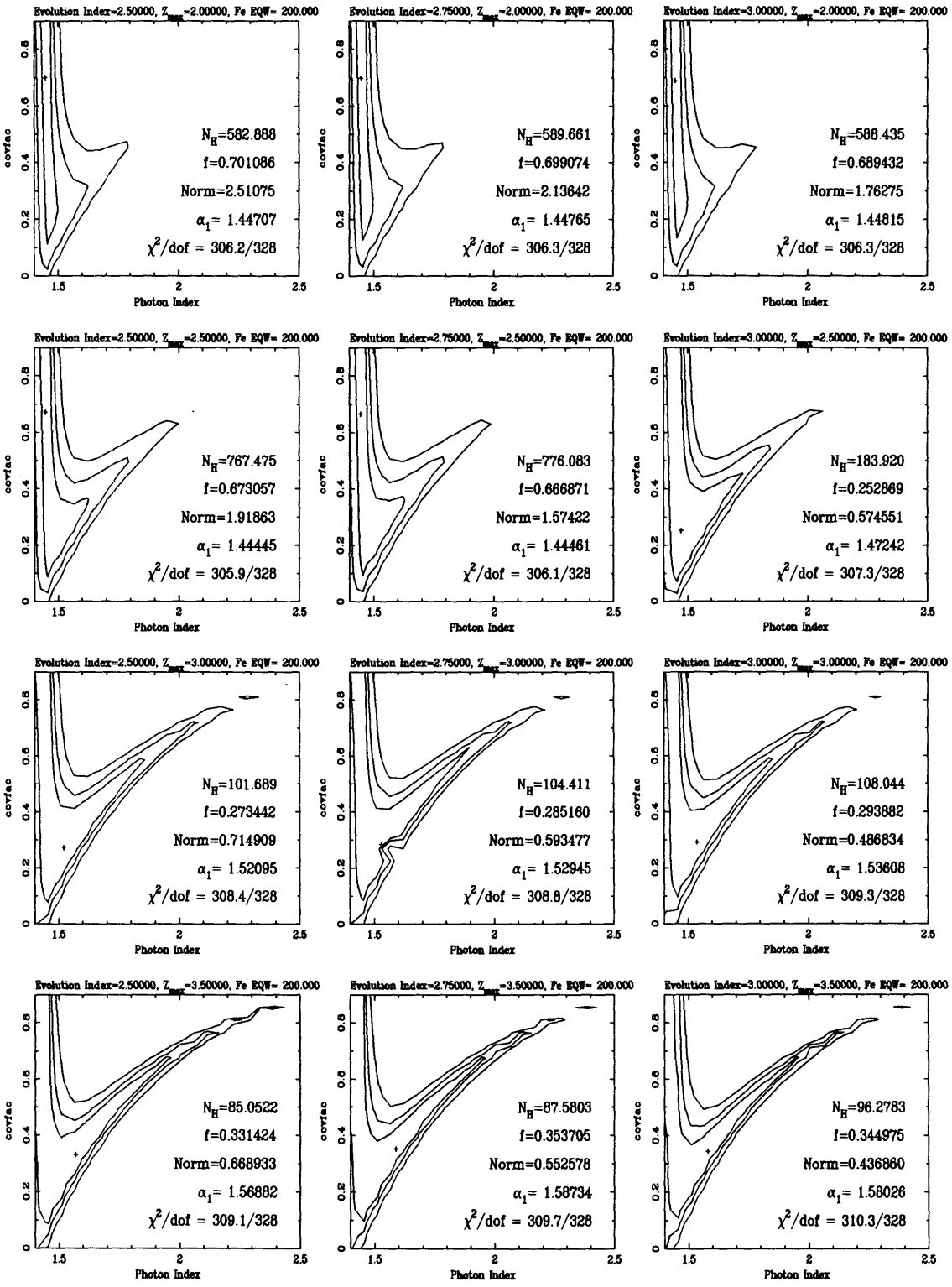

Figure 4-20: AGN source model fit results for the 1.2-6 keV Band where the iron K line equivalent width has been fixed at 200 eV. The volume emissivity is unconstrained. The fit parameters in each panel correspond to the best fit (indicated by the cross). "Norm" is B_{loc} in units of 10^{39} h_{50} $ergs$ s^{-1} Mpc^{-3}. The contours show 67%, 90%, and 99% confidence levels.

4.8.3 Additional Independent Observational Constraints

We can further limit our parameter space if we use some AGN observational constraints. We can also check consistency between various models and observations. Observations of individual AGNs limit acceptable instrinsict spectral properties such as the break energy and power law indices. Also, we can obtain typical ranges of values for the column density in Seyfert 2s. If simple assumptions can be made about the contribution of scattered radiation, then the covering fraction f in our model can be converted to a ratio of Seyfert 2 to Seyfert 1 galaxies, which, in principle, is something which can be independently observed. However, the observational data on Seyfert 2 to Seyfert 1 number densities is plagued by selection bias due to the difficulties associated with detecting Seyfert 2 galaxies. Catalog data such as compiled by Boyle *etal* (1994) and Piccinotti *etal* (1982) can be used to constrain our estimates of AGN luminosity evolution parameters Z_{max}, and γ_{evol}. Each of these constraints will be discussed below in regards to the ASCA data.

The Local Volume X-Ray Emissivity

An important observational quantity is the local universe X-ray volume emissivity. This quantity comes from the local X-ray luminosity function $\Phi(L_X)$ which is the number density per cubic megaparsec of sources per unit luminosity with luminosity L_X. The luminosity L_X of an object is the energy output of the object in ergs s$^-$1 within a specified energy band. For most of the discussion here, we assume this band is 2-10 keV. The local volume emissivity is then given by:

$$B_{loc} = \int dL_X L_X \Phi(L_X) \tag{4.6}$$

Miyaji (1994) took Grossan's (1992) luminosity function for local AGN and computed what the local volume emissivity would be.

For the present analysis, we constrain the volume emissivity to be less than the upper limit, $5.5 \times 10^{38} h_{50} ergs^{-1} Mpc^{-3}$, found by Miyaji (1994). In figures 4-21 and 4-22 we show the resulting contours where the iron equivalent width has been fixed at 0 and 200 eV respectively. Note that this severely limits the phase space of models shown in figure 4-20. In particular, models where the evolution index is 2.5 or less or where z_{max} is less than 2.5 are rejected due to large χ^2 values.

Figure 4-23 shows our confidence contours in the Z_{max}- γ_{evol} plane for models with several selected low energy power law index varying from 1.7 to 2.0 and the volume emissivity constrained as before.. We put strong lower limits on the evolution index and Z_{max}, depending on the assumed source power law index. We also put upper limits on the evolution index. Note that with ASCA data alone, we need to be careful when using large Z_{max} values as the spectrum above the break energy in the source will start to come into the ASCA bandpass. To do this properly, higher energy data (such as from the A2 experiment) would be required for a joint fit.

The rest frame spectrum of a composite source with the best fit parameters corresponding to the $z_{max} = 3.5$ and the $\gamma_{evol} = 3.0$ solution shown in figure 4-22 is shown in figure 4-24. This spectrum is a weighted sum of the typical Seyfert 1 and Seyfert 2 galaxies shown in figure 4-25. The weighting is (1-f) for the Seyfert 1 spectrum and f for the Seyfert 2 spectrum. In this model, the covering fraction (f) is 0.38, the neutral hydrogen column density (N_H) is 9.3×10^23 cm$^-2$, the soft power law photon index of the intrinsic source spectrum (α_1) is 1.6, the iron K line equivalent width is 200 eV, and the local volume emissivity (B_{loc}) is $4.56\times10^{38}h_{50}ergs^{-1}Mpc^{-3}$. The fractional contribution of these sources with redshift for the same model is shown in figure 4-26. Notice that except for small scale fluctuations, the AGN at different redshifts contribute nearly equally. This is due primarily to the fact that the evolution index in the equation for B_{loc} nearly cancels the cosmological rate of volume decrease (ie volume$\sim (1+z)^{-3}$ in standard cosmologies).

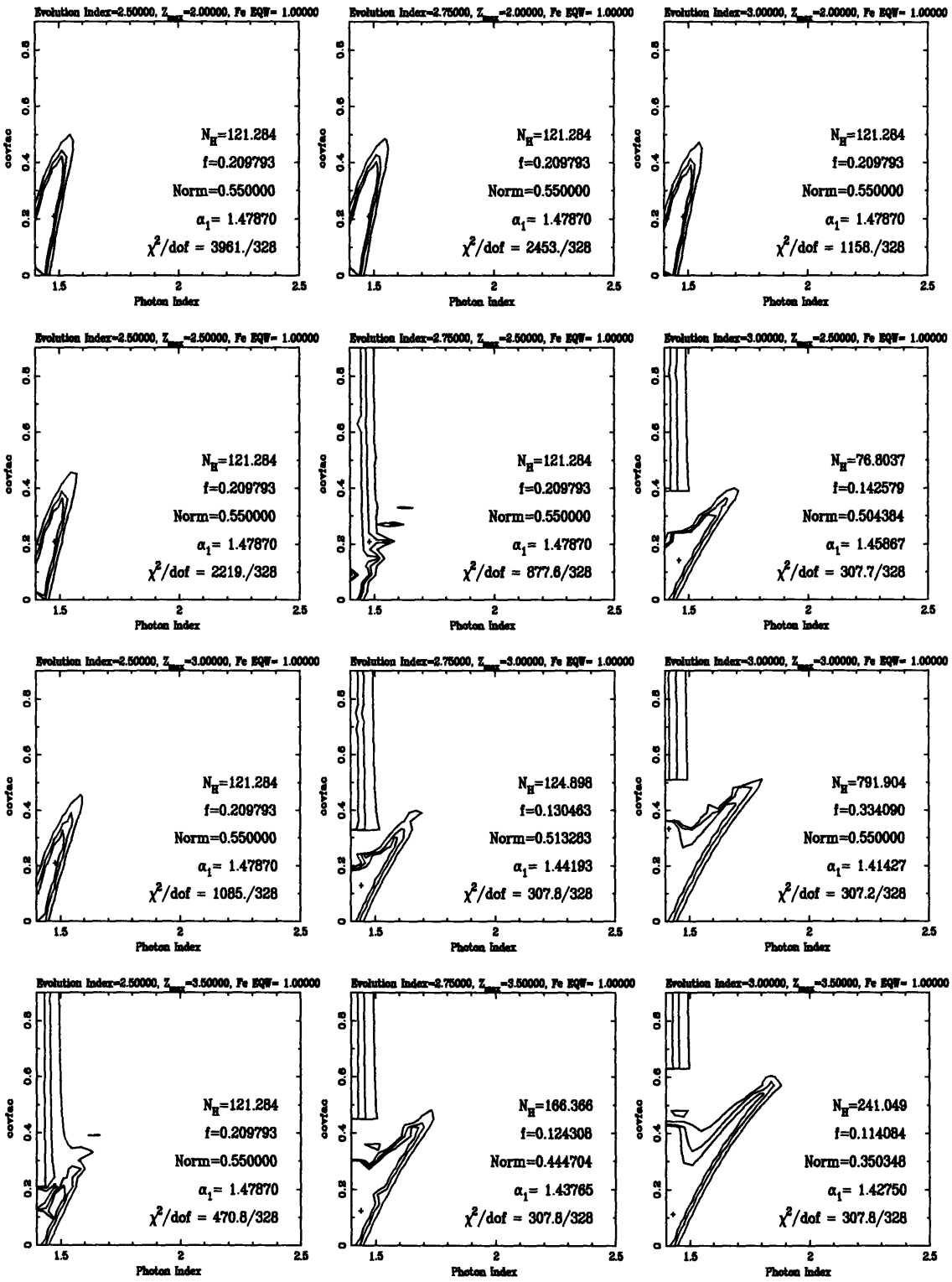

Figure 4-21: AGN source model fit results for the 1.2-6 keV Band where the iron K line equivalent width has been fixed at 0 eV. The volume emissivity is constrained to Miyaji's upper limit. The fit parameters in each panel correspond to the best fit (indicated by the cross).

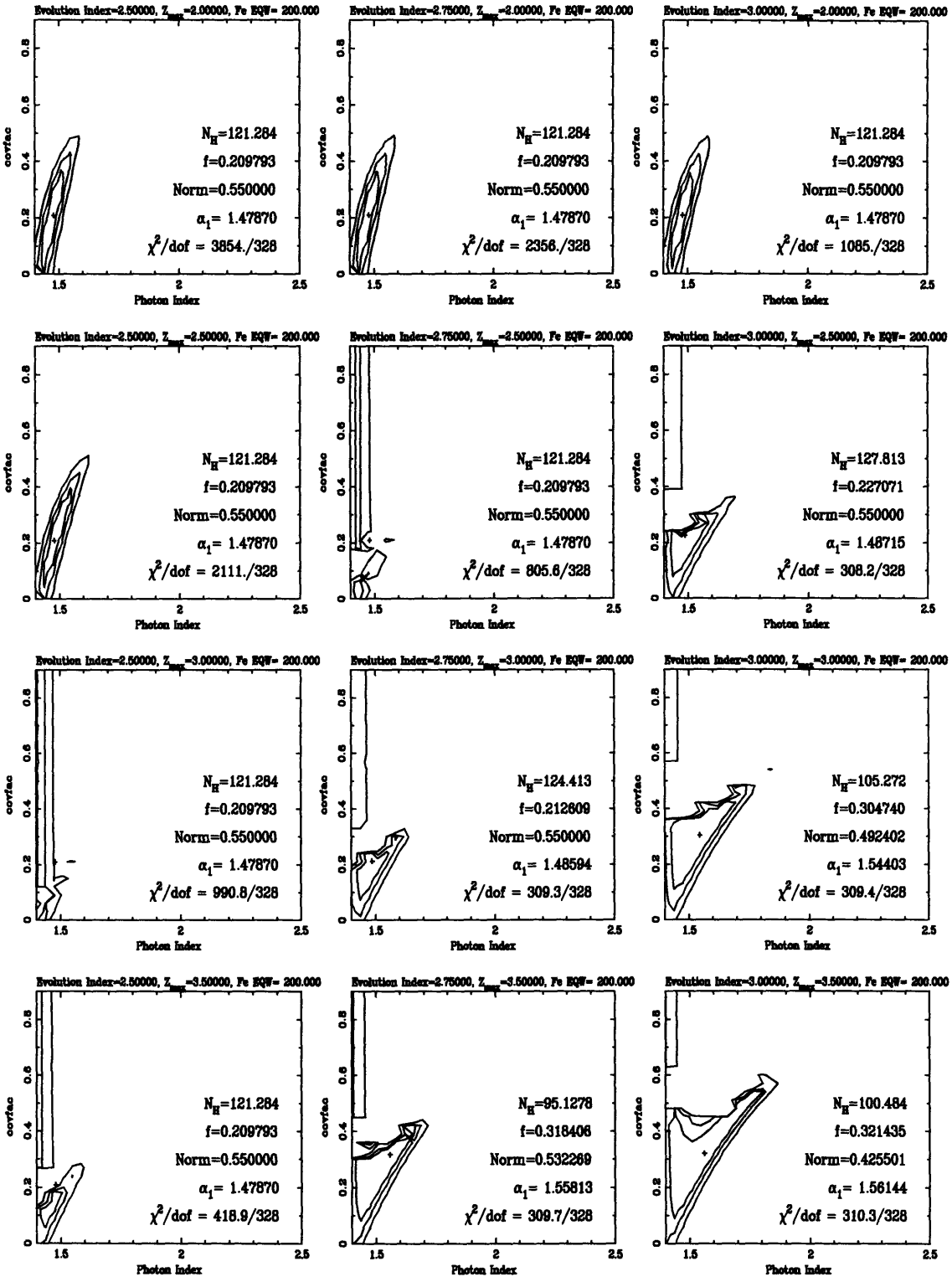

Figure 4-22: AGN source model fit results for the 1.2-6 keV Band where the iron K line equivalent width has been fixed at 200 eV. The volume emissivity is constrained to be less than Miyaji's upper limit. The fit parameters in each panel correspond to the best fit (indicated by the cross).

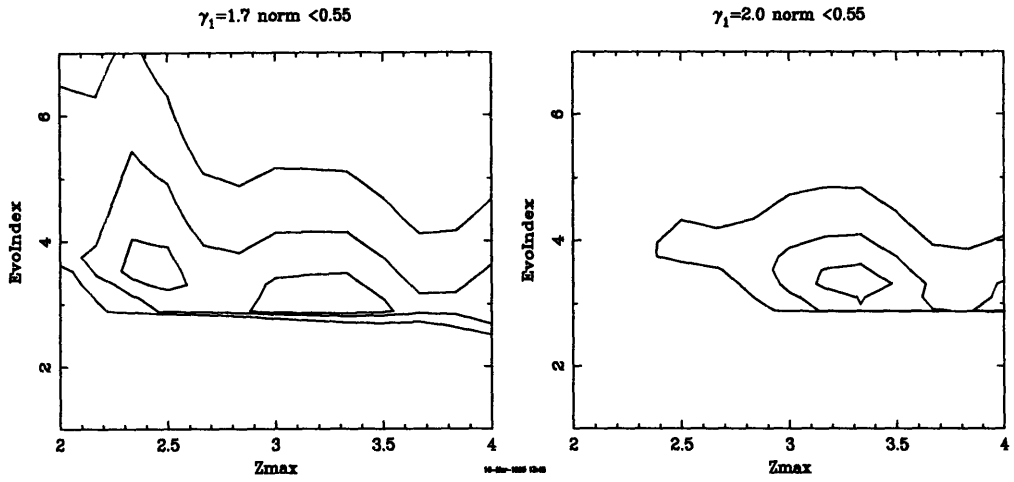

Figure 4-23: 67%, 90%, and 99% confidence contours for the luminosity evolution parameters for various assumptions on the source intrinsic power law index. The left hand figure has α_1=1.7 while the right hand figure has α_1=2.0. Both have B_{loc} constrained to be less than Miyaji's upper limit.

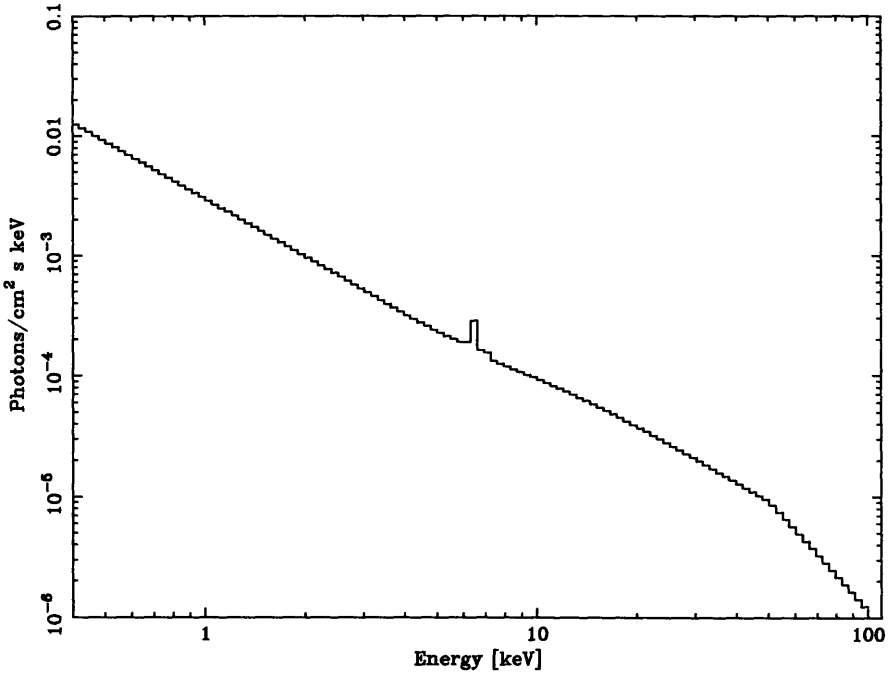

Figure 4-24: The rest frame spectrum of a composite source implied by model in the lower right hand panel of figure 4-21.

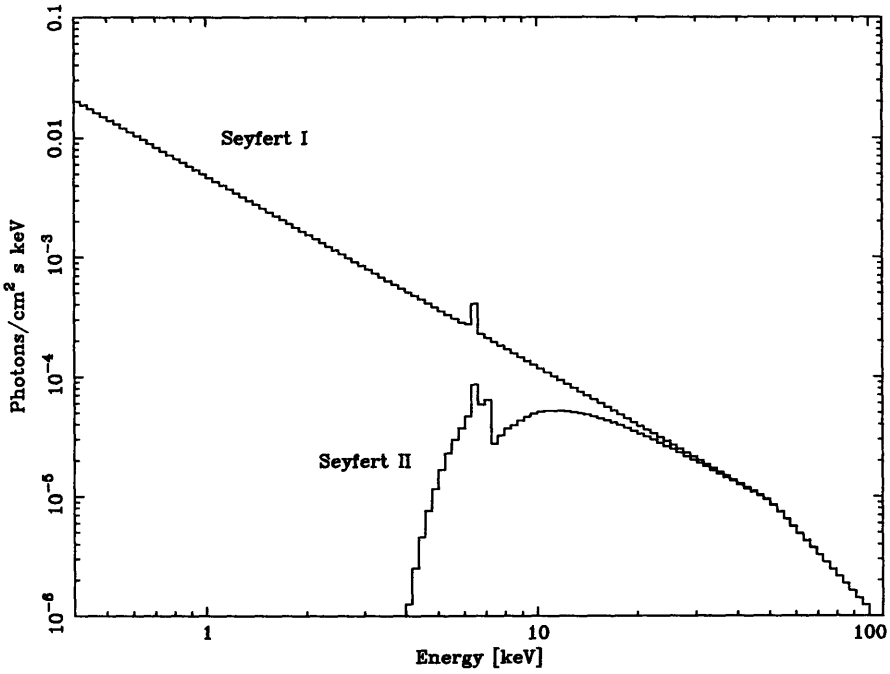

Figure 4-25: The rest frame spectrum of the typical Seyfert 1 and Sefert 2 galaxies implied by model in the lower right hand panel of figure 4-21.

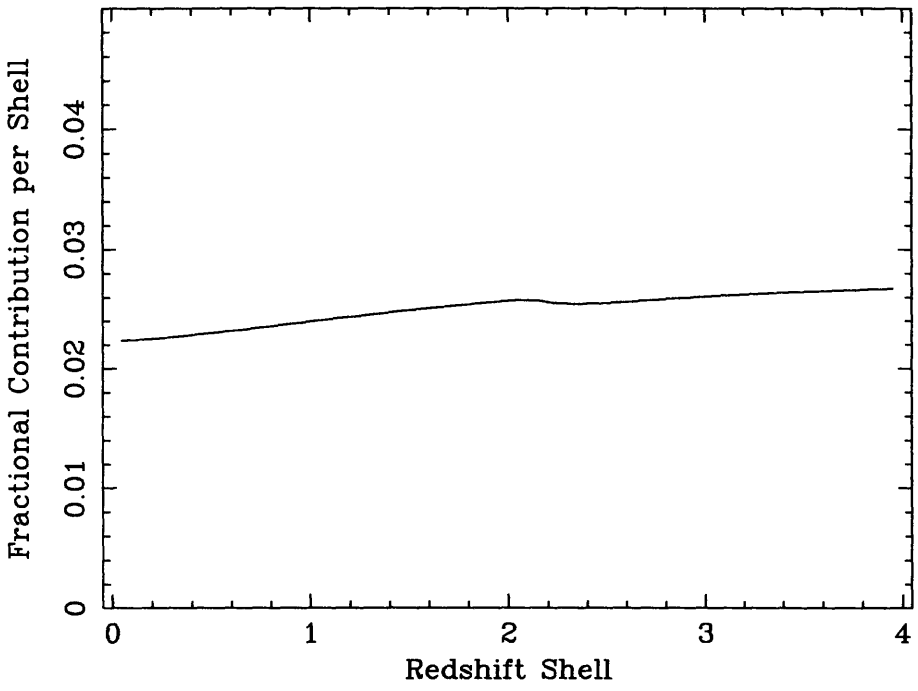

Figure 4-26: The fractional contribution with redshift of sources with spectrum in figure 4-23 using the model of the lower right hand panel of figure 4-21. The wiggle at about a redshift of 2 corresponds to the iron line being shifted outside of the 2-10 keV band used to calculate the flux.

Intrinsic AGN spectra, Absorption, and Covering Fraction

For α_1, Seyfert 1s and radio-quiet quasars are likely to have $\alpha_1 \sim 1.9 - 2.0$ but individual objects do show a spread down to $\alpha_1 \sim 1.5$ (see. e.g. Nandra & Pounds 1994). Seyfert 2s tend to have $\alpha_1 \sim 1.5 - 1.8$ (e.g. Awaki et al 1991) and radio-loud quasars $\alpha_1 \sim 1.7$ (Zdziarki et al 1995). The "nominal" α_1 index for AGN is 1.7±0.15 (Mushotzky 1984, Turner & Pounds 1989).

If we take one of our volume emissivity limited contour plots like figure 4-22 and project onto the covering fraction dimension where α_1=1.7±0.15 lie, then we can estimate the Seyfert 2 to Seyfert 1 number ratio, r_{21} using the expression:

$$r_{21} = \frac{f}{1-f} \tag{4.7}$$

Figure 4-27 shows an example of this projection procedure for the contour plot of the lower right hand panel of figure 4-22. In this figure, the covering fractions for AGN with the nominal soft power law index of 1.7 spans from f=0.43 to f=0.53. Using equation 4.7, this corresponds to a confidence interval for the number ratio of Seyfert 2 to Seyfert 1 galaxies ranging from 0.75 to 1.13. Similarly, I have projected the nominal spread of AGN spectral indices (1.7±0.15) onto the covering fraction dimension using the ASCA confidence contours. Here, the range of covering fractions goes from ~0.23 to ~0.55, corresponding to a Seyfert 2 to Seyfert 1 number ratio ranging from 0.29 to 1.22.

Doing this for all the contour plots on figure 4-22, we find that the allowed range of answers increases with luminosity evolution parameters Z_{max} and γ_{evol} and that acceptable covering fractions range from about 0.2 to 0.6. This gives r_{21} a range of 0.25 to 1.5. This seems true even if we unconstrain the volume emissivity (ie. use figure 4-20).

These number ratios are somewhat on the low side compared to the wide range of published Seyfert 2/Seyfert 1 observations. Osterbrock and Shaw (1988) estimated from optical data that there are eight Seyfert 2s for each Seyfert 1 ($f = 0.89$). Salzer (1989) has found only five ($f = 0.83$). Most recently, Huchra and Burge (1992) have arrived at a value of 2.3 ± 0.7 ($f = 0.62 - 0.75$). Using Infrared data, Barcons et al. (1995) have arrived at ratios from one to two ($f = 0.5 - 0.66$). It is interesting that the reported number ratio is decreasing with time of publication.

If we include the effects of Compton scattering in the column transmission for the source

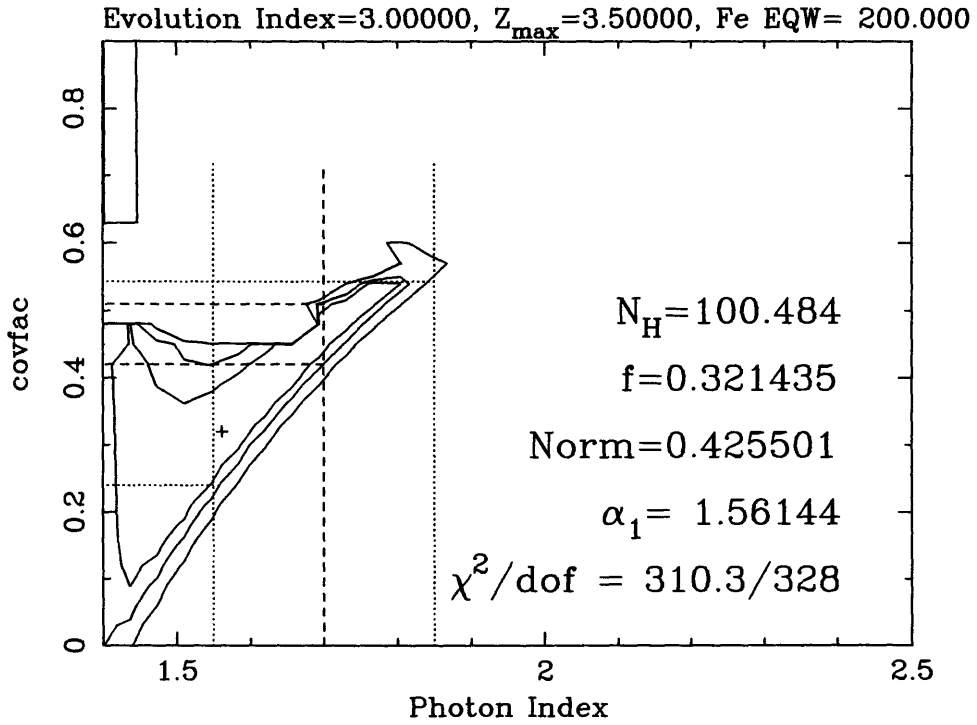

Figure 4-27: An example of the projection procedure using the lower right hand panel of figure 4-21. Here, the nominal AGN spectra power law index of 1.7 is projected to a range of acceptable covering fractions by taking the intersection of the 90% confidence contour with the dashed line corresponding to α_1= 1.7. The nominal spread of 0.15 about the 1.7 index is also projected (dotted lines).

spectra, then we would need to modify equation 4.7. The sense of this change is to make covering fractions bigger by some small amount (probably less than 10% - Yaqoob, private communication) and thus the inferred Seyfert 2 to Seyfert 1 ratios would get bigger. This is a small effect, though.

Another systematic effect which would change the covering fraction is the relation between the covering fraction and the power law index. It is apparent in contour plots such as figure 4-27 that as the power law index gets bigger, then the covering fraction and r_{21} tend to increase.

The Luminosity Evolution Parameters

There is independent optical and X-ray data on the luminosity evolution of AGN. Recently, Boyle et al. (1993) have taken over 450 AGN from several medium deep X-ray surveys by the X-ray missions, ROSAT and Einstein, and have computed a luminosity function

as a function of redshift. To this data, they have fit several luminosity evolution models–including one in the same form as we have assumed in our model above. These models provide independent data on the luminosity evolution index, γ_{evol} as well as the maximum redshift, z_{max}. If we take Boyle et al's (1993) values for these parameters as constraints, we can explore limits on other parameters in our model. We have elected to look at limits on the column densities and covering fractions for a few selected α_1 values, with the iron equivalent width fixed at 200 eV. Figure 4-28 shows confidence contours for covering fractions and column densities with the Boyle et al luminosity evolution result fixed.

Note that when the local X-ray volume emissivity is constrained to be less than Miyaji's upper limit, then the resulting models produce unacceptable $\chi^2/d.o.f.$ values (refer to the middle top panel of figure 4-22). This result suggests that Miyaji's results and Boyle's results are inconsistent. However, keep in mind that Miyaji's volume emissivity figure comes from 2-10 keV x-ray observations, while Boyle's figures are based on 0.5-2 keV x-ray observations.

4.8.4 Summary of ASCA's Spectral Constraints on the Seyfert 1- Seyfert 2 XRB Synthesis Model

The most important observation of this section is that ASCA does not observe any sharp spectral features in the 1.2 to 6 keV XRB spectrum. This is a particularly strong statement in that it is hard to construct calibration errors which could extinguish such a feature. The only way we could conceivably extinguish such a feature would be if the resolution of the CCD was much worse than we expected. Clearly, the instrumental background lines are sharp enough to rule this out. In fact, if ASCA did detect such a feature, we would need to be quite cautious in our interpretation, as many of the AGN synthesis models predict features near our instrument response edges (aluminum K, silicon K, gold M).

In this section, we have applied to the ASCA data an AGN synthesis model for the XRB spectrum which makes use of the unified AGN model (Antonucci, 1993). In this application, we have explored the sensitivity of AGN spectral, evolution, and population properties on the ASCA XRB spectrum. We also explore the role of the local 2-10 keV X-ray volume emissivity. The AGN spectral properties include the low energy power law index, absorber column density, and fluorescent iron Kα line emission. We have used a standard form of the AGN evolution function which goes as $(1+z)^{\gamma_{evol}}$ up to a maximum redshift z_{max}. We have classified the AGN into two basic types: unabsorbed Seyfert 1 galaxies and absorbed

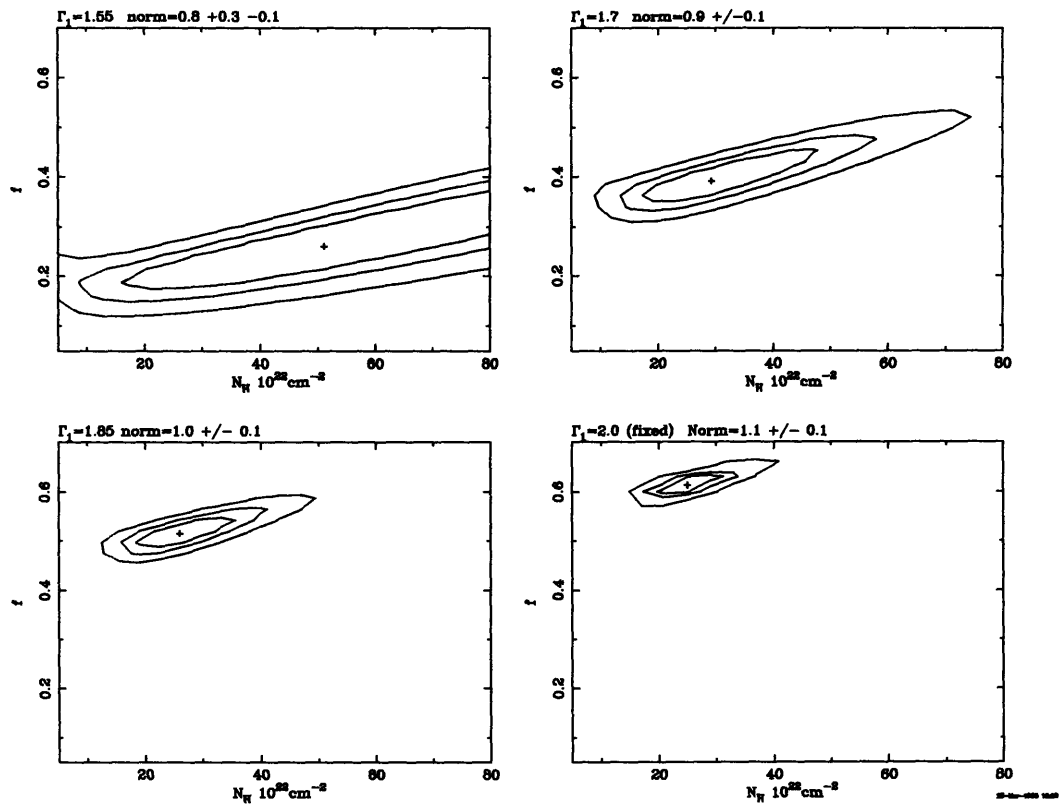

Figure 4-28: Confidence Contours in the covering fraction vs N_H plane where the luminosity evolution parameters have been fixed at those found by Boyle et al (1993). Thus for each of these plots, $\gamma_{evol} = 2.75$ and Z_{max}=2.0. Four values for the intrinsic power law index of the source are presented, spanning the range of observered AGN values. The listed "norm" value is the volume X-ray emissivity in units of 10^{39} h_{50} erg s^{-1} Mpc^{-3}.

Seyfert 2 galaxies. In our application of the model, we have put constraints in the relative number of Seyfert 2 and Seyfert 1 galaxies.

We list the basic conclusions of this model below:

• The ASCA data suggests that the maximum redshift, z_{max}, in the AGN evolution function must be greater than or equal to 2.5. This conclusion becomes stronger when we take the independently derived local X-ray volume emissivity as a constraint. This result is in contradiction with the result of Boyle *et al* (1993), which suggested that $z_{max} = 2$. The discrepancy may be due to the fact that Boyle *et al*'s result is from 0.5 to 2 keV data while the volume emissivity constraint comes from 2-10 keV X-ray data (Miyaji, 1994). The model which I have applied here may also be incorrect due to several reasons. First, in this

application of the model, I have treated the contribution due to all other types of sources as negligible. The contributions of non-Seyfert sources may diminish the requirement for flux from distant Seyferts to make up the XRB. Also, it is possible that intermediate types of Seyfert galaxies exhist which have properties of both Seyfert 1 and Seyfert 2 galaxies.

- We have put upper limits of 600 eV to 320 eV for the equivalent rest frame width of an iron Kα line in the intrinsict AGN spectra. The upper limit decreases as one considers models with increasing z_{max}.

- The allowed range of covering fractions (and thus the relative number of Seyfert 2 to Seyfert 1 galaxies) increases as the instrinsict low energy power law index increases.

- When we constrain the local 2-10 keV X-ray volume emissivity to be less than the independently observered upper limit of Miyaji (1994), the ASCA data puts a hard lower limit on γ_{evol} in the AGN luminosity evolution function. This limit is that $\gamma_{evol} > 2.5$.

- With the assumption that the intrinsict AGN power law index is within the canonical range of 1.7 ± 0.15, we put limits on the covering fraction from $\sim$0.23 to $\sim$0.55. This range of covering fractions corresponds to a relative number of Seyfert 2 to Seyfert 1 galaxies ranging from 0.29 to 1.22. This ratio is marginally consistent with Barcons *et al* (1995) figure of 1 to 2. Our number is rather low compared to earlier figures on the relative number of Seyfert 2 to Seyfert 1 galaxies.

An interesting observation- not directly related to this work- is that the AGN luminosity evolution index seems to nearly exactly cancel out the rate at which the cosmological scale volume size decreases. This is part of the reason why we do not see any sharp iron emission line features in the XRB spectrum.

With this data alone, we have no handle on the higher energy parameters of this model. To constrain break energies and the high energy power law index, we must use data such as the HEA01-A2 results. Figure 4-29 shows an extrapolation of one our our best fit models to high energies. The model is roughly consistent with the 40 keV bremsstrahlung spectrum described by Marshall *et al* (1980). Future work should include simultaneous fitting of this model with both the HEAO1-A2 data and the ASCA data.

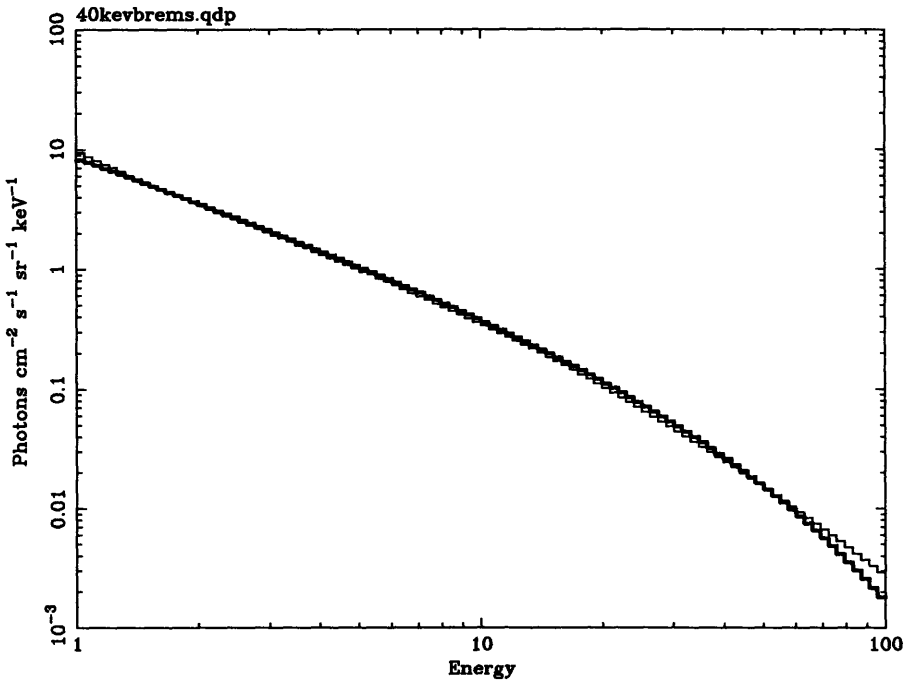

Figure 4-29: An extrapolation of one of our models (fine line) superimposed on a 40 keV bremsstrahlung spectrum (dark line). The low energy power law index is 1.7. The high energy index is 2.65 with a break at 90 keV.

Bibliography

R. R. Antonucci, 1993, *Ann. Rev. Astron. Astrophys.*, **31**, 473.

H. Awaki, K. Koyama, H. Inoue, J.P. Halpern, 1991, *Publ. Astron. Soc. Japan*, **43**, 195.

X. Barcons, A. Franceschini, G. De Zotti, L. Danese, T. Miyaji, 1995, Preprint.

BB, *Scientific Satellite ASTRO-D Interim Report*, 1991, ISAS SES Data Center.

P. Bevington & D. Robinson, *Data Reduction and Error Analysis for the Physical Sciences*, (McGraw-Hill, N.Y., 1992).

E. Boldt, 1987, *Phys. Rev.*, **146**, 215.

B.J. Boyle, R.E. Griffiths, T. Shanks, G.C. Stewart, I. Georgantopoulos, 1993, MNRAS, 260, 49.

B.E. Burke, R.W. Mountain, D.C. Harrison, M.W. Bautz, J.P. Doty, G.R. Ricker, and P.J. Daniels, 1991, *IEEE Transactions on Electron Devices* vol 38 no 5, pgs 1069-1076.

B.E. Burke, Mountain, R. W., Daniels, P.J., Cooper, M.J., and Dolat, V.S., SPIE 20006, 1993.

E.A. Burke, 1986, *IEEE Trans. Nuc. Sci,* NS-33, 1276.

W. Burrell, *Calculation of Proton Penetration and Dose Rates*, 1964, NASA Technical Memorandum TMXX-53063 (George C. Marshall Space Flight Center).

W. Cash, 1979, *ApJ*, **228**, 939-947.

A. Comastri, G. Setti, G. Zamorani, G. Hasinger, 1995, *Astron. & Astrophys.*, **296**, 1.

R. Coswik, and E. Kobetich, 1972, *ApJ*, **177**, 585.

Dale, C. and Marshall, P., 1991, "Displacement Damage in Silicon Imagers for Space Applications," SPIE Electronic Imaging Science and Technology Conference, San Jose.

A. C. Fabian, and X. Barcons, 1992, *Ann. Rev. Astron. Astrophys.*, **30**, 429-56.

A.C. Fabian, I.M. George, S. Miyoshi, M.J. Rees, 1990, MNRAS, **242**, 14-16P.

G.B. Field and S.C. Perrenod, 1977, *ApJ*, **215**, 717.

Y. Fukazawa, *et al.*, 1994, *Publ. Astron. Soc. Japan*, **46**, L141-L146.

G.P. Garmire, D. Burrows, C. Canizares, G. Clark, S.A. Collins, E. Feigelson, J. Morrison, J. Nousek,S.H. Pravdo, S.A. Rappaport, G. Ricker, G.R. Riegler, and D. Weedman, 1986, "The AXAF CCD Imaging Spectrometer," X-ray Instrumentation in Astronomy, J.L. Culhane, ed., Proc. SPIE 597, pp. 261-266.

K.C. Gendreau, M.W. Bautz, G.R. Ricker, 1993, *Nucl. Inst. Meth. Phys. Res. A*, **335**, 318.

K.C. Gendreau, 1994, ASCA News.

K.C. Gendreau, *et al.*, 1995, *Publ. Astron. Soc. Japan.* **47**, L5-L9.

K.C. Gendreau, G.Y. Prighozin, R. Huang, M.W. Bautz, 1995, *IEEE Transactions on Electrons Devices*, submitted.

I.M. George and A.C. Fabian, 1991, MNRAS, **249**, 352.

R. Giacconi, H. Gursky, R. Paolini, B. Rossi, 1962, *Pys Rev. Letters*, **9**, 439.
J. Grindlay and M. Luke, 1990, in High Resolution X-ray Spectroscopy of Cosmic Plasmas, Cambridge University Press, 276.
B. Grossan, 1992, Ph.D. thesis, Massachusetts Institute of Technology.
D.A. Gruber, 1992, in The X-Ray Background Edited by X. Barcons and A. C. Fabian, 44, Cambridge University Press.
P.W. Guilbert, and A.C. Fabian, 1986, MNRAS, **220**, 439.
G. Hasinger, 1992, in The X-Ray Background Edited by X. Barcons and A. C. Fabian, 229-239, Cambridge University Press.
G. Hasinger, R. Burg, R. Giacconi, G. Hartner, M. Schmidt, J. Trumper, G. Zamorani, 1993, *Astron. & Astrophys.*, **275** ,1-15.
K. Hayashida, 1990. Ph.D. thesis, Univ. Tokyo.
C. Hill, W. Ritchie, and K. Simpson, 1965, "Data Compilation and Evaluation of Space Shielding Problems," vol 1, NASA Engineering Report ER 7777, (George C. Marshall Space Flight Center).
A. Holland, 1990, Ph.D. thesis, University of Leicester.
S. Holt, 1992, in The X-Ray Background Edited by X. Barcons and A. C. Fabian, Cambridge University Press.
M.J. Howes and D.V. Morgan, *Charge-Coupled Devices and Systems*, (John Wiley and Sons, N.Y., 1979).
Huchra and Burg, 1992, *ApJ*, **393**, 90.
H. Inoue, K. Koyama, M. Matsuoka, T. Ohashi, and Y. Tanaka, 1979, *ApJ*, **227**, L85-L88.
J. Janesick, G. Soli, T. Elliott, and S. Collins, Proc. SPIE vol. 1147, (1991).
G. Knoll, *Radiation Detection and Measurement*, (John Wiley and Sons, N.Y., 1979).
D. Lumb and J. Nousek, 1992, Proc SPIE 1736.
P. Madau, G. Ghisellini, and A.C. Fabian, 1993, *ApJ*, **410**, L7.
P. Madau, G. Ghisellini, and A.C. Fabian, 1994, MNRAS, **270**, L17.
F. E. Marshall, E.A. Boldt, S.S. Holt, R.B. Miller, R.F. Mushotzky, L.A. Rose, R.E. Rothschild, and P.J. Serlemitsos, 1980, *ApJ* **235**, 4.
J.C. Mather, *et al.*, 1990, *ApJ*, **354**, L37.
G. Matt, 1994, Preprint of Talk at Vulcana workshop 1994.
G. Matt and A.C. Fabian, 1994, MNRAS, **267**, 187.
D. McCammon and W.T. Sanders, 1990, *Ann. Rev. Astron. Astrophys.*, **28**, 657-88.
T. Miyaji, T. 1994, Ph.D. thesis, Univ. Maryland.
A. Mohsen and M. Tompsett, 1974, *IEEE Transactions on Electron Devices*, ED-21, No. 11, pg. 701.
K. Morisawa, M. Matsuoka, F. Takahara, L. Piro, 1990, *Astron. & Astrophys.*, **236**, 299-304.

R. Mushotzky, 1984, *Adv. Space Res.*, **3**, 157.
K. Nandra and K. Pounds, 1994, MNRAS, **268**, 405.
T. Ohashi, M. Makishima, M. Ishida, M. Tsuru, M. Tashiro, T. Mihara, Y. Kohmura, H. Inoue, 1991, SPIE 1549.
Osterbrock and Shaw, 1988, *ApJ*, **327**,89.
Piccinotti, G. *et al.*1982, *ApJ*, **253**, 485.
K. Pounds, K. Nandra, G. Stewart, I. George, A. Fabian, 1990, *Nature*, **344**, 132.
J.C. Raymond and B.W. Smith, *ApJ Suppl*, **35**, 419.
Salzer, 1989, *ApJ*, **347**, 152.

D.A. Schwartz, 1992, in The X-Ray Background Edited by X. Barcons and A. C. Fabian, 149-168, Cambridge University Press.

D.A. Schwartz and H. Gursky, 1974, in *X-ray Astronomy*, eds., H. Gursky and R. Giacconi, (Dordrecht: D Reidel), 359.

P.J. Serlimitsos, *et al.*, 1995, *Publ. Astron. Soc. Japan*, **47**, 105-114.

G. Setti and L. Woltjer, 1989 *Astron. & Astrophys.*, **224**, L21-23.

T. Shanks, I. Georgantopoulos, G.C. Stewart, K.A. Pounds, B.J. Boyle, and R.E. Griffiths, 1991, *Nature*, **353**, 315.

W. Shockley and W. Reed, 1952 *Phys. Rev.*, **87**, 685-691.

S.L. Snowden, D.P. Cox, D. McCammon, and W.T. Sanders, 1990, *ApJ* **354**.

E.G. Stassinoupolos, and J.M. Barth, 1991, "Astro-D Charged Particle Environment Study, NASA report X-900-91-07.

A.A. Stark, C.F. Gammie, R.W. Wilson, J. Bally, R.A. Linke, C. Heiles, and M. Hurwitz, 1992, *ApJ Sup*, **79**, 77-105.

Y. Tanaka, H. Inoue, and S.S. Holt, 1994, *Publ. Astron. Soc.Japan*, **46**, L37-41.

Y. Tanaka and J.A.M. Bleeker, 1977, *Space Sci. Rev.*, **20**, 815-88

N. Teresawa,1991, *ApJ Let*, **378**, L11.

T.J. Turner and K.A. Pounds, 1989, MNRAS, **190**, 243.

R.S. Warwick and G.C. Stewart, 1989, In X-Ray Astronomy, 2. AGN and the X-Ray Background, pp 727-31, Noordwijk: ESA SP-296.

J. Watts and T. Parnell, "Approximate Angular Distribution and Spectra for Geomagnetically Trapped Protons in Low-Earth Orbit," in High Energy Radiation Background in Space, Rester, A. and Tombka, J., ed., AIP Conference Procedings 186, p 75.

K.W. Wenzel, D.H. Lo, R.D. Petrasso, J.W. Coleman, C.K. Li, J.R. Lierzer, C. Borras, and T. Wei, 1992, *Rev. Sci. Instr.*, vol 63, no 10, pp 4837-4839.

E.L. Wright *et al.*, 1994, *ApJ*, **420**, 450.

X. Wu, T. Hamilton, D.J. Helfand, Q. Wang, 1991, *ApJ* **379**, 564.

T. Yaqoob, P.J. Serlimitsos, A. Ptak, 1995, in preparation.

A. Zdziarski, P.T. Zycki, R .Svensson, and E. Boldt, 1993, *ApJ*, **405**, 125.

A. Zdziarski, W. Neil Johnson, C. Done, D. Smith, and K. McNaron-Brown, 1995, *ApJ* **438**, L63-L66.

M.V. Zombeck, *Handbook of Space Astronomy and Astrophysics*, (Cambridge University Press, NY, 1990).

Appendix A

Basic Principles of CCD Operation

The CCD in its most basic form is an array of Metal-Oxide Semiconductor (MOS) capacitors. These capacitors store charge within potential wells and then pass the charge to adjacent capacitors. Here is a brief review of some of the essential components and operation of a CCD. The discussion will be limited to buried channel devices. A more complete review can be found in Howes and Morgan (1979).

A.1 The MOS Capacitor

Consider a metal (or polysilicon) gate separated from a slab of silicon by an oxide/nitride layer as shown in figure A-1. The silicon is P-type with an N-type layer of thickness "t". When one applies a potential to the gate, a potential well forms in the silicon. The form of the potential is given by the solution to Poisson's equation:

$$\nabla^2 V = -\frac{e(N_d(\vec{r}) - N_a(\vec{r}) - n(\vec{r}) + p(\vec{r}))}{\epsilon_{Si}\epsilon_0} \tag{A.1}$$

where, e is the electron charge, ϵ_{Si} is the permittivity of silicon, ϵ_0 is the permittivity of free space, N_d is the concentration of doped donors, N_a is the concentration of doped acceptors, n is the concentration of free electrons, and p is the concentration of holes. At low temperatures, the thermal noise is very low and thus n and p are effectively 0 in the absence of photon induced free charge. In practice, it is very difficult to evaluate

equation A.1 analytically, especially when one considers structure in the planes orthogonal to the plane of figure A-1.

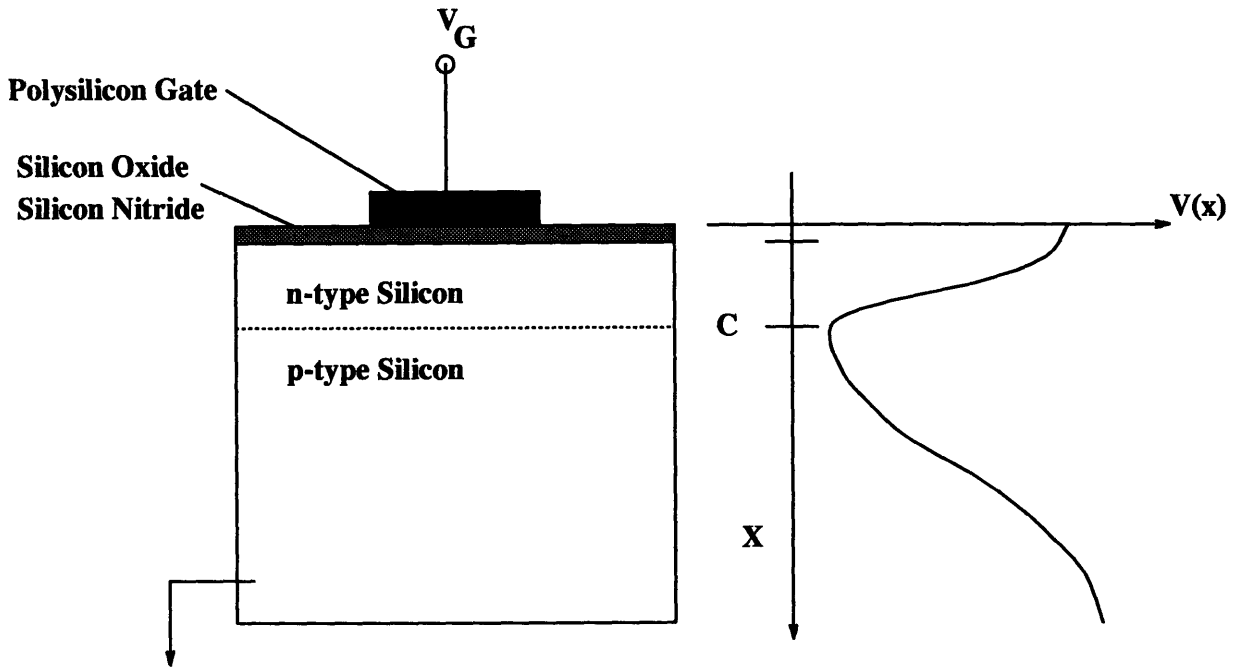

Figure A-1: A MOS capacitor with a schematic of the potential function.

To glimpse the basic features of the system, consider the simple case of one dimension with donor and acceptor profiles as shown in figure A-2. Here, equation A.1 reduces to:

$$\begin{aligned} \frac{d^2V(x)}{dx^2} &= 0 \qquad -d < x < 0 \\ &= -\frac{eN_d}{\epsilon_{Si}\epsilon_0} \qquad 0 < x < C \\ &= +\frac{eN_a}{\epsilon_{Si}\epsilon_0} \qquad C < x < D \end{aligned} \tag{A.2}$$

where, C is the depth from the oxide/nitride interface at which the donor profile ends and D is the depth at which the potential and electric field go to zero. D is the "depletion depth" which plays a major role in defining the high X-ray energy detection efficiency in CCDs.

The boundary conditions for ths problem are

$$\begin{aligned} V(x=-d) &= V_G \\ V(x=D) &= 0 \\ \frac{dV(x=D)}{dx} &= 0 \end{aligned} \tag{A.3}$$

There are three parameters to solve for in this system: the maximum potential V_{max}, the depth of maximum potential M, and the depletion depth D.

An easy way to solve this problem is by working with the electric field solution. The electric field is the first derivative of the potential. Given equation A.2, the electric field becomes a set of piecewise linear segments as shown in panel C of figure A-2. The slopes of the electric fields in the various regions of the device are given by the poisson equation A.2. Note that the negative of the integral of the electric field over x must equal the gate potential, V_G. Since the electric field is piecewise linear, this integral is just the sum of areas of rectangles and triangles. Using simple geometry and panel C of figure A-2, one gets the following:

$$D = C + \frac{N_d}{N_a}(C - M) \tag{A.4}$$

and

$$M = -N_a \left(-N_d\, d - N_d\, c - \frac{N_d^2 c}{N_a} + \frac{N_d \sqrt{d^2 N_a + 2\, d N_a\, c + 2\, d N_d\, c + c^2 N_a + N_d\, c^2 + 2\, V_G}}{\sqrt{N_a}} \right) N_d^{-2} \tag{A.5}$$

For most CCDs, the donor concentration is several orders of magnitude greater than the acceptor concentration. Also, the insulator thickness is much smaller than C or D. In the limit that the ratio $\frac{N_d}{N_a} \rightarrow$ inf, M approaches C. The continuity of the electric field at C coupled with the large value of $\frac{N_d}{N_a}$ drives the depletion depth to be large. In this limit, the integral of the electric field is dominated by the area of the triangle from C to D. Equating $-V_G$ to this integral, one obtains for the depletion depth:

$$D = \left(\frac{2\epsilon_{Si}\epsilon_0 V_G}{e N_a}\right)^{\frac{1}{2}} + C \tag{A.6}$$

The resistivity of the silicon goes as $1/N_a$. Thus the depletion depth goes as the square root of the resistivity.

Also, the maxumum potential follows the gate potential linearly.

A.2 Arrays of MOS Capacitors: The CCD

CCDs are arrays of MOS capacitors. Figure A-3 shows two pixels of a register in a "three phase" CCD. Each pixel contains three "phases" or "sub pixels" which are simple MOS capacitors. Corresponding phases on different pixels are electrically connected, so that for a single linear array of pixels, there are three phases. There exist CCDs with a two or four phase architecture, but the ASCA CCDs are three phase CCDs. By applying suitable potentials in sequence to the various phases, charge can be transfered from one pixel to the next. Linear arrays are composed of many pixels. Figure A-3 shows a sequence of phase potentials similar to those used in the normal operation of the ASCA CCDs. In this figure, the CCD is performing its fundamental operartion, charge transfer.

Parallel linear arrays share common phases. Thus one can transfer charge down parallel arrays of registers with just three potential signals- or "clock lines".

The ASCA CCDs have 420 parallel columns of 420 pixel long registers in their imaging and frame store sections. Each column of the imaging array feeds into a column of the frame store array. The last pixel of each frame store array column feeds into a pixel of a single linear array called the serial register. The serial register is arranged to be orthognonal to the parallel frame store and imaging arrays. The last pixel of the serial array transfers charge to the begining stage of a signal amplifier which eventually provides the pulseheight information for the CCD. The basic arrangement is shown in figure A-4.

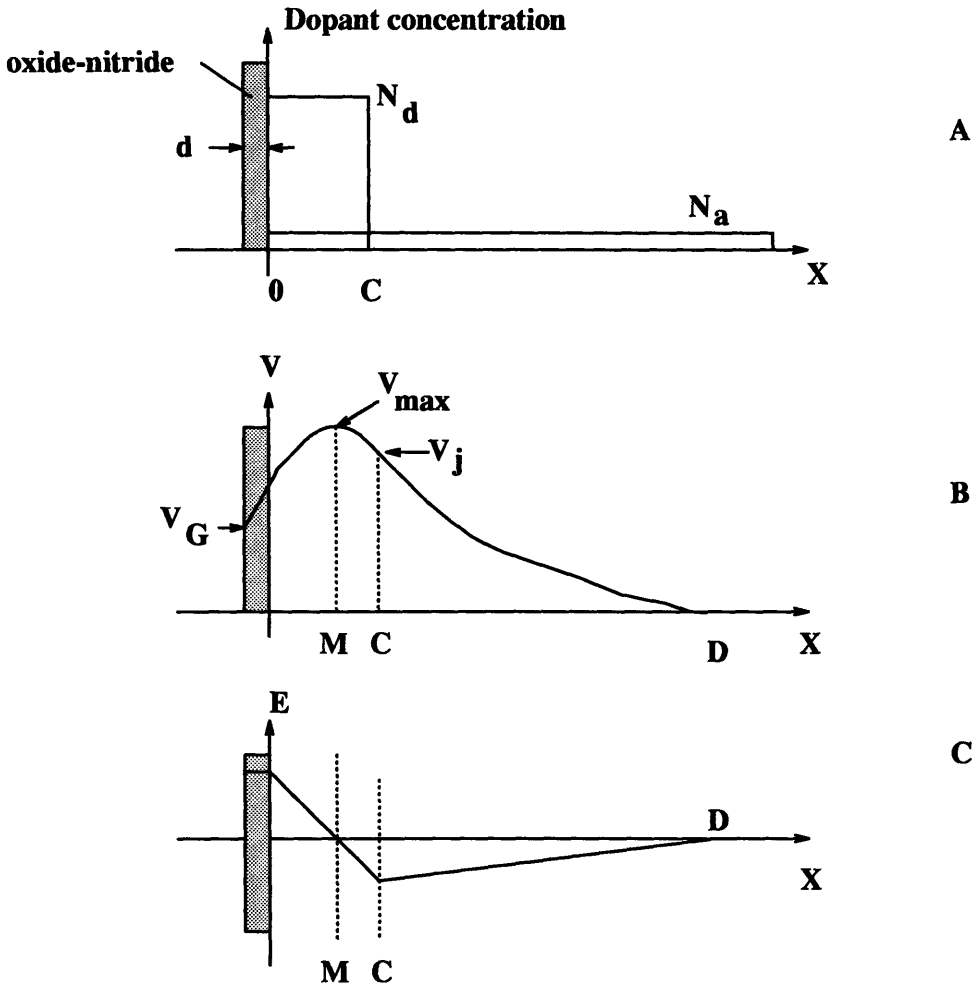

Figure A-2: Dopant concentration, potential, and electric field for a simple one dimension MOS capacitor

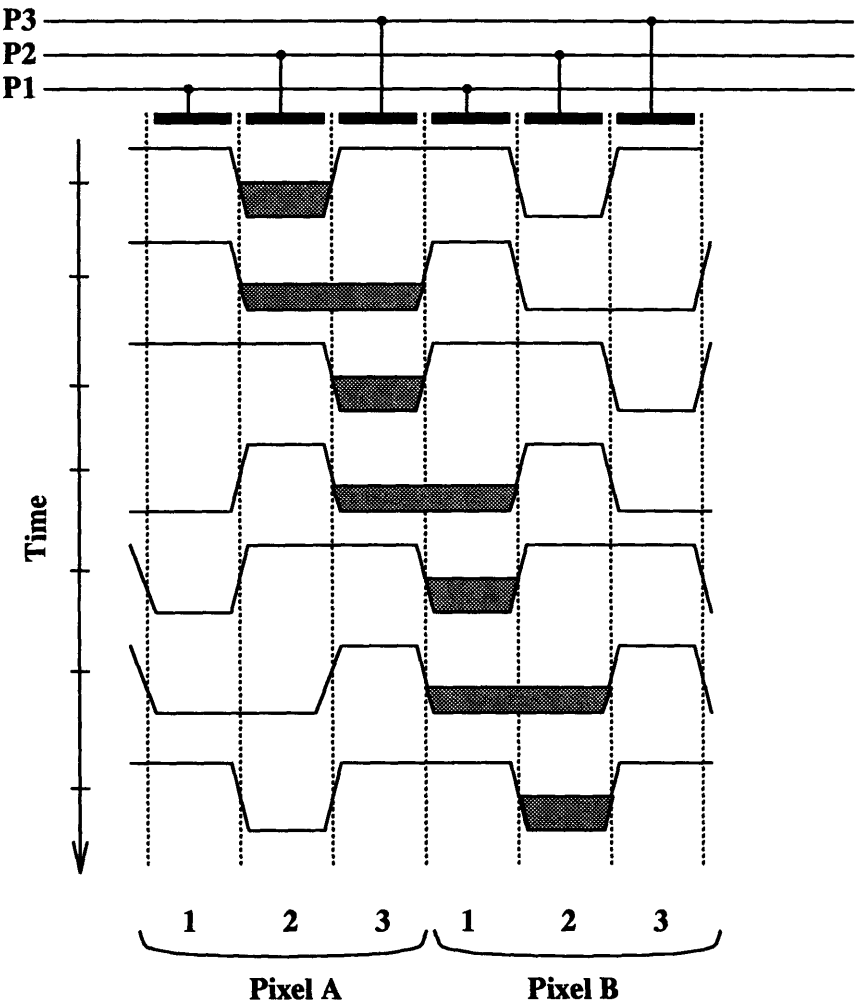

Figure A-3: Transfering Charge in a three phase CCD. This shows how charge (the shaded region) is transferred from phase 2 of pixel A to ohase 2 of pixel B. Time moves down the figure. The curve at each time step represents the potential level in the CCD under the various phases.

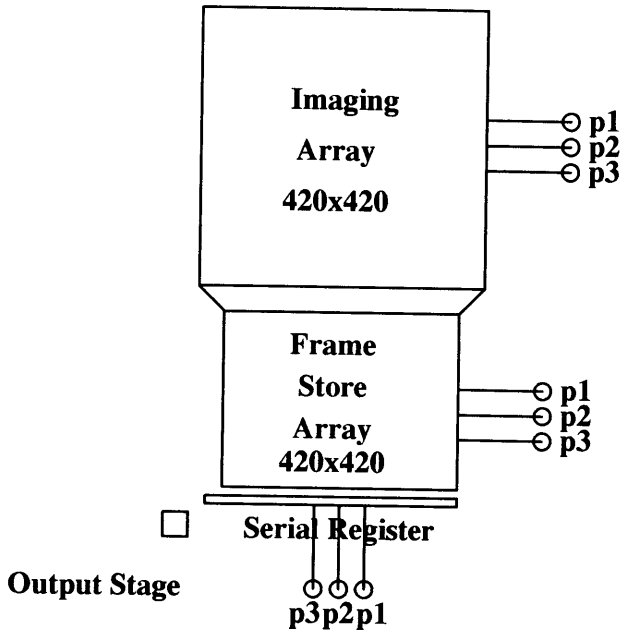

Figure A-4: A schematic of the ASCA CCD showing the various regions and phases. The device is a CCID7 made by Lincoln Laboratory.

Appendix B

Event Detection and Classification For the SIS

Much of this discussion comes from "the blue book", a japanese manual for ASCA (BB, 1991).

In a normal imaging mode, the SIS analog electronics (AE) passes raw ccd data in the form of 12 bit digitally encoded pulseheights for each CCD pixel to the SIS digital electronics (DE). We call the units of this pulseheight data "Analog to Digital Units" or "ADU". For the SIS analog electronics and CCD output stages, one ADU is within 20% of one electron.

The pulseheight data includes a bias level offset, introduced by the AE, a dark level offset, introduced by the thermal noise of the CCD and any diffuse optical light landing on the CCD, and and additional charge due to impinging X-ray photons. The job of the DE is to subtract the bias and dark level offsets and find "events". Depending on the observation mode ("bright mode" or "faint mode") of the SIS, these events will be classified either on the satellite by the satellites digital processor (DP) or on the ground by the observer. In this appendix, I describe this process from the calculation of the dark frame to the detection of events and finally to the classification. The discussion here is limited to the imaging modes of the SIS.

B.1 Dark Level Calculation

The dark level is generally a spatially and temporally varying quantity. Ideally, one should make a dark level map (a dark frame) with a spatial resolution of one detector pixel under

conditions of no X-ray illumination. Using this dark frame, one can subtract the dark level on a pixel by pixel basis from subsequent X-ray frames.

In standard laboratory work, we use this procedure. The dark frame is made by averaging several CCD frames taken while a X-ray shutter is closed. While keeping the operating conditions of the CCD the same, we take X-ray data frames with the X-ray shutter open. Changing operating conditions such as the CCD voltage levels, temperature, and optical light contamination may invalidate the dark frame and require a new dark frame. To follow this procedure for an individual ASCA SIS CCD array (four 420×420 pixel CCDs), one requires: 1) a minimum of 2.5 Mbytes of readable/writable memory to do the pixel by pixel subtraction, 2) approximately 2.5 Mbytes of readable/writable memory to make the dark frame, 3) a shutter to block the X-rays, and 4) a processor which can keep up with the data rate from the CCDs. Since there are two SIS sensors on ASCA, the perfect algorithm requires twice the number of resources listed above.

Due to practical considerations such as weight, power, and radiation hardness, ASCA does not satisfy any of these requirements. Here, I describe how the dark level is computed for ASCA. While ASCA algorithm does not produce the most accurate estimation of the CCD dark level, it is the most efficient given the resources and constraints available.

To address the limited amount of memory and computation resources available on ASCA, the ASCA algorithm produces a much coarser resolution dark frame. Instead of producing a 420×420 pixel dark frame for each of the four CCDs of one SIS sensor, the algorithm produces a 64×64 dark frame for each CCD. For dark frame subtraction from X-ray data, the DE subtracts a single dark frame level for each CCD pixel which lies with in a given dark frame cell.

To address the absence of a shutter, the ASCA algorithm builds the dark frame over time by using pixels which do not have an obvious X-ray event. The selection of pixels used for this calculation is based on pulsehight windowing within lower and upper "dark frame pixel thresholds". The dark level for a given dark frame cell is then taken as the "running average" over several CCD readouts according to the equation:

$$new\ level = old\ level + \frac{PHA}{N+1} \tag{B.1}$$

where, PHA is the average value of the pulseheights of dark frame pixel threshold

windowed pixels within the dark frame cell in question, and N is a number which determines the time constant for dark frame updating. The typical value for N is 4, resulting in a dark frame updating time constant of a few minutes for a CCD exposure time of 16 seconds. This means that changes which occur on time scales faster than a few minutes will not factor into the dark frame. On ASCA, the dark frame error (DFE) due to this effect occurs typically when ambient optical lighting conditions around the satellite change suddenly.

B.2 Event Definition and Classification

An event is any pixel whose dark/bias frame subtracted pulseheight is within lower and upper event thresholds and is a local maximum compared to pulseheights of neighboring pixels. The DE saves both the pulseheights of the peak pixel and the surrounding 8 pixels as well as the location of the peak pixel in the CCD array for each event in temporary memory. The satellite digital processor (DP) can read this memory and continues the event processing.

The DP can follow one of two modes in the subsequent processing: "Faint" or "Bright" mode. In faint mode, the DP simply passes all of the event data directly from the DE's temporary memory to the satellite telemetry stream (or data storage recorder). In bright mode, the DP first classifies the events and then passes reduced information on the events to the telemetry stream. In standard analysis on the ground, the observer typically converts faint mode data to bright mode. However, with faint mode data, the observer and instrument team has more handle on systematic effects.

In bright mode, the DP groups events into eight different shape classification. This classification is done both to optimize the energy resolution of the CCD and also to help reject events due to the non X-ray background. To do this, the DP compares the pulseheights of the eight pixels surrounding the central pixel of an event to a "split event threshold" (SPT). If an adjacent pixel has a pulseheight above this threshold, then we say that the event is split between this pixel and the central pixel. It is possible for events to be multiply split. Figure B-1 shows examples of the different grade types. For brevity, I call pixels which have pulseheights above SPT "split pixels". Grade "0" events are single pixel events that have no adjacent pixel above the split event threshold. Grade "1" events are single events which have one or more diagonally adjacent pixels above SPT. Grade "2" events are

single sided vertically split events which may or may not have diagonally split pixels which are not adjacent to the vertically split event. Grade "3" and "4" events are left and right handed split events, respectively. As for the vertical events, grades "3" and "4" may or may not have diagonally split pixels which are not adjacent to the horizontally split event. Grade "5" events are either horizonally or vertically single sided split events which have a diagonally split pixel adjacent to the other split pixel. Grade "6" events include all events with both a horizontally split and vertically split pixel. Grade "6" events may also have several diagonally split pixels, as long as they do not surround a horizontally or vertically split pixel. Grade "7" events are all those events which fail to fit in the above classifications.

The DP also computes a pulseheight for the graded events. The final pulseheight is the sum of the central pixel pulseheight with all the horizontally and vertically split pixel pulseheights. Only for grade "6" events will the DP include the pulseheights of some diagonally split pixels.

B.3 What are the Grades Telling us about the Events?

The association of these grades with X-ray spectral quality and background rejection is discussed heavily in the ASTRO-D Interim report of 1991 (also MIT ASTRO-D memo no. 452). Briefly I review the findings below.

Good X-ray events are usually associated with grades 0, 2, 3, and 4. Grade 0 events are nominally the best events in terms of energy resolution. See chapter 2 for examples of the improved energy resolution obtained by taking single as opposed to total events. However, a problem with the flight electronics called "charge echo" tends to transform single events into right split events. In fact the charge echo effect tends to transform all of the grades at some level. Phenomenologically, it is observed that a pixel immediaely to the right of a pixel with some significant amount of charge in it will contain a certain fraction of the lead pixels pulseheight. The origin of the charge echo effect is in the analog processing of CCD pulseheight data in the AE. In fact the origin is an echo. Basically, the charge echo seen in one pixel is due to an echo of a signal from the preceeding pixel processeed by the analog processing chain in the AE. It is for this reason that bright mode differentiates between left and right split events.

Grade 6 events are also almost always due to X-rays, but the large amount of splitting

results in somewhat worse energy resolution. Grade 6 is useful when the X-ray flux is low, and the observer needs the most data available.

Grade 5 events are usually the result of "pile up". This phenomena occurs when more than one photon affect a given 3×3 event cell.

Grade 7 events are almost always due to non X-ray events. They are the primary way to reduce background- see appendix F.

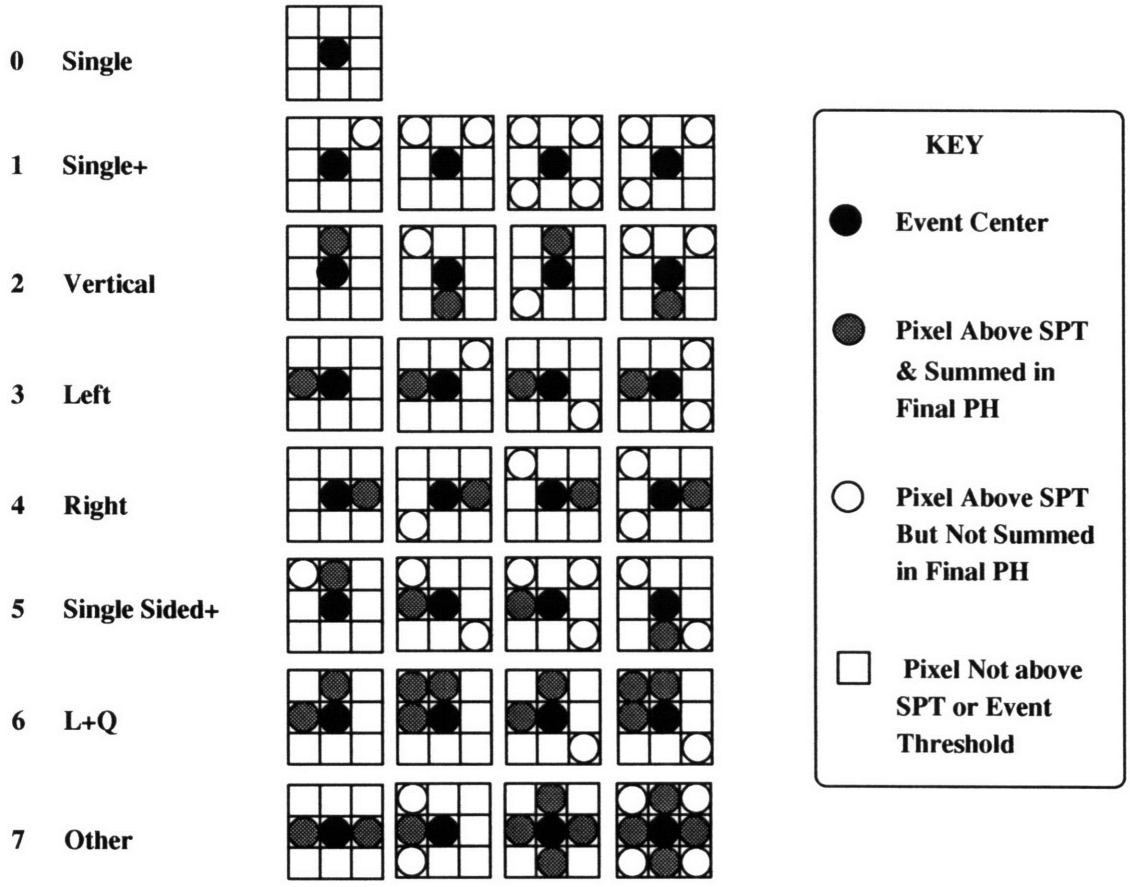

Figure B-1: Event grade definitions for the ASCA SIS with some examples.

Appendix C

CCD Escape Peak Modeling

This describes a simple escape peak model for CCDs. A more complicated model is also discussed. Both predict the ratio of escape peak counts to primary pulse height counts. Most of the calculations were done in the "ccd-model" *Mathematica* notebook described in ASTRO-D Memo # 478. Experimental results are also presented which confirm some aspects of the simple model but differ in others. The principal results are that the relative intensity of the escape peak is energy dependent and depletion depth dependent. A consequence of this is that a measurement of the ratio of escape peak counts to primary peak counts due to an Fe55 source (for instance) could give you a measure of the depletion depth, which in turn will tell you what the high energy QE is, which will tell you what the absolute intensity of the Fe55 source is. The depletion depth is a function of the parallel clock voltage, which suggests that the housekeeping value for the parallel clock voltage should be included in the response matrix calculation (it probably should anyhow since it directly affects the high energy quantum efficiency). The more complicated model tries to account for the way in which the channel stops affect the gate side boundary of the depletion region.

C.1 The Silicon K Escape Peak Model- Simple Version

This model for the escape peak probability is also described in the *Mathematica* notebook of ASTRO-D Memo # 478. However, an error was discovered in a critical integral, so I will rehash the model below. The probability of a silicon escape pulseheight being registered for an incident photon of energy E is given by the probability that the incident photon will interact in the depletion region times the probability that Si Kα flourescence will occur

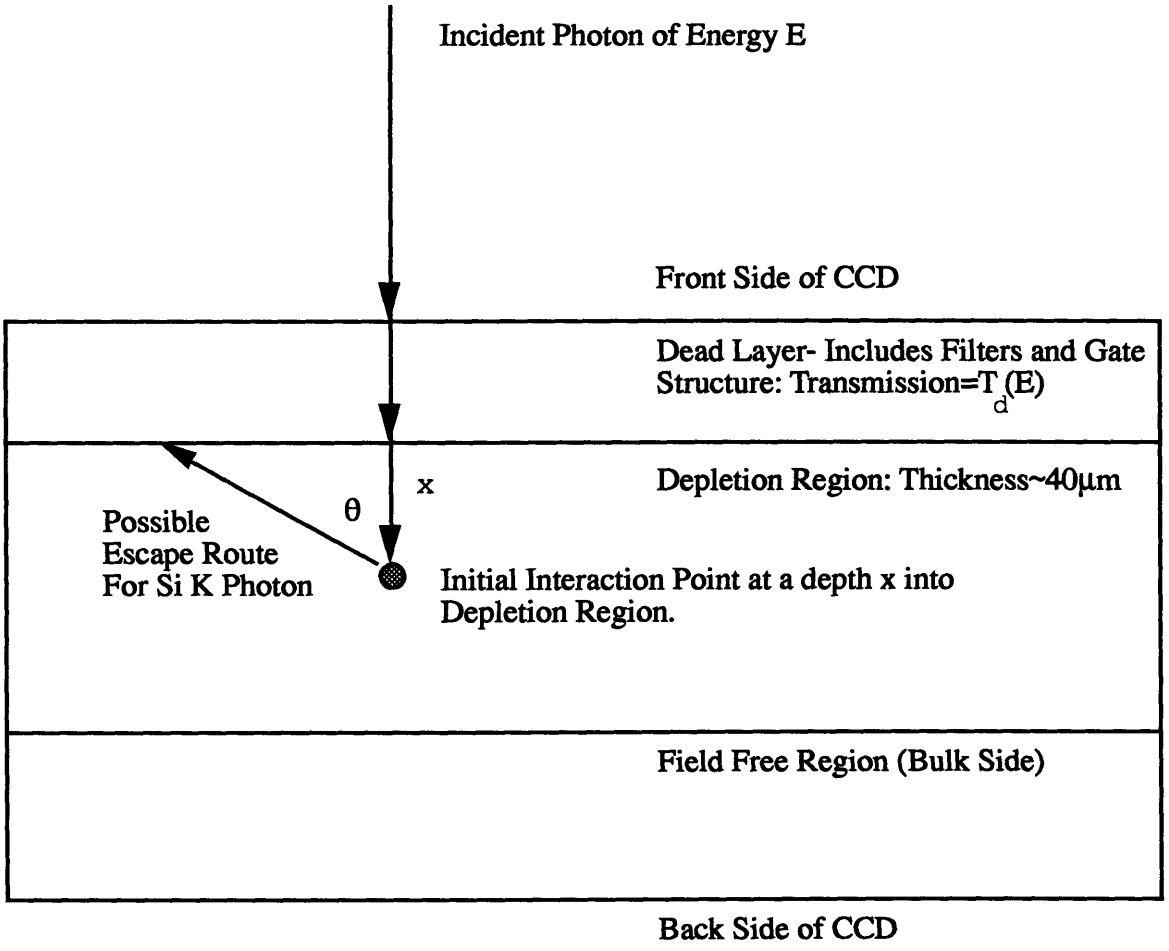

Figure C-1: Escape Peak Geometry

times the probability that the Si Kα photon will leave the depletion region. We consider here only incident photons with enough energy to kick out a K-shell electron of the silicon atom. Figure C-1 shows the simple geometry for the escape calculations. Later on, a more complicated geometry, due to the channel stops, will be discussed.

The probability, $P_{interaction}(E, x)$, that an incident photon will interact at a depth x into the depletion region of the SIS CCD can be calculated by:

$$T_x(E) = e^{\frac{-\lambda_{Si}(E)}{x}} \tag{C.1}$$

$$P_i(E, x) = \frac{T_x(E)}{\lambda_{Si}(E)} T_d(E) \tag{C.2}$$

Where, $T_d(E)$ is the transmission through the dead layer, $T_x(E)$ is the transmission

through the depth x of the depletion region by a photon of energy E, and $\lambda_{Si}(E)$ is the mean free path of the photon in silicon. $T_d(E)$ is complicated but will divide out when we consider the ratio of escape peak events to detected events.

Once the interaction has occured, the silicon atom which actually lost its K-shell electron is both excited and ionized. There are several possibilites of what will happen to it next. One possibility is that it will emit Auger electrons from its outer shells to deexcite. Another possibility is that it will radiatively deexcite by emitting a characteristic photon- primarily a Si-K photon. Dyson's **Xrays in Atomic and Nuclear Physics** has a good discussion of the situation on pg 74. The upshot of this is that 4.6% of the time, the fluorescence will occur. This is called the "fluorescence yield",

$$\omega_K = 0.046. \tag{C.3}$$

The Si Kα photon has a mean free path of about 12.3 microns in silicon. The fluorescence photon is assumed to go in any direction. We are interested in calculating the probability that the photon will leave the charge collection region, leaving the balance of the origional photons energy as the escape event. This probability is dependent on the boundary of the depletion region.

For this simple model, the boundary is simply a set of flat planes- the depletion region is a simple slab. The upper plane separates the gate structure from the depletion region, while the lower plane separates the bulk side field free region from the depletion region. In the more complicated model to be discussed later, the upper boundary is made "wiggly" like lassangia by the channel stops.

We will consider here only integrated events where we combine the charge from 3×3 neighborhoods. This makes escapes out the sides into adjacent pixels extremely unlikely, since they must go more than 2 attenuation lengths to escape.

Consider figure C-1. The probability that the Si-Kα photon will escape out through an infinite plane a distance x away in silicon from its origin is given by:

$$I_{extinct}(x) = \int_0^{\pi/2} d\theta \int_0^{2\pi} d\phi \frac{sin(\theta)}{4\pi} e^{-\frac{x}{\lambda_{Si}(Si_{K\alpha})cos(\theta)}}$$

$$= \int_0^{\pi/2} d\theta \frac{sin(\theta)}{2} e^{-\frac{x}{\lambda_{Si}(Si_{K\alpha})cos(\theta)}} \tag{C.4}$$

I call this integral the escape integral. It has eluded any exact analytical calculation, but it has been fitted by an analytical expression to some precision. The fitted expression which was used in later calculations is given by:

$$I^{fit}_{extinction}(b) = 0.2213 \times e^{-3.659b} + 0.2426 \times e^{-1.278b} \tag{C.5}$$

Given this integral, the fluorescence yield, and the interaction probability, the escape event probability for an incident photon of energy E is given by:

$$P_{escape}(E, d_{dep}) = \omega_K \times \int_0^{d_{dep}} P_i(E, x) \times [I_{extinct}(x) + I_{extinct}(d_{dep} - x)]dx \tag{C.6}$$

Where d_{dep} is the depletion depth. The ratio of escape peak counts to primary peak counts is given by:

$$r(E, d_{dep}) = \frac{P_{escape}(E, d_{dep})}{QE(E, d_{dep}) - P_{escape}(E, d_{dep})} \tag{C.7}$$

Where the CCD quantum efficiency $QE(E, d_{dep})$ is given by:

$$QE(E, d_{dep}) = T_d(E) \times [1 - e^{-\frac{d_{dep}}{\lambda_{Si}(E)}}] \tag{C.8}$$

Thus we see that the dead layer factor divides out in the ratio yielding:

$$r(E, d_{dep}) = \frac{\omega_K \times \int_0^{d_{dep}} \frac{e^{-\frac{\lambda_{Si}(E)}{x}}}{\lambda_{Si}(E)} \times [I_{extinct}(x) + I_{extinct}(d_{dep} - x)]dx}{1 - e^{-\frac{d_{dep}}{\lambda_{Si}(E)}} - \omega_K \times \int_0^{d_{dep}} \frac{e^{-\frac{\lambda_{Si}(E)}{x}}}{\lambda_{Si}(E)} \times [I_{extinct}(x) + I_{extinct}(d_{dep} - x)]dx} \tag{C.9}$$

Figure C-2 shows the ratio as a function of incident photon energy for several depletion depths. Figure C-3 shows the ratio as a function of depletion depth for 5.9 keV xrays from an Fe55 source. A depletion depth of 30-50 microns is expected for the SIS. This model suggests that after 100,000 counts in the 5.9 keV line, one might be able to measure the depletion depth to within about 8 microns. The results shown in figure C-3 can be fitted

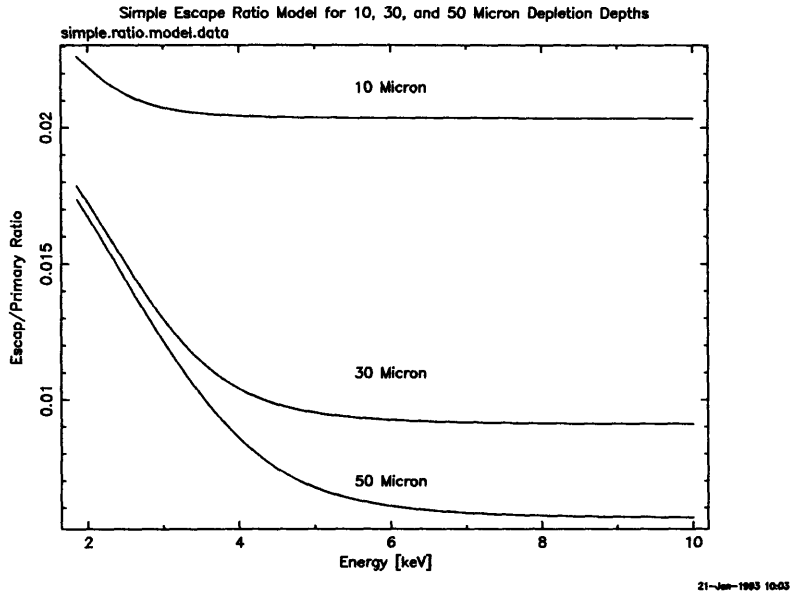

Figure C-2: Ratio of Escape Peak to Primary Peak Using the Simple Model with 10, 30, and 50 micron Depletion Depths.

approximately by:

$$r_{fit}(5.9keV, d) = 0.02645e^{-(d-2.146)/14.98} + 0.00277e^{-(d-383.94)/603.99} \quad \text{(C.10)}$$

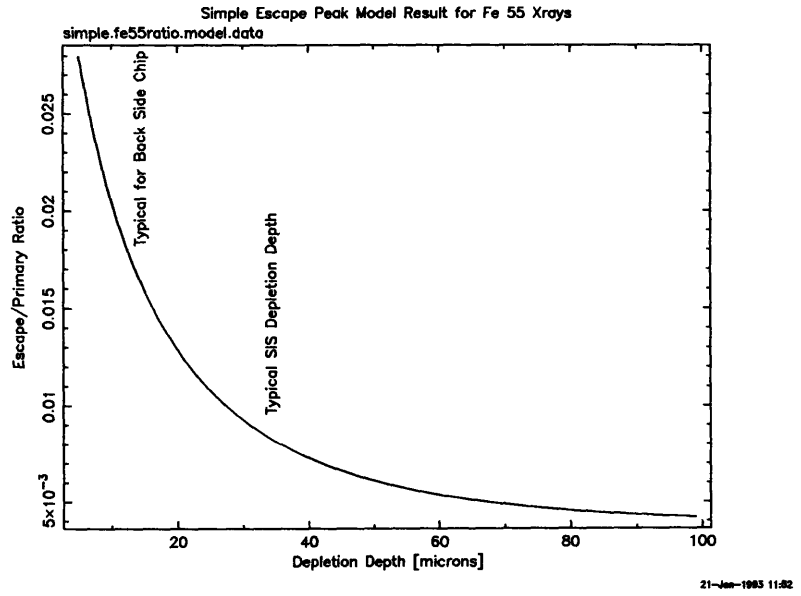

Figure C-3: Ratio of Escape Peak to Primary Peak Using the Simple Model 5.9 keV Xrays.

C.2 Comparison of Simple Escape Peak Model to CCD Data

The depletion depth is a function of parallel clock voltage. Thus by adjusting the parallel clock voltage, we may be able to detect a trend as shown in figure 3. Figure C-4 shows data for the single chip CCID7-367-6 which is of the same lot as the flight devices. Half of the device was irradiated at the Harvard Cyclotron. The data shown comes from the unirradiated side.

The data shows a slight trend toward higher escape to primary ratio as the voltage drops, thinning the depletion region. This data is consistant with a range of depletion depths from about 30 to 50 microns. The mean depletion which it suggests is about 35 microns. When equation C.10 is used with an expression for the depletion depth of the form:

$$d(v) = p_1\sqrt{v - p_2}, \tag{C.11}$$

the data can be fit to yield the depletion depth in microns as a function of the parallel clock voltage, v [volts] (see figure C-4). This fitting yields the following equation for the depletion

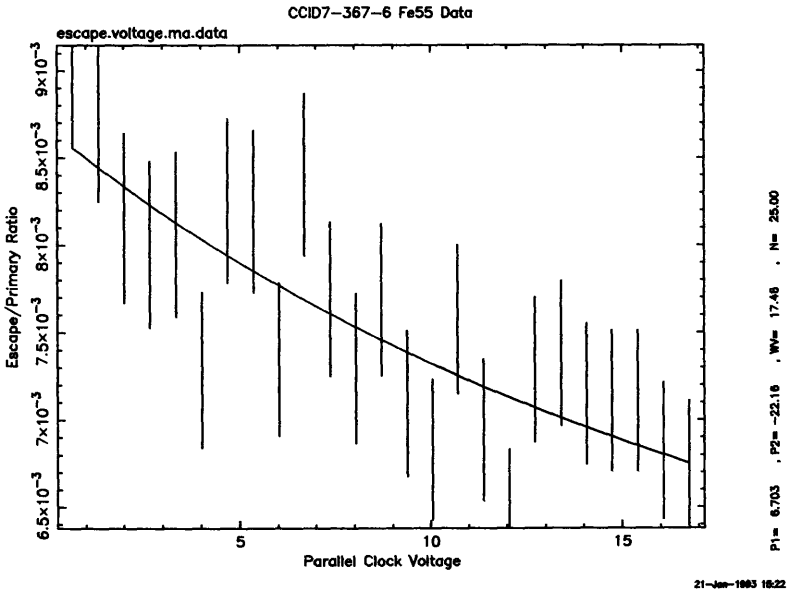

Figure C-4: Fe55 Data from CCID7-367-6: The dependence of the escape to primary peak ratio as a function of parallel clock voltage. The line is the result of a fit to the depletion depth as a function of voltage.

depth:

$$d(v) = 6.7\sqrt{v + 22.16} \ \ [microns] \tag{C.12}$$

You should beware of this result until further confirmation comes from other sources (QE measurements, simulation,...). A particularly interesting thing to do would be to compare the ratio of quantum efficiencies at several voltages to constrain the depletion depth dependence on voltage even further.

We also have data from other devices at different energies. In particular, the White Sands data has data all the way up to 10 keV. Figure C-5 shows measured escape to primary ratios at several energies up to 5.9 keV. All the points were aquired from devices running at roughly 9 volts. The points below 5.9 keV were acquired at White Sands with ADQ7 (a former flight device) while the point at 5.9 keV comes from CCID7-367-6. The curves shown on the same plot are results of the simple escape peak model at several depletion depths.

The 5.9 keV data suggests that the depletion depth is about 35-40 microns. The 4.51 keV data is also consistant with this result. However the data below 3 keV does not follow-

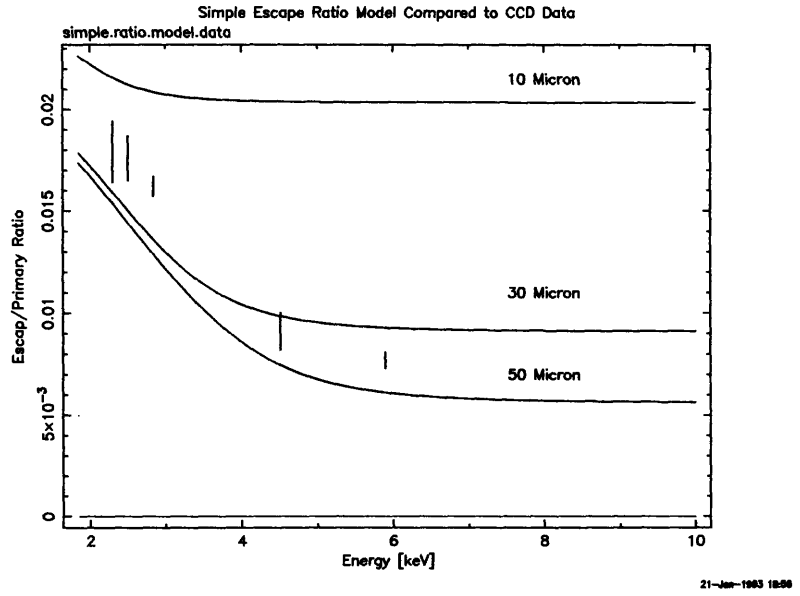

Figure C-5: Escape Peak Data at several energies compared to simple escape peak models.

it seems consistant with a depletion depth smaller than 30 microns.

C.3 The Silicon K Escape Peak Model- Complicated Version

The discrepancy between the high and low energy escape data may suggest a more complicated boundary on the gate side of the depletion region. Low energy photons will interact closer to this surface on average than higher enrgy photons will due to their shorter attenuation lengths. The attenuation length of 6 keV photons is 29 microns in silicon, while 3 keV xrays travel less than 5 microns. Figure C-6 shows the attenuation length of photons in silicon as a function of energy. The softer xrays would be affected by structure on the scale of a few microns on this front side surface.

The channel stops may lead to some deviations from a flat frontside depletion region boundary. The p+ channel stops extend about 1 micron into the depletion region but only get slightly depleted. They are about 6 microns wide as compared to the 27 micron width of the pixel. This leads to a wiggly surface (like lasagna) on the gate side boundary of the depletion region. Figure C-7 shows a cross section of the modified surface.

The wiggling introduces more probable escape avenues for fluorescence due to photons which

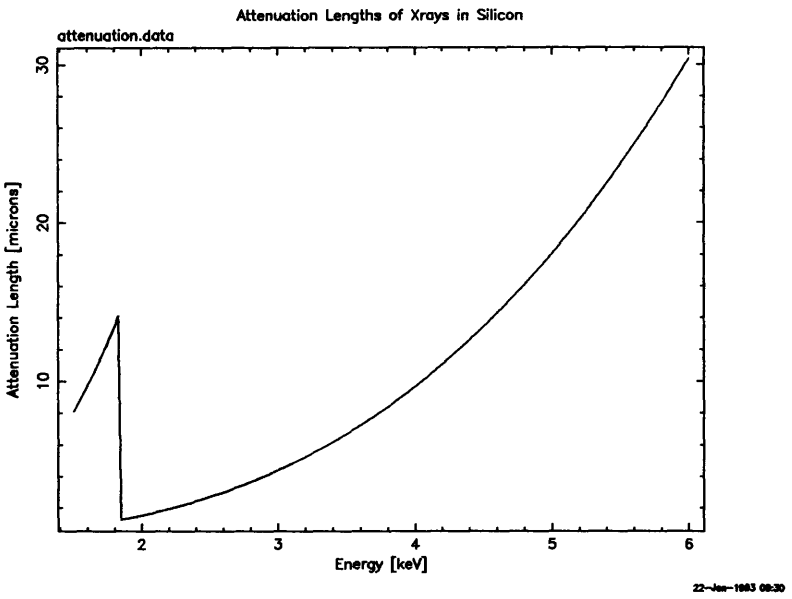

Figure C-6: Attenuation Lengths of Xrays in Silicon.

only interact within a few microns of the front side. The wiggling will also appear to be a good approximation to flat for fluorescence photons which follow interactions due to incident photons which can travel deeper into the depletion region. Thus for lower energy xrays, the escape to primary ratio would be enhanced.

This interpretation hinges on the assumption that Si-K photons which interact in the channel stops do not get detected. This may be a bad assumption, since the cross sectional area (perpendicular to the charge transfer direction) of the region is not too much bigger than the initial charge cloud size you would expect from the Si-K photon interaction. Diffusion would carry some of the escaping charge to the surface where it would be lost to recombination on the surface. It will also carry some backinto the pixels immediately surrounding the pixel of the origional interaction. A detailed calculation would have to be made to asses the total amount of charge returned to the escape pulse height- but most likely it is less than half.

I have not gone through this model in detail yet.

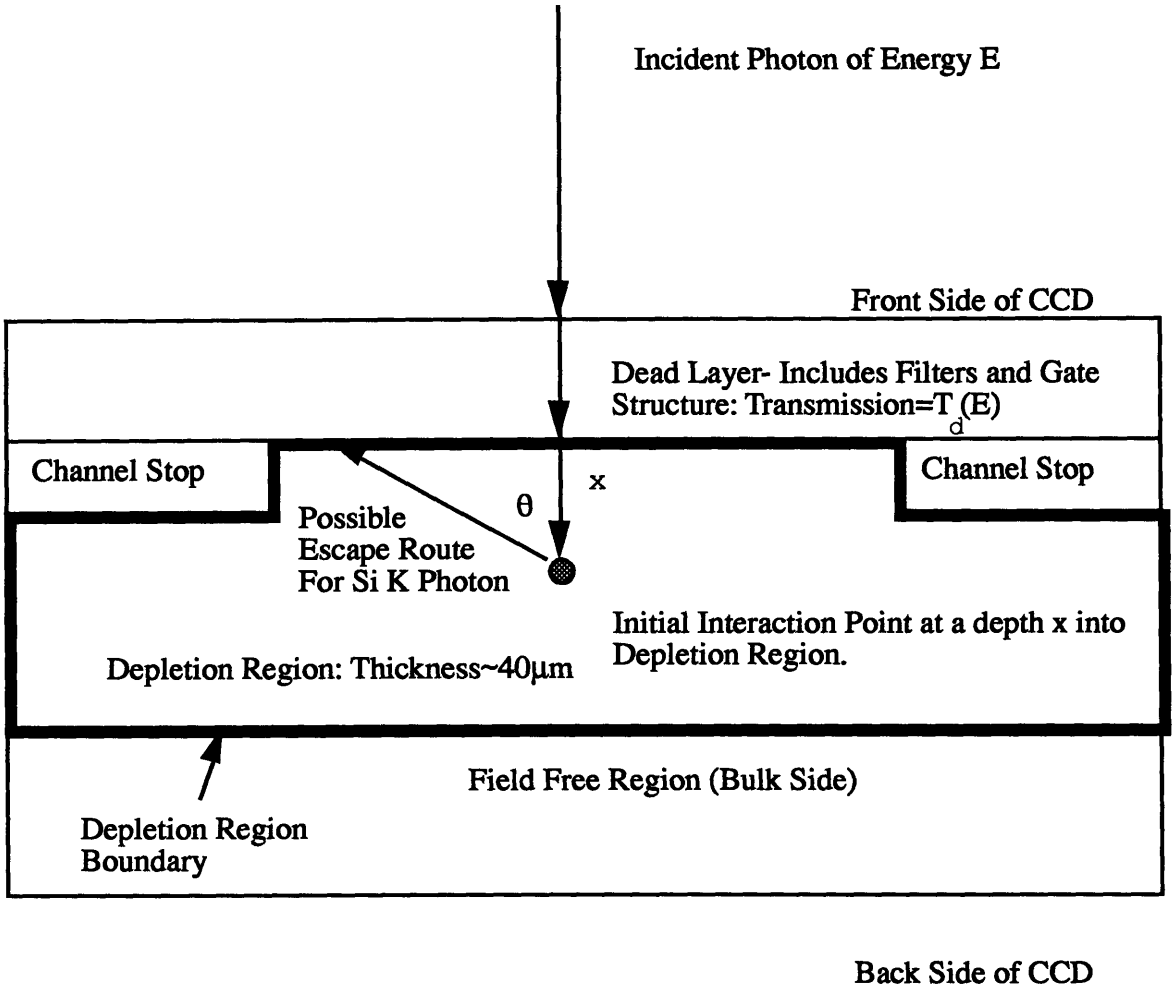

Figure C-7: A More Complicated Escape Peak Geometry. Note: Not to scale and chrge transfer direction is perpendicular to page.

Appendix D

Three Different Ways to Measure Depletion Depths in Xray CCDs as a Function of Parallel Clock Voltage

Presented here are three different ways to measure the frontside depletion region thickness in xray CCDs. These methods are independent of using quantum efficiency measurements to arrive at depletion layer thicknesses. In fact, the methods described here may be used to predict QE in the Astro-D CCDs above 4 keV (or where the deadlayer transmission is practically unity). The dependence of depletion depth on voltage is also addressed with these methods. This dependence yields a rather large QE variation with parallel clock voltage. For instance, the QE at 5.9 keV varies by 35% over the range of allowable parallel clock voltages. Finally, the depletion dependence on voltage will be extended to predict how power law spectrums detected by Astro-D will appear for different parallel clock voltages.

D.1 Introduction

The depletion region is the region of non-zero electric field below the gates of the parallel clock phases. It can be thought of as a volume bounded between two parallel planes: one plane at the gate/channel interface; the other plane at a depth d_d (the 'depletion depth')

below the gates. 'Any' charge which ends up in this region will be detected. In particular, in our quantum efficiency (QE) models, xray interactions occuring in this region will be detected. This region is particularly important for high energy photons. As photon energy increases, so does the mean free path for that photon (at least above the Si-K edge), thus reducing its chance that it will stop in the depletion region. We have gone through great efforts to thicken the depletion region as much as possible to increase the high energy QE. Currently, there are some questions about the high energy QE measurements falling short of prediction. Some of this shortcoming may be due to a misunderstanding of what the actual depletion depth is in the flight devices.

Astro-D memo #s 386 and 463 discuss measurements and simulations made (by GYP) to address the depletion depth question. The measurements described concern the offset between the gate potential and the channel potential. The simulations are one and two dimensional calculations of the depletion depths as a function of channel potential. It appears that the depletion depths go as the square root of the channel potential with different proportionality constants depending on the complexity of the calculation (ie. one or two dimensional). There has been some effort to get a three dimensional Poisson simulator in order to make a more realistic calculation, but there has been no success yet. For all the work presented in this memo, I assume a depletion depth dependence on voltage of the following form:

$$d_d(v) = p_1\sqrt{v - p_2}, \tag{D.1}$$

where p_1 and p_2 are parameters to be fit for. The p_2 parameter closely resembles the channel potential to gate potential offset. For some of the fits to data, the results of channel to gate potential offstes describes in Astro-D memo #386 are used for p_2.

We are left, for now, with empirical methods to get the depletion depth. In this memo, all measurements are made using Fe-55 sources. In addition to the method of absolute QE measurement, three new self contained methods will be described. The new methods require only CCD data. This is unlike the QE method, which requires reference detector measurements. The new methods make use of:

1) escape peak to primary peak ratios (escape method),

2) Kα peak to Kβ peak ratios (relative energy method),

3) relative QE at different parallel clock voltages (relative voltage method).

These three methods are applied to Fe-55 data taken with the protected half of the irradiated CCID7-367-6 at a wide range of parallel clock voltages.

D.2 The Methods

D.2.1 Absolute QE Method

The most direct way is to measure the QE at high energies, correct for the dead layer transmission using the low energy calibration (or assume it is unity for high enough energies), and make use of the equation:

$$QE(E) = T_d(E) \times (1 - e^{\frac{-d_d}{\lambda_{Si}(E)}}) \tag{D.2}$$

where,

$T_d(E)$	is the transmission through the dead layer (1, if energy is high enough),
d_d	is the depletion depth (should be around 35 microns),
$\lambda_{Si}(E)$	is the attenuation length of a photon of energy E in silicon.

At this point, our QE numbers are suspect. Possible problems are the reference detector calibration and source-detector geometric effects. Both of these problems are absent from the new methods.

D.2.2 Escape Method

The physics to this method is described in Astro-D memo #497 and appendix XXX. A result of the escape peak model is that the escape peak to primary peak ratio depends on the depletion depth. In particular, the escape to primary ratio with 5.9 keV xrays can be fitted by:

$$r_{fit}(5.9keV, d_d) = 0.02645e^{-(d_d-2.146)/14.98} + 0.00277e^{-(d_d-383.94)/603.99} \tag{D.3}$$

Using equation D.1, this expression can be used to fit actual data as described in Astro-D memo #497. In that memo, data analysed with a split threshhold of 50 was used in the

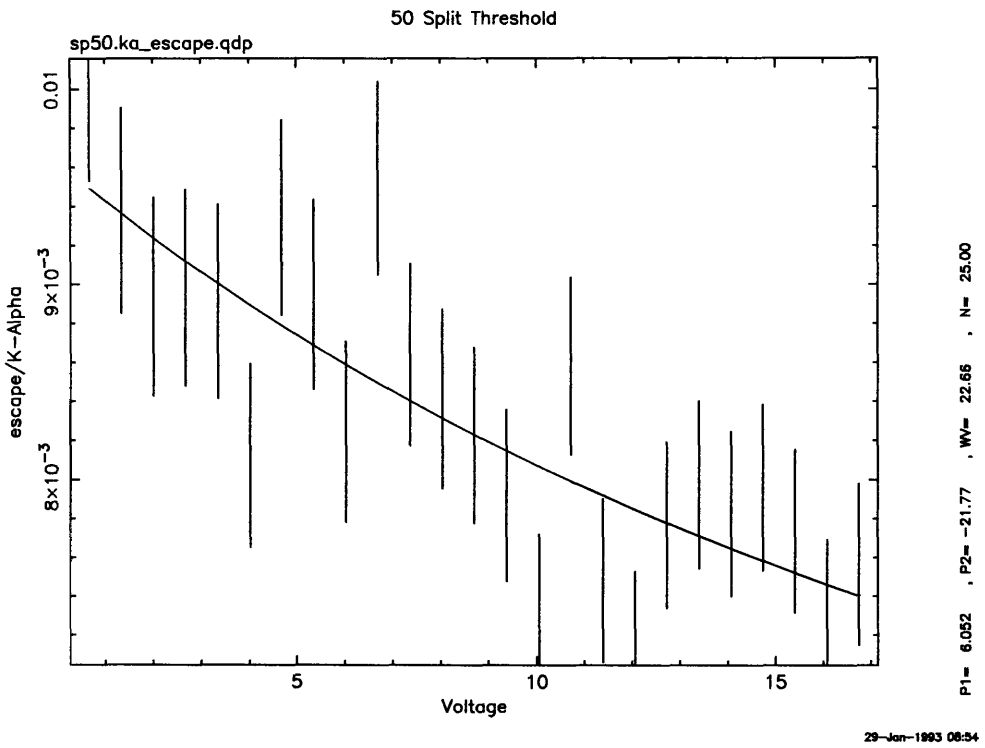

Figure D-1: Escape Ratio Analysis:Split Threshold=50

fits. Here we the data analysed with a range of split thresholds. Figures D-1 and D-2 show fits for data anaylsed with split theshholds of 50 and 120. Notice that the 120 split level data has smaller error bars and that the fit 'looks' better. The dependence on split threshhold to these fits must be examined closely. In the next section, the depletion depth functions that these two fits suggest will be compared.

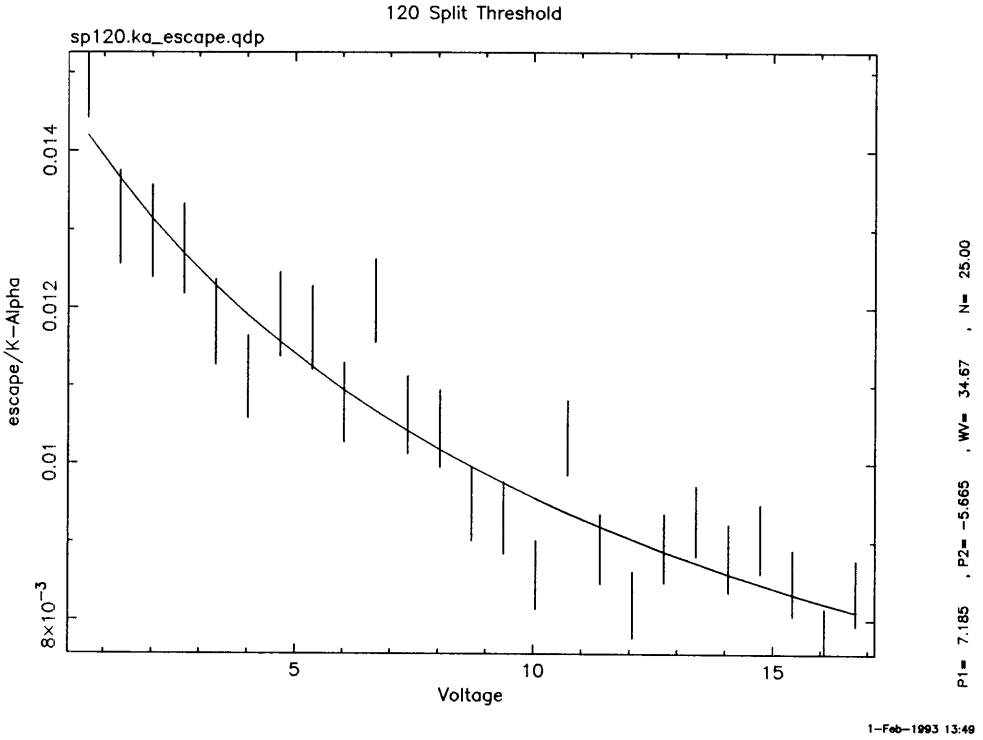

Figure D-2: Escape Ratio Analysis:Split Threshold=120

D.2.3 Relative Voltage Method

In this method, the QE at a given photon energy is compared for different parallel clock voltages. Taking equations (1) and (2), the ratio of the QE at photon energy E for voltages v_1 and v_2 is given by:

$$ratio(E, v_1, v_2) = \frac{(1 - e^{\frac{-p_1\sqrt{v_1 - p_2}}{\lambda_{Si}(E)}})}{(1 - e^{\frac{-p_1\sqrt{v_2 - p_2}}{\lambda_{Si}(E)}})} \tag{D.4}$$

This can be applied to the 5.9 keV x-rays from Fe-55 sources. A 5.9 keV photon has a mean free path of about 29 microns in silicon. Figure D-3 shows detected 5.9 keV x-ray count rate at different parallel clock voltages relative to the rate detected with a parallel clock voltage of 0.67 volts. This shows that over a reasonable range of clock voltages, the QE at 5.9 keV can vary by 35%. The curve drawn on the data is a fit using equation D.4. It suggests that the depletion depth parameters described in equation D.1 are: p_1=9.88 and p_2= -6.39. This fit is fairly insensitive to split threshold level making it a more robust method than the escape peak method.

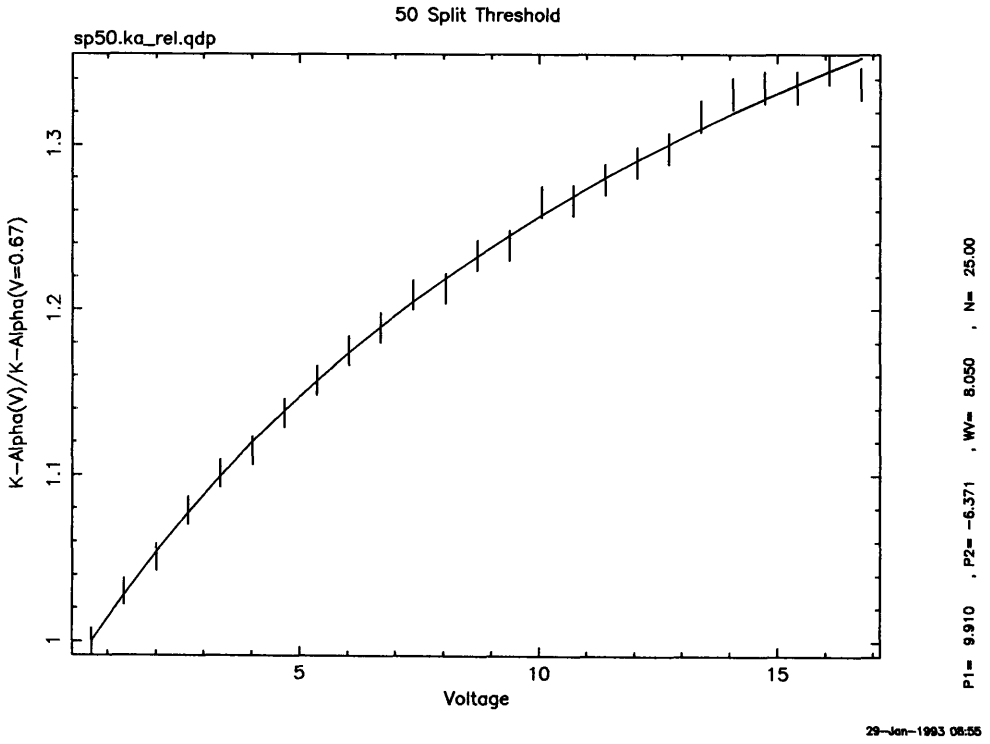

Figure D-3: Relative Voltage Analysis:Split Threshold=50

Figure D-4 shows what the depletion depth is as a function of voltage based on param-

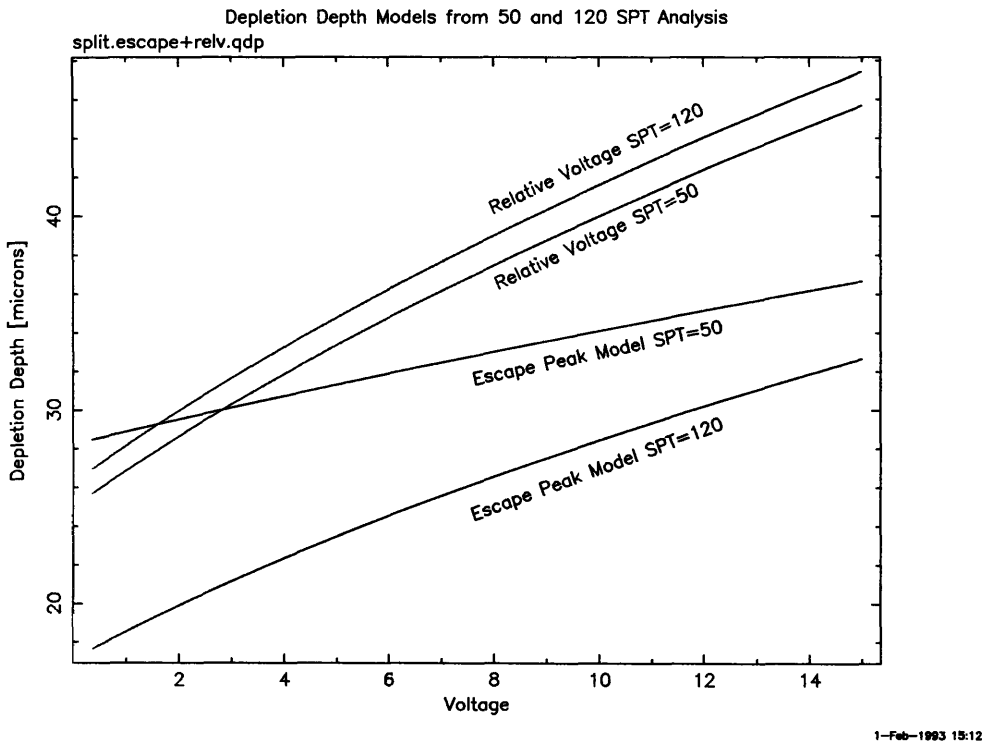

Figure D-4: Comparison of Depletion Depth Models: Escape and Relative Voltage Methods at Different Split Threshold Levels.

eters fitted with the escape peak and relative voltage models at split threshold levels of 50 and 120. A particularly nice result of the relative voltage fit for the depletion depth is that the fitted p_2 values agree with GYP's measurements of the gate-channel potential offsets (ADM # 386).

D.2.4 Relative Energy Method

This method compares count rates for two different energy lines as a function of voltage. The intrinsic ratio of the fluxes is assumed to be constant and is infact a fit parameter in addition to p_1 and p_2. The Fe-55 sources offer two lines (5.89 and 6.49 keV) for this purpose. Taking equations D.1 and D.2, the ratio of the count rates for two lines at energies E_1 and E_2 whose intrinsic flux ratio is p_3 at parallel clock voltage v is given by:

$$ratio(E_1, E_2, p_3, v) = p_3 \times \frac{(1 - e^{\frac{-p_1\sqrt{v-p_2}}{\lambda_{Si}(E_1)}})}{(1 - e^{\frac{-p_1\sqrt{v-p_2}}{\lambda_{Si}(E_2)}})} \tag{D.5}$$

Figure D-5 shows the ratio of detected Mn Kα and Kβ counts for several voltages using a split threshold of 50 along with the relative energy model fit. Figure D-6 shows the same data fit with the p_2 paramter fixed to -6.38 and the p_1 paramter fixed to 9.91 matching the channel potential measurement result and relative voltage result (as in figure D-3). Both fits seem to match the data fairly well. It appears that the relative energy method is not very powerful when using 5.9 and 6.5 keV lines. Perhaps if there were an independent way to fix the p_3 parameter, this method would be a useful tool.

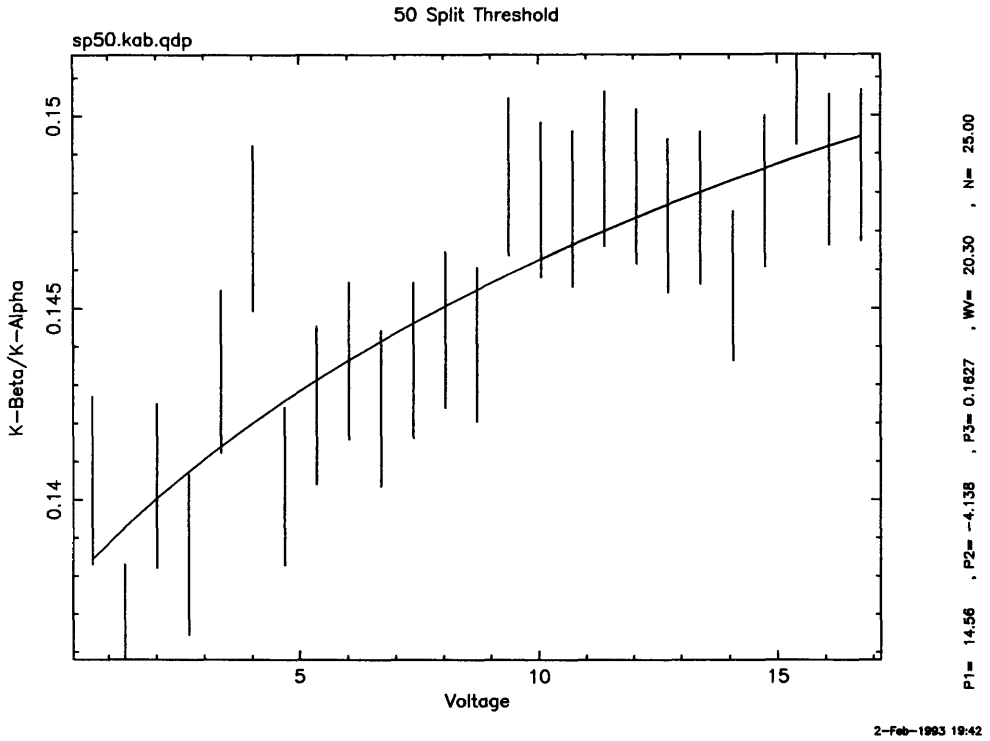

Figure D-5: Fe-55 Data With a Split Threshold of 50 and a Relative Energy Fit

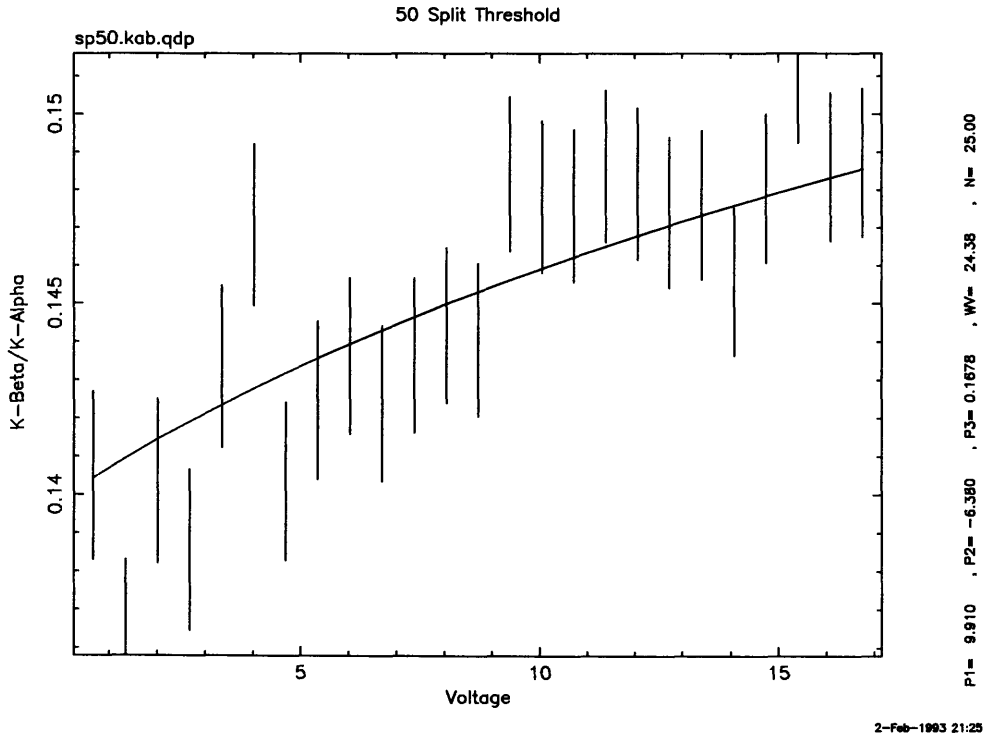

Figure D-6: Fe-55 Data With a Split Threshold of 50 and a Fixed Relative Energy FitUsing Depletion Depth Parameters Matching Those in Figure 3

D.3 Effect of Parallel Clock Voltage on Detected Crab Spectrum

It appears that the relative voltage method gives the most robust evaluation of the depletion depth's voltage dependence. Using the parameters derived from the fit of figure D-3, figure D-7 shows the Astro-D (1 XRT + 1 SIS) effective area for a parallel clock voltage of 3 volts and 16 volts. As expected, the effect is most noticable at high energies.

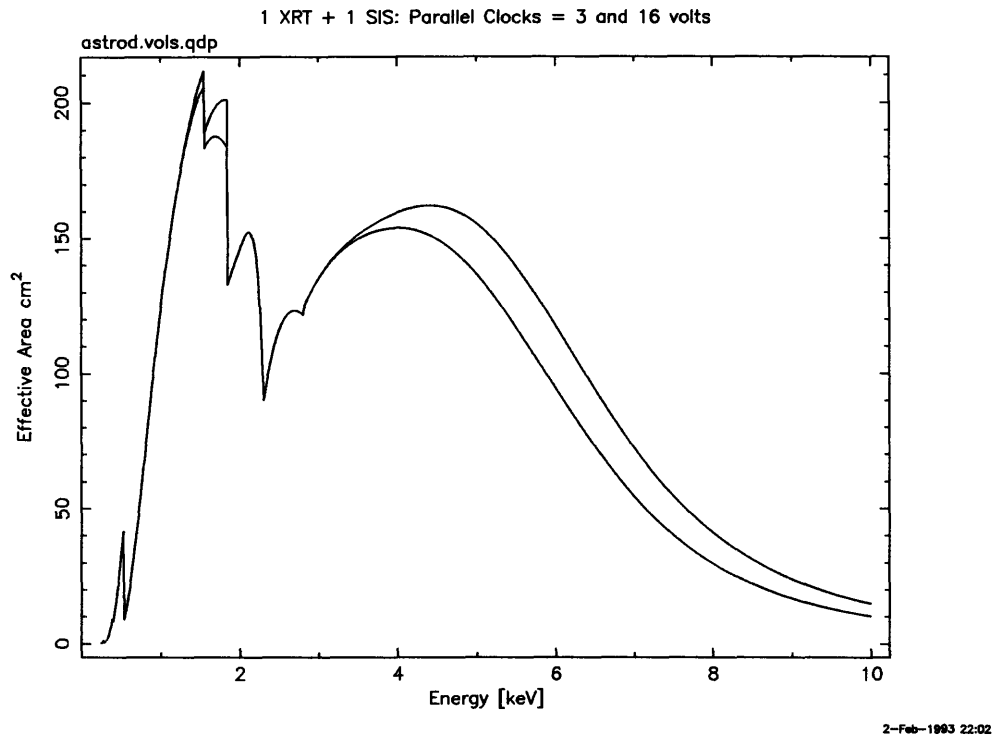

Figure D-7: Astro-D Effective Area for 3 and 16 Volts

Figure D-8 shows the different predicted Astro-D detected spectra (with 6 electrons of noise) when these two effective area curves are applied to the crab nebula. The crab spectrum is an ISM absorbed power law given by:

$$Flux = 10 \times E^{-2.05} \times e^{-\sigma_e(E)N_H} photons/cm^2/sec/keV, \tag{D.6}$$

where $N_H = 3 \times 10^{21} cm^{-2}$.

It may be interesting to pass both of the ph spectra through the current XSPEC response matrices to see how an error in the depletion depth affects the fit of the photon index or

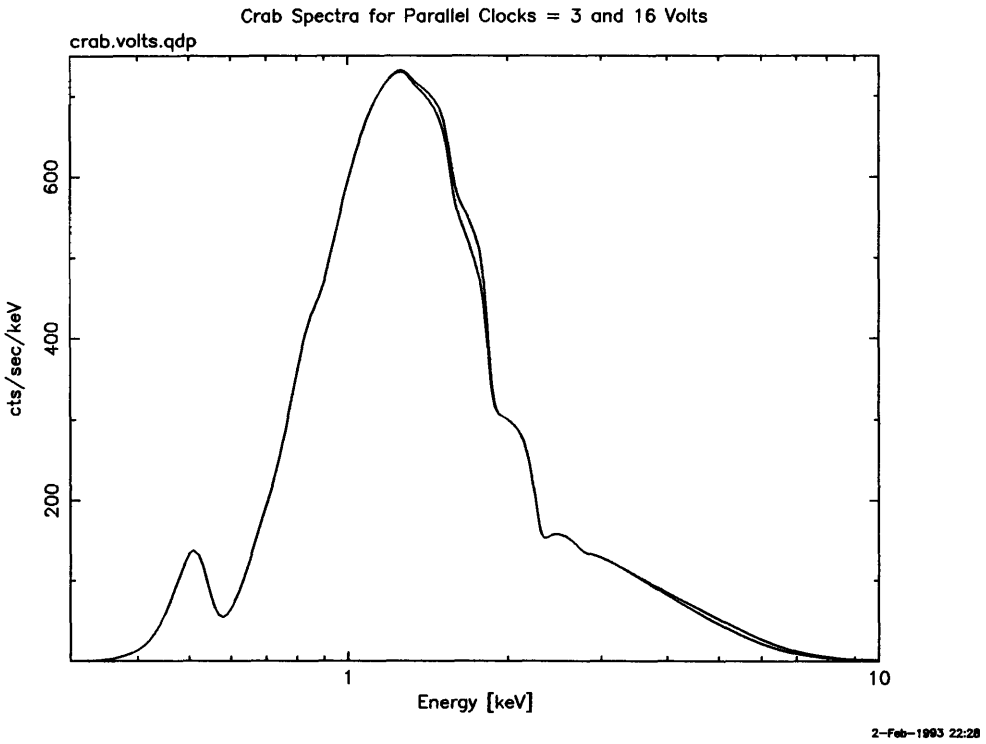

Figure D-8: Detected Crab Spectra: 3 and 16 Volts

normalization. This could be a somewhat serious issue for those people thinking that they will get good science with Astro-D. While the difference may seem slight for the crab, it may make a more significant difference with harder xray sources or those with Fe lines. An example of the Fe lines in the Coma cluster with 3 and 16 volts on the parallel clocks is shown in figure D-9.

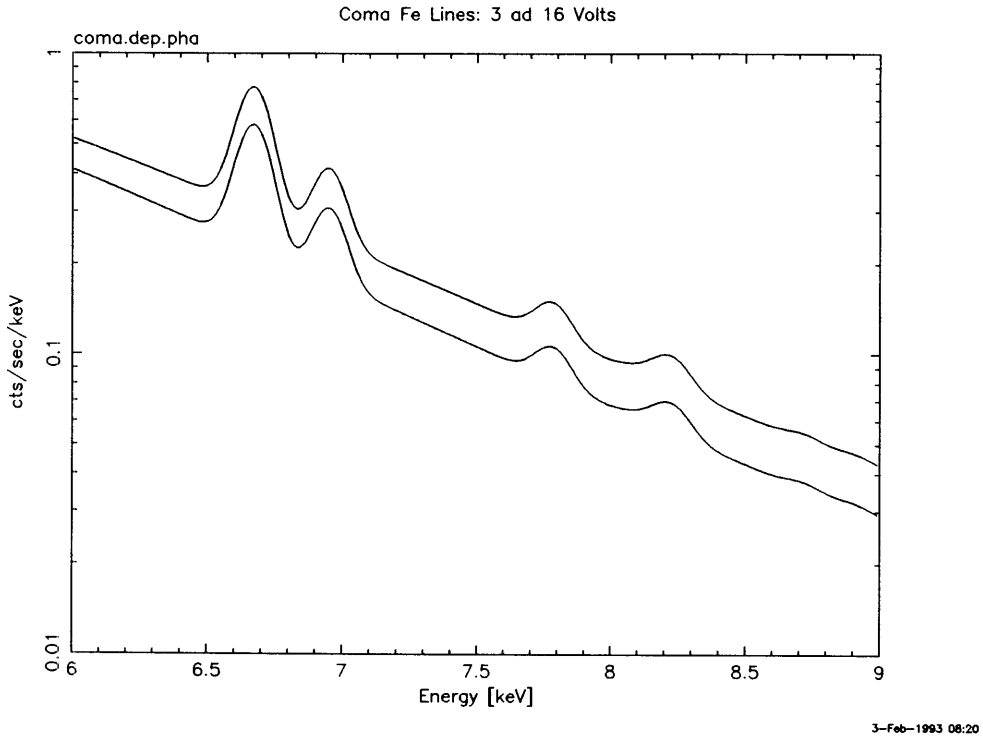

Figure D-9: Detected Coma Fe Lines: 3 and 16 Volts

Appendix E

Wafers Used For the SIS CCDs

Here we list the wafer and die numbers for each of the SIS CCDs. The first 3 digits are the wafer number, while the last digit is the die number.

Table E.1: Wafers and Dies Used For the SIS CCDs

Sensor	Serial Number	Quad Package	Chip 0	Chip 1	Chip 2	Chip 3
SIS-S0	5	ADQ20	463-5	453-1	469-9	469-5
SIS-S1	3	ADQ11	471-3	471-7	471-1	471-9
Flight Spare	4	ADQ19	463-5	453-1	469-9	469-5

Appendix F

The Instrumental Background of the SIS on ASCA

I present an initial report on the instrumental background of the Solid State Imaging Spectrometers aboard ASCA. Factors which affect the intrumental background include the local magnetic rigidity and CCD clocking mode. I will discuss the spatial, spectral, and temporal dependence of the background.

F.1 A Brief Description of the Intrumentation

The two Solid State Imaging Spectrometers (SIS) aboard ASCA are X-Ray CCD cameras made at MIT. In order to understand some of the instrumental background features of the SIS, I review here a basic description of the detectors.

Each detector consists of a hybrid array of four edge abuttable frame-store CCDs made at MIT's Lincoln Laboratory. Each CCD has 27×27 micron pixels in the imaging array and 18×24 micron pixels in the framestore array. Both the imaging array and framestore array have 420×420 pixels.

Each CCD is approximately 380 microns thick, of which about 25-30 microns are depleted for charge detection. The charge cloud produced by an event occuring inside this front 25-30 micron depletion region will be completely collected and registered (usually) as a single pixel or two pixel event. The remaining 350-355 microns of silicon will still participate in photoelectric and other ionizing events with X-rays, Gammas, and high energy particles, but the charge clouds produced will expand freely with time until either recombination

occurs or the charge enters a depletion region. Events which interact deep from the front surface in the CCD tend to be higher energy photons or particles. The expanding charge clouds from these deep background events can encompass several pixels and thus tend to get graded as multiple pixel events (grades 6 and 7; see the AO discription of event grading or Ricker et al, 1994). Figure 3-17 shows and image of CCD data taken before onboard event selection and grading has taken place. In this figure, several cosmic ray events are easily discerned from the X-ray events.

A factor which affects some of this grade rejection of the background is a feature on the CCD called the "Back Diode". The Back Diode is plate attached to the back side of the CCD which can be set at a high potential. The plate then can deplete the silicon reducing the 350-355 micron field free region by about 200 microns. The effect is to reduce the maximum size that an individual deep-interacting event can affect, thus reducing dead area. On ASCA, the back diode has two states: a high voltage ($\sim$ 70 volts) and a low voltage ($\sim$ 12 volts) state. These result in different back delpetion region depth, and thus a possible effect on the grading of deep-interacting background events. Figure F-1 shows a cross section of a part of the CCD with the various depletion and field free regions shown.

Burke, et al (1991) provides a more complete description of the CCDs.

The CCD is mounted on a ceramic plate inside of a gold coated kovar (iron, nickel, cobalt alloy) package. The package is mounted within a gold coated aluminum housing, which is surrounded by a polyethelyn shield. Figure F-2 shows a shematic of the arrangement. The polyethelyn shield and aluminum housing provide protection against radiation damage in the CCD (Gendreau et al , 1993). The optical block filter shown in the figure above the CCD is extremely thin (1000 $\AA$ Lexan + 800 $\AA$ aluminum). A beryllium door is also near the CCD (but not in a clear line of sight). The door was closed for the first few days after the SIS turn on and is now permanently open.

F.2 A Two Component Model for the Origin of the Instrumental Background and the Effects of CCD Operating Mode

The internal background of the SIS can be divided into two components:

1) internal background falling on the imaging array and 2) internal background falling

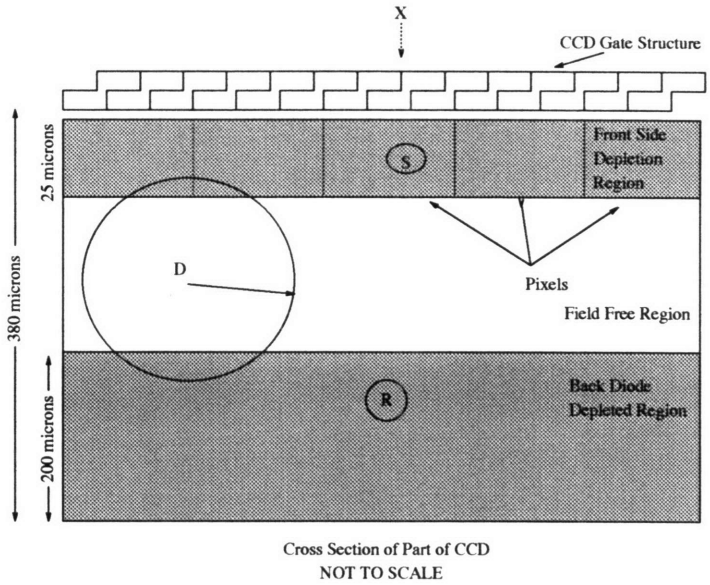

Figure F-1: Cross section of CCD (not to scale) showing X-rays (X) illuminating the CCD from above. The X-rays pass through a thin deadlayer gate structure consisting of polysilicon, silicon oxide, and silicon nitride. X-rays which interact within the front side depletion region usually produce charge clouds which are entirely collected within 1 or 2 pixels (event "S"). Higher energy photons and particles interact deeper in the silicon. Events which originate in the field free region (event "D") will produce expanding charge clouds which affect several pixels. Particles which interact even deeper in the "back diode depletion region" will be entirely collected by the back diode ("R") and not register as an event. All dimensions in the figure are approximate.

on the framestore array.

The first component is proportional to the live time (the sky exposure time), while the second component is proportional to the number of readouts. The number of readouts (N_r) is proportional to the live time (T_l) by the following formula:

$$N_r = \frac{T_l}{T_m}, \tag{F.1}$$

where the frame exposure time (T_m) is a function of clocking mode:

$$T_m = \begin{array}{ll} 4 \text{ seconds} & \text{for 1 CCD mode} \\ 8 \text{ seconds} & \text{for 2 CCD mode} \\ 16 \text{ seconds} & \text{for 4 CCD mode} \end{array} \tag{F.2}$$

Thus if you calculate internal background rates based on sky exposure time, the contribution of the internal background on the Framestore array will be higher as you go from 4 to 2 to

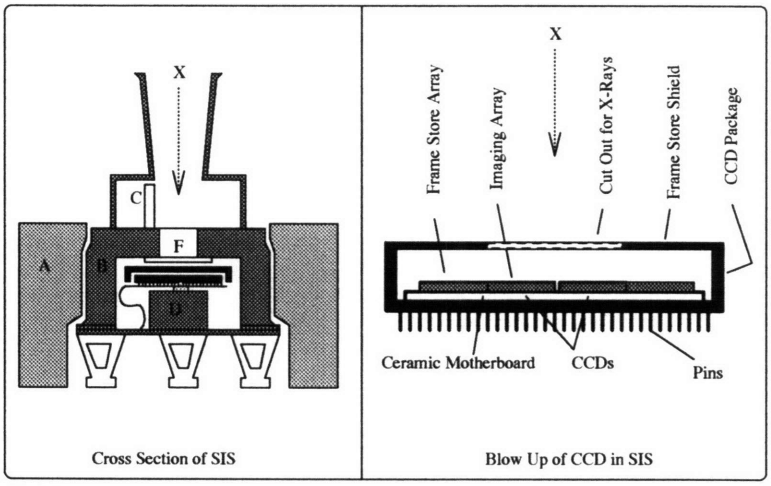

Figure F-2: Cross section of CCD camera (not to scale) showing X-rays (X) illuminating the detector from above. The figure to the left is slice through the whole camera. A polyethelyn shield (A) surrounds the gold plated aluminum housing (B) of the camera. Other material around the CCD include: a berylium door (C) now permanently opened, an aluminized lexan optical blocking filter (F), and a gold plated kovar block (D). The figure to the right is a blow up of the cross section of the region around the CCDs. The CCDs sit on a ceramic plate inside of a gold plated kovar package. A gold plated kovar framestore shield is mounted on the package so as to allow X-rays to allow illumination of the imaging arrays of the CCDs.

1 CCD mode.

In general, there will be a position dependence (in detector coordinates) to the internal background. For the imaging array, it is not easy to see where the background is coming from since the geometry is rather complicated. For the component due to the internal background on the framestore array, the rate will increase with row number, since the "exposure time" of a row in the framestore area increases with row number. Considering this, below is an expression for the background counting rate per row (R(r)) read out:

$$R(r) = D(r) + I_i(r) + (I_0 \times R_{row} \times \frac{r}{T_m} \times P_a), \tag{F.3}$$

where,

D(r) is the sky background (0 when looking at Dark Earth) in counts s^{-1} row^{-1},

$I_i(r)$ is the internal background per row on imaging array in counts s^{-1} row^{-1},

I_0 is the intrinsic internal background rate per row on the framestore region in counts s^{-1} row^{-1},

R_{row} is the readout time per row (9.4 msec)

P_a is the ratio of the pixel areas in the imaging and framestore region (= 0.59)

Thus I should see a slope to the internal background with row.

When equation F.3 is multiplied by the live time, T_l, then it is easy to see that the sky and image area components scale with time, and that (via equation F.1) the framestore component is proportional to the number of readouts.

If one integrate equation F.3 over 420 rows and then divide by 420 rows, then one will get the counting rate per ccd per second (C_m):

$$C_m = \frac{420}{2}\frac{I_0 R_{row} P_a}{T_m} + \frac{1}{420}\int_0^{420} dr(D(r) + I_i(r)). \tag{F.4}$$

We can use equation F.4 to figure out the ratio of internal counting rates for different CCD clocking modes. This could also be used to predict total background rates (Sky+internal) for different modes. For now, consider looking at the dark earth, then we may approximate that:

$$D(r) = 0 \tag{F.5}$$

If we make the additional assumption that:

$$I_i(r) = I_0. \tag{F.6}$$

Then equation F.4 yields the following results for 1, 2, and 4 CCD mode operation:

$$\begin{aligned} C_1 &= 1.29 I_0 \\ C_2 &= 1.14 I_0 \\ C_4 &= 1.07 I_0. \end{aligned} \tag{F.7}$$

In particular, the predicted ratio of internal background rates for both 4 CCD to 1 CCD

mode and also 4 CCD to 2 CCD mode observations per CCD should be:

$$\begin{aligned} \frac{C_1}{C_4} &= 1.203 \\ \frac{C_2}{C_4} &= 1.068. \end{aligned} \tag{F.8}$$

F.3 The Data

F.3.1 Event Grade Rejection

We normally do science analysis with data of grade less than 5. This practice results in a rejection of about 98 % of the all cosmic ray induced events. The higher grade events occur with a frequency of about 1count $s^{-1}cm^{-2}$ of detector. The two component model applies here, and thus the rate is clocking mode dependent and row dependent. There is some evidence that the high grade event rate in the framestore array is larger than it is in the imaging array (F-3). This may be a result of both showering effects from the framestore shield as well as by grading differences due to the smaller pixels in the frame store array. Since we can reject the high grade events so easily, we will not discuss them further here.

F.3.2 Dark Earth Data Selection and Cleaning

To handle the remaining 2% of the internal background, 1, 2, and 4 CCD mode data were collected from April to November 1993 during satellite night while ASCA was looking at the dark side of the earth. We took this "dark earth" data only during satellite night to avoid optical light leakage problems. In addition, we selected data taken atleast 250 seconds after the satellite day-night transition to avoid complications due to dark frame error (DFE) (see Otani et al 1994). Under these restrictions, 300 ksec, 30 ksec, and 160 ksec of 4, 2, and 1 CCD mode data, respectively, was collected.

The SIS is sensitive to optical light. Optical light contamination affects the SIS in two ways: it will lead to high grade events often time resulting in telemetry saturation (in particular with chips 2 and 3 of SIS-S0), and it will lead to gain offsets for normal X-rays. An addition effect that comes with optical light contamination in proximety to the bright earth is the associated atomic oxgen K emission line (0.54 keV) from the bright earth atmosphere.

Hot and Flickering pixels were removed from the data by disregarding any pixels which registered an event twice. This is a reasonable thing to do considering as each CCD has over

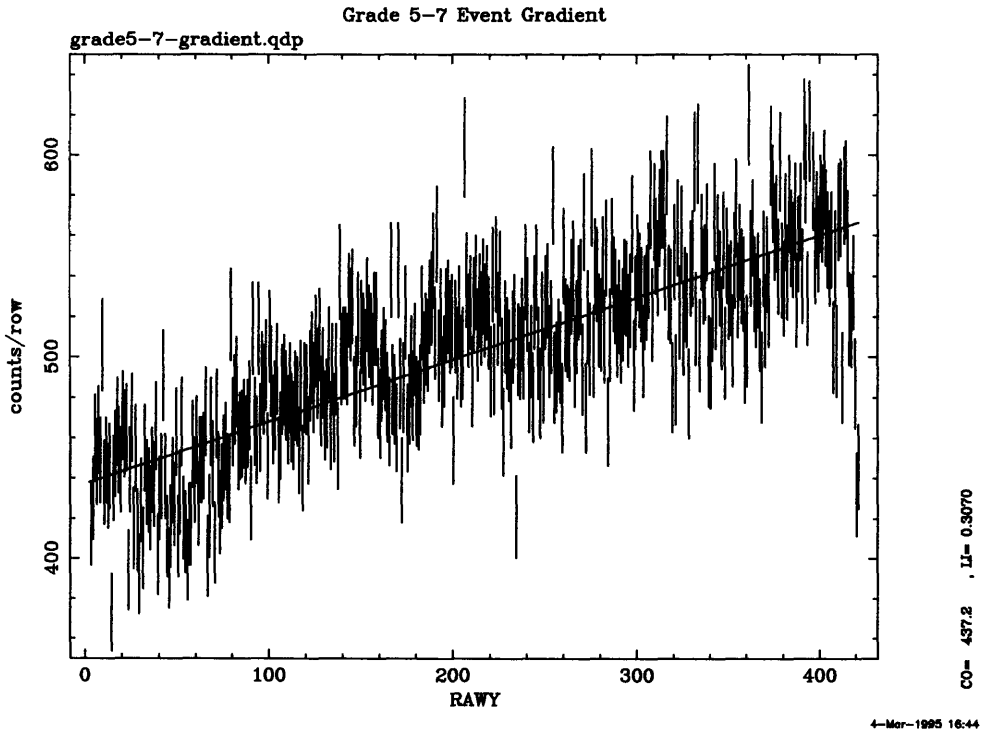

Figure F-3: The gradient in grade 5-7 events with row for the dark earth data. The events represent those from pulseheights for 400 eV to 12 keV. All 8 chips of the 2 SISs are combined here to show the effect. 4 CCD mode was employed. A line is fit to the data. The slope and intercept imply that the intrinsic rate of high grade events is twice as high in the framestore region as it is in the imaging region.

160,000 pixels and during the 300 ksec each accumulates about 3000 internal background events. If the high frequency flickering pixels (hot pixels) are left in, then several "lines" will appear in the resulting pulseheight spectra. The inclusion of the very lowest frequency flickering pixels (e.g. including pixels which registered events 2 or 3 times during this 110 ksec) results in a steep power law feature in the spectra.

F.3.3 Row Dependence

Equation F.3 describes how the background counting rate should vary with row due to the extra exposure time in the framestore region. Figures F-4 and F-5 show the variation in grade 0-4 counts (in 0.4-12 keV) with row for the dark earth data using 4 and 1 CCD mode. The "S" wave shape in the 4 CCD mode data suggests a nonuniform flux on the imaging array- perhaps the background is enhanced along the rows near the framestore area.

F.3.4 Spectral Features

The spectra (figure F-6) of the cleaned dark earth data sets can be characterized by a steep soft power law plus a nearly flat hard continuum, fitted without using the telescope and detector responses, with fluorescence lines due to iron, nickel, aluminum, silicon, cobalt, and gold. Table F.1 lists the line features as well as the possible origin for most of the lines. Due to geometric considerations (see figure F-2), the origin of the cobalt, iron, and nickel emission lines is most likely particle induced fluorescence in the kovar framestore shield. The X-rays from framestore shield will be landing mostly on the framestore array of the CCD leading to strong spatial gradients and clocking mode effects by the two component model described above. There is also some evidence for a gold M absorbtion edge. There is

Table F.1: Spectral Features in the Instrumental Background of the SIS

Element	Designation	Energy keV	Probable Origin
Aluminum	Kα	1.49	Camera Body
Silicon	Kα	1.74	CCD
Iron	Kα	6.40	Framestore Shield
	Kβ	7.06	
Cobalt	Kα	6.92	Framestore Shield
	Kβ	7.65	
Nickel	Kα	7.48	Framestore Shield
	Kβ	8.27	
Gold	Mα	2.12	Gold plating
	L$\alpha - 1$	9.71	Camera Body, Framestore Shield
	L$\beta - 1$	11.44	

also an oxygen line present, which we consider to be most likely of atmospheric origin since there is no Si-K line of comparable strength seen in the spectrum while the fluorescence yield of oxygen is more than an order of magnitude smaller than that of silicon and there is much more silicon around the sensitive part of the detector. The average spectrum of the dark-earth data set from the two SIS sensors has a total intensity of 7.3×10^{-4} ct s^{-1} keV $^{-1}$ per CCD (6×10^{-4} ct s^{-1} keV $^{-1}cm^{-2}$) when in 4 CCD mode. More detailed rates will be given below.

F.3.5 Magnetic Rigidity Effects and Counting Rates

The background rates have a dependence on the local magnetic rigidity in which the satellite is located. Figure F-7 shows a histogram of fractional exposure as a function of magnetic rigidity. In this figure, you can see that for a typical observation, the local magnetic rigidity ranges from 4 to 15 GeV/C with a large hump peaked at about 12 GeV/C. To examine the rigidity effects on the background, we have divided the dark earth data set into low (less than 12 GeV/C) and high (greater than 12 GeV/C) subsets. Table F.2 shows some of the count rates and model parameters found for these two rigidity ranges. The values quoted in table F.2 are mean values for the listed sensor.

The model parameters refer to "/b" models found in the XSPEC fitting package. We fit power laws and multiple gaussian models to the data using the "/b" (background) option which allows us to use the detector response matrix without using the effective area information (ie. we only use the spectral redistribution information and gain relation). For more information type "help background" in XSPEC.

Table F.2: Rigidity Dependencies and Sensor to Sensor Variations

	Less than 12 GeV/C		Greater than 12 GeV/C	
Component	SIS-S0	SIS-S1	SIS-S0	SIS-S1
Counting Rate ($\times 10^{-3}$ c s^{-1} CCD^{-1}) (0.4-10.0 keV)	7.8 ± 0.4	8.7 ± 0.4	5.5 ± 0.3	6.2 ± 0.3
Powerlaw Index	0.37	0.24	0.26	0.23
Powerlaw Norm	1.11×10^{-3}	1.02×10^{-3}	7.2×10^{-4}	7.8×10^{-4}
Line Intensities: ($\times 10^{-5} s^{-1} CCD^{-1}$)				
Al $K\alpha$	32	14	14	8
Iron $K\alpha$	9.8	47	4.8	33
Iron $K\beta$	6.6	22	2	7
Nickel $K\alpha$	50	62	41	42
Nickel $K\beta$	8	6	1	1

There are a few things to notice in table F.2:

(1) The total counting rate of SIS-S1 is 12% bigger than that of SIS-S0.

(2) The iron line intensity on S1 is about 5 times bigger than it is on S0 while having very similar nickel intensities. This may indicate that the gold plating on the framestore shield of S0 is thicker than it is for S1. The iron and nickel lines most likely originate in the kovar (an Fe/Ni alloy) framestore shield which is plated with a nominal thickness of 2 microns of

gold. The 1/e lenghth of a 6.4 keV photon in gold is about 1.5 microns, so the transmitted intensity would vary greatly with variations of the gold plating thickness.

(3) The aluminum line intensity is about 2 times bigger on S0 than it is on S1. This may be due to variations in the thickness of gold plating on the aluminum camera bodies of the sensors.

(4) The fluorescent line intensity is about 2 times bigger for the lower magnetic rigidity data than for the higher rigidity data. This may just reflect that the lines are a result of particle induced fluorescence and the particle intensity increases as the local magnetic rigidity decreases.

Figure F-8 shows a plot of combined SIS-S0 and SIS-S1 count rates for different energy bands as a function of magnetic rigidity. There is a general trend that the count rate increases with decreasing magnetic rigidity. However, there is also a region of enhanced counting rates from about 8 GeV/c to 12 GeV/c. This enhancement is particularly strong for the 0.4-0.9 keV energy band. Notice that the count rate for this energy band also dramatically increases for magnetic rigidity less than 5.5 GeV/c.

For most of the analysis we have done, we choose data taken with magnetic rigidity greater than 8 GeV/C. Table F.3 shows the fit parameters for each of the individual CCDs with this rigidity selection. Again, the parameters apply to "/b" models found in XSPEC. Also, all lines are assumed to have a width (sigma) of 1 eV. Line intensities are given in counts $s^{-1}CCD^{-1}$. We used the XSPEC model "mo pōwerlaw/b + gaussian/b + gaussian/b + gaussian/b + gaussian/b + gaussian/b + gaussian/b".

Table F.3: Background Model Parameters for Dark Earth Data with Rigidity Greater than 8 GeV/C

Component	*Units*	SIS-S0				SIS-S1			
	Per CCD	0	1	2	3	0	1	2	3
Powerlaw Index	N/A	0.11	0.29	0.24	0.25	0.16	0.19	0.17	0.17
Powerlaw Norm	10^{-4}	6.7	9.2	7.8	8.5	8.1	8.5	9.0	9.2
Al $K\alpha$	10^{-4}	1.28	2.54	2.37	2.63	1.39	1.47	0.56	1.13
Iron $K\alpha$	10^{-4}	0.84	0.63	0.92	0.00	3.79	4.03	2.57	3.80
Iron $K\beta$	10^{-4}	0.00	1.00	0.01	0.28	1.22	1.92	0.38	0.78
Nickel $K\alpha$	10^{-4}	4.14	2.24	5.30	3.66	5.05	3.33	6.02	4.17
Nickel $K\beta$	10^{-4}	0.28	0.19	0.21	0.34	0.29	0.92	0.00	0.00
Gold $L\alpha_1$	10^{-4}	0.70	0.79	0.70	0.28	0.88	0.38	1.33	0.94

Typical errors (90% confidence) on the powerlaw index and normalization are: ± 0.1

and $\pm 3 \times 10^{-4}$. The errors on the bright lines (the $K\alpha$ and $L\alpha$ lines) are typically about $\pm 1 \times 10^{-4}$.

F.3.6 Temporal Stability of the Instrumental Background

For a typical observation, the local magnetic rigidity defines the short term intensity of the instrumental background. Although, the number of flickering pixels may change suddenly during passages across the night/day terminator of the orbit as well as near the bright earth. This will be discussed elsewhere.

To address the longterm stability, we have looked at the intensity of the 8-12 keV spectrum from all of the deep survey fields observed with ASCA. The instrumental background dominates over the cosmic X-ray background in this energy range (Gendreau et al, 1995). The observations occurred at various times from March, 1994 to September, 1994. No significant variations in the 8-12 keV flux was measured.

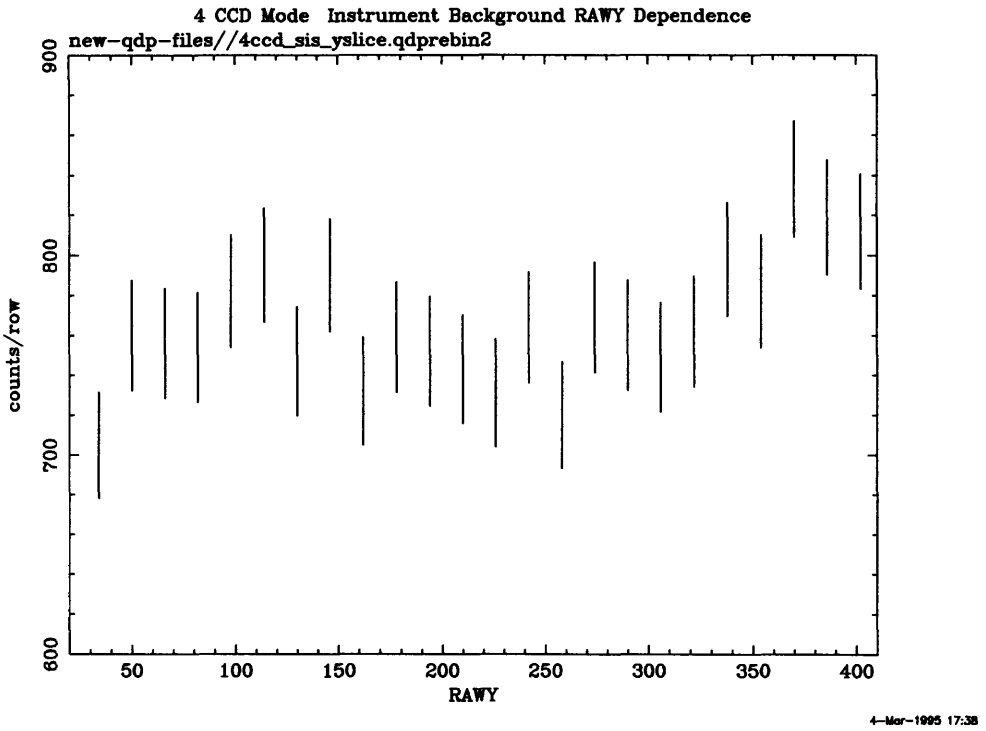

Figure F-4: The gradient in grade 0-4 events with row for the dark earth data. The events represent those from pulseheights for 400 eV to 12 keV. All 8 chips of the 2 SISs are combined here to show the effect. 4 CCD mode was employed. The "S" wave in the flux may indicate that the background is enhanced for regions of the imaging array near the framestore shield.

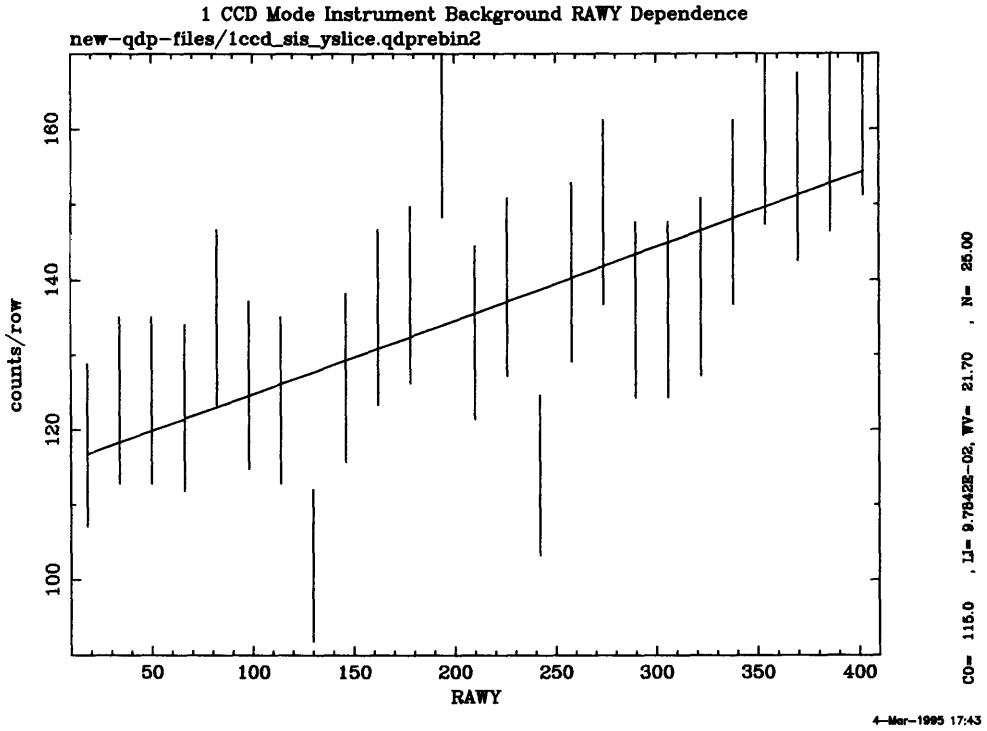

Figure F-5: The gradient in grade 0-4 events with row for the dark earth data. The events represent those from pulseheights for 400 eV to 12 keV. All 8 chips of the 2 SISs are combined here to show the effect. 1 CCD mode was employed.

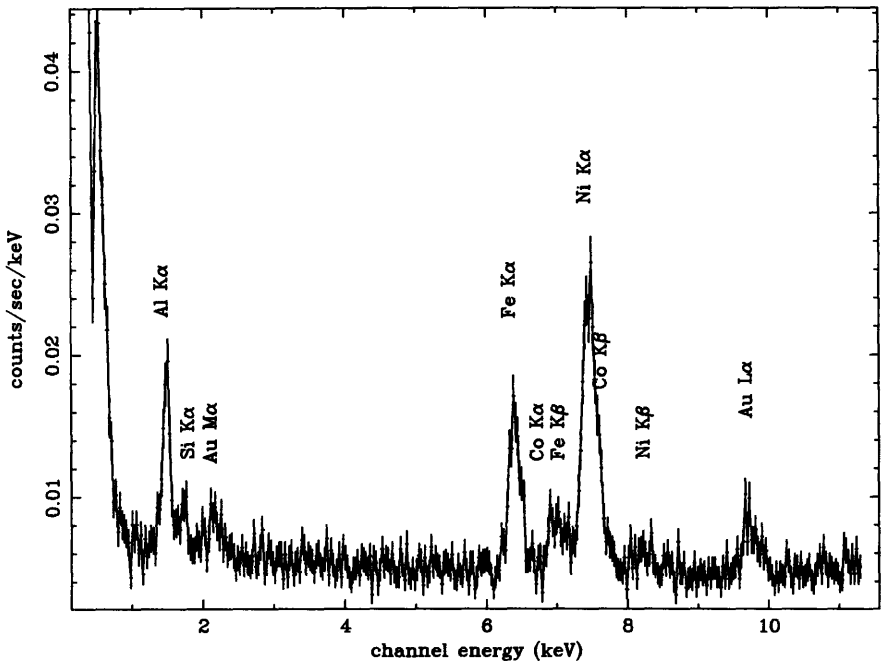

Figure F-6: The spectrum grade 0-4 events for the 4 CCD mode dark earth data. The events represent those from pulseheights for 400 eV to 10 keV. The spectrum is the sum of data from each of the eight CCDs on ASCA.

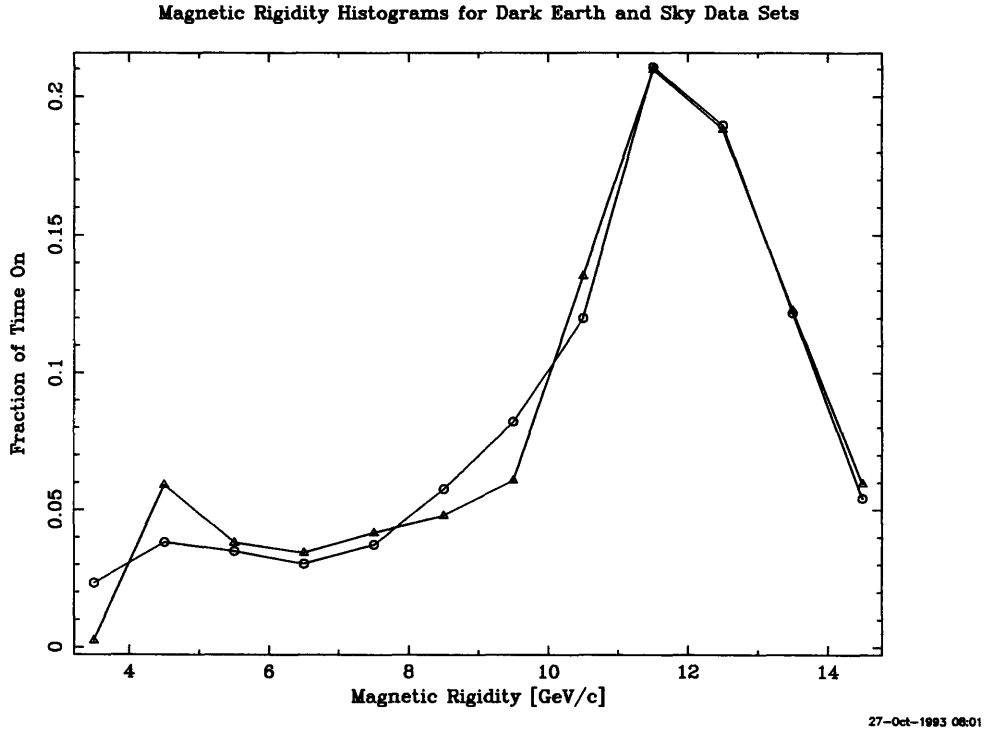

Figure F-7: A histogram showing the fraction of an observation that is done while the satellite is within a region of given local magnetic rigidity. For the plot above, two histograms are shown: one for the collection of dark earth data taken and one for the cosmic XRB data taken. The similarity of the curves helps to justify the use of the dark earth data as background for the XRB data.

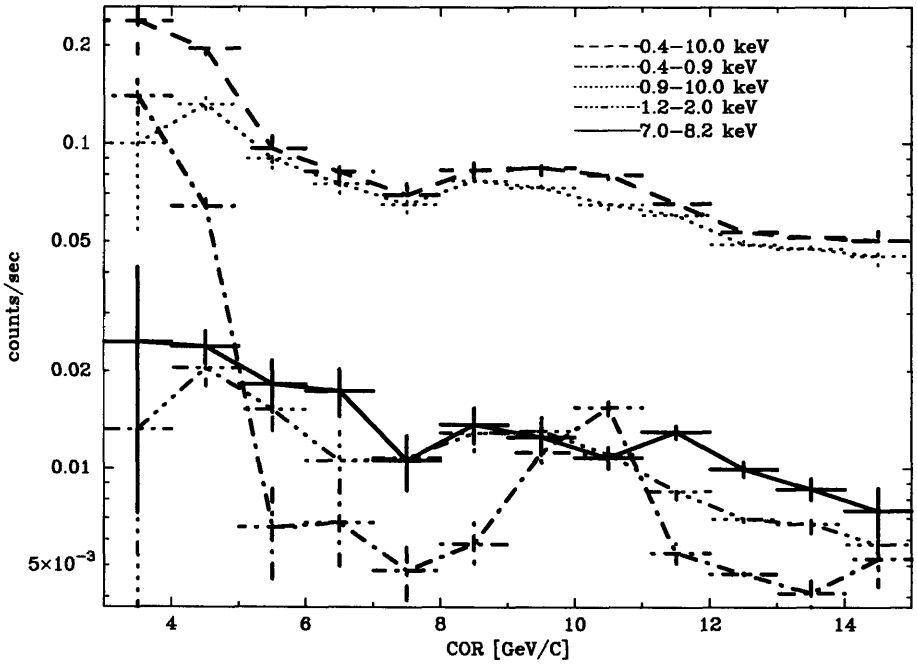

Figure F-8: Combined SIS-S0 and SIS-S1 count rates as a function of magnetic rigidity in different energy bands. There is a general trend that the count rate increases with decreasing magnetic rigidity. However, there is also a region of enhanced counting rates from about 8 GeV/c to 12 GeV/c.

F.4 Discussion

We have presented a two component model to the instrumental background on the SIS. This model should hold for any CCD used in frame transfer mode. Two important results of this model are that the measured instrumental background rates should change with clocking mode and that there should be a gradient in the instrumental background with row. This model can be exploited to try and understand the spectral differences of the instrumental background on the framestore array and imaging array. This type of analysis still needs to be done. A knowledge of the differences could be used to evaluate schemes for reducing the background by modifying the framestore array. Some modifications could be made with the SIS now on ASCA (at the cost of extra calibration), while others would be reserved for future missions with CCDs. Possible modifications include:

1) Changing the clock voltages on the framestore array to reduce the quantum efficiency of the array for particle induced events. This is currently possible with the SIS- but some recalibration may be necessary. This may also modify hot pixel (flickering pixel) growth rates.

2) Modification of split threshold level and grades in event detection. The pixels are smaller and shaped differently in the framestore region leading to differences in the grading of events. This is partly doable with the SIS, but would require a huge recalibration effort.

3) Modification of pixel shapes and sizes in the framestore array to enhance rejection by grade of particle induced events. This would be something to consider for future missions. A possible modification would be to make the framestore pixels really small so that even X-Rays produced by particle interactions in materials near the framestore array appear as large events.

4) Modification of the framestore shield to reduce unwanted background features. Again, this would be something to consider for future missions. Possible modifications would be to increase the gold plating thickness so that the iron and nickel lines do not come through (if kovar is still used).

Finally, we must consider where the instrumental background stands compared to the cosmic X-ray background. Figure F-9 (Gendreau et al, 1995) shows the data from several deep field observations made during the ASCA PV phase. The models fitted to the dark earth data of figure F-6 are drawn into figure F-9. For energies less than about 5 keV,

the sky background is more important than the instrumental background. Although, the aluminum K line at 1.5 keV might pose a problem in some cases.

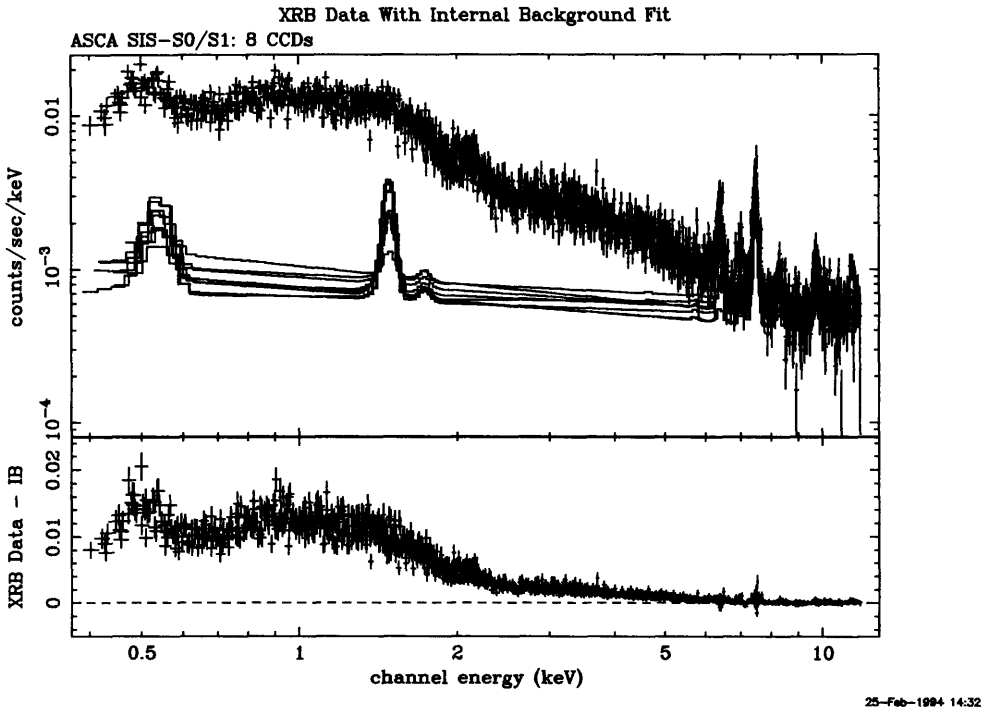

Figure F-9: The spectrum of the Cosmic X-Ray background shown against the instrumental background. All data taken with magnetic rigidity greater than 8 GeV/C.

Appendix G

Calibration Scripts

I have listed here some of the basic UNIX CSH scripts used in the data acquisition.

For reference, "bones" is a NEXT machine, "jano" is a Sun Sparc 2 station, "erg" is a Sun Sparc 1+ station.

G.1 Absolute Quantum Efficiency Data Acquisition Script

```
#script to do a qe run:
# This will get a starting scanposition, a scan stepsize, a number of steps
# an mca exposure time perstep, a ccd framecount perstep, and an fpc-ccd
# chop number per step.
#
#For each step, it will move the scan and then....
#
# At each step it will do the following <chops> times:
# 1) move to fpc position
# 2) get an fpc exposure ->mca.<scan position>.<chop #>.dat
# 3) move to ccd position
# 4) Take the specified number of CCD frames.
# ->ccd.<scan position>.<chop #>.<frame numbers>.fits
#
#
#The analysis is done elswhere.
#
# This script expects that you alias "fpc" to move the fpc in line,
# as well as aliasing "ccd" to move the ccd into place.
# A typical alias for these would be:
#  alias fpc "rsh -n bones 'neat310 mh+; sleep 15; neat310 mr-4400'"
#  alias ccd "rsh -n bones 'neat310 mh-; sleep 15; neat310 mr3000'"
```

```
#
#
# I suggest putting thes aliases in a file that has all the spectrometer
# and source settings also described.......
if ($#argv <8) then
cat <<ENDHLP

qerunpos <start scan> <scan step> <# steps> <mca LT> <ccd frames cnt>
< # chops > <Quad name> <ccd position name>

qerun will start at a given scan position reading and step in a given
stepsize for a given number of steps.
At each step, it will do a given number of chops.
For each chop it will take an mca exposure and a number of
ccd images.

For each step, it will put the relevant data in a directory
given by scan<scanpoosition>.

Quad name is used to get a header name per the "newdir" standard.

ENDHLP
exit 1
endif

set ccdposition=$8

source qesetup.${ccdposition}

set scanpos=$1
set i=0

#START LOOP

while (${i}< $3)
@ i++

#first move the grating
rsh -n bones "~kcg/hettrick/scan/scan ${scanpos}"

#make a new directory
mkdir scan${scanpos}.${ccdposition}
cp *.hdr scan${scanpos}.${ccdposition}
cd scan${scanpos}.${ccdposition}

set j=0

#START CHOP LOOP
```

```
while (${j}<$6)
@ j++

#move in FPC (This assumes an alias of the sort described above)
echo Moving FPC into beam.
fpc
sleep 2

#get mcadata
echo Getting mca data...

rsh -n bones "cd `pwd`;~kcg/hettrick/neat310/mcaget \\
mca.${ccdposition}.${scanpos}.${j}.dat $4"

echo Got mca data for chop $j.
echo

#get ccd data (This assumes an alias of the sort described above)
echo moving CCD into beam

ccd
sleep 2
echo Getting CCD data...

rsh -n jano "cd `pwd`;rappendhk <$7.hdr >\\
ccd.${ccdposition}.scan${scanpos}.${j}.hdr"


rsh -n bones "cd `pwd`;movie ${5} \\
ccd.${ccdposition}.scan${scanpos}.${j}.hdr"

echo Got CCD data for chop $j.

#End Chop loop

end

#Now move scan to next position....

cd ../

echo Moving scan to next postion...


set scanpos=`opstrm $scanpos $2 + = q`

#End main loop
```

```
end
```

G.2 Relative Quantum Efficiency Data Acquisition

```
#script to do a qe run:
# This will get a starting scanposition, a scan stepsize, a number of steps
# , a ccd framecount perstep, and a
# chop number per step.
#
#For each step, it will move the scan and then....
#
# At each step it will do the following <chops> times:
# 1) move to ccd position 1
# 2) get ccd data at neatposition 1
# ->ccd.neat<position 1>.<scan position>.<chop #>.<frame numbers>.fits
# 3) move to ccd position 2
# 4) get ccd data at neat position 2
# ->ccd.neat<position 2>.<scan position>.<chop #>.<frame numbers>.fits
#
#
#The analysis is done elswhere.
#
#
if ($#argv <8) then
cat <<ENDHLP

qerelrun <start scan> <scan step> <# steps>  <ccd frames cnt>
< # chops > <Quad name> <position 1> <position 2>

qerelrun will start at a given scan position reading and step in a given
stepsize for a given number of steps.
At each step, it will do a given number of chops.
For each chop it will get data at two neat310 positions
ccd images.

For each step, it will put the relevant data in a directory
given by scan<scanposition>.

Quad name is used to get a header name per the "newdir" standard.

ENDHLP
exit 1
```

```
endif


set scanpos=$1
set scanstep=$2
set scancount=$3
set chop=$5
set quad=$6
set count=$4
set pos1=$7
set pos2=$8
set i=0

#START LOOP

while (${i}< ${scancount})
@ i++

#first move the grating
rsh -n bones "~kcg/hettrick/scan/scan ${scanpos}"

#make a new directory
mkdir scan${scanpos}
cp *.hdr scan${scanpos}
cd scan${scanpos}

set j=0

#START CHOP LOOP

while (${j}<$chop)
@ j++

#move to position 1
rsh -n bones "neat310 mh-; sleep 5 ; neat310 mr${pos1}"
sleep 5

#get ccd data at position 1
echo Getting position 1 data...

rsh -n jano "cd `pwd`;rappendhk <${quad}.hdr >\\
ccd.neat${pos1}.scan${scanpos}.${j}.hdr"

rsh -n bones "cd `pwd`;cineplex ${count} \\
ccd.neat${pos1}.scan${scanpos}.${j}.hdr"

echo Got CCD data for chop $j Position 1.
```

```
echo
# go to position 2
rsh -n bones "neat310 mh-; sleep 5 ; neat310 mr${pos2}"
sleep 5
#get ccd data at position 2

echo Getting CCD data...

rsh -n jano "cd `pwd`;rappendhk <${quad}.hdr >\\
ccd.neat${pos2}.scan${scanpos}.${j}.hdr"

rsh -n bones "cd `pwd`;cineplex ${count} \\
ccd.neat${pos2}.scan${scanpos}.${j}.hdr"

echo Got CCD data for chop $j Position 2.


#End Chop loop

end

#Now move scan to next position....

cd ../

echo Moving scan to next postion...


set scanpos=`opstrm $scanpos $scanstep + = q`

#End main loop

end
```

Appendix H

Acronyms

ACS Attitude Control System

ADU Analog to Digital Unit

AE Analog Electronics

AGN Active Galactic Nuclei

ASCA Advanced Satellite for Cosmology and Astrophysics

AXAF Advanced X-ray Astrophysics Facility

BCP Beneficiary Charge Packet

BDR Bubble Data Recorder

CCD Charged-Coupled Device

CMB Cosmic Microwave Background

CTE Charge Transfer Efficiency

CTI Charge Transfer Inefficiency

DAC Digital to Analog Converter

DD Deuterium-Deuterium

DE Digitial Electronics

DFE Dark Frame Error

DP Digital Processor

EOB Extendable Optical Bench

FOV Field of View

FPC Flow Proportional Counter

FWHM Full Width at Half Maximum

GIS Gas Imaging Spectrometer

GSFC Goddard Space Flight Center

HCL Harvard Cyclotron Labortory

HEAO High Energy Astrophysics Observatory

HK Housekeeping

ISAS Institute of Space and Astronautical Science

KSC Kagoshima Space Center

LN2 Liquid Nitrogen

LL Lincoln Laboratory

MCA Multichannel Analyzer

MOS Metal-Oxide-Semiconductor

NEAT New England Affiliated Technologies (translation stage)

PFC Plasma Fusion Center

PH Pulse Height

PSF Point Spread Function

P-V Phosphorus-Vacancy

PV Performance Verification

QE Quantum Efficiency

RBM Radiation Belt Monitor

RMS Root Mean Square

SAA South Atlantic Anomoly

SBD Surface Barrier Diode

SCP Sacrificial Charge Packet

SIS Solid State Imaging Spectrometer

SPT Split Event Threshold

TEC Thermal Electric Cooler

UV Ultraviolet

XMM X-ray Multi-Mirror Mission

XRB X-ray Background

XRT X-ray Telescope